REVERSE FLOW CATALYTIC MEMBRANE REACTORS FOR ENERGY EFFICIENT SYNGAS PRODUCTION

Samenstelling promotiecommissie:

Prof. dr. ing. M. Wessling, voorzitter	Universiteit Twente
Prof. dr. ir. J.A.M. Kuipers, promotor	Universiteit Twente
Dr. ir. M. van Sint Annaland, assistent-promotor	Universiteit Twente
Prof. dr. ir. L. Lefferts	Universiteit Twente
Prof. dr. ir. G.F. Versteeg	Universiteit Twente
Prof. Dr. hab. inz. K. Gosiewski	Jan Dlugosz University
Prof. Dr.-Ing. U. Nieken	Universität Stuttgart
Dr. H.P.C.E. Kuipers	Shell Global Solutions
Ir. P.P.A.C. Pex	ECN

The research reported in this thesis was funded by the Dutch Technology Foundation STW, the Energy research Centre of the Netherlands ECN and the Association of Industrial Advisory Council Members of the Dutch Institute for Catalysis Research VIRAN and was carried out within STW project UPC 5037, "Catalytic partial oxidation (CPO) of methane combined with air separation: from molecular event to pilot plant".

Publisher: PrintPartners Ipskamp B.V., P.O. Box 333, 7500 AH Enschede, The Netherlands

---

Smit, J.
Reverse Flow Catalytic Membrane Reactors for Energy Efficient Syngas Production
PhD thesis, University of Twente, The Netherlands
ISBN: 90-365-2308-7

REVERSE FLOW CATALYTIC MEMBRANE REACTORS FOR ENERGY EFFICIENT SYNGAS PRODUCTION

PROEFSCHRIFT

ter verkrijging van
de graad van doctor aan de Universiteit Twente,
op gezag van de rector magnificus,
prof. dr. W.H.M. Zijm,
volgens besluit van het College van Promoties
in het openbaar te verdedigen
op vrijdag 27 januari 2006 om 15.00 uur

door

Joris Smit

geboren op 17 december 1976

te Sint-Oedenrode

Dit proefschrift is goedgekeurd door de promotor

Prof. dr. ir. J.A.M. Kuipers

en de assistent-promotor

Dr. ir. M. van Sint Annaland

Aan mijn ouders

CONTENTS

Summary

Natural gas is becoming an increasingly important energy source, due to the increasing energy demands and declining oil reserves, whereas large volumes of natural gas are still widely available, especially at remote locations. In view of the existing infrastructure for liquid fuels, natural gas is most efficiently used in the transport sector by converting it to liquid fuels via the Gas-To-Liquid (GTL) process. The GTL-process consists of an air separation unit followed by a partial oxidation (POX) unit where CH_4 is converted with pure O_2 to syngas (a mixture of CO and H_2). In a third unit syngas is converted to liquid fuels via the Fischer-Tropsch reaction. Although several different syngas production technologies have been commercialised, so far the GTL-process has not found widespread application yet, mainly because of the enormous investment costs ($>$ 1 billion US \$) related to the air separation and POX units. To decrease these investment costs, two areas of possible cost reduction have been identified: improved recuperative heat exchange, which reduces the pure O_2 consumption, and an alternative air separation. To improve the recuperative heat exchange, a Reverse Flow Catalytic Membrane Reactor (RFCMR) with porous membranes is proposed in this thesis, in which very efficient heat exchange between the feed and product streams is achieved by using the reverse flow concept (*i.e.* periodic alternation of the flow direction of the gas through a fixed catalyst bed). In this novel reactor concept porous membranes (or filters) are employed to distributively feed the O_2 to the CH_4, so that hot spots and premixed feeds with the risk of the formation of an explosive mixture can be avoided. Furthermore, the porous membranes are filled with a catalyst to promote the partial oxidation reactions (*i.e.* catalytic partial oxidation, CPO). The porous membranes can be replaced by O_2 perm-selective perovskite membranes (*i.e.* a RFCMR with perovskite membranes), so that also air separation can be integrated. In this thesis these RFCMR concepts with porous or perm-selective

membranes have been developed and their feasibilities have been investigated with simulation and experimental studies.

To illustrate the importance of recuperative heat exchange for POX processes and to quantify the thermodynamic potential of both RFCMR concepts, an adiabatic thermodynamic analysis has been carried out. It was found that for POX processes with stoichiometric feeds of CH_4 and O_2 very high feed temperatures and thus very expensive high temperature heat exchangers are required to achieve high syngas yields, which is not economically feasible. When excess O_2 is used to partially preheat the feeds by combustion of part of the CH_4, lower feed temperatures suffice, but at the cost of a lower CO selectivity with respect to CO_2 and a lower H_2 selectivity with respect to H_2O. Therefore, in commercialised POX processes usually the feeds are preheated to about 700 K and O_2/CH_4 ratios of 0.6-0.7 are employed, which limits the selectivities of CO and H_2 to about 90 %. When the POX process is carried out in the RFCMR concepts, the CO and H_2 selectivities can in principle be increased up to close to 100 % and the consumption of pure O_2 can be decreased by 25-40 %, because of the improved and integrated recuperative heat exchange.

For a thorough assessment of the conceptual feasibility of the RFCMR concepts, detailed reactor models have been developed. Very similar to a conventional reverse flow reactor, the RFCMR can be described by a system of strongly coupled non-stationary, convection dominated, partial differential equations (PDE's) with strongly nonlinear source terms. Because of the steep concentration and temperature gradients prevailing in these type of reactors and the large differences in time scales of mass and heat accumulation, a numerically very efficient algorithm is required to solve the system of PDE's within an acceptable CPU time. Therefore, a numerical algorithm has been developed and programmed, which is based on a finite volume technique with implicit higher order singly diagonal implicit Runge-Kutta (SDIRK) schemes for the time integration and higher order weighted essentially non-oscillatory (WENO) schemes for the discretisation of the convection terms. Furthermore, a local grid adaptation procedure was developed that makes effective use of the smoothness indicators and interpolation polynomials of the WENO schemes and also automatic time step adaptation was incorporated. Using the simulation of a conventional reverse flow reactor, it has been shown that with the developed numerical algorithm the number of grid cells required to accurately capture the steep concentration and

temperature gradients can be greatly reduced (by a factor of up to 100) and that very large time steps can be used, both of which decrease the CPU demand enormously, so that the RFCMR concepts concepts can be studied in detail.

To demonstrate the conceptual feasibility of the RFCMR concept with porous membranes, two 1-D reactor models have been developed: the Dynamic Model (DM), that takes the dynamic behaviour of the reactor fully into account and a limiting case of this model, the High Switching Frequency Model (HSFM). In the HSFM a steady state is reached, which requires much less CPU time in comparison to the DM, where it takes a long computation time to compute the cyclic steady state. Both models include a detailed description of the prevailing heat and mass transfer processes and reaction kinetics of the relevant reactions. Firstly, with HSFM simulations the RFCMR concept was further developed. It was found that a small amount of CH_4 should be combusted in the O_2 compartment just before the membrane section to establish the desired trapezoidal temperature profile and, furthermore, that a small amount of H_2O has to be added to the O_2 feed to avoid runaways in the centre of the reactor. Subsequently, DM simulations were carried out to evaluate the dynamic reactor performance in terms of syngas selectivities for different CPO catalyst particle diameters, membrane lengths, switching times and tube diameters. The simulation results showed that very high syngas selectivities (> 98 %) can be achieved for O_2/CH_4 ratios as low as 0.45, which clearly demonstrates the great potential of the RFCMR concept with porous membranes for energy efficient syngas production.

In order to evaluate the technical feasibility of the RFCMR concept with porous membranes, a demonstration unit has been constructed. Different CPO catalysts and ceramic porous membranes have been tested in a separate isothermal membrane reactor and it was shown that with a Rh/Al_2O_3 catalyst and a porous Al_2O_3 membrane very high syngas selectivities could be achieved. To determine the optimal operating conditions in the air compartment of the RFCMR (air was used instead of O_2 for safety reasons), the demonstration unit was first tested as a conventional reverse flow reactor. It was found that even small radial heat losses greatly affect the reactor behaviour, as expected, and that as a result significantly higher flow rates and CH_4 inlet fractions had to be used than would be required for an industrial scale reactor to establish the desired trapezoidal temperature profile. A reactor model has been developed that includes a detailed description of the heat loss through the insulation layer,

with which the measured axial temperature profiles could be very well described. Because of the fragility and rigidness of the Al_2O_3 support tubes and porous membranes, it was very difficult to implement these in the demonstration unit. Therefore, as an alternative, a metal filter was developed, consisting of a tube in which a number of small holes were made with a laser. Subsequently, experiments were carried out in the demonstration unit at different operating conditions and it was shown that indeed very high CO and H_2 selectivities, up to 95 %, could be achieved without using any compensatory heating to counteract radial heat losses. Moreover, no hot spots were observed in the axial temperature profiles, indicating safe reactor operation. The measured axial temperature profiles could be very well described with the developed reactor model and also the agreement between the measured and predicted CO and H_2 selectivities was good. Although the maximal on-stream time of the demonstration unit was limited to about 12 hours due to cokes formation on the Al_2O_3 particles in the support tubes and because of fouling of the filter, these results clearly demonstrate the technical feasibility of the RFCMR concept with porous membranes and strongly support the results of the conceptual feasibility study.

Also for the RFCMR concept with perovskite membranes detailed reactor models have been developed and its conceptual feasibility was investigated by means of a simulation study. In order to accurately capture the influences of the local syngas composition and the temperature on the O_2 permeation rate, the O_2 permeation rate through a commercially available perovskite membrane with composition $(LaCa)(CoFe)O_{3-\delta}$ was studied experimentally in a differentially operated isothermal membrane reactor at varying operating conditions. It was found that the O_2 permeation rate is greatly enhanced in the presence of reducing gasses such as CO and H_2 on the permeate side of the membrane. Also when the temperature was increased or the membrane thickness was decreased, the O_2 permeation rate increased. From the experimental results it could be concluded that the O_2 permeation through the perovskite membrane under investigation was dominated by bulk diffusion even when a reducing atmosphere was applied at the permeate side of the membrane. The O_2 permeation rate could be well described with the Wagner equation and, when sweeping with CO or H_2, the O_2 partial pressure at the membrane surface at the permeate side of the membrane could be calculated by assuming local thermodynamic equilibrium. With the experimentally determined permeation expression, HSFM simulations were performed to determine design parameters such as the membrane length

and plateau temperature. These simulations revealed that the local heat production and consumption varies enormously along the membrane, which results in an undesired axial temperature profile and therefore also in an undesired axial O_2 permeation rate profile. This makes it very difficult to control the overall $CH_4/H_2O/O_2$ feed ratio and thus the nett heat production inside the reactor and consequently runaways were observed in the simulations. To circumvent these runaway problems, use of a porous support is proposed that acts as an additional mass transfer resistance, which is almost independent of the temperature and provides for a relatively constant O_2 permeation flux. Moreover, the porous support can be used to enhance the mechanical properties of the membrane. Provided that that a constant axial O_2 flux profile can be achieved, it has been demonstrated with DM simulations that also with the RFCMR with perovskite membranes very high syngas selectivities could be achieved, while fully integrating the air separation and recuperative heat exchange.

Samenvatting

Aardgas zal in de nabije toekomst als energiedrager een steeds belangrijkere rol spelen vanwege de toenemende energievraag en de afnemende oliereserves, terwijl er wereldwijd nog grote hoeveelheden aardgas voorradig zijn, vooral in afgelegen gebieden. Gezien de reeds aanwezige infrastructuur voor vloeibare brandstoffen, kan aardgas het meest efficiënt gebruikt worden in de transportsector door het om te zetten naar vloeibare brandstoffen via het zogenaamde "Gas-To-Liquid" (GTL) proces. Dit GTL proces bestaat uit een luchtscheidingsstap, waarin zuiver zuurstof (O_2) uit lucht wordt gewonnen, gevolgd door een partiële oxidatie (POX) reactor waarin CH_4 (aardgas) en de zuivere O_2 omgezet worden in synthese gas, een mengsel van koolstofmonoxide (CO) en waterstof (H_2). In een derde stap wordt het synthese gas omgezet in vloeibare brandstoffen middels het Fischer-Tropsch proces. Alhoewel er reeds verscheidene synthese gas productietechnologieën gecommercialiseerd zijn, wordt het GTL proces nog niet op grote schaal toegepast, voornamelijk vanwege de enorme investeringskosten ($>$ 1 miljard Euro) in de luchtscheidingsfabriek en de POX reactor. Om deze investeringskosten te beperken, zijn er twee gebieden voor mogelijke kostenbesparingen geïdentificeerd: verbeterde warmteterugwinning, waardoor het O_2 verbruik in de POX reactor kan worden verminderd, en een alternatieve luchtscheiding. Om de warmteterugwinning te verbeteren wordt in dit proefschrift een nieuw reactorconcept voorgesteld, een zogenaamde "Reverse Flow Catalytic Membrane Reactor" (RFCMR), waarin zeer efficiënte warmte-uitwisseling tussen de voedingstromen en productstromen gerealiseerd wordt door de gasstromen in de reactor periodiek om te keren (het zogenaamde "reverse flow" concept, ook wel omkeerreactor genoemd). In dit nieuwe reactorconcept worden poreuze membranen (of filters) toegepast om O_2 distributief aan CH_4 te kunnen voeden, zodat het lokaal uit de hand lopen van de temperatuur (zogenaamde "hot spots") en voorgemengde voedingen met het gevaar

van het vormen van explosieve mengsels, vermeden kunnen worden. Tevens zijn de poreuze membranen gevuld met een katalysator om de partiële oxidatie reactie te versnellen (aangeduid met "Catalytic Partial Oxidation", CPO). De poreuze membranen kunnen worden vervangen door perovskiet membranen die selectief O_2 doorlaten, waarmee ook luchtscheiding in de reactor geïntegreerd kan worden (een RFCMR met perovskiet membranen). In dit proefschrift zijn de RFCMR concepten met poreuze of perovskiet membranen verder ontwikkeld en is de haalbaarheid van beide concepten onderzocht door middel van zowel simulatie als experimentele studies.

Om het belang van warmteterugwinning voor POX processen te illustreren en om het thermodynamisch potentieel van beide RFCMR concepten te kwantificeren, is een adiabatische thermodynamische analyse uitgevoerd. Uit deze analyse bleek dat voor stoïchiometrische voedingen van CH_4 en O_2, d.w.z een O_2/CH_4 verhouding van 0.5, zeer hoge voedingstemperaturen nodig zijn om hoge synthese gas opbrengsten te kunnen realiseren, waarvoor zeer dure externe warmtewisselaren benodigd zijn die bestand zijn tegen deze hoge temperaturen, hetgeen economisch gezien niet haalbaar is. Wanneer een overmaat O_2 gebruikt wordt om de voedingsstromen gedeeltelijk voor te verwarmen door een deel van de CH_4 te verbranden, kan met een lagere voedingstemperatuur gewerkt worden, maar dit gaat gepaard met een lagere selectiviteit van CO ten opzichte van CO_2 (koolstofdioxide) en een lagere selectiviteit van H_2 ten opzichte van H_2O (water). Daarom worden de voedingstromen in gecommercialiseerde POX processen gewoonlijk voorverwarmd tot ongeveer 400 °C en worden O_2/CH_4 ratio's van 0.6-0.7 gebruikt, waardoor de maximaal haalbare CO en H_2 selectiviteiten beperkt zijn tot ongeveer 90 %. Als het POX proces in een van de RFCMR concepten wordt uitgevoerd, kunnen de selectiviteiten in principe verhoogd worden tot nabij 100 % en kan het O_2 verbruik beperkt worden met 25-40 %, vanwege de verbeterde geïntegreerde warmteterugwinning.

Voor een gedegen conceptuele haalbaarheidstudie van de RFCMR concepten zijn gedetailleerde reactormodellen ontwikkeld. Analoog aan de beschrijving van conventionele omkeerreactoren kunnen de RFCMR concepten beschreven worden met een stelsel van sterk gekoppelde, niet-stationaire, convectie gedomineerde, partiële differentiaalvergelijkingen (PDE's) met sterk niet-lineaire brontermen. Vanwege de steile concentratie- en temperatuurgradiënten die in dit type reactoren voorkomen en de grote verschillen in massa- en warmte-accumulatie, is een zeer efficiënt nu-

meriek algoritme vereist om het stelsel van PDE's op te kunnen lossen binnen een aanvaardbare rekentijd. Daarom is een numeriek algoritme ontwikkeld en geprogrammeerd, dat gebaseerd is op een eindige volume techniek en dat gebruik maakt van zogenaamde "Singly Diagonal Implicit Runge-Kutta" (SDIRK) schema's voor de discretisatie van de accumulatie termen en zogenaamde "Weighted Essentially Non-Oscillatory" (WENO) schema's voor de discretisatie van de convectietermen. Tevens is een locale grid adaptatie procedure ontwikkeld, die effectief gebruik maakt van de steilheidsindicatoren en interpolatiepolynomen van de WENO schema's en tevens is een automatische tijdstapadaptatie geïmplementeerd. Middels het simuleren van een conventionele omkeerreactor is gedemonstreerd dat met het ontwikkelde numerieke algoritme het aantal gridcellen dat vereist is om de steile concentratie- en temperatuurgradiënten nauwkeurig te kunnen beschrijven, sterk verminderd kan worden (tot een factor 100) en eveneens dat zeer grote tijdstappen gebruikt kunnen worden. Hiermee is de vereiste rekentijd sterk verminderd, zodat de RFCMR concepten tot in detail bestudeerd kunnen worden.

Om de conceptuele haalbaarheid van het RFCMR concept met poreuze membranen te bestuderen, zijn twee 1-dimensionale modellen ontwikkeld: het zogenaamde "Dynamic Model" (DM), waarin het dynamisch gedrag van de reactor volledig wordt meegenomen en een speciaal geval van dit model, het zogenaamde "High Switching Frequency Model" (HSFM). In het HSFM wordt een stationaire toestand bereikt, waardoor het HSFM veel minder rekentijd vergt dan het DM, omdat in het DM een zeer grote rekentijd noodzakelijk is om de cyclisch stationaire toestand te bereiken. In beide modellen is een gedetailleerde beschrijving opgenomen van de relevante massa- en warmtetransportprocessen en de reactiekinetiek van de relevante chemische omzettingen. Met behulp van HSFM simulaties is het RFCMR concept met poreuze membranen eerst verder doorontwikkeld. Zo bleek dat een kleine hoeveelheid CH_4 verbrand moet worden in het O_2 compartiment net voor het begin van de membraansectie om het gewenste trapezoïde temperatuurprofiel te creëren en tevens dat een kleine hoeveelheid H_2O toegevoegd moet worden aan de O_2 voeding om te waarborgen dat de temperatuur in het centrum van de reactor begrensd kan worden (voorkomen van zogenaamde "runaways"). Met het DM zijn vervolgens simulaties uitgevoerd voor verschillende diameters van de CPO katalysator, membraanlengtes, schakeltijden en buisdiameters. Uit de simulaties kwam naar voren dat inderdaad zeer hoge CO and H_2 selectiviteiten (> 98 %) kunnen worden bereikt voor zeer lage

O_2/CH_4 ratio's (0.45), wat duidelijk het grote potentieel van het RFCMR concept met poreuze membranen aantoont.

Om de technische haalbaarheid van het RFCMR concept met poreuze membranen te evalueren, is een demonstratie opstelling geconstrueerd. Verschillende CPO katalysatoren en poreuze membranen zijn eerst apart getest in een isotherme membraan reactor. Met een Rh/Al_2O_3 katalysator en een poreus Al_2O_3 membraan werden zeer hoge CO and H_2 selectiviteiten bereikt. Om de optimale bedrijfscondities te bepalen van het lucht compartiment (lucht is gebruikt in plaats van O_2 uit veiligheidsoverwegingen), is de demonstratie opstelling in eerste instantie bedreven als een conventionele omkeerreactor. Het bleek dat reeds kleine radiële warmteverliezen een grote invloed hebben op het gedrag van de reactor, zoals verwacht, en dat beduidend hogere debieten en CH_4 fracties gebruikt moesten worden dan vereist zouden zijn voor een reactor van industriële grootte ten einde het gewenste trapezoïde temperatuurprofiel te creëren. Een reactormodel is ontwikkeld waarin een gedetailleerde beschrijving van het warmteverlies door de isolatielaag is meegenomen, waarmee de gemeten axiale temperatuurprofielen zeer goed beschreven konden worden. Vanwege de breekbaarheid en starheid van de poreuze Al_2O_3 membranen bleek het niet mogelijk om deze te gebruiken in de demonstratie opstelling. Daarom is als alternatief een stalen filter ontwikkeld bestaande uit een stalen buis, waarin een aantal kleine gaatjes zijn gemaakt door middel van een laser. Met deze filter zijn vervolgens experimenten uitgevoerd in de demonstratie opstelling voor verschillende bedrijfscondities en het is aangetoond dat inderdaad zeer hoge CO en H_2 selectiviteiten (95 %) bereikt kunnen worden zonder enige toevoeging van warmte om de radiële warmteverliezen te compenseren. Tevens zijn er geen runaways en excessieve temperaturen geobserveerd, wat aanduidt dat de reactor veilig bedreven kon worden. Met het ontwikkelde reactormodel konden de axiale temperatuurprofielen zeer goed beschreven worden en ook de gemeten CO and H_2 selectiviteiten konden redelijk goed worden voorspeld. Ondanks het feit dat de maximale bedrijfstijd beperkt was tot ongeveer 12 uur vanwege koolvorming op de inerte deeltjes in de ondersteunende buizen en verstopping van de filter, tonen deze resultaten duidelijk de technische haalbaarheid van het RFCMR concept met poreuze membranen aan en worden de bevindingen van de conceptuele haalbaarheidstudie sterk ondersteund.

Ook voor het RFCMR concept met perovskiet membranen zijn gedetailleerde re-

actormodellen ontwikkeld en is de conceptuele haalbaarheid onderzocht door middel van een simulatiestudie. Om de effecten van de temperatuur en de locale samenstelling van het synthese gas op de O_2 permeatiesnelheid goed te kunnen beschrijven in de reactormodellen, is de O_2 permeatiesnelheid door een commercieel verkrijgbaar perovskiet membraan met samenstelling $(LaCa)(CoFe)O_{3-\delta}$ bestudeerd in een differentieel bedreven isotherme membraanreactor bij verschillende experimentele condities. Uit experimenten bleek dat de O_2 permeatiesnelheid sterk toeneemt als de permeatiezijde van het membraan wordt blootgesteld aan een reducerende atmosfeer van CO en/of H_2. Ook wanneer de temperatuur verhoogd wordt of wanneer een dunner membraan gebruikt wordt, neemt de O_2 permeatiesnelheid toe. Uit deze experimentele resultaten is geconcludeerd dat de O_2 permeatiesnelheid voor het bestudeerde perovskiet membraan gedomineerd wordt door bulk-diffusie, ook wanneer er een reducerende amtosfeer aanwezig is aan de permeaatzijde van het membraan. Derhalve kon de O_2 permeatiesnelheid goed worden beschreven met de Wagner-vergelijking en, indien er een reducerende atmosfeer aanwezig was aan de permeatiezijde van het membraan, kon de O_2 partiaaldruk berekend worden door lokaal thermodynamisch evenwicht te veronderstellen. Met de experimenteel bepaalde uitdrukking voor de O_2 permeatiesnelheid zijn vervolgens HSFM simulaties uitgevoerd om ontwerpparameters zoals de lengte van het membraan en de plateautemperatuur te bepalen. Uit deze simulaties kwam naar voren dat de lokale warmteproductie en -consumptie nogal varieert langs het membraan, hetgeen resulteerde in een ongewenst axiaal temperatuurprofiel en derhalve ook een ongewenst axiaal O_2 permeatieprofiel. Hierdoor bleek het bijzonder lastig te zijn om de totale $CH_4/H_2O/O_2$ voedingsverhoudingen op elkaar af te stemmen en daarmee ook de nettowarmte die geproduceerd werd in de reactor, zodat de temperatuur in het centrum niet begrensd kon worden (runways). Om de temperatuur te kunnen beheersen zou een poreuze laag aan het perovskiet membraan toegevoegd kunnen worden, welke fungeert als een massatransport-beperking (moderator) die vrijwel onafhankelijk is van de temperatuur en daarmee zorgt voor een relatief constante O_2 permeatieflux. Tevens kan met deze poreuze laag de mechanische sterkte van het membraan verbeterd worden. Gesteld dat een constant O_2 permeatieprofiel gerealiseerd kan worden, is met DM simulaties aangetoond dat ook met het RFCMR concept met perovskiet membranen zeer hoge CO and H_2 selectiviteiten behaald kunnen worden, terwijl de luchtscheiding en warmteterugwinning volledig geïntegreerd zijn.

CHAPTER 1

General Introduction

Abstract

Natural gas is becoming an increasingly important energy source, due to the increasing energy demands and declining oil reserves, whereas large volumes of natural gas are still widely available at remote locations. In view of the existing infrastructure for liquid fuels, natural gas is most efficiently used in the transport sector by converting it to liquid fuels via the Gas-To-Liquid process. In this process natural gas is converted with pure O_2, obtained from cryogenic air distillation, to syngas, which is converted to higher hydrocarbons in the Fischer-Tropsch process. Although numerous syngas production technologies have been commercialised, so far the Gas-To-Liquid process has not found widespread application yet, mainly because of the enormous investment costs related to the air separation and syngas production units. To decrease these investment costs, two areas of possible cost reduction have been identified: improved recuperative heat exchange, which also reduces the pure O_2 consumption, and an alternative air separation. Out of the numerous alternative reactor concepts that have been proposed in the literature for the syngas production unit, the most interesting concepts appear to be the reverse flow reactor with its integrated recuperative heat exchange and the porous membrane reactor with its distributive feeding of O_2 avoiding premixed feeds and hot spots. To combine the advantages of these concepts and eliminate their disadvantages, a reverse flow catalytic membrane reactor with porous membranes is proposed, in which recuperative heat exchange and the partial oxidation reaction are integrated into a single apparatus. To eliminate the investments costs associated with cryogenic air distillation, membrane reactors with alternative air separation via perovskite membranes have been proposed in the literature. However, due to the presence of a large amount of inert N_2, additional preheating of the feeds with the corresponding additional external recuperative heat exchange equipment is required, which increases the investment costs substantially. To reduce these investment costs, again the reverse flow concept can be used. Therefore, also a reverse flow catalytic membrane reactor with perovskite membranes is proposed, in which recuperative heat exchange, air separation and the partial oxidation reaction are integrated into a single apparatus. In this thesis the reverse flow catalytic membrane reactor concept with porous or perovskite membranes are developed on basis of a combined theoretical and experimental study. Finally, this chapter concludes with an outline of the thesis.

1.1 Introduction

Natural gas is becoming an increasingly important energy source because of the increasing energy demands and declining oil reserves with the accompanying rise in oil prices, which are expected to peak in the middle of the 21st century (International Energy Outlook 2004). Large volumes of natural gas are still widely available at remote locations, which have not yet been economically exploited (see Figure 1.1) and it is expected that the consumption of natural gas will increase by 70 % from 2001 to 2025. Furthermore, processing of natural gas is cleaner than oil and coal processing in terms of CO_2, NO_x and SO_2 emissions. In view of the already existing infrastructure for liquid fuels, the fact that most natural gas reserves are at remote locations and the limited availability of these reserves, converting natural gas to liquid fuels is a good mid-term solution for the near future energy demand in the transport sector. In addition natural gas can be used for large-scale power generation, using liquefaction to facilitate transportation (*i.e.* Liquefied Natural Gas, LNG).

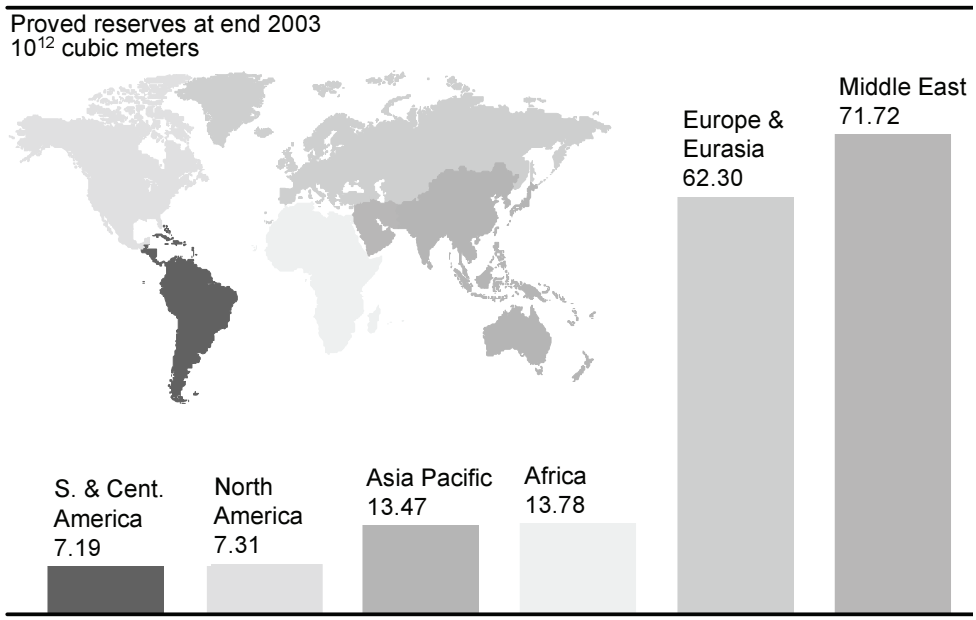

Figure 1.1: Natural gas reserves around the world (Statistical Review of World Energy, 2004).

In this section, firstly the Gas-To-Liquid process and commercial syngas production technologies will be discussed. Based on a comparison of their advantages and disadvantages, areas for conceptual improvements and investment cost reduction are identified.

1.1.1 The Gas-To-Liquid process

A well-known route to convert natural gas to liquid fuels is the so-called Gas-To-Liquid (GTL) process. A schematic overview of the GTL-process is given in Figure 1.2. In the GTL-process natural gas (here simply considered as pure CH_4) is converted with pure O_2 to syngas, a mixture of CO and H_2, via the Partial OXidation of CH_4 (POX):

$$CH_4 + \tfrac{1}{2}O_2 \rightarrow CO + 2H_2 \tag{1.1}$$

Other reactions that occur in parallel with POX are full combustion of CH_4:

$$CH_4 + 2O_2 \rightarrow CO_2 + 2H_2O \tag{1.2}$$

Steam Methane Reforming (SMR):

$$CH_4 + H_2O \rightleftharpoons CO + 3H_2 \tag{1.3}$$

dry reforming:

$$CH_4 + CO_2 \rightleftharpoons 2CO + 2H_2 \tag{1.4}$$

and the Water-Gas-Shift (WGS) reaction:

$$CO + H_2O \rightleftharpoons CO_2 + H_2 \tag{1.5}$$

Subsequently, the produced syngas is converted to higher hydrocarbons (olefines, parafines) in the famous Fischer-Tropsch (FT) process (Fischer and Tropsch, 1926):

$$nCO + 2nH_2 \rightarrow (CH_2)_n + nH_2O \tag{1.6}$$

Besides natural gas, also pure O_2 is used as feedstock in the GTL-process, which is obtained by cryogenic air distillation. An air-based GTL-process would lead to substantial additional compression costs upstream of the syngas production unit and would yield syngas with a N_2 content of about 50 %, which requires large purge gas streams in the FT-reactor, rendering an air-blown process economically unfeasible

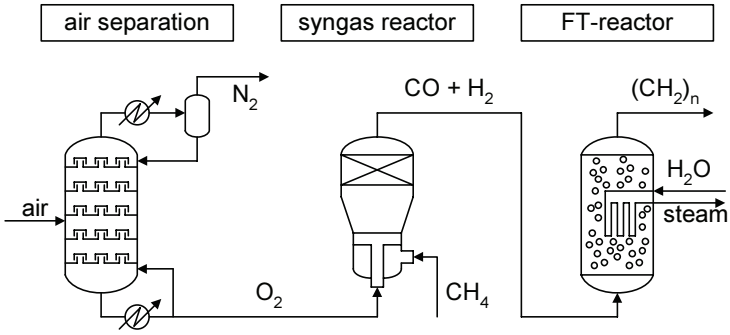

Figure 1.2: Schematic overview of the GTL-process.

(Wilhelm et al., 2001). Currently, there are about 40 projects worldwide to build GTL-plants with capacities up to 100.000 barrels/day (Sinor, 2001).

Another route to convert natural gas into liquid fuels is direct oxidative coupling of CH_4 and much research was focussed on this route in the 1980's. However, due to low C_2H_6 and C_2H_4 yields, so far this route has not been commercialised (Lunsford, 2000). This thesis focusses on the technology to convert natural gas into syngas.

1.1.2 Commercial syngas production technologies

The conventional route from CH_4 to syngas is the energy-consuming SMR process, which is usually carried out in a fixed bed of a supported Nickel catalyst (Rostrup-Nielsen, 1984). SMR-technologies have been developed by a number of companies (such as Air Products, KTI, ICI, BP/Kværner, Kellog, Haldor Topsoe, Krupp Uhde and Lurgi) and are used mainly for the production of NH_3 and CH_3OH. However, for a GTL-process a SMR unit makes up about 60-70 % of the total cost (Foulds and Lapszewicz, 1994) and the H_2/CO ratio of the produced syngas is not optimal for the FT-process (≈ 3). The ideal H_2/CO ratio for the FT-process (≈ 2) can be directly produced with the POX reaction, see Equation 1.1. Therefore, in this study POX will be considered as the most interesting route for syngas production.

The eldest commercial POX technologies were developed by Shell and Texaco and use a burner (Brejc and Supp, 1989). This technology is also used in Shell's GTL-plant in Malaysia. The disadvantages of this technology are the very high reactor

outlet temperature (± 1600 K), the high required O_2/CH_4 ratio (± 0.7) with the accompanying moderate syngas selectivities (< 90 %) and the somewhat low H_2/CO ratio (± 1.7-1.8) of the syngas produced. To increase the H_2/CO ratio to the optimal value for the FT-process, SMR units are operated in parallel.

A variant of the POX burner is the so-called Auto-Thermal Reformer (ATR), which also uses a burner to carry out the POX reaction. A fixed bed consisting of a reforming catalyst is positioned downstream the burner section to allow the hot gasses to approach equilibrium. The ATR has a lower reactor outlet temperature (± 1300 K) and the required O_2/CH_4 ratio is lower, typically about 0.6, which results in higher syngas selectivities (± 90 %). Furthermore, some H_2O is added to the CH_4 feed (H_2O/CH_4 ratio is about 0.2-0.6) to tune the H_2/CO ratio. This type of design is offered by Lurgi, Haldor Topsoe and ICI. The Haldor Topsoe technology is used in Sasol's GTL-plant in South Africa.

ExxonMobile has developed a fluidised bed reactor, where CH_4 and H_2O act as fluidising agent and O_2 is injected via nozzles (Eisenberg et al., 1999). The feed streams and the reactor outlet temperature are very similar to that of the ATR, but problems were reported related to local hot spots at the O_2 injection nozzles, destroying the catalyst particles.

Yet another family of POX technologies are the so-called gas-heated reformers, in which SMR is indirectly combined with ATR using internal heat exchange. Such technologies are offered by Air Products, BP/Kværner, Haldor Topsoe, ICI, Kellogg, Krupp Uhde, KTI and Lurgi. Lurgi's technology is used in the Mossgas GTL-plant in South Africa, but problems have been reported related to burner operation and lifetime and also metal dusting (Wilhelm et al., 2001).

For a conventional GTL-process with a commercial syngas production technology as discussed above, up to 60 % of the investment costs is related to cryogenic air distillation and syngas production (Aasberg-Petersen et al., 2001; Wilhelm et al., 2001), where both units contribute about 30 % each. Operating costs are relatively small and 65 % of the production costs of a FT-liquid is related to the investment costs. Besides the fact that the production of pure O_2 is expensive, it is also hazardous to handle. In 1997 there was an explosion in Shell's GTL-plant in Malaysia, shutting down production for over 5 years (Wilhelm et al., 2001). Comparing the different

commercial syngas production technologies, they are quite similar with respect to feed streams, operating pressures (20-60 bar) and in- and outlet temperatures. All technologies require expensive, pure O_2. Furthermore, the CH_4 and O_2 (and H_2O) feeds are preheated to about 650 K and excess O_2 is used to further preheat the feeds to the desired operating temperatures using the additional reaction heat from CH_4 combustion. The reactor outlet temperature ranges from 1300-1600 K, whereas the FT-process typically operates at 500-600 K. These differences in the low inlet and downstream temperatures on one hand and the high reactor outlet temperature on the other hand require very expensive heat exchange equipment and constitute an important contribution to the high investment costs of a conventional GTL-plant. The observations discussed above point to two areas for conceptual improvements to reduce the investment costs:

- Improved recuperative heat exchange, which reduces the cost of expensive external heat exchangers and reduces the consumption of pure O_2;
- Alternative air separation, which avoids expensive cryogenic air distillation.

1.2 Literature review on alternative reactor concepts

Many alternative reactor concepts for the production of syngas have been proposed in the literature. In this section an overview is given, where it is stressed that the objective of this review is not to give an exhaustive overview of all the work that has been done on syngas production in the open literature and elsewhere. The overview intends to provide a sound basis for the development of novel reactor concepts.

1.2.1 Plasma reactors

As an alternative to the burners used in POX and ATR technologies, plasma reactors have been proposed (Caldwell et al., 2001; Czernichowski, 2001). In these reactors CH_4 and O_2 are converted to syngas by electric discharges, which produce extremely active species that facilitate conversion towards equilibrium compositions. Usually a rather short residence time is employed and a catalytic fixed bed zone is added to allow for additional steam and dry reforming, very similar to the ATR reactor. Reasonable conversions and selectivities were reported, but the performance was poorer than for conventional technologies. It was claimed that plasma reactors could be 30-45 %

less expensive than ATR reactors and that high temperatures can be avoided, but a major disadvantage of plasma reactors is the premixed feed of CH_4 and O_2 with the accompanying possible formation of explosive mixtures. This process has been developed to pilot plant scale by Synergy (Czernichowski, 2001), but this company ceased to exist shortly after.

1.2.2 Fixed bed reactors

In order to carry out the POX reaction at lower temperatures than used in burners and to reduce the residence time, fixed bed reactors have been proposed. Catalysts for the Catalytic Partial Oxidation (CPO) of CH_4 have been researched since the 1920's (Liander, 1929) and in early work Ni/Al_2O_3 was identified as a very active catalyst, but problems related to carbon formation were reported. In the last decades also other catalysts and supports were studied extensively in literature. Suitable catalysts were found to be supported Nickel, Cobalt or Iron catalysts, supported noble metal catalysts, transition metal carbide catalysts and supported metal oxide catalysts. Reviews can be found in for instance Foulds and Lapszewicz (1994), Tsang et al. (1995), Peña et al. (1996), Freni et al. (2000) and York et al. (2003).

Although many suitable catalysts have been reported to carry out CPO in a fixed bed reactor, the fixed bed reactor concept has two principal disadvantages; the premixed feed of O_2 and CH_4 and the formation of hot spots. When hot spots are formed, the reaction heat is released in a very small part of the catalyst bed. This leads to very high local temperatures, which are detrimental for the CPO catalyst, especially for noble metal catalysts. Not surprisingly, this phenomenon has been the explanation of the very high conversions and selectivities at moderate outlet temperatures reported in early work. The risks of premixed feeds and hot spots were nicely illustrated by the results of Heitnes et al. (1994), who found that at low space-hour velocities (defined as the ratio of volumetric flow rate of reactants per hour at standard conditions to the total catalyst volume) the maximum temperature in the fixed bed was already reached before the beginning of the catalytically active section.

To avoid hot spots and flashbacks in the fixed bed reactor, a number of solutions have been proposed. One solution is to carry out CPO at very high space-hour velocities to keep the maximum temperature peak in the catalytically active section of the bed and broaden the reaction zone. This was demonstrated by Hohn and

Schmidt (2001), who measured equilibrium conversions for space-hour velocities as high as $2{\cdot}10^6$ h^{-1}. Another approach was proposed by Ioannides and Verykios (1997), who studied a heat-integrated wall reactor consisting of an open, small tube placed in a larger, single-ended tube. In this reactor concept, the premixed feed is fed to the smaller tube filled with a combustion catalyst to combust part of the CH_4, after which the gas enters the larger tube, filled with a reforming catalyst. The small and large tube are positioned in such a way that the gasses flow in counter-current mode separated only by the wall of the small tube. The idea is that the heat produced in the combustion section is transported through the wall of the small tube to the reforming section, so that hot spots can be avoided. A similar, dual bed reactor concept was recently proposed by Zhu et al. (2004). The feasibility of this reactor concept will be determined by the radial temperature gradients that can be allowed and therefore the diameter of and the distance between the tubes.

Although very active CPO catalysts for fixed bed reactors have been reported in the literature and different operation modes and reactor configurations have been studied that could avoid hot spots and flashbacks, the fixed bed reactor concept requires pure O_2 and the feeds need to be mixed and preheated. The auto-ignition temperature of a mixed O_2/CH_4 feed is only about 500 K and the temperature to which the feed can be preheated should be lower than this. Since for an ATR reactor the feeds are typically preheated to 600-700 K, a CPO reactor requires higher O_2/CH_4 ratios in comparison to the ATR reactor to arrive at the same equilibrium temperature. Therefore, the CPO reactor has a higher O_2 consumption and lower syngas selectivities than the ATR reactor. For these reasons, the feasibility of CPO fixed bed reactors for the production of syngas on industrial scale is regarded with scepticism in industry (Aasberg-Petersen et al., 2003).

1.2.3 Fluidised bed reactors

To overcome the problems of hot spots in fixed beds reactors, usually fluidised bed reactors are employed due to their excellent heat transfer characteristics. In the literature, fluidised bed reactors for CPO with premixed feeds operating in the bubbling regime were studied by numerous research groups (Bharadwaj and Schmidt, 1994; Olsbye et al., 1994; Santos et al., 1994; Mleczko and Wurzel, 1997) and it was found that selectivities and conversions close to equilibrium could be obtained, without any

hot spots. Later also other operating regimes were studied both experimentally (Marnasidou et al., 1999; Marshall and Mleczko, 1999, 2000) and by simulations (Pugsley and Malcus, 1997). It was found that the internally circulating fluidised bed or the spouted fluidised bed are to be preferred at industrial scales.

Considering the advantages and disadvantages, very much the same conclusions can be drawn for the fluidised bed reactors as for the fixed bed reactors. Although there are no problems related to hot spot formation in the fluidised bed reactor, the disadvantage of a premixed feed and the accompanying higher O_2/CH_4 ratios compared to an ATR reactor remain. Alternatively, the O_2 could be injected via nozzles into the fluidised bed, which leads to ExxonMobile's reactor discussed in the previous section.

1.2.4 Reverse flow reactors

A special type of fixed bed reactor is the reverse flow reactor, in which recuperative heat exchange is integrated. In this reactor the reactants are fed to the reactor without preheating and the flow direction is periodically reversed. This results in low temperatures at the reactor in- and outlet, steep temperature gradients close to the in- and outlet and a high temperature plateau in the centre of the reactor, where the reactions take place. The plateau temperature is typically much higher than the adiabatic temperature rise, whereas the time-averaged temperature difference between the in- and outlet is equal to the adiabatic temperature rise. Because of the low heat capacity of the gas compared to the catalyst bed, the steep temperature fronts travel slowly through the bed, so that the flow direction has to be switched typically only a few times per hour. Reverse flow reactors have been applied in industry for a number of processes such as air purification to remove volatile organic compounds, SO_2 oxidation, NO_x reduction and sulfur production, see Matros and Bunimovich (1996) for an overview. More recently the reverse flow concept has also been used to couple endothermic and exothermic reactions (Kolios et al., 2000; van Sint Annaland et al., 2002a,b).

The reverse flow concept was also applied to CPO by Blanks et al. (1990) in a pilot-plant scale reactor with a premixed feed of air and CH_4 operating at nearly atmospheric pressures. Very high conversions and syngas selectivities were obtained for a cold, nearly stoichiometric feed, whereas the maximum temperature was lim-

ited to 1200 K. However, simulation studies revealed that for O_2/CH_4 mixtures at elevated pressures, very high maximum temperatures, up to 2000 K, can be expected (De Groote and Froment, 1996; Gosiewski et al., 1999; Gosiewski, 2000, 2001) and no CPO catalyst can withstand such high temperatures. It can be concluded that the reverse flow reactor concept is a very interesting concept for CPO with respect to the integrated recuperative heat exchange and reduced O_2 consumption, but the possible formation of hot spots and the requirement of a premixed feed are major disadvantages.

1.2.5 Catalytic membrane reactors with porous membranes

To overcome the problems associated with premixed O_2/CH_4 feeds and hot spots, Alibrando et al. (1997) investigated the use of a porous membrane reactor for CPO with a shell-and-tube configuration. In this reactor CH_4 is fed to the shell filled with a CPO catalyst and O_2 is fed to the tube consisting of a single support tube connected to a porous membrane, which is closed at the other end, so that all O_2 is fed distributively to the CH_4. High conversions and selectivities were reported, although for very high space-hour velocities the performance was less than that of fixed bed reactors, due to the staged addition of O_2 and poor mixing of the CH_4. The inherently safe operation and absence of hot spots give this reactor concept a major advantage over the other reactor concepts discussed so far. However, also in this concept the feed needs to be preheated and still external recuperative heat exchange is required, so that this concept has no significant advantages over existing commercial technologies.

1.2.6 Catalytic membrane reactors with perovskite membranes

The reactor concepts that have been discussed so far, focussed only on the syngas production unit and all concepts require pure O_2, whereas the air separation unit in a conventional GTL-process is also a major cost driver. Alternative air separation has recently become possible with the development of O_2 perm-selective perovskite membranes, see Bouwmeester (2003) for a review. Since the operating temperatures of these membranes correspond to those required for CPO, integration of air separation and CPO into a single apparatus seems very attractive. Furthermore, due to the O_2 consumption by the POX reaction, the O_2 concentration at the membrane surface on the syngas side is strongly reduced, which results in a high driving force over

the membrane and a high accompanying permeation flux, because the permeation rate through perovskites is related to the difference in chemical potential of O_2 over the membrane. For the same reason, the air side can be operated at atmospheric pressures, while higher pressures can be used at the syngas side. Since the air is now separated *in situ*, premixed feeds are avoided and since the O_2 is fed distributively, also hot spots are avoided. The integration of air separation with perovskite membranes and CPO into a single reactor has already been demonstrated on lab-scale by a few research groups (Balachandran et al., 1995; Tsai et al., 1997; Jin et al., 2000; Dong et al., 2001) and also on a pilot plant-scale in the Air Products ITM project (Chen, 2004). Indeed this reactor concept appears to be very promising and an investment cost of reduction of up to 33 % compared to conventional technologies was estimated (Chen et al., 2001), but the long-term chemical stability and mechanical strength of the perovskite membranes are still issues to be dealt with and also the allowed pressure difference between the air and syngas compartment is a point of attention. A disadvantage compared to conventional technologies is that the gas flow rates are more than doubled because of the N_2 present in the air, leading to increased preheating duty and additional recuperative heat exchange and therefore higher investment costs.

1.3 This thesis

In this thesis two novel reactor concepts for the production of syngas are proposed, based on the integration of the reverse flow concept in catalytic membrane reactors. In this section a short introduction to these new reactor concepts is given, followed by the outline of the thesis.

1.3.1 Reverse flow catalytic membrane reactors

Based on a review of commercially available syngas production technologies two areas for conceptual improvements and cost reduction were identified, *viz.* improved recuperative heat exchange, which reduces the cost of expensive external heat exchangers and the consumption of the expensive pure O_2, and alternative air separation, which avoids expensive cryogenic air distillation. Subsequently, alternative reactor concepts studied in the literature were reviewed. In the reverse flow reactor studied by Blanks et al. (1990) recuperative heat exchange was integrated inside the reactor, however this reactor concept has the disadvantages of hot spot formation and premixed feeds.

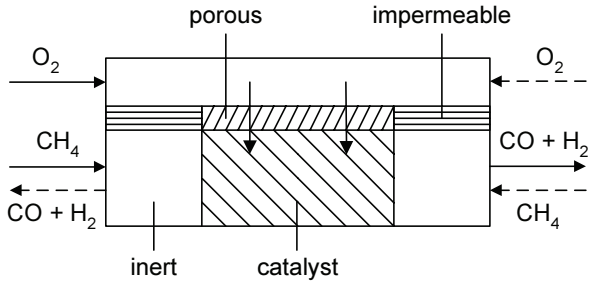

Figure 1.3: Schematic overview of the RFCMR concept with porous membranes.

These disadvantages are circumvented in the porous membrane reactor concept studied by Alibrando et al. (1997), but in this concept the recuperative heat exchange is not integrated inside the reactor. To combine the advantages of both these reactor concepts and eliminate their disadvantages, a novel reactor concept is now proposed, a reverse flow catalytic membrane reactor (RFCMR) with porous membranes, in which the recuperative heat exchange, CPO and the distributive feeding of O_2 are integrated into a single apparatus. This RFCMR basically consists of two compartments (*e.g.* shell-and-tube configuration), which are separated by porous membranes in the centre of the reactor and by impermeable walls at the in- and outlet, as schematically represented in Figure 1.3. The gas streams are fed co-currently to the compartments and the flow directions are periodically alternated to create the reverse flow behaviour. At the centre, the syngas compartment is filled with CPO catalyst, whereas at the in- and outlet of this compartment and also throughout the O_2 compartment inert material is positioned for additional heat capacity and to prevent back-reactions. With the RFCMR with porous membranes, improved recuperative heat exchange, reduced O_2 consumption (20-40 %) and higher syngas selectivities ($>$ 95 %) compared to conventional technologies are aimed for and therefore lower investment costs for the syngas production and the air separation unit.

With the RFCMR with porous membranes, still expensive cryogenic air distillation is required, despite the fact that the O_2 consumption is reduced. With the catalytic membrane reactor concept with perovskite membranes studied by Balachandran et al. (1995), air separation can be integrated inside the reactor and the expensive air separation unit can be eliminated. However, since N_2 is also fed to the syngas reactor, the gas flow rates are more than doubled. Therefore, additional preheating of the feeds

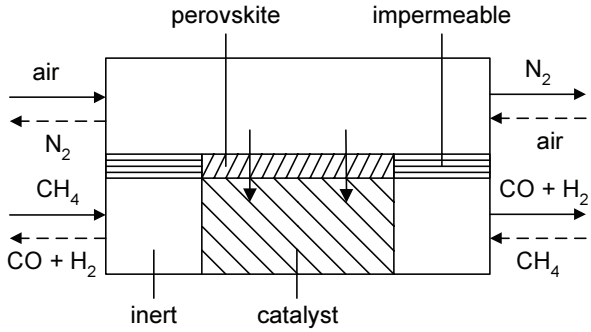

Figure 1.4: Schematic overview of the RFCMR concept with perovskite membranes.

and additional external recuperative heat exchange is required, which increases the investment costs substantially. To reduce these investment costs, again the reverse flow concept can be used. Therefore a second novel reactor concept is proposed, a RFCMR with perovskite membranes, in which recuperative heat exchange, air separation and CPO are integrated into a single apparatus. The reactor geometry of this reactor concept is very similar to that of the RFCMR with porous membranes, only the porous membranes are replaced with perovskite membranes, see Figure 1.4 for a schematic overview.

In Table 1.1 the advantages and disadvantages of commercial syngas production technologies, alternative reactor concepts proposed in the literature and the proposed new RFCMR concepts are summarised with respect to premixed feeds, hot spots, recuperative heat exchange and integrated air separation.

Table 1.1: Advantages (+) and disadvantages (–) of different reactor concepts for syngas production.

	absence of hot spots	absence of premixed feeds	integrated recuperative heat exchange	integrated air separation
ATR (commercial)	+	+	–	–
POX (commercial)	+	+	–	–
Fixed bed reactor	–	–	–	–
Fluidised bed reactor	+	–	–	–
Reverse flow reactor	–	–	+	–
Membrane reactor				
porous	+	+	–	–
perovskite	+	+	–	+
RFCMR				
porous	+	+	+	–
perovskite	+	+	+	+

1.3.2 Thesis outline

In the previous sections it was found that different feed compositions (O_2/CH_4 and H_2O/CH_4 ratio) and feed temperatures as well as different operating pressures are used in industrial practice. The main reason for this is related to the heat management of the reactor. To quantify these observations, in Chapter 2 an adiabatic thermodynamic analysis of the POX reaction for a pure O_2 and air feed is performed. Furthermore, the adiabatic thermodynamic analysis quantifies the importance of recuperative heat exchange.

To describe the proposed RFCMR concepts and to study their feasibility, detailed reactor models, consisting of a system of strongly coupled non-stationary convection-diffusion-reaction Partial Differential Equations (PDE's) with strongly non-linear source terms, are developed. The numerical solution of these models is a very CPU demanding task because of the prevailing steep concentration and temperature gradients requiring very small grid sizes and time steps, whereas very long simulation times are required to attain the cyclic steady state temperature profiles. Because of the unique geometry and operation of the RFCMR concepts, available numerical algorithms cannot be used. Therefore, in Chapter 3 a powerful numerical algorithm is developed, which employs higher order discretisation schemes for the accumulation and convection terms and also automatic, local grid and time step adaptation procedures in order to minimise the CPU demand.

In Chapter 4 a reactor model is developed to describe the RFCMR concept with porous membranes. Subsequently, simulations are carried out to assess the conceptual feasibility of the reactor concept and to determine the optimal geometry and operating conditions.

To demonstrate the technical feasibility of the RFCMR concept with porous membranes with experiments, a set-up was constructed to measure axial temperature profiles and the composition of the produced syngas in a small lab-scale reactor. In Chapter 5 the experimental results are presented and discussed. Furthermore, a reactor model is developed to describe the reactor behaviour.

In Chapter 6 a reactor model is developed to describe the RFCMR concept with perovskite membranes. In order to capture the influences of the operating conditions

and the syngas compositions on the O_2 permeation behaviour in the reactor model, the O_2 permeation rate through a perovskite membrane is studied experimentally for different operating conditions. Finally, the conceptual feasibility of also this novel reactor concept is demonstrated by simulations.

Acknowledgement

The financial support of the Dutch Technology Foundation STW, the Energy research Centre of the Netherlands ECN and the Association of Industrial Advisory Council Members of the Dutch Institute for Catalysis Research VIRAN is gratefully acknowledged.

Bibliography

Aasberg-Petersen, K., Bak Hansen, J. H., Christensen, T. S., Dybkjaer, I., Seier Christensen, P., Stub Nielsen, C., Winter Madsen, S. E. L., Rostrup-Nielsen, J. R., "Technologies for large scale gas conversion", Applied Catalysis A: General, 221(1-2), 379–387 (2001)

Aasberg-Petersen, K., Christensen, T. S., Stub Nielsen, C., Dybkjær, I., "Recent developments in autothermal reforming and pre-reforming for synthesis gas production in GTL applications", Fuel Processing Technology, 83(1-3), 253–261 (2003)

Alibrando, M., Hahm, H. S., Wolf, E. E., "Partial oxidation of methane to synthesis gas on a Rh/TiO_2 catalyst in a fast flow porous membrane reactor", Catalysis Letters, 49(1-2), 1–12 (1997)

Balachandran, U., Dusek, J. T., Mieville, R. L., Poeppel, R. B., Kleefisch, M. S., Pei, S., Kobylinski, T. P., Udovich, C. A., Bose, A. C., "Dense ceramic membranes for partial oxidation of methane to syngas", Applied Catalysis A: General, 133(1), 19–29 (1995)

Bharadwaj, S. S., Schmidt, L. D., "Synthesis gas formation of catalytic oxidation of methane in fluidized bed reactors", Journal of Catalysis, 146(1), 11–21 (1994)

Blanks, R. F., Wittrig, T. S., Peterson, D. A., "Bidirectional adiabatic synthesis gas generator", Chemical Engineering Science, 45(8), 2407–2413 (1990)

Bouwmeester, H. J. M., "Dense ceramic membranes for methane conversion", Catalysis Today, 82(1-4), 141–150 (2003)

Brejc, M., Supp, E., "Non-catalytic partial oxidation and special gasification process for higher-boiling hydrocarbons", in "Ullmanns Encyclopedia of Industrial Chemistry", Elvers, B., Hawkins, S., Ravenscroft, M., Rounsaville, J. F., Shulz, G. Eds., 5th Edition, Vol. A12, VCH Verlagsgesellschaft, Weinheim, 204–214 (1989)

Caldwell, T. A., Le, H., Lobban, L. L., Mallinson, R. G., "Partial oxidation of methane to form synthesis gas in a tubular AC plasma reactor", Studies in Surface Science and Catalysis, 136, 265–270 (2001)

Chen, C. M., "Ceramic membrane reactor systems for converting natural gas to hydrogen (ITM syngas)", US Department of Energy (2004)
URL `http://www.eere.energy.gov`

Chen, C. M., Dyer, P. N., Gerdes, K. F., Lowe, C. M., Akhave, S. R., Rowley, D. R., Asen, K. I., Eriksen, E. H., "An integrated ITM syngas/Fischer-Tropsch process for GTL conversion", in "Studies in Surface Science and Catalysis", Spivey, J. J., Iglesia, E., Fleisch, T. H. Eds., Vol. 136, Elsevier Science B.V., 45–50 (2001)

Czernichowski, A., "GlidArc assisted preparation of the synthesis gas from natural and waste hydrocarbons gases", Oil & Gas Science and Technology-Revue de l'Institut-Français du Petrol, 56(2), 181–198 (2001)

De Groote, A. M., Froment, G. F., "Simulation of the catalytic partial oxidation of methane to syngas", Applied Catalysis A: General, 138(2), 245–264 (1996)

Dong, H., Shao, Z., Xiong, G., Tong, J., Sheng, S., Yang, W., "Investigation on POM reaction in a new perovskite membrane reactor", Catalysis Today, 67(1-3), 3–13 (2001)

Eisenberg, B., Fiato, R. A., Kaufmann, T. G., Bauman, R. F., "The evolution of advanced gas-to-liquids technology", Chemtech, 29(10), 32–37 (1999)

Fischer, F., Tropsch, H., "The direct synthesis of petroleum hydrocarbons with standard pressure", Berichte der Deutschen Chemischen Gesellschaft, 59, 830–832 (1926)

Foulds, G. A., Lapszewicz, J. A., "Catalytic partial oxidation of methane to synthesis gas (Syngas)", Catalysis, 11, 412–440 (1994)

Freni, S., Calogero, G., Cavallaro, S., "Hydrogen production from methane through catalytical partial oxidation reactions", Journal of Power Sources, 87(1-2), 28–38 (2000)

Gosiewski, K., "Mathematical simulations of reactors for catalytic conversion of methane to syngas with forced concentration cycling", Chemical Engineering and Processing, 39(5), 459–469 (2000)

Gosiewski, K., "Simulations of non-stationary reactors for the catalytic conversion of methane to syngas", Chemical Engineering Science, 56(4), 1501–1510 (2001)

Gosiewski, K., Bartmann, U., Moszcynski, M., Mleczko, L., "Effect of the intraparticle mass transport limitations on temperature profiles and catalytic performance of the reverse-flow reactor for the partial oxidation of methane to synthesis gas", Chemical Engineering Science, 54(20), 4589–4602 (1999)

Heitnes, K. Lindberg, S., Rokstad, O. A., Holmen, A., "Catalytic partial oxidation of methane to synthesis gas using monolithic reactors", Catalysis Today, 21(2-3), 471–480 (1994)

Hohn, K. L., Schmidt, L. D., "Partial oxidation of methane to syngas at high space velocities over Rh-coated spheres", Applied Catalysis A: General, 211(1), 53–68 (2001)

International Energy Outlook, US Department of Energy (2004)
URL `http://www.eia.doe.gov`

Ioannides, T., Verykios, X. E., "Catalytic partial oxidation of methane in a novel heat-integrated wall reactor", Catalysis Letters, 47(3-4), 183–188 (1997)

Jin, W., Lia, S., Huanga, P., Xu, N., Shia, J., Lin, Y. S., "Tubular lanthanum cobaltite perovskite-type membrane reactors for partial oxidation of methane to syngas", Journal of Membrane Science, 166(1), 13–22 (2000)

Kolios, G., Frauhammer, J., Eigenberger, G., "Autothermal fixed-bed reactor concepts", Chemical Engineering Science, 55(24), 5945–5967 (2000)

Liander, H., "The utilization of natural gases for the ammonia process", Transactions of the Faraday Society, 25, 462–471 (1929)

Lunsford, J. H., "Catalytic conversion of methane to more useful chemicals and fuels: a challenge for the 21st century", Catalysis Today, 63(2-4), 165–174 (2000)

Marnasidou, K. G., Voutetakis, S. S., Tjatiopoulos, G. J., Vasalos, I. A., "Catalytical partial oxidation of methane to synthesis gas in a pilot-plant-scale spouted-bed reactor", Chemical Engineering Science, 54(15-16), 3691–3699 (1999)

Marshall, K.-J., Mleczko, L., "Short-contact-time reactor for partial oxidation of methane", Industrial & Engineering Chemistry Research, 38(5), 1813–1821 (1999)

Marshall, K.-J., Mleczko, L., "Experimental investigations of catalytical partial oxidation of methane to synthesis gas in various types of fluidized bed reactors", Chemical Engineering & Technology, 23(1), 31–37 (2000)

Matros, Y. S., Bunimovich, G. A., "Reverse-flow operation in fixed bed catalytic reactors", Catalysis Reviews-Science and Engineering, 38(1), 1–68 (1996)

Mleczko, L., Wurzel, T., "Experimental studies of catalytical partial oxidation of methane to synthesis gas in a bubbling-fluidized reactor", Chemical Engineering Journal, 66(3), 193–200 (1997)

Olsbye, U., Tangstad, E., Dahl, I. M., "Partial oxidation of methane to synthesis gas in a fluidized-bed reactor", Studies in Surface Science and Catalysis, 81, 303–308 (1994)

Peña, M. A., Gomez, J., Fierro, J. L. G., "New catalytic routes for syngas and hydrogen production", Applied Catalysis A: General, 144(1-2), 7–75 (1996)

Pugsley, T. S., Malcus, S., "Partial oxidation of methane in a circulating fluidized-bed catalytic reactor", Industrial & Engineering Chemistry Research, 36(11), 4567–4571 (1997)

Rostrup-Nielsen, J. R., "Catalytic steam reforming", in "Catalysis Science and Technology", Anderson, J. R., Boudart, M. Eds., Springer-Verlag, New York, 1–117 (1984)

Santos, A., Menendez, M., Santamaria, J., "Partial oxidation of methane to carbon monoxide and hydrogen in a fluidized bed reactor", Catalysis Today, 21(2-3), 481–488 (1994)

Sinor, J. E., "GTL projects blossoming around the world", The Sinor synthetic fuels report, 8(1), 5–1 (2001)

Statistical Review of World Energy, BP (2004)
URL `http://www.bp.com`

Tsai, C. Y., Dixon, A. G., Moser, W. R., Ma, Y. H., "Dense perovskite membrane reactors for partial oxidation of methane to syngas", AIChE Journal, 43(11), 2741–2750 (1997)

Tsang, S. C., Claridge, J. B., Green, M. L. H., "Recent advances in the conversion of methane to synthesis gas", Catalysis Today, 23(1), 3–15 (1995)

van Sint Annaland, M., Scholts, H. A. R., Kuipers, J. A. M., van Swaaij, W. P. M., "A novel reverse flow reactor coupling endothermic and exothermic reactions. Part I: Comparison of reactor configurations for irreversible endothermic reactions", Chemical Engineering Science, 57(5), 833–854 (2002a)

van Sint Annaland, M., Scholts, H. A. R., Kuipers, J. A. M., van Swaaij, W. P. M., "A novel reverse flow reactor coupling endothermic and exothermic reactions. Part II: Sequential reactor configuration for reversible endothermic reactions", Chemical Engineering Science, 57(5), 855–872 (2002b)

Wilhelm, D. J., Simbeck, D. R., Karp, A. D., Dickenson, R. L., "Syngas production for gas-to-liquids applications: technologies, issues and outlook", Fuel Processing Technology, 71(1-3), 139–148 (2001)

York, A. P. E., Xiao, T. C., Green, M. L. H., "Brief overview of the partial oxidation of methane to synthesis gas", Topics in Catalysis, 22(3-4), 345–358 (2003)

Zhu, J., Mujeebur Rahuman, M. S. M., van Ommen, J. G., Lefferts, L., "Dual catalyst bed concept for catalytic partial oxidation of methane to synthesis gas", Applied Catalysis A: General, 259(1), 95–100 (2004)

CHAPTER 2

Adiabatic Thermodynamic Analysis of the POX process

Abstract

In commercial syngas production technologies, the natural gas and O_2 feed streams are usually only partially preheated and excess O_2 is used to further preheat the feeds by combustion of part of the CH_4, which reduces the syngas yields and selectivities significantly. Moreover, high investment costs associated with external high temperature heat exchangers are required. This signifies the importance of efficient recuperative heat exchange. When also air separation is integrated in a POX reactor recuperative heat exchange becomes even more important, because of the large amounts of inert N_2 that need to be preheated next to the O_2. To illustrate the importance of recuperative heat exchange for O_2- and air-based POX processes, an adiabatic thermodynamic analysis was performed. With the adiabatic thermodynamic analysis the influences of the feed temperature, the operating pressure and the $O_2/H_2O/CH_4$ ratios of the feed streams on the syngas yields and selectivities have been investigated. For a stoichiometric O_2-based process, it was found that very high feed temperatures are required to obtain high syngas yields. Excess O_2 can be used to lower the required feed temperature substantially, but at the cost of lower syngas yields and selectivities. When the POX reaction is carried out in the RFCMR concept with porous membranes, the syngas selectivities can in principle be increased from 90 % up to 100 % and the O_2 consumption can be decreased by 20-40 % compared to commercialised technologies. Furthermore, the reaction heat produced in the POX reaction can be used to produce additional syngas via steam reforming. For an air-based POX process it was found that much higher feed temperatures are required at much larger flow rates compared to O_2-based processes to obtain similarly high syngas yields and that excess air can decrease the required feed temperatures only to some extent. As a result, recuperative heat exchange is even more important for an air-based POX process than for an O_2-based POX process, signifying the potential of the RFCMR concept with perovskite membranes.

This chapter is based on the paper:
Smit, J., van Sint Annaland, M., and Kuipers, J.A.M., Development of a novel reactor concept for the partial oxidation of methane to syngas, Chemical Engineering Research and Design, 82(A2), 245-251 (2004)

2.1 Introduction

The partial oxidation of CH_4 is only a slightly exothermic reaction ($\pm$ 23 kJ/mol CH_4), so that the adiabatic temperature rise is only moderate for a stoichiometric feed. To reach the very high temperatures required to produce syngas with high selectivities, the cold CH_4 and O_2 feeds could be preheated by the hot syngas using heat exchangers, because the FT-process operates at much lower temperatures. Nevertheless, in commercialised syngas production technologies the feeds are usually only partially preheated and excess O_2 is used to further preheat the feed by combustion of part of the CH_4, as reviewed in Chapter 1, and this reduces the syngas yields and selectivities significantly (Brejc and Supp, 1989; Aasberg-Petersen et al., 2001). The main reasons for the use of excess O_2 appear to be related to the heat management of the POX reactor and the high investment costs of external high temperature heat exchangers. This indicates that efficient recuperative heat exchange is very important. When also air separation is integrated in a POX reactor, also large amounts of inert N_2 will have to be preheated to the high reaction temperatures, which makes efficient recuperative heat exchange essential to render such a reactor economically feasible. Therefore, the main objective of this chapter is to quantify the importance of recuperative heat exchange for both O_2- and air-based POX processes and to illustrate the potential of the RFCMR concepts proposed in Chapter 1 to achieve higher syngas yields and selectivities with lower consumption of expensive pure O_2 compared to commercial technologies.

Because reaction rates in POX processes are known to be very fast, especially if (noble metal) catalysts are employed (e.g. Hickman and Schmidt, 1992), the reactor outlet compositions are usually close to equilibrium. Furthermore, because of the large size of the equipment used, the reactor can be considered to be close to adiabatic. Therefore, the required operating conditions and feed compositions to achieve high syngas yields and selectivities can be determined by an adiabatic thermodynamic analysis. For a POX process the influence of the pressure and feed temperature on the equilibrium composition and the possible formation of undesired by-products such as solid carbon (coking) are of particular interest. As discussed above, also the influence of the feed composition in terms of the molar O_2/CH_4 and H_2O/CH_4 ratio is important and therefore, besides CO and H_2, also the combustion products CO_2 and H_2O are considered in the thermodynamic analysis.

In most thermodynamic analyses about the POX reaction reported in the literature only isothermal systems were considered (Foulds and Lapszewicz, 1994; Tsang et al., 1995; Peña et al., 1996; Zhu et al., 2001; York et al., 2003). Also some adiabatic analyses were reported (Chan and Wang, 2000; Seo et al., 2002), but these studies were concerned with air/CH_4/H_2O mixtures at atmospheric pressure. In commercial technologies and in the RFCMR concepts N_2 is not present in the syngas product. Furthermore, in this study elevated pressures will be considered since also in commercial technologies and in the RFCMR concepts elevated pressures are employed because of the required operating pressure of the FT-reactor that follows downstream of the POX-reactor.

To evaluate the operating conditions of commercial POX technologies and the RFCMR concepts, some performance indicators are required. In this study the molar syngas yield (H_2 + CO) relative to the molar CH_4 feed (ideally about 3) and the molar H_2/CO ratio (ideally about 2) have been considered. The optimal values for these numbers depend on downstream (or upstream) processes and follow from an overall economic analysis. For instance, the desired H_2/CO ratio depends on the FT-process conditions and type of catalyst (Dry, 2002). An additional criterion is the absence of solid carbon (to prevent coking), which is assumed here to be formed as graphite.

In this chapter firstly the theory of chemical equilibrium and a multi-phase Gibb's free energy minimisation method are discussed. Then the importance of performing an adiabatic thermodynamic analysis rather than an isothermal analysis is illustrated for an O_2-based process. Subsequently, the influence of the operating pressure, feed temperature and feed composition on the syngas yields and H_2/CO ratio will be discussed for a conventional O_2-based process and the potential of the RFCMR concept with porous membranes is demonstrated. Finally, also the air-based process is evaluated with respect to the operating conditions and feed compositions.

2.2 Adiabatic thermodynamic analysis

In this section firstly the theory of chemical equilibrium is shortly addressed and subsequently a Gibb's free energy minimisation method is discussed, which has been used to calculate the equilibrium compositions.

2.2.1 Theory of chemical equilibrium

A closed system of species will be at chemical equilibrium when the Gibb's free energy of this system is minimal. The Gibb's free energy of a system containing N different species in Φ phases is defined by:

$$G(\mathbf{n}) = \sum_{\phi=1}^{\Phi} \left(\sum_{\mathrm{i}=1}^{\mathrm{N}} n_{\mathrm{i},\phi} \mu_{\mathrm{i},\phi} \right) \tag{2.1}$$

where the chemical potential for an ideal gas (in this study assumed for all gaseous species due to the relatively low pressures) is given by:

$$\mu_{\mathrm{i,g}} = \mu_{\mathrm{i,g}}^{\ominus} + RT \ln \left(\frac{p_{\mathrm{g}}}{p_{\mathrm{g}}^{\ominus}} \frac{n_{\mathrm{i,g}}}{\sum_{\mathrm{i}=1}^{\mathrm{N}} n_{\mathrm{i,g}}} \right) \tag{2.2}$$

and for a pure solid:

$$\mu_{\mathrm{i,s}} = \mu_{\mathrm{i,s}}^{\ominus} \tag{2.3}$$

The chemical potential is usually taken as the partial molar Gibb's free energy of formation:

$$\mu_{\mathrm{i},\phi}^{\ominus} = \Delta g_{\mathrm{f,i},\phi}^{\ominus} = \Delta h_{\mathrm{f,i},\phi}^{\ominus} - T \Delta s_{\mathrm{f,i},\phi}^{\ominus} \tag{2.4}$$

The partial molar heat of formation and the partial molar entropy of formation at standard pressure for each species can be found in a number of data collections. In this study the data collected by Daubert and Danner (1985) were used, summarised in Appendix 2.A for the relevant components considered here. The equilibrium composition of a system with a known inlet composition and known temperature and pressure, can now be calculated by minimising the Gibb's free energy with the conservation equations of mass of the individual elements as constraints:

$$\sum_{\phi=1}^{\Phi} \left(\sum_{\mathrm{i}=1}^{\mathrm{N}} a_{\mathrm{k,i}} n_{\mathrm{i},\phi,\mathrm{in}} \right) = \sum_{\phi=1}^{\Phi} \left(\sum_{\mathrm{i}=1}^{\mathrm{N}} a_{\mathrm{k,i}} n_{\mathrm{i},\phi,\mathrm{eq}} \right) = b_{\mathrm{k}} \qquad k = 1..M \tag{2.5}$$

2.2.2 Minimisation of the Gibb's free energy

The minimisation of the Gibb's free energy constitutes a constrained optimisation problem. Numerous numerical methods have been proposed to minimise the Gibb's

free energy (Smith and Missen, 1982). Here, a non-stoichiometric method is used, which allows an easy extension to a large number of different species and a straightforward treatment of multi-phase systems. Furthermore, no information is required about the reaction scheme. In this method the minimisation problem is reduced to a set of non-linear equations using Lagrange multipliers to incorporate the constraints:

$$\mathcal{L}(n,\lambda) = \sum_{\phi=1}^{\Phi}\left(\sum_{\mathrm{i}=1}^{\mathrm{N}} n_{\mathrm{i},\phi}\mu_{\mathrm{i},\phi}\right) + \sum_{\mathrm{k}=1}^{\mathrm{M}}\lambda_{\mathrm{k}}\left(b_{\mathrm{k}} - \sum_{\phi=1}^{\Phi}\left(\sum_{\mathrm{i}=1}^{\mathrm{N}} a_{\mathrm{k,i}} n_{\mathrm{i},\phi}\right)\right) \tag{2.6}$$

The conditions for the minimal Gibb's free energy are now given by:

$$\left(\frac{\partial\mathcal{L}}{\partial n_{\mathrm{i},\phi}}\right)_{\mathrm{n_{j\neq i}},\lambda} = \mu_{\mathrm{i},\phi} - \sum_{\mathrm{k}=1}^{\mathrm{M}} a_{\mathrm{k,i}}\lambda_{\mathrm{k}} = 0 \qquad \wedge \qquad n_{\mathrm{i},\phi} > 0 \tag{2.7}$$

Equation 2.7 implies that $n_{\mathrm{i},\phi} > 0$ for all species and all phases. However, if no pure solid phase is present at equilibrium, the following condition applies:

$$\left(\frac{\partial\mathcal{L}}{\partial n_{\mathrm{i},\phi}}\right)_{\mathrm{n_{j\neq i}},\lambda} = \mu^{\ominus}_{\mathrm{i},\phi} - \sum_{\mathrm{k}=1}^{\mathrm{M}} a_{\mathrm{k,i}}\lambda_{\mathrm{k}} > 0 \qquad \wedge \qquad n_{\mathrm{i},\phi} = 0 \tag{2.8}$$

In a gas-solid system first the set of Equations 2.5 and 2.7 is solved for a gas mixture only. Then the derivatives in Equation 2.8 are calculated for the pure solid phases. In case of negative derivatives, meaning that pure solid phases will be present at equilibrium, the phase with the lowest derivative is included in Equations 2.5 and 2.7, after which the set of equations is solved again. This procedure is repeated until all derivatives in Equation 2.8 are non-negative for the pure solid phases.

To calculate the equilibrium composition and temperature of an adiabatic system at a certain operating pressure with a given feed composition and feed temperature, also the energy balance has to be included. This balance states that the enthalpy of the system at equilibrium must be equal to that of the inlet mixture:

$$\sum_{\phi=1}^{\Phi}\sum_{\mathrm{i}=1}^{\mathrm{N}} n_{\mathrm{i},\phi,\mathrm{eq}} h_{\mathrm{i},\phi,\mathrm{eq}} = \sum_{\phi=1}^{\Phi}\sum_{\mathrm{i}=1}^{\mathrm{N}} n_{\mathrm{i},\phi,\mathrm{in}} h_{\mathrm{i},\phi,\mathrm{in}} \tag{2.9}$$

The system of non-linear equations to be solved now consists of $(\Phi\cdot N + M + 1)$ equations (2.5, 2.7-2.9) for the unknowns $n_{\mathrm{i=1},\phi=1},..,n_{\mathrm{i=N},\phi=\Phi},\lambda_1,..,\lambda_{\mathrm{M}}$ and T_{eq}. This system can be solved numerically using Newton's method.

2.3 Analysis results for O_2-based POX

To demonstrate the importance of performing an adiabatic thermodynamic analysis of the POX reaction rather than an isothermal analysis, in this section firstly the results obtained from an isothermal and adiabatic analysis are compared for a stoichiometric POX process. Then the influences of different feed compositions, pressures and feed temperatures are discussed and the obtained results are compared with data available for commercialised technologies. Finally, the potential of the RFCMR concept with porous membranes to achieve higher syngas yields with lower O_2 consumption compared to commercialised technologies is discussed.

2.3.1 Isothermal versus adiabatic thermodynamic analysis

In many thermodynamic studies of the POX reaction only isothermal systems were considered. An isothermal thermodynamic analysis can give a good indication on the required reactor outlet temperature. This is shown in Figure 2.1, where the syngas and carbon yield and the H_2/CO ratio are plotted as a function of the temperature for different pressures and a stoichiometric O_2/CH_4 feed (= 0.5). It is observed that very high temperatures are required to reach high syngas yields, especially at elevated pressures. At these high temperatures the H_2/CO ratio is close to its ideal value of 2

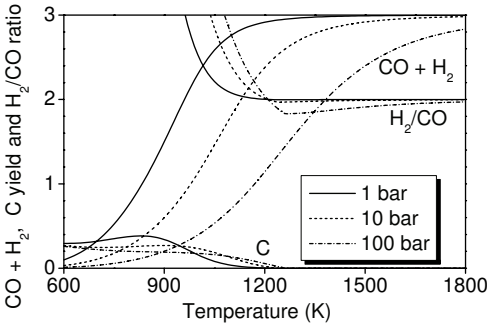

Figure 2.1: Syngas and carbon yield and H_2/CO ratio as a function of the feed temperature for different pressures, isothermal case, O_2-based ($O_2/CH_4 = 0.5$).

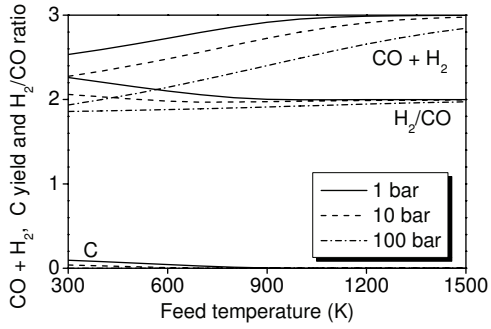

Figure 2.2: Syngas and carbon yield and H_2/CO ratio as a function of the feed temperature for different pressures, adiabatic case, O_2-based ($O_2/CH_4 = 0.5$).

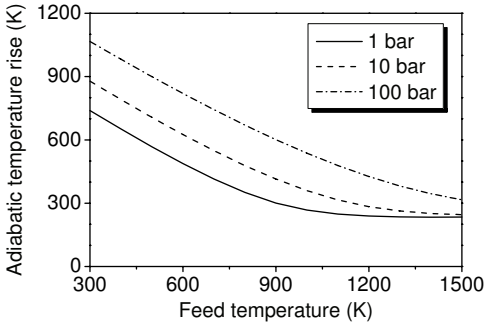

Figure 2.3: Adiabatic temperature rise as a function of the feed temperature for different pressures, O_2-based ($O_2/CH_4 = 0.5$).

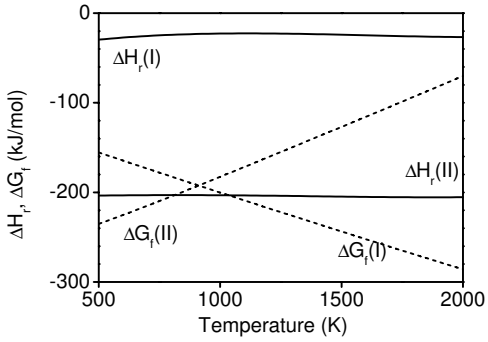

Figure 2.4: ΔH_r and ΔG_f as a function of the temperature for reactions I and II (Equations 2.10-2.11).

and solid carbon is absent. In Figure 2.2 the syngas and carbon yield and the H_2/CO ratio are plotted as a function of the feed temperature for an adiabatic system, again for different pressures and a stoichiometric feed. It is observed that reasonable syngas yields are already obtained for relatively low feed temperatures because of the high adiabatic temperature rise, see Figure 2.3. However, in order to obtain high syngas yields very high feed temperatures are required, because the adiabatic temperature rise decreases with increasing feed temperature. This can be conveniently illustrated by comparing the Gibb's free energy ΔG_f of the reaction products and the reaction heat ΔH_r of the "ideal" POX reaction ("I"):

$$\frac{1}{2}O_2 + CH_4 \rightarrow CO + 2H_2 \tag{2.10}$$

and that of a reaction seemingly prevailing at lower temperatures ("II"):

$$\frac{1}{2}O_2 + CH_4 \rightarrow \frac{1}{2}C + \frac{1}{2}CH_4 + H_2O \tag{2.11}$$

In Figure 2.4 the Gibb's free energy of the reaction products and the reaction heat of reactions I and II are plotted as a function of the temperature for an isothermal system. From this figure it can be seen that the Gibb's free energy of reaction I decreases with temperature and that of reaction II increases with temperature, so that reaction I is dominant at high temperatures and reaction II at low temperatures. The reaction heats are about constant with respect to temperature, but that of reaction I is much smaller (in absolute value) than that of reaction II. Because of this the adiabatic tem-

perature rise decreases with increasing feed temperature (Figure 2.3) and accordingly the syngas yield increases only slowly (Figure 2.2). In addition to reaction II also other reactions producing CO_2 contribute to the high adiabatic temperature rise at low feed temperatures.

2.3.2 Influence of feed composition

For an adiabatic stoichiometric POX process, it was found that very high feed temperatures are required to achieve high syngas yields, especially at elevated pressures. However, these high feed temperatures are uneconomical because of the large preheat duty and because heat exchange at high temperatures is very expensive (Rostrup-Nielsen, 2002). For this reason in industrial practice usually the feeds are only partially preheated and excess O_2 is used to further preheat the feed by combustion of part of the CH_4. In this way the required feed temperature can be reduced substantially, while still reasonable syngas yields can be achieved. This is illustrated in Figures 2.5 and 2.6, where the syngas and carbon yield, the H_2/CO ratio and the equilibrium temperature are plotted as a function of the O_2/CH_4 ratio for different feed temperatures and pressures. A typical operating pressure of 20 bar and a feed temperature of 700 K were selected as reference cases. It is observed that the syngas yield has an optimum for an O_2/CH_4 ratio of about 0.6-0.7 giving an H_2/CO ratio of about 2 depending on the feed temperature and operating pressure. In this region

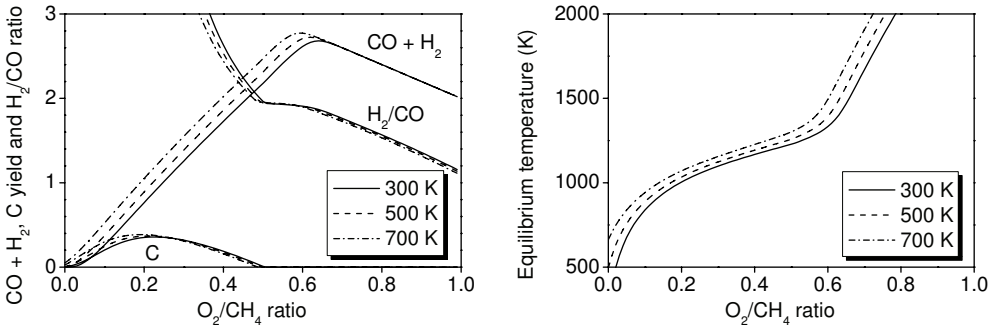

Figure 2.5: Syngas and carbon yield, H_2/CO ratio (left) and equilibrium temperature (right) as a function of the O_2/CH_4 ratio for different feed temperatures, O_2-based ($p = 20$ bar).

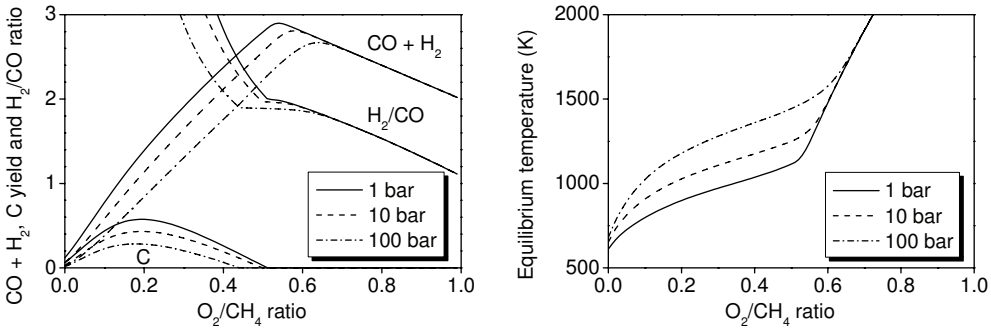

Figure 2.6: Syngas and carbon yield, H_2/CO ratio (left) and equilibrium temperature (right) as a function of the O_2/CH_4 ratio for different pressures, O_2-based ($T_{\text{feed}} = 700$ K).

solid carbon is always absent. When increasing the feed temperature, the maximal syngas yield is observed at a lower O_2/CH_4 ratio, but the H_2/CO ratio is hardly affected. Increasing the pressure leads to a lower maximal syngas yield at a higher O_2/CH_4 ratio, but again the effect on the H_2/CO ratio is limited. With respect to the equilibrium temperature, it is observed that when increasing the O_2/CH_4 ratio above 0.6-0.7, the equilibrium temperature increases sharply, because the syngas is combusted by the excess O_2. Furthermore, the equilibrium temperature at which the maximal syngas yield is achieved is primarily determined by the pressure.

From Figures 2.5 and 2.6 it can be concluded that the syngas yield and H_2/CO ratio can be optimised to acceptable values and minimal preheat duty by selecting the appropriate feed temperature, operating pressure and O_2/CH_4 ratio. In industrial ATR processes also some H_2O is added to the feed, which increases the H_2/CO ratio to the optimal value for the FT-process avoiding the need of separate steam reforming units. Although the syngas yield is hardly affected as is shown in Figure 2.7, the equilibrium temperature is significantly decreased, which poses less severe demands on the construction materials.

The influences of the pressure, feed temperature, O_2/CH_4 ratio and H_2O/CH_4 ratio on the syngas yield, the H_2/CO ratio and the equilibrium temperature have been summarised qualitatively in Table 2.1, where the following symbols have been used to show how the quantity is affected when the parameter is increased: +, the quantity

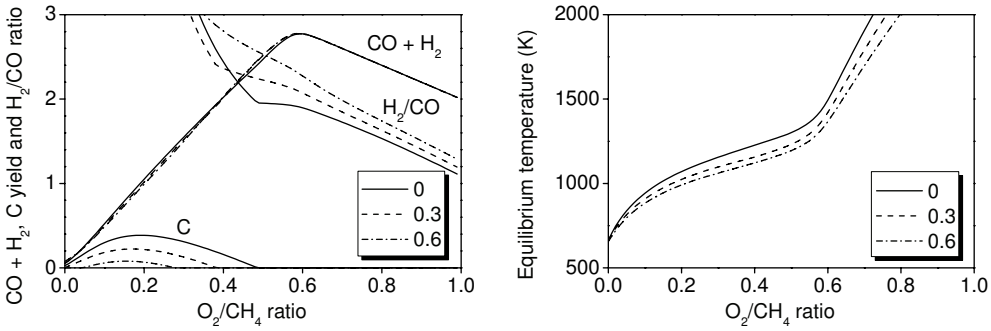

Figure 2.7: Syngas and carbon yield, H_2/CO ratio (left) and equilibrium temperature (right) as a function of the O_2/CH_4 ratio for different H_2O/CH_4 ratios, O_2-based ($p = 20$ bar, $T_{\text{feed}} = 700$ K).

Table 2.1: Influence of increasing operating parameters in a POX process.

Quantity/parameter	Pressure	Feed temperature	O_2/CH_4	H_2O/CH_4
Syngas yield	−	+	+/−	0
H_2/CO ratio	−	−	−	+
Equilibrium temperature	+	+	+	−

is increased; −, the quantity is decreased; +/−, the quantity is first increased and then decreased; 0, the quantity is hardly affected. Figures 2.5-2.7 and Table 2.1 can provide some design guidelines and correspond with typical operating conditions of commercial technologies (Brejc and Supp, 1989; Aasberg-Petersen et al., 2001) such as the O_2/CH_4 ratio (0.6-0.7), the H_2O/CH_4 ratio (0-0.5), the operating pressure (20-60 bar), the feed temperature (500-700 K) and the equilibrium temperatures (1300-1600 K). However, the optimal values of these parameters are determined by reaction kinetics, space hour velocity and reactor size and also by up- and downstream conditions and the composition of the natural gas feed stock.

2.3.3 Potential of the RFCMR concept with porous membranes

When using excess O_2 it was found that the required feed temperature can be reduced substantially, while still reasonable syngas selectivities are obtained. In the RFCMR concept with porous membranes the recuperative heat exchange is fully integrated,

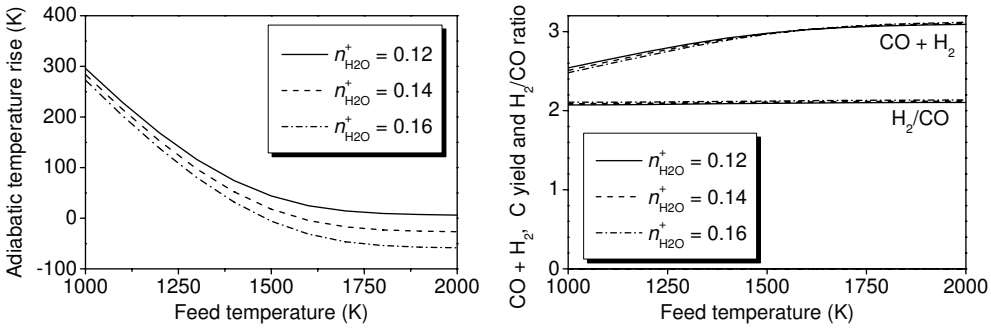

Figure 2.8: Adiabatic temperature rise (left) and syngas yield and H_2/CO ratio (right) rise as a function of the feed temperature for different amounts of added H_2O ($n^+_{H_2O}$) and CH_4 ($n^+_{CH_4} = n^+_{H_2O}$), O_2-based ($p = 20$ bar).

so no preheating of the feed nor excess O_2 is required. As a result, the O_2 and CH_4 streams can be fed stoichiometrically, which reduces the O_2 consumption by 20-40 % compared to commercial technologies. Furthermore, syngas yields and selectivities up to 100 % can be achieved, whereas for commercial technologies the selectivities are limited to about 90 % (Aasberg-Petersen et al., 2001).

For a stoichiometric feed the adiabatic temperature rise of the POX reaction is at least 200 K, see Figure 2.2. This excess heat can be used to produce additional syngas via endothermic steam reforming by feeding some additional H_2O and CH_4:

$$CH_4 + H_2O \rightleftharpoons CO + 3H_2 \tag{2.12}$$

To determine how much additional H_2O and CH_4 is required to use all excess heat for syngas production, in Figure 2.8 the adiabatic temperature rise is given as a function of the feed temperature for a pressure of 20 bar and for different amounts of H_2O and CH_4 (in moles) that are added to a stoichiometric feed of CH_4 (1 mole) and O_2. Depending on the feed temperature and desired equilibrium temperature (and pressure), about 0.12-0.15 moles of H_2O and CH_4 for the SMR reaction can be added to every mole of CH_4 that is used in the POX reaction to achieve isothermal conditions. The accompanying syngas yields and H_2/CO ratios are also plotted in Figure 2.8 and it is observed that because of the SMR reaction the syngas yields and H_2/CO ratios (≈ 2.12) are somewhat increased, because in the SMR reaction a H_2/CO ratio of 3 is produced. This is not a problem, but rather an advantage, because in the

FT-process usually H_2/CO ratios above 2 are desired, depending on the operating conditions and catalyst. For instance for Cobalt-based catalysts, H_2/CO ratios of 2.15 are employed in industry (Dry, 2002).

2.4 Analysis results for air-based POX

If perovskite membranes are integrated inside a POX reactor for *in situ* air separation, also the N_2 present in the air feed needs to be preheated, which has a large impact on the heat management of the reactor. This is illustrated in Figure 2.9, where the syngas and carbon yield and the H_2/CO ratio are plotted as a function of the feed temperature for a stoichiometric, air-based POX process. In these calculations N_2 was considered in the heat balance only, because N_2 is not present on the syngas side. The same trends are observed as for the O_2-based POX process, but higher feed temperatures (at larger volumetric flow rates) are required to achieve similar syngas yields because of the lower adiabatic temperature rise, *cf.* Figures 2.2 and 2.10.

To increase the syngas yield when using low feed temperatures excess air could be used similar to using excess O_2 in the O_2-based process. In Figure 2.11 the syngas and carbon yield, the H_2/CO ratio and the equilibrium temperature are plotted as a function of the O_2/CH_4 ratio for different feed temperatures. It is observed that considerably lower syngas yields are achieved than for the O_2-based process for the same

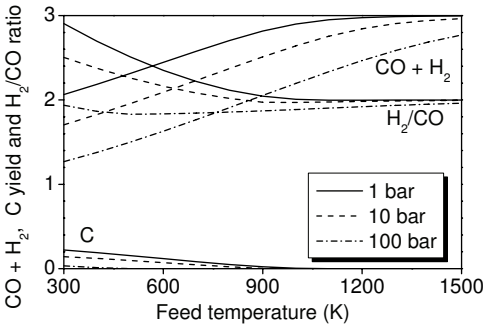

Figure 2.9: Syngas and carbon yield and H_2/CO ratio as a function of the feed temperature for different pressures, air-based ($O_2/CH_4 = 0.5$).

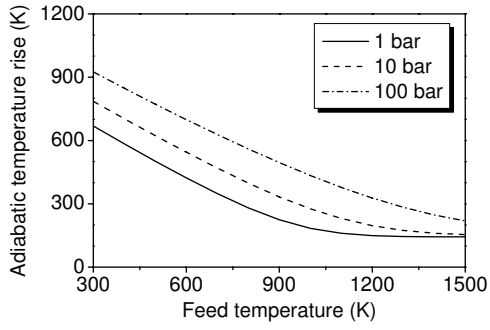

Figure 2.10: Adiabatic temperature rise (K) as a function of the feed temperature for different pressures, air based ($O_2/CH_4 = 0.5$).

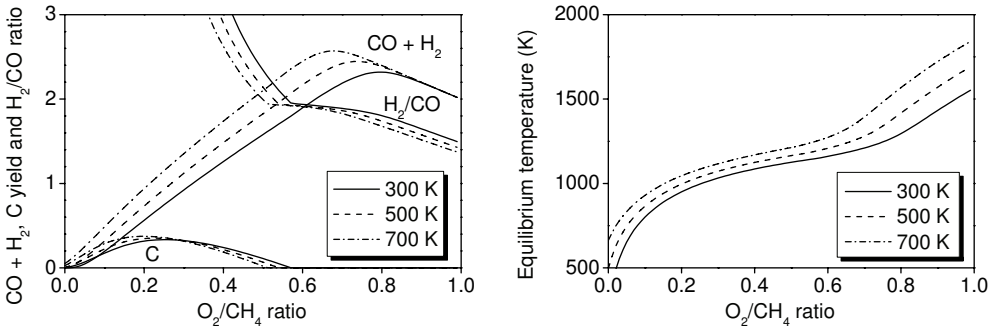

Figure 2.11: Syngas and carbon yield, H_2/CO ratio (left) and equilibrium temperature (right) as a function of the O_2/CH_4 ratio for different feed temperatures, air-based ($p = 20$ bar).

feed temperature. This can again be explained by the lower equilibrium temperatures given in Figure 2.11 compared to those of the O_2-based process given in Figure 2.5. Whereas in O_2-based process low feed temperatures and excess O_2 can be allowed and reasonable syngas yields are achieved, similarly low feed temperatures and excess air do not give reasonable syngas yields for the air-based process, making additional recuperative heat exchange by preheating the feeds to higher temperatures essential. Since external recuperative heat exchange at high temperatures is very expensive, the reduction in investment costs due to the integrated air separation are diminished by the additional investment costs for the required external high temperature heat exchange. This clearly signifies the advantages of the RFCMR concept with perovskite membranes with its integrated recuperative heat exchange. Again, the excess reaction heat of the POX reaction can be used to produce additional syngas, similar to the RFCMR concept with porous membranes.

2.5 Conclusions

To quantify the importance of recuperative heat exchange for an O_2-based POX reactor and for a POX reactor with integrated air separation, an adiabatic thermodynamic analysis was performed. The analysis focussed on the influences of the feed temperatures, the operating pressures and the $O_2/H_2O/CH_4$ ratios of the feed streams and was intended to highlight the potential of the RFCMR concepts to achieve higher

syngas yields with lower O_2 consumption compared to commercialised technologies by integrating the recuperative heat exchange inside the reactor.

For a stoichiometric O_2-based process, the adiabatic thermodynamic analysis showed that very high feed temperatures are required to obtain high syngas yields. In commercial, O_2-based POX processes usually excess O_2 is used to further preheat the feed by combusting part of the CH_4. By selecting a somewhat higher than stoichiometric O_2/CH_4 ratio the syngas yield can be optimised to reasonable values. Furthermore, the H_2/CO ratio can be increased by adding some H_2O, which also decreases the equilibrium temperature.

When the POX reaction is carried out in the RFCMR concept with porous membranes, recuperative heat exchange is fully integrated so that no preheating of the feed nor excess O_2 is required and a stoichiometric feed can be used. This increases the syngas selectivities (from 90 % up to 100 %) and decreases the consumption of expensive pure O_2 substantially (20-40 %) compared to commercialised technologies, illustrating the potential of the RFCMR concept with porous membranes. The reaction heat produced in the POX reaction can be used to produce additional syngas via steam reforming by adding some CH_4 and H_2O to the feeds. This increases the H_2/CO ratio slightly, which is an advantage, because in the FT-process usually H_2/CO ratios slightly higher than 2 are desired.

With an adiabatic thermodynamic analysis of an air-based POX process it was found that much higher feed temperatures are required at larger flow rates compared to O_2-based processes to obtain similarly high syngas yields. Excess air can improve the syngas yield to some extent, but only moderately. As a result, significant additional recuperative heat exchange is required for an air-based POX process compared to an O_2-based POX process and the related investment costs of external heat exchange equipment will be substantially higher, neutralising the reduction in investment costs due to the integration of the air separation. This clearly signifies the potential for the RFCMR concept with perovskite membranes with its integrated recuperative heat exchange.

Acknowledgement

The financial support of the Dutch Technology Foundation STW, the Energy research Centre of the Netherlands ECN and the Association of Industrial Advisory Council Members of the Dutch Institute for Catalysis Research VIRAN is gratefully acknowledged.

Nomenclature

$a_{\mathrm{k,i}}$	Number of atoms of element k per molecule of species i
A_{j}	Constant in the correlations for $h_{\mathrm{j}}^{\ominus}$ and $s_{\mathrm{j}}^{\ominus}$
b_{k}	Total amount of element k present in the system, mol
B_{j}	Constant in the correlations for $h_{\mathrm{j}}^{\ominus}$ and $s_{\mathrm{j}}^{\ominus}$
C_{j}	Constant in the correlations for $h_{\mathrm{j}}^{\ominus}$ and $s_{\mathrm{j}}^{\ominus}$
D_{j}	Constant in the correlations for $h_{\mathrm{j}}^{\ominus}$ and $s_{\mathrm{j}}^{\ominus}$
E_{j}	Constant in the correlations for $h_{\mathrm{j}}^{\ominus}$ and $s_{\mathrm{j}}^{\ominus}$
g	Partial molar Gibb's free energy, J/mol
G	Gibb's free energy, J
h	Partial molar enthalpy, J/mol
n	Amount of moles, mol
n_{CH4}^{+}	Amount of moles of CH_4 that are added to a stoichiometric feed of CH_4 and O_2, mol
n_{H2O}^{+}	Amount of moles of H_2O that are added to a stoichiometric feed of CH_4 and O_2, mol
M	Number of elements
N	Number of species
p	Pressure, Pa
R_{g}	Gas constant, 8.314 J/mol/K
s	Partial molar entropy, J/mol/K
T	Temperature, K
T_{ref}	Reference temperature, 298.15 K

Greek letters

λ	Lagrange parameter, J/mol
$\mathcal{L}$	Lagrangian, J

μ	Chemical potential, J/mol
Φ	Number of phases

Subscripts

f	Formation
g	Gas
i, j	Species i, j
k	Element k
s	Solid
φ	Phase

Superscripts

in	Initial
eq	Equilibrium
$\ominus$	At standard pressure

Bibliography

Aasberg-Petersen, K., Bak Hansen, J. H., Christensen, T. S., Dybkjaer, I., Seier Christensen, P., Stub Nielsen, C., Winter Madsen, S. E. L., Rostrup-Nielsen, J. R., "Technologies for large scale gas conversion", Applied Catalysis A: General, 221(1-2), 379–387 (2001)

Brejc, M., Supp, E., "Non-catalytic partial oxidation and special gasification process for higher-boiling hydrocarbons", in "Ullmanns Encyclopedia of Industrial Chemistry", Elvers, B., Hawkins, S., Ravenscroft, M., Rounsaville, J. F., Shulz, G. Eds., 5$^{\text{th}}$ Edition, Vol. A12, VCH Verlagsgesellschaft, Weinheim, 204–214 (1989)

Chan, S. H., Wang, H. M., "Thermodynamic analysis of natural-gas fuel processing for fuel cell applications", International Journal of Hydrogen Energy, 25(5), 441–449 (2000)

Daubert, T. E., Danner, R. P., "Data Compilation Tables of Properties of Pure Compounds", American Institute of Chemical Engineers, New York (1985)

Dry, M. E., "The Fischer-Tropsch process: 1950-2000", Catalysis Today, 71(3-4), 227–241 (2002)

Foulds, G. A., Lapszewicz, J. A., "Catalytic partial oxidation of methane to synthesis gas (Syngas)", Catalysis, 11, 412–440 (1994)

Hickman, D. A., Schmidt, L. D., "Synthesis gas formation by direct oxidation of methane over Pt monoliths", Journal Catalysis, 138(1), 267–282 (1992)

Peña, M. A., Gomez, J., Fierro, J. L. G., "New catalytic routes for syngas and hydrogen production", Applied Catalysis A: General, 144(1-2), 7–75 (1996)

Rostrup-Nielsen, J. R., "Syngas in perspective", Catalysis Today, 71(3-4), 243–247 (2002)

Seo, Y. S., Shirley, A., Kolaczkowski, S. T., "Evaluation of thermodynamically favourable operating conditions for production of hydrogen in three different reforming technologies", Journal of Power Sources, 108(1-2), 213–225 (2002)

Smith, W. R., Missen, R. W., "Chemical Reaction Equilibrium Analysis: Theory and Algorithms", John Wiley & Sons, New York (1982)

Tsang, S. C., Claridge, J. B., Green, M. L. H., "Recent advances in the conversion of methane to synthesis gas", Catalysis Today, 23(1), 3–15 (1995)

York, A. P. E., Xiao, T. C., Green, M. L. H., "Brief overview of the partial oxidation of methane to synthesis gas", Topics in Catalysis, 22(3-4), 345–358 (2003)

Zhu, J., Zhang, D., King, K. D., "Reforming of CH4 by partial oxidation: thermodynamic and kinetic analyses", Fuel, 80(7), 899–903 (2001)

2.A Physical properties: enthalpy and entropy

In the data compilation of Daubert and Danner (1985) the partial molar enthalpy $h_{\mathrm{j}}^{\ominus}$ and the partial molar entropy $s_{\mathrm{j}}^{\ominus}$ of gaseous species at standard pressure are correlated with:

$$\begin{aligned} h_{\mathrm{j}}^{\ominus} =& h_{\mathrm{f,j}} + A_{\mathrm{j}}\left(T - T_{\mathrm{ref}}\right) + B_{\mathrm{j}}C_{\mathrm{j}}\left(\coth\left(\frac{C_{\mathrm{j}}}{T}\right) - \coth\left(\frac{C_{\mathrm{j}}}{T_{\mathrm{ref}}}\right)\right) \\ & - D_{\mathrm{j}}E_{\mathrm{j}}\left(\tanh\left(\frac{E_{\mathrm{j}}}{T}\right) - \tanh\left(\frac{E_{\mathrm{j}}}{T_{\mathrm{ref}}}\right)\right) \end{aligned} \tag{2.13}$$

$$
\begin{aligned}
s_{\mathrm{j}}^{\ominus} &= s_{\mathrm{f,j}} + A_{\mathrm{j}} \ln\left(\frac{T}{T_{\mathrm{ref}}}\right) + \\
&+ B_{\mathrm{j}} \left[\frac{C_{\mathrm{j}}}{T} \coth\left(\frac{C_{\mathrm{j}}}{T}\right) - \frac{C_{\mathrm{j}}}{T_{\mathrm{ref}}} \coth\left(\frac{C_{\mathrm{j}}}{T_{\mathrm{ref}}}\right) - \ln\left(\frac{\sinh\left(\frac{C_{\mathrm{j}}}{T}\right)}{\sinh\left(\frac{C_{\mathrm{j}}}{T_{\mathrm{ref}}}\right)} \right) \right] \\
&- D_{\mathrm{j}} \left[\frac{E_{\mathrm{j}}}{T} \tanh\left(\frac{E_{\mathrm{j}}}{T}\right) - \frac{E_{\mathrm{j}}}{T_{\mathrm{ref}}} \tanh\left(\frac{E_{\mathrm{j}}}{T_{\mathrm{ref}}}\right) - \ln\left(\frac{\cosh\left(\frac{E_{\mathrm{j}}}{T}\right)}{\cosh\left(\frac{E_{\mathrm{j}}}{T_{\mathrm{ref}}}\right)} \right) \right]
\end{aligned}
\tag{2.14}
$$

For solid species, $h_{\mathrm{j}}^{\ominus}$ and $s_{\mathrm{j}}^{\ominus}$ are correlated by:

$$
\begin{aligned}
h_{\mathrm{j}}^{\ominus} =& h_{\mathrm{f,j}} + A_{\mathrm{j}} \left(T - T_{\mathrm{ref}}\right) + \frac{1}{2} B_{\mathrm{j}} \left(T^2 - T_{\mathrm{ref}}^2\right) + \frac{1}{3} C_{\mathrm{j}} \left(T^3 - T_{\mathrm{ref}}^3\right) \\
&+ \frac{1}{4} D_{\mathrm{j}} \left(T^4 - T_{\mathrm{ref}}^4\right) + \frac{1}{5} E_{\mathrm{j}} \left(T^5 - T_{\mathrm{ref}}^5\right)
\end{aligned}
\tag{2.15}
$$

$$
\begin{aligned}
s_{\mathrm{j}}^{\ominus} =& s_{\mathrm{f,j}} + A_{\mathrm{j}} \ln\left(\frac{T}{T_{\mathrm{ref}}}\right) + B_{\mathrm{j}} \left(T - T_{\mathrm{ref}}\right) + \frac{1}{2} C_{\mathrm{j}} \left(T^2 - T_{\mathrm{ref}}^2\right) \\
&+ \frac{1}{3} D_{\mathrm{j}} \left(T^3 - T_{\mathrm{ref}}^3\right) + \frac{1}{4} E_{\mathrm{j}} \left(T^4 - T_{\mathrm{ref}}^4\right)
\end{aligned}
\tag{2.16}
$$

The constants used in the correlations 2.13-2.16 are given in Table 2.2 for species relevant for CPO and ATR reactors. The heat of formation $h_{\mathrm{j}}^{\mathrm{f}}$ and absolute entropy $s_{\mathrm{j}}^{\mathrm{f}}$ are given in Table 2.3.

Table 2.2: Constants used in the calculation of $h_{\mathrm{j}}^{\ominus}$ and $s_{\mathrm{j}}^{\ominus}$ taken from Daubert and Danner (1985).

	A_{j}	B_{j}	C_{j}	D_{j}	E_{j}
C_s	$-7.3530 \cdot 10^{3}$	$6.9494 \cdot 10^{1}$	$-6.4040 \cdot 10^{-2}$	$2.8510 \cdot 10^{-5}$	$-4.9877 \cdot 10^{-9}$
$CH_{4,g}$	$3.3298 \cdot 10^{4}$	$7.9933 \cdot 10^{4}$	$2.0869 \cdot 10^{3}$	$4.1602 \cdot 10^{4}$	$9.9196 \cdot 10^{2}$
CO_g	$2.9108 \cdot 10^{4}$	$8.7730 \cdot 10^{3}$	$3.0851 \cdot 10^{3}$	$8.4553 \cdot 10^{3}$	$1.5382 \cdot 10^{3}$
$CO_{2,g}$	$2.9370 \cdot 10^{4}$	$3.4540 \cdot 10^{4}$	$-1.4280 \cdot 10^{3}$	$2.6400 \cdot 10^{4}$	$5.8800 \cdot 10^{2}$
$H_{2,g}$	$2.7617 \cdot 10^{4}$	$9.5600 \cdot 10^{3}$	$2.4660 \cdot 10^{3}$	$3.7600 \cdot 10^{3}$	$5.6760 \cdot 10^{2}$
H_2O_g	$3.3363 \cdot 10^{4}$	$2.6790 \cdot 10^{4}$	$2.6105 \cdot 10^{3}$	$8.8960 \cdot 10^{3}$	$1.1690 \cdot 10^{3}$
$N_{2,g}$	$2.9105 \cdot 10^{4}$	$8.6149 \cdot 10^{3}$	$1.7016 \cdot 10^{3}$	$1.0347 \cdot 10^{2}$	$9.0979 \cdot 10^{2}$
$O_{2,g}$	$2.9103 \cdot 10^{4}$	$1.0040 \cdot 10^{4}$	$2.5265 \cdot 10^{3}$	$9.3560 \cdot 10^{3}$	$1.1538 \cdot 10^{3}$

Table 2.3: Heat of formation h_j^f and absolute entropy s_j^f taken from Daubert and Danner (1985).

	h_j^f (J/kmol)	s_j^f (J/kmol)
C_s	0	$5.74 \cdot 10^3$
$CH_{4,g}$	$-7.452 \cdot 10^7$	$1.8627 \cdot 10^5$
CO_g	$-1.1053 \cdot 10^8$	$1.9754 \cdot 10^5$
$CO_{2,g}$	$-3.9352 \cdot 10^8$	$2.1369 \cdot 10^5$
$H_{2,g}$	0	$1.3068 \cdot 10^5$
H_2O_g	$-2.4181 \cdot 10^8$	$1.8872 \cdot 10^5$
$N_{2,g}$	0	$1.9150 \cdot 10^5$
$O_{2,g}$	0	$2.0504 \cdot 10^5$

CHAPTER 3

Numerical Algorithm

Abstract

Reverse flow (catalytic membrane) reactors can be described by a system of strongly coupled non-stationary, convection dominated Partial Differential Equations (PDE's) with strongly non-linear source terms. Because of the steep concentration and temperature gradients prevailing in these type of reactors and the large differences in time scales of mass and heat accumulation a numerically very efficient algorithm is required to solve the system of PDE's. Therefore, a numerical algorithm was developed and implemented based on higher order discretisation schemes for the convection and accumulation terms of the PDE's combined with automatic time step and local grid adaptation. The system of PDE's is solved with the method of lines. For the time integration, implicit higher order Singly Diagonal Implicit Runge-Kutta schemes are used and it is shown that with these schemes the computational effort can be reduced significantly compared to the often used 1^{st} order Euler scheme. For the discretisation of the convection terms of the PDE's, higher order Weighted Essentially Non-Oscillatory (WENO) schemes are used and explicit equations for non-uniform grids are derived. Furthermore, a local grid adaptation procedure is presented that makes effective use of the smoothness indicators and interpolation polynomials of the WENO schemes. It is shown that the number of grid cells (and hence computation time) required to accurately capture steep gradients can be greatly reduced with the WENO schemes and the local grid adaptation procedure. Finally, the capabilities of the numerical algorithm are demonstrated for the simulation of a conventional reverse flow reactor and it is shown that especially the combination of the higher order schemes and the automatic time step and local grid adaptation procedures reduces the CPU demand enormously.

This chapter is based on the paper:
Smit, J., van Sint Annaland, M., and Kuipers, J.A.M., Grid adaptation with WENO schemes for non-uniform grids to solve convection dominated partial differential equations, Chemical Engineering Science, 60(10), 2609-2619 (2005)

3.1 Introduction

To describe and study the feasibility of the Reverse Flow Catalytic Membrane Reactor (RFCMR) concepts proposed in Chapter 1, detailed reactor models are required. These reactor models consist of a system (mass and heat balances) of strongly coupled non-stationary convection-diffusion-reaction Partial Differential Equations (PDE's) with strongly non-linear source terms, typically in the form of Equation 3.1:

$$\frac{\partial u}{\partial t} + v\frac{\partial u}{\partial x} = D\frac{\partial}{\partial x}\left(\frac{\partial u}{\partial x}\right) + S\left(u\right) \tag{3.1}$$

The numerical solution of this system of PDE's is a very CPU demanding task. One important reason for this is the very large variation in time scales of mass accumulation (small) and energy accumulation (large). Because of these differences very small time steps ($< 1{\cdot}10^{-4}$ s) are required to solve the component mass balances accurately, while on the other hand simulation times can take comparatively long ($> 1{\cdot}10^{5}$ s) before a periodic steady state is reached with respect to the temperature profiles. Therefore, it is desirable to utilise an efficient time integration algorithm by means of a higher order time discretisation scheme combined with an automatic time step adaptation. Another major contribution to the computational effort is the presence of very steep gradients in the temperature and concentration profiles at different and varying locations, requiring a very fine grid and accordingly a very large number of grid cells. Therefore, it is also desirable to have as few grid cells as possible using higher order discretisation schemes for the spatial derivatives together with (local) grid adaptation.

In the literature numerous papers have appeared on the dynamic simulation of conventional reverse flow reactors in the last decade, employing a number of different numerical solution techniques, see Aubé and Sapoundjiev (2000) for an overview. Usually the system of equations to be solved is highly application specific and most researchers develop their own algorithms. The system of PDE's to be solved in this study is also highly application specific because of the combination of a reverse flow reactor and a membrane reactor in the RFCMR concepts. Therefore, a numerical algorithm was developed, which was specifically designed to solve the models that describe the RFCMR behaviour accurately and very efficiently.

A commonly used approach to solve the system of PDE's describing a conventional reverse flow reactor is the method of lines (*e.g.* Schiesser, 1991). In the method of lines

a PDE is transformed into an ordinary differential equation (ODE) by replacing the spatial partial derivatives with finite difference or finite volume discretisations. After the PDE is transformed into an ODE, time integration can be performed with an efficient ODE-solver, such as Runge-Kutta methods (*e.g.* Hairer and Wanner, 1991; Ascher and Petzold, 1998). In this study also the method of lines was employed with implicit, higher order Runge-Kutta methods for the time integration, which will be discussed in further detail in this chapter. Furthermore, automatic time step adaptation will be addressed.

Higher order discretisation schemes for the convection term in convection dominated PDE's have been subject of research for decades (see *e.g.* Finlayson, 1992). The Weighted Essentially Non-Oscillatory (WENO) schemes (Liu et al., 1994; Jiang and Shu, 1996; Shu, 1998) are probably the most modern schemes currently available and eliminate most of the disadvantages encountered in other schemes (*e.g.* the Total Variation Diminishing and Essentially Non-Oscillatory schemes), especially concerning the loss of accuracy near discontinuities. WENO schemes have also been applied successfully on non-uniform grids (Friedrich, 1998; Hu and Shu, 1999), where the WENO coefficients were computed numerically. WENO schemes for non-uniform grids are also employed in this study and explicit equations for the coefficients are derived.

Grid adaptation techniques can be divided into two categories: moving grid algorithms and local grid refinement algorithms (see *e.g.* Wouwer et al., 1998). In moving grid algorithms a fixed number of grid cells is moved in the spatial domain. In local grid refinement algorithms, grid cells are locally added or removed within a fixed grid, depending on the local smoothness of the solution. The RFCMR concepts considered in this study consist of several sections due to the presence of a membrane and also the shape and steepness of the solution change in time. Hence, the number of required grid cells to meet a specified accuracy will also vary locally and in time. Therefore, a novel local grid adaptation technique is developed in this chapter, which makes effective use of the smoothness indicators and the interpolation polynomials already obtained in the WENO schemes.

Finally in this chapter, the numerical algorithm will be demonstrated for two test cases, which are described with convection dominated PDE's. The accuracies of the different discretisation schemes are verified by solving the 1-D convection equation for

a smooth initial profile. Subsequently, the advantages of using automatic time step and local grid adaptation are demonstrated by solving the 1-D convection equation for a non-smooth initial profile and by simulating a conventional reverse flow reactor.

3.2 Time integration

In this section, firstly the time integration of the system of PDE's using the method of lines is discussed in general. Subsequently, the automatic time step adaptation procedure will be addressed. Finally, implicit higher order time discretisation schemes will be discussed.

3.2.1 Method of Lines

When solving non-stationary convection-diffusion-reaction PDE's with the method of lines, it is well known that numerical instability might arise when solving one of the convection, diffusion or reaction terms explicitly, unless a very small time step is selected, typically much smaller than would be required to meet a specified accuracy. For the explicit discretisation of the convection term the stability is determined by the well-known Courant-Friedrichs-Lewy (CFL) condition (Courant et al., 1928):

$$v\frac{\Delta t}{\Delta x} < 1 \tag{3.2}$$

and similarly for the diffusion term:

$$D\frac{\Delta t}{\Delta x^2} < 0.5 \tag{3.3}$$

Especially this last condition might pose a severe restriction on the permissable time step when small grid cells are required due to the presence of steep spatial gradients. When the convection and diffusion terms are treated implicitly, the resulting system of linear equations can be solved simultaneously with a direct matrix solver and therefore the solution is stable with respect to these terms for much larger time steps (but not necessarily accurate!).

When using the conventional 1^{st} order Euler scheme for the accumulation term, the 1^{st} order Upwind scheme for the convection term and the 2^{nd} order central differencing scheme for the diffusion term on a non-uniform grid, Equation 3.1 can be discretised

as follows (assuming $v > 0$):

$$\begin{aligned}\frac{\bar{u}_{\mathrm{i}}^{\mathrm{n}+1} - \bar{u}_{\mathrm{i}}^{\mathrm{n}}}{\Delta t} = & - v \frac{\bar{u}_{\mathrm{i}}^{\mathrm{n}+1} - \bar{u}_{\mathrm{i}-1}^{\mathrm{n}+1}}{x_{\mathrm{i}+1/2} - x_{\mathrm{i}-1/2}} + S\left(\bar{u}_{\mathrm{i}}^{\mathrm{n}+1}\right) \\ & + \frac{2D}{x_{\mathrm{i}+1/2} - x_{\mathrm{i}-1/2}} \left(\frac{\bar{u}_{\mathrm{i}+1}^{\mathrm{n}+1} - \bar{u}_{\mathrm{i}}^{\mathrm{n}+1}}{x_{\mathrm{i}+3/2} - x_{\mathrm{i}-1/2}} - \frac{\bar{u}_{\mathrm{i}}^{\mathrm{n}+1} - \bar{u}_{\mathrm{i}-1}^{\mathrm{n}+1}}{x_{\mathrm{i}+1/2} - x_{\mathrm{i}-3/2}} \right)\end{aligned} \tag{3.4}$$

here $\bar{u}$ indicates the volume averaged value of variable u, i the grid cell and n the time level. $x_{\mathrm{i}+1/2}$ and $x_{\mathrm{i}-1/2}$ indicate the cell faces of grid cell i. To solve the linear system of N Equations 3.4 and N unknowns, where N is the number of grid cells (in case of one variable), the system can be written in a matrix notation of the form $\mathbf{A} \cdot \mathbf{x} = \mathbf{b}$. $\mathbf{A}$ contains the coefficients of the implicit terms of Equation 3.4 and $\mathbf{x}$ is a vector of the variable(s) u at the new time level $n+1$ to be solved (*i.e.* $\bar{u}_1^{\mathrm{n}+1}, \ldots, \bar{u}_{\mathrm{i}}^{\mathrm{n}+1}, \ldots \bar{u}_{\mathrm{N}}^{\mathrm{n}+1}$). $\mathbf{b}$ contains the old values of u at the previous time level n (*i.e.* $\bar{u}_1^{\mathrm{n}}, \ldots, \bar{u}_{\mathrm{i}}^{\mathrm{n}}, \ldots \bar{u}_{\mathrm{N}}^{\mathrm{n}}$) and if present also the explicit terms of the equation. Because $\mathbf{A}$ is a (block) tridiagonal matrix, the system can be solved efficiently with a modified Crout's algorithm optimised for block-tridiagonal matrices.

The source term $S(u)$ of Equation 3.1 is usually non-linear due to the reaction terms and is easily linearised with the Newton-Rhapson method:

$$S\left(\bar{u}_{\mathrm{i}}^{\mathrm{n}+1}\right) = S\left(\bar{u}_{\mathrm{i}}^{\mathrm{m}}\right) + \left(\bar{u}_{\mathrm{i}}^{\mathrm{n}+1} - \bar{u}_{\mathrm{i}}^{\mathrm{m}}\right) \left.\frac{\partial S}{\partial u}\right|_{\mathrm{i,m}} \tag{3.5}$$

The derivative $\partial S / \partial u$ can be derived analytically or computed numerically. In the latter case it is approximated by:

$$\left.\frac{\partial S}{\partial u}\right|_{\mathrm{i,m}} = \frac{S\left(\bar{u}_{\mathrm{i}}^{\mathrm{m}} + \varepsilon\right) - S\left(\bar{u}_{\mathrm{i}}^{\mathrm{m}}\right)}{\varepsilon} \tag{3.6}$$

where ε is a small constant (typically $1{\cdot}10^{-5} - 1{\cdot}10^{-3}$). $\bar{u}_{\mathrm{i}}^{\mathrm{m}}$ is the latest value computed for $\bar{u}_{\mathrm{i}}^{\mathrm{n}+1}$ within the Newton-iteration loop and is initially taken as $\bar{u}_{\mathrm{i}}^{\mathrm{n}}$. After each iteration $\bar{u}_{\mathrm{i}}^{\mathrm{m}}$ is updated with the calculated $\bar{u}_{\mathrm{i}}^{\mathrm{n}+1}$ until after a number of iterations convergence is reached and $\bar{u}_{\mathrm{i}}^{\mathrm{m}} \approx \bar{u}_{\mathrm{i}}^{\mathrm{n}+1}$. In this study the convergence is evaluated by comparing the absolute, spatially averaged difference between $\bar{u}_{\mathrm{i}}^{\mathrm{n}+1}$ and $\bar{u}_{\mathrm{i}}^{\mathrm{m}}$, tol_{it}:

$$tol_{\mathrm{it}} = \frac{1}{L} \sum_{\mathrm{i}}^{\mathrm{N}} \left(\left(x_{\mathrm{i}+1/2} - x_{\mathrm{i}-1/2}\right) \left| \bar{u}_{\mathrm{i}}^{\mathrm{n}+1} - \bar{u}_{\mathrm{i}}^{\mathrm{m}} \right| \right) \tag{3.7}$$

If tol_{it} is smaller than a pre-specified value the solution is accepted. When no convergence is reached after a specified number of iterations, the calculation is repeated with a smaller time step.

3.2.2 Time step adaptation

For both efficiency and accuracy reasons it is important that the error in the time discretisation of a PDE is kept below a specified tolerance level. In order to have a good estimate of this error, in this study the new solution $\bar{u}_{\mathrm{i}}^{\mathrm{n}+1}$, which was calculated from the previous time level $\bar{u}_{\mathrm{i}}^{\mathrm{n}}$ by taking a time step of size Δt, was compared with the solution obtained by taking 2 steps of size $\Delta t/2$, following Alexander (1977). The absolute, spatially averaged error tol_{t} is computed analogously to the computation of tol_{it} used in the Newton-Rhapson iteration procedure:

$$tol_{\mathrm{t}} = \frac{1}{L} \sum_{\mathrm{i}}^{\mathrm{N}} \left(\left(x_{\mathrm{i}+1/2} - x_{\mathrm{i}-1/2} \right) \left| \bar{u}_{\mathrm{i}}^{\mathrm{n}+1} \left(t + \Delta t \right) - \bar{u}_{\mathrm{i}}^{\mathrm{n}+1} \left(t + 2 \cdot \Delta t/2 \right) \right| \right) \tag{3.8}$$

If tol_{t} exceeds a maximal error tolerance $tol_{\mathrm{t,max}}$, Δt is decreased (*e.g.* by 10 %) for the next time step and if tol_{t} is lower than a minimal tolerance $tol_{\mathrm{t,min}}$, Δt is increased (*e.g.* by 10 %). In this study $tol_{\mathrm{t,min}}$ and $tol_{\mathrm{t,max}}$ were chosen in such a way that $tol_{\mathrm{t,max}} = tol_{\mathrm{t,it}}$ and $tol_{\mathrm{t,min}} = 0.1 \cdot tol_{\mathrm{it}}$.

3.2.3 Singly Diagonal Implicit Runge-Kutta methods

To solve ODE's implicitly, numerous techniques have been developed (*e.g.* Hairer and Wanner, 1991; Ascher and Petzold, 1998). Regretfully no time discretisation method to solve PDE's exists that guarantees unconditional stability. Therefore, the error of the solution always has to be controlled by adjusting the time step, as discussed previously. Nevertheless, some (implicit) methods have much better stability properties than other (explicit) methods, avoiding the need of very small time steps when accuracy is not an issue. For these stability properties several criteria have been proposed. Most criteria have been derived by considering a linear, 1^{st} order ODE of the form:

$$\frac{\partial u}{\partial t} = \lambda u \tag{3.9}$$

Here λ is an arbitrary constant. A commonly used stability criterion is A-stability, which means that the solution does not diverge for $\lambda < 0$:

$$\left| \bar{u}_{\mathrm{i}}^{\mathrm{n}+1} \right| < \left| \bar{u}_{\mathrm{i}}^{\mathrm{n}} \right| \tag{3.10}$$

Explicit methods are not A-stable, but most implicit and semi-implicit methods are. Besides A-stability there is also a more stringent criterion called L-stability, which

requires in addition that possible oscillations in the solution caused by stiffness (*i.e.* $\lambda \rightarrow \infty$) are damped:

$$\lim_{\lambda \rightarrow \infty} \frac{\left|\bar{u}_{\mathrm{i}}^{\mathrm{n}+1}\right|}{\left|\bar{u}_{\mathrm{i}}^{\mathrm{n}}\right|} = 0 \tag{3.11}$$

For methods that have only A-stability these oscillations are not damped, which could give misleading results when using a large time step.

The most simple and robust discretisation scheme to solve ODE's, which is L-stable, is the 1^{st} order accurate implicit Euler scheme. To simplify the discussion, only the accumulation and source terms of Equation 3.1 are considered here:

$$\frac{\bar{u}_{\mathrm{i}}^{\mathrm{n}+1} - \bar{u}_{\mathrm{i}}^{\mathrm{n}}}{\Delta t} = S\left(\bar{u}_{\mathrm{i}}^{\mathrm{n}+1}\right) \tag{3.12}$$

A large number of methods have been developed to achieve higher order accuracy, which can be divided into two groups: one-step methods that only require the values of the previous time level and multiple-step methods that require the values of multiple time levels. Since grid adaptation is used at each time step in this study, one-step methods are to be preferred. Out of the numerous higher order one-step methods to solve ODE's, the family of Diagonally Implicit Runge-Kutta (DIRK) methods is especially suitable to solve PDE's with the method of lines, because in DIRK methods no system of linear equations has to be solved in the time domain (see also Alexander, 1977; Ascher and Petzold, 1998). In the first stage of DIRK methods an implicit Euler step of certain size is made, which solution is then used in the second stage. The solution of the first and second stage are subsequently used for the third stage and so on. There are two sorts of DIRK methods: methods that have s stages and $(s+1)$ order accuracy with A-stability (referred to as DIRK) and methods with s stages and s order accuracy with L-stability (called Singly DIRK, SDIRK in short). Because of the stiffness of the PDE's that describe reverse flow (catalytic membrane) reactors due to the strongly non-linear reaction terms, L-stability is essential and therefore SDIRK schemes have been selected in this work. The 2^{nd} order SDIRK (referred to as SDIRK2) scheme reads:

$$\begin{aligned}
\frac{\bar{u}_{\mathrm{i}}^{1} - \bar{u}_{\mathrm{i}}^{\mathrm{n}}}{\Delta t} &= \alpha S\left(\bar{u}_{\mathrm{i}}^{1}\right) \\
\frac{\bar{u}_{\mathrm{i}}^{\mathrm{n}+1} - \bar{u}_{\mathrm{i}}^{\mathrm{n}}}{\Delta t} &= (1-\alpha) S\left(\bar{u}_{\mathrm{i}}^{1}\right) + \alpha S\left(\bar{u}_{\mathrm{i}}^{\mathrm{n}+1}\right) \\
\alpha &= 1 - \frac{1}{2}\sqrt{2}
\end{aligned} \tag{3.13}$$

The 3rd order SDIRK scheme (referred to as SDIRK3) can be summarised as:

$$\begin{aligned}
\frac{\bar{u}_{\mathrm{i}}^{1}-\bar{u}_{\mathrm{i}}^{\mathrm{n}}}{\Delta t} &= \alpha S\left(\bar{u}_{\mathrm{i}}^{1}\right) \\
\frac{\bar{u}_{\mathrm{i}}^{2}-\bar{u}_{\mathrm{i}}^{\mathrm{n}}}{\Delta t} &= (\beta-\alpha)\, S\left(\bar{u}_{\mathrm{i}}^{1}\right)+\alpha S\left(\bar{u}_{\mathrm{i}}^{2}\right) \\
\frac{\bar{u}_{\mathrm{i}}^{\mathrm{n+1}}-\bar{u}_{\mathrm{i}}^{\mathrm{n}}}{\Delta t} &= \gamma S\left(\bar{u}_{\mathrm{i}}^{1}\right)+(1-\gamma-\alpha)\, S\left(\bar{u}_{\mathrm{i}}^{2}\right)+\alpha S\left(\bar{u}_{\mathrm{i}}^{\mathrm{n+1}}\right) \\
\alpha &= 1+\frac{1}{\sqrt{2}}\left(\sqrt{3}\sin(\delta)-\cos(\delta)\right) \\
\beta &= \frac{1+\alpha}{2} \\
\gamma &= -\frac{1}{4}\left(6\alpha^{2}-16\alpha+1\right) \\
\delta &= \frac{1}{3}\arctan\left(\frac{\sqrt{2}}{4}\right)
\end{aligned} \tag{3.14}$$

Although SDIRK methods have higher order accuracy for simple ODE's such as Equation 3.9, they are known to have considerable order reduction when there are stiff derivatives of the form $\partial S/\partial t, \partial^2 S/\partial t^2$ and $\partial^2 S/\partial u^2$ in the source term (Frank et al., 1985; Ascher and Petzold, 1998). In this study these derivatives are absent.

3.3 WENO schemes for non-uniform grids

To discretise the spatial derivatives in Equation 3.1, in this study the finite volume approach is employed. In this approach the convection term is discretised as follows:

$$v\frac{\partial u}{\partial x} = v\frac{\hat{u}_{\mathrm{i+1/2}}-\hat{u}_{1-1/2}}{x_{\mathrm{i+1/2}}-x_{\mathrm{i-1/2}}} \tag{3.15}$$

where $\hat{u}_{\mathrm{i+1/2}}$ and $\hat{u}_{\mathrm{i-1/2}}$ are the point values of u at the cell faces and have to be interpolated:

$$\begin{aligned}
v\frac{\partial u}{\partial x} &= v\frac{\hat{u}^{-}_{\mathrm{i+1/2}}-\hat{u}^{-}_{\mathrm{i-1/2}}}{x_{\mathrm{i+1/2}}-x_{\mathrm{i-1/2}}} \qquad v>0 \\
v\frac{\partial u}{\partial x} &= v\frac{\hat{u}^{+}_{\mathrm{i+1/2}}-\hat{u}^{+}_{\mathrm{i-1/2}}}{x_{\mathrm{i+1/2}}-x_{\mathrm{i-1/2}}} \qquad v<0
\end{aligned} \tag{3.16}$$

where $\hat{u}^{-}_{\mathrm{i+1/2}}$ and $\hat{u}^{+}_{\mathrm{i-1/2}}$ are the forward and backward interpolations of $\hat{u}_{\mathrm{i+1/2}}$ and $\hat{u}_{\mathrm{i-1/2}}$, respectively, to be obtained with a particular discretisation scheme (see also Figure 3.1). In the 1st order accurate Upwind scheme $\hat{u}^{-}_{\mathrm{i+1/2}}$ and $\hat{u}^{+}_{\mathrm{i-1/2}}$ are simply

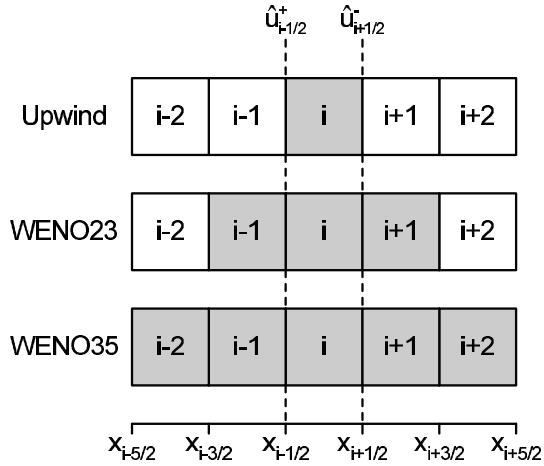

Figure 3.1: Interpolation stencils (grey) used for $\hat{u}^{-}_{\mathrm{i}+1/2}$ and $\hat{u}^{+}_{\mathrm{i}-1/2}$ according to the Upwind, WENO23 and WENO35 discretisation schemes.

taken as the cell averaged value of the downstream grid cell $\bar{u}_{\mathrm{i}}$. The basic idea of WENO schemes is to use different higher order interpolation polynomials for the calculation of $\hat{u}^{-}_{\mathrm{i}+1/2}$ and $\hat{u}^{+}_{\mathrm{i}-1/2}$ in such a way that higher order accuracy than that of the polynomials is obtained in smooth regions and non-oscillatory behaviour is assured in non-smooth regions, while retaining the accuracy order of the polynomials.

The construction of WENO schemes will be briefly discussed here based on the paper of Shu (1998). In the WENO schemes the Lagrange interpolation polynomial of $u(x)$ around i is used to approximate $\hat{u}^{-}_{\mathrm{i}+1/2}$ and $\hat{u}^{+}_{\mathrm{i}-1/2}$:

$$u_{\mathrm{r}}(x)|_{\mathrm{i}} = \sum_{\mathrm{j}=0}^{\mathrm{k}-1} \left[\sum_{\mathrm{m}=\mathrm{j}+1}^{\mathrm{k}} \left(\frac{\sum_{p=0,\,p\neq m}^{\mathrm{k}} \prod_{q=0,\,q\neq m,p}^{\mathrm{k}} \left(x - x_{\mathrm{i}-\mathrm{r}+\mathrm{q}-1/2}\right)}{\prod_{p=0,\,p\neq m}^{\mathrm{k}} \left(x_{\mathrm{i}-\mathrm{r}+\mathrm{m}-1/2} - x_{\mathrm{i}-\mathrm{r}+\mathrm{p}-1/2}\right)} \right) \times \left(x_{\mathrm{i}-\mathrm{r}+\mathrm{j}+1/2} - x_{\mathrm{i}-\mathrm{r}+\mathrm{j}-1/2}\right) \bar{u}_{\mathrm{i}-\mathrm{r}+\mathrm{j}} \right] \tag{3.17}$$

here $r\,(0 \ldots k-1)$ indicates the stencil $\left(x_{\mathrm{i}-\mathrm{r}-1/2} \ldots x_{\mathrm{i}-\mathrm{r}+\mathrm{k}-1/2}\right)$ used for the construction of the polynomial and k indicates the order of accuracy of the polynomial. The different $\hat{u}^{-}_{\mathrm{i}+1/2,\mathrm{r}}$ and $\hat{u}^{+}_{\mathrm{i}-1/2,\mathrm{r}}$, obtained by evaluating $u_{\mathrm{r}}(x)\,|_{\mathrm{i}}$ at $x_{\mathrm{i}+1/2}$ and $x_{\mathrm{i}-1/2}$,

respectively, are combined using weight factors to calculate $\hat{u}^-_{\mathrm{i}+1/2}$ and $\hat{u}^+_{\mathrm{i}-1/2}$:

$$\hat{u}^-_{\mathrm{i}+1/2} = \sum_{\mathrm{r}=0}^{\mathrm{k}-1} w^-_{\mathrm{i}+1/2,\mathrm{r}} \hat{u}^-_{\mathrm{i}+1/2,\mathrm{r}} \quad , \qquad \hat{u}^+_{\mathrm{i}-1/2} = \sum_{\mathrm{r}=0}^{\mathrm{k}-1} w^+_{\mathrm{i}-1/2,\mathrm{r}} \hat{u}^+_{\mathrm{i}-1/2,\mathrm{r}} \tag{3.18}$$

where w_r are the weight factors ($\sum w_\mathrm{r} = 1$) given to a particular interpolation function, which are defined as:

$$w^-_{\mathrm{i}+1/2,\mathrm{r}} = \frac{C^-_{\mathrm{i}+1/2,\mathrm{r}}}{(IS_{\mathrm{i,r}})^\mathrm{p} \sum_{\mathrm{s}=0}^{\mathrm{k}-1} \frac{C^-_{\mathrm{i}+1/2,\mathrm{s}}}{(IS_{\mathrm{i,s}})^\mathrm{p}}} \quad , \qquad w^+_{\mathrm{i}-1/2,\mathrm{r}} = \frac{C^+_{\mathrm{i}-1/2,\mathrm{r}}}{(IS_{\mathrm{i,r}})^\mathrm{p} \sum_{\mathrm{s}=0}^{\mathrm{k}-1} \frac{C^+_{\mathrm{i}-1/2,\mathrm{s}}}{(IS_{\mathrm{i,s}})^\mathrm{p}}} \tag{3.19}$$

where p is a constant, usually taken as 2. The different IS_r are the so-called smoothness indicators, which are a measure of the smoothness of the particular interpolation polynomial, and are defined as the sum of the L^2-norm of all derivatives of the interpolation polynomial $u_\mathrm{r}(x)|_\mathrm{i}$ over the interval $\left(x_{\mathrm{i}-1/2} \ldots x_{\mathrm{i}+1/2}\right)$:

$$IS_{\mathrm{i,r}} = \sum_{\mathrm{m}=1}^{\mathrm{k}-1} \left(\left(x_{\mathrm{i}+1/2} - x_{\mathrm{i}-1/2}\right)^{2\mathrm{m}-1} \int_{x_{\mathrm{i}-1/2}}^{x_{\mathrm{i}+1/2}} \left(\frac{\partial^\mathrm{m} \left(u_\mathrm{r}(x)|_\mathrm{i} \right)}{\partial^\mathrm{m}(x)} \right) dx \right) \tag{3.20}$$

To prevent the denominator in the expression for the weight factors w_r to become zero, usually a very small constant ϵ is added to the IS_r. In smooth regions the IS_r are identical and thus vanish in w_r, so that $w_\mathrm{r} = C_\mathrm{r}$:

$$\hat{u}^-_{\mathrm{i}+1/2} = \sum_{\mathrm{r}=0}^{\mathrm{k}-1} w^-_{\mathrm{i}+1/2,\mathrm{r}} \hat{u}^-_{\mathrm{i}+1/2,\mathrm{r}} \quad = \sum_{\mathrm{r}=0}^{\mathrm{k}-1} C^-_{\mathrm{i}+1/2,\mathrm{r}} \hat{u}^-_{\mathrm{i}+1/2,\mathrm{r}} \tag{3.21}$$

The coefficients C_r ($\sum C_\mathrm{r} = 1$) are chosen in such a way that a $(2k-1)$ order accuracy is achieved in smooth regions for interpolation polynomials of order k. This is achieved when the interpolation $\hat{u}_{\mathrm{i}+1/2}$ of order k (here indicated with the last part of the subscript) is equal to the interpolation $\hat{u}_{\mathrm{i}+1/2,\mathrm{r}}$ of order $(2k-1)$ on the same stencil. The coefficients C_r are thus obtained by solving the equation:

$$\sum_{\mathrm{r}=0}^{\mathrm{k}-1} C^-_{\mathrm{i}+1/2,\mathrm{r,k}} \hat{u}^-_{\mathrm{i}+1/2,\mathrm{r,k}} = \hat{u}^-_{\mathrm{i}+1/2,\mathrm{k},2\mathrm{k}-1} \tag{3.22}$$

The WENO scheme for $k = 2$, which uses the stencil indicated in the middle of Figure 3.1, is 2^{nd} order accurate in non-smooth regions and 3^{rd} order accurate in smooth regions (referred to as WENO23). It can be derived quite easily for uniform

Table 3.1: WENO23 scheme for non-uniform and uniform grids.

	non-uniform grid	uniform grid
$\hat{u}^{-}_{\mathrm{i}+1/2,0}$	$= \left(\frac{x_{\mathrm{i}+3/2}-x_{\mathrm{i}+1/2}}{x_{\mathrm{i}+3/2}-x_{\mathrm{i}-1/2}}\right)\bar{u}_{\mathrm{i}} + \left(\frac{x_{\mathrm{i}+1/2}-x_{\mathrm{i}-1/2}}{x_{\mathrm{i}+3/2}-x_{\mathrm{i}-1/2}}\right)\bar{u}_{\mathrm{i}+1}$	$= \frac{1}{2}\bar{u}_{\mathrm{i}} + \frac{1}{2}\bar{u}_{\mathrm{i}+1}$
$\hat{u}^{-}_{\mathrm{i}+1/2,1}$	$= \left(1+\frac{x_{\mathrm{i}+1/2}-x_{\mathrm{i}-1/2}}{x_{\mathrm{i}+1/2}-x_{\mathrm{i}-3/2}}\right)\bar{u}_{\mathrm{i}} - \left(\frac{x_{\mathrm{i}+1/2}-x_{\mathrm{i}-1/2}}{x_{\mathrm{i}+1/2}-x_{\mathrm{i}-3/2}}\right)\bar{u}_{\mathrm{i}-1}$	$= \frac{3}{2}\bar{u}_{\mathrm{i}} - \frac{1}{2}\bar{u}_{\mathrm{i}-1}$
$\hat{u}^{+}_{\mathrm{i}-1/2,0}$	$= \left(1+\frac{x_{\mathrm{i}+1/2}-x_{\mathrm{i}-1/2}}{x_{\mathrm{i}+3/2}-x_{\mathrm{i}-1/2}}\right)\bar{u}_{\mathrm{i}} - \left(\frac{x_{\mathrm{i}+1/2}-x_{\mathrm{i}-1/2}}{x_{\mathrm{i}+3/2}-x_{\mathrm{i}-1/2}}\right)\bar{u}_{\mathrm{i}+1}$	$= \frac{3}{2}\bar{u}_{\mathrm{i}} - \frac{1}{2}\bar{u}_{\mathrm{i}+1}$
$\hat{u}^{+}_{\mathrm{i}-1/2,1}$	$= \left(\frac{x_{\mathrm{i}-1/2}-x_{\mathrm{i}-3/2}}{x_{\mathrm{i}+1/2}-x_{\mathrm{i}-3/2}}\right)\bar{u}_{\mathrm{i}-1} + \left(\frac{x_{\mathrm{i}+1/2}-x_{\mathrm{i}-1/2}}{x_{\mathrm{i}+1/2}-x_{\mathrm{i}-3/2}}\right)\bar{u}_{\mathrm{i}}$	$= \frac{1}{2}\bar{u}_{\mathrm{i}-1} + \frac{1}{2}\bar{u}_{\mathrm{i}}$
$C^{-}_{\mathrm{i}+1/2,0}$	$= \frac{x_{\mathrm{i}+1/2}-x_{\mathrm{i}-3/2}}{x_{\mathrm{i}+3/2}-x_{\mathrm{i}-3/2}}$	$= \frac{2}{3}$
$C^{-}_{\mathrm{i}+1/2,1}$	$= \frac{x_{\mathrm{i}+3/2}-x_{\mathrm{i}+1/2}}{x_{\mathrm{i}+3/2}-x_{\mathrm{i}-3/2}}$	$= \frac{1}{3}$
$C^{+}_{\mathrm{i}-1/2,0}$	$= \frac{x_{\mathrm{i}-1/2}-x_{\mathrm{i}-3/2}}{x_{\mathrm{i}+3/2}-x_{\mathrm{i}-3/2}}$	$= \frac{1}{3}$
$C^{+}_{\mathrm{i}-1/2,1}$	$= \frac{x_{\mathrm{i}+3/2}-x_{\mathrm{i}-1/2}}{x_{\mathrm{i}+3/2}-x_{\mathrm{i}-3/2}}$	$= \frac{2}{3}$
$IS_{\mathrm{i},0}$	$= 4\left(\frac{\left(x_{\mathrm{i}+1/2}-x_{\mathrm{i}-1/2}\right)\left(\bar{u}_{\mathrm{i}+1}-\bar{u}_{\mathrm{i}}\right)}{x_{\mathrm{i}+3/2}-x_{\mathrm{i}-1/2}}\right)^2$	$= \left(\bar{u}_{\mathrm{i}+1}-\bar{u}_{\mathrm{i}}\right)^2$
$IS_{\mathrm{i},1}$	$= 4\left(\frac{\left(x_{\mathrm{i}+1/2}-x_{\mathrm{i}-1/2}\right)\left(\bar{u}_{\mathrm{i}}-\bar{u}_{\mathrm{i}-1}\right)}{x_{\mathrm{i}+1/2}-x_{\mathrm{i}-3/2}}\right)^2$	$= \left(\bar{u}_{\mathrm{i}}-\bar{u}_{\mathrm{i}-1}\right)^2$

grids and the results are given in Table 3.1. The derivation for non-uniform grids is quite complex and explicit equations have not been reported in the literature before. Instead, the related coefficients were computed (Friedrich, 1998; Hu and Shu, 1999). In this study, explicit equations for the coefficients were derived analytically, facilitating the implementation of the WENO schemes. Explicit equations for the WENO23 scheme for non-uniform grids are also given in Table 3.1. The WENO scheme obtained for $k = 3$, which uses the stencil indicated in the bottom of Figure 3.1, is 3^{rd} order accurate in non-smooth regions and 5^{th} order accurate in smooth regions (referred to as WENO35). Because of the lengthy equations involved the equations have been given in Appendix 3.A. Obviously, higher order schemes would involve even more

complex equations and the analytic derivation would be very difficult, but for these cases the different coefficients can better be computed numerically.

3.4 WENO-based grid adaptation

In WENO schemes the local smoothness of the PDE is measured with smoothness indicators IS_{r}, which are subsequently used in the calculation of the weight factors given to a particular interpolation function as discussed in the previous section. The idea now is to also use these smoothness indicators to determine whether the grid needs to be locally adapted. For this purpose, firstly the maximal difference between the different smoothness indicators for a single grid cell is computed:

$$\Delta IS_{\mathrm{i}} = \max\left(\left|IS_{\mathrm{i,r}} - IS_{\mathrm{i,s\neq r}}\right|_{\mathrm{r,s=0\ldots k-1}}\right) \tag{3.23}$$

If for a certain grid cell ΔIS is larger than a user-specified value $\Delta IS_{\max}$, *i.e.* the solution is very non-smooth and more grid cells are required locally to accurately capture the solution in that part of the spatial domain, the cell is split in two. If for a certain grid cell and an adjactent grid cell ΔIS is smaller than a user specified value $\Delta IS_{\min}$, *i.e.* the solution is very smooth in both grid cells, these grid cells are merged. The splitting and merging of grid cells is schematically depicted in Figure 3.2. The optimal values for $\Delta IS_{\max}$ and $\Delta IS_{\min}$ are problem specific and have to be found by trial and error. The grid adaptation is carried out after each time-step (or alternatively after several time steps), which requires new values of $\bar{u}_{\mathrm{i}}$ (and $\bar{u}_{\mathrm{i+1}}$ in case of addition of a grid cell) for the new grid cells, to be obtained via interpolation. When merging two grid cells, the interpolated value $\bar{u}^*_{\mathrm{i}}$ (* refers to the new grid) is

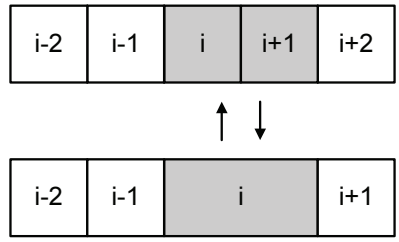

Figure 3.2: Local grid adaptation

simply the spatial average of $\bar{u}_{\mathrm{i}}$ and $\bar{u}_{\mathrm{i+1}}$:

$$\bar{u}_{\mathrm{i}}^{*} = \bar{u}_{\mathrm{i+1}} \left(\frac{x_{\mathrm{i+3/2}} - x_{\mathrm{i+1/2}}}{x_{\mathrm{i+3/2}} - x_{\mathrm{i-1/2}}} \right) + \bar{u}_{\mathrm{i}} \left(\frac{x_{\mathrm{i+1/2}} - x_{\mathrm{i-1/2}}}{x_{\mathrm{i+3/2}} - x_{\mathrm{i-1/2}}} \right) \tag{3.24}$$

When a grid cell needs to be added, the situation is somewhat more complicated. To prevent loss of stability and accuracy it is proposed to interpolate $\bar{u}_{\mathrm{i}}^{*}$ and $\bar{u}_{\mathrm{i+1}}^{*}$ using the WENO interpolation functions. This can be achieved by integrating the interpolation polynomials $u\left(x\right)|_{\mathrm{i,r}}$ (Equation 3.17) over the new cell widths $x_{\mathrm{i-1/2}}^{*} \ldots x_{\mathrm{i+1/2}}^{*}$ and $x_{\mathrm{i+1/2}}^{*} \ldots x_{\mathrm{i+3/2}}^{*}$, respectively:

$$\begin{aligned} \bar{u}_{\mathrm{i,r}}^{*} &= \frac{1}{x_{\mathrm{i+1/2}}^{*} - x_{\mathrm{i-1/2}}^{*}} \int_{\mathrm{x}_{\mathrm{i-1/2}}^{*}}^{\mathrm{x}_{\mathrm{i+1/2}}^{*}} u_{\mathrm{r}}\left(x\right)|_{\mathrm{i}} dx \\ \bar{u}_{\mathrm{i+1,r}}^{*} &= \frac{1}{x_{\mathrm{i+3/2}}^{*} - x_{\mathrm{i+1/2}}^{*}} \int_{\mathrm{x}_{\mathrm{i+1/2}}^{*}}^{\mathrm{x}_{\mathrm{i+3/2}}^{*}} u_{\mathrm{r}}\left(x\right)|_{\mathrm{i}} dx \end{aligned} \tag{3.25}$$

The different $\bar{u}_{\mathrm{i,r}}^{*}$ and $\bar{u}_{\mathrm{i+1,r}}^{*}$ are then combined using weight factors to calculate $\bar{u}_{\mathrm{i}}^{*}$ and $\bar{u}_{\mathrm{i+1}}^{*}$ as discussed in the previous section:

$$\bar{u}_{\mathrm{i}}^{*} = \sum_{\mathrm{r}=0}^{\mathrm{k-1}} w_{\mathrm{i,r}}^{*} \bar{u}_{\mathrm{i,r}}^{*} \quad , \qquad \bar{u}_{\mathrm{i+1}}^{*} = \sum_{\mathrm{r}=0}^{\mathrm{k-1}} w_{\mathrm{i+1,r}}^{*} \bar{u}_{\mathrm{i+1,r}}^{*} \tag{3.26}$$

and the weight factors w_{r}^{*} are again calculated via:

$$w_{\mathrm{i,r}}^{*} = \frac{C_{\mathrm{i,r}}^{*}}{\left(IS_{\mathrm{i,r}}\right)^{\mathrm{p}} \sum_{\mathrm{s}=0}^{\mathrm{k-1}} \frac{C_{\mathrm{i,s}}^{*}}{\left(IS_{\mathrm{i,s}}\right)^{\mathrm{p}}}} \quad , \qquad w_{\mathrm{i+1,r}}^{*} = \frac{C_{\mathrm{i+1,r}}^{*}}{\left(IS_{\mathrm{i,r}}\right)^{\mathrm{p}} \sum_{\mathrm{s}=0}^{\mathrm{k-1}} \frac{C_{\mathrm{i+1,s}}^{*}}{\left(IS_{\mathrm{i,s}}\right)^{\mathrm{p}}}} \tag{3.27}$$

The coefficients C_{r}^{*} can be determined by using the higher order $(2k-1)$ interpolations $\bar{u}_{\mathrm{i,r}}^{*}$ and $\bar{u}_{\mathrm{i+1,r}}^{*}$ on the interpolation stencil $\left(x_{\mathrm{i-k-1/2}} \ldots x_{\mathrm{i+k-1/2}}\right)$, see Equation 3.21. The $IS_{\mathrm{i,r}}$ were already calculated in the WENO schemes, see Equation 3.20. Explicit expressions for the grid adaptation procedure for the WENO23 scheme are given in Table 3.2 and those for the WENO35 scheme are given in Appendix 3.A. To facilitate the implementation of the grid adaptation procedure, the grid adaptation algorithm is given Appendix 3.B.

Table 3.2: Grid adaptation according to the WENO23 scheme.

$\bar{u}^*_{\mathrm{i},0}$	$= \left(2 + \dfrac{x_{\mathrm{i}+1/2} - x_{\mathrm{i}-1/2}}{x_{\mathrm{i}+3/2} - x_{\mathrm{i}-1/2}}\right) \dfrac{\bar{u}_{\mathrm{i}}}{2} - \left(\dfrac{x_{\mathrm{i}+1/2} - x_{\mathrm{i}-1/2}}{x_{\mathrm{i}+3/2} - x_{\mathrm{i}-1/2}}\right) \dfrac{\bar{u}_{\mathrm{i}+1}}{2}$
$\bar{u}^*_{\mathrm{i},1}$	$= \left(1 + \dfrac{x_{\mathrm{i}-1/2} - x_{\mathrm{i}-3/2}}{x_{\mathrm{i}+1/2} - x_{\mathrm{i}-3/2}}\right) \dfrac{\bar{u}_{\mathrm{i}}}{2} + \left(\dfrac{x_{\mathrm{i}+1/2} - x_{\mathrm{i}-1/2}}{x_{\mathrm{i}+1/2} - x_{\mathrm{i}-3/2}}\right) \dfrac{\bar{u}_{\mathrm{i}-1}}{2}$
$\bar{u}^*_{\mathrm{i}+1,0}$	$= \left(1 + \dfrac{x_{\mathrm{i}+3/2} - x_{\mathrm{i}+1/2}}{x_{\mathrm{i}+3/2} - x_{\mathrm{i}-1/2}}\right) \dfrac{\bar{u}_{\mathrm{i}}}{2} + \left(\dfrac{x_{\mathrm{i}+1/2} - x_{\mathrm{i}-1/2}}{x_{\mathrm{i}+3/2} - x_{\mathrm{i}-1/2}}\right) \dfrac{\bar{u}_{\mathrm{i}+1}}{2}$
$\bar{u}^*_{\mathrm{i}+1,1}$	$= \left(2 + \dfrac{x_{\mathrm{i}+1/2} - x_{\mathrm{i}-1/2}}{x_{\mathrm{i}+1/2} - x_{\mathrm{i}-3/2}}\right) \dfrac{\bar{u}_{\mathrm{i}}}{2} - \left(\dfrac{x_{\mathrm{i}+1/2} - x_{\mathrm{i}-1/2}}{x_{\mathrm{i}+1/2} - x_{\mathrm{i}-3/2}}\right) \dfrac{\bar{u}_{\mathrm{i}-1}}{2}$
$C^*_{\mathrm{i},0}, C^*_{\mathrm{i}+1,0}$	$= \dfrac{1}{2}\left(\dfrac{x_{\mathrm{i}+1/2} + x_{\mathrm{i}-1/2} - 2x_{\mathrm{i}-3/2}}{x_{\mathrm{i}+3/2} - x_{\mathrm{i}-3/2}}\right)$
$C^*_{\mathrm{i},1}, C^*_{\mathrm{i}+1,1}$	$= \dfrac{1}{2}\left(\dfrac{2x_{\mathrm{i}+3/2} - x_{\mathrm{i}+1/2} - x_{\mathrm{i}-1/2}}{x_{\mathrm{i}+3/2} - x_{\mathrm{i}-3/2}}\right)$

3.5 Demonstration of the numerical algorithm

To demonstrate the capabilities of the developed numerical algorithm, two test cases were studied: the 1-D convection equation and a conventional reverse flow reactor described with a strongly coupled system of 1-D convection dominated PDE's. Firstly, the accuracy of the different schemes are evaluated by solving the 1-D convection equation with an initially smooth profile. Then, the advantages of using automatic time step and local grid adaptation are demonstrated by solving the 1-D convection equation for an initially non-smooth profile and also by simulating the reverse flow reactor.

3.5.1 1-D convection equation: accuracy tests

To test the accuracy of the different schemes, a simple but numerically difficult to solve PDE, namely the 1-D convection equation, was studied for a smooth initial profile. The PDE and the initial and boundary conditions and also the analytical solution are given in Table 3.3. Firstly, a non-uniform grid was used with a sufficiently small time step to obtain a solution independent of the time discretisation scheme and the time step size and also without local grid adaptation to demonstrate that the WENO23 and WENO35 schemes indeed achieve 3^{rd} and 5^{th} order accuracy, respectively. For this purpose the following arbitrary grid was used:

$$\begin{aligned} x_{1/2} &= -1 \\ x_{3/2} &= -1 + 0.8/N \\ x_{\text{i}+1/2} &= x_{\text{i}-3/2} + 4/N \qquad i = 2 \ldots N \end{aligned} \tag{3.28}$$

The order of accuracy was measured with the L_1 norm (average error) and the

Table 3.3: 1-D convection equation: smooth problem.

$\dfrac{\partial u}{\partial t} + \dfrac{\partial u}{\partial x}$	$= 0$		
$u\,(0, x)$	$= \sin(\pi x)$	x_{interval}	$= -1 \ldots 1$ m
$u\,(t, 0)$	$=$ periodic	t_{interval}	$= 0 \ldots 1$ s
$u\,(t, x)$	$= \sin(\pi(t - x))$	ϵ	$= 1{\cdot}10^{-6}$

L_∞ norm (maximal error):

$$L_1 = \frac{1}{L}\sum_{\mathrm{i}=1}^{\mathrm{N}} \left(\left(x_{\mathrm{i}+1/2} - x_{\mathrm{i}-1/2} \right) \left| \bar{u}_{\mathrm{i,computed}} - \bar{u}_{\mathrm{i,analytic}} \right| \right) \tag{3.29}$$

$$L_\infty = \max \left(\left| \bar{u}_{\mathrm{i,computed}} - \bar{u}_{\mathrm{i,analytic}} \right| \right) \tag{3.30}$$

The results are presented in Table 3.4. The Upwind scheme has the expected 1$^{\mathrm{st}}$ order accuracy and the WENO23 scheme 3$^{\mathrm{rd}}$ order accuracy, but only when employing a reasonably large number of grid cells, while the WENO35 scheme reaches 5$^{\mathrm{th}}$ order accuracy already for a small number of grid cells. Obviously, the WENO35 scheme is superior to the other two schemes. Furthermore, the obtained accuracy orders on the non-uniform grid were very similar to those obtained for uniform grids (Shu, 1998).

Table 3.4: Accuracy test of WENO schemes on non-uniform grids.

Scheme	N	L_∞	L_∞ order	L_1	L_1 order
	10	$7.06{\cdot}10^{-1}$		$4.48{\cdot}10^{-1}$	
	20	$4.84{\cdot}10^{-1}$	0.54	$3.12{\cdot}10^{-1}$	0.52
	40	$2.83{\cdot}10^{-1}$	0.77	$1.82{\cdot}10^{-1}$	0.78
Upwind	80	$1.56{\cdot}10^{-1}$	0.85	$9.86{\cdot}10^{-1}$	0.88
	160	$8.20{\cdot}10^{-2}$	0.93	$5.15{\cdot}10^{-2}$	0.94
	320	$4.20{\cdot}10^{-2}$	0.97	$2.63{\cdot}10^{-2}$	0.97
	640	$2.12{\cdot}10^{-2}$	0.98	$1.33{\cdot}10^{-2}$	0.98
	10	$3.16{\cdot}10^{-1}$		$1.48{\cdot}10^{-1}$	
	20	$1.28{\cdot}10^{-1}$	1.30	$6.02{\cdot}10^{-2}$	1.29
	40	$5.41{\cdot}10^{-2}$	1.25	$1.82{\cdot}10^{-2}$	1.73
WENO23	80	$2.07{\cdot}10^{-2}$	1.39	$4.56{\cdot}10^{-3}$	2.00
	160	$7.18{\cdot}10^{-3}$	1.53	$1.00{\cdot}10^{-3}$	2.18
	320	$1.86{\cdot}10^{-3}$	1.95	$1.60{\cdot}10^{-4}$	2.65
	640	$2.36{\cdot}10^{-4}$	2.98	$1.42{\cdot}10^{-5}$	3.50
	10	$4.55{\cdot}10^{-2}$		$1.88{\cdot}10^{-2}$	
	20	$1.67{\cdot}10^{-3}$	4.76	$8.51{\cdot}10^{-4}$	4.46
	40	$4.46{\cdot}10^{-5}$	5.23	$1.90{\cdot}10^{-5}$	5.48
WENO35	80	$1.24{\cdot}10^{-6}$	5.19	$4.79{\cdot}10^{-7}$	5.33
	160	$3.73{\cdot}10^{-8}$	5.22	$1.45{\cdot}10^{-8}$	5.26
	320	$1.04{\cdot}10^{-9}$	4.98	$3.41{\cdot}10^{-10}$	5.18
	640	$3.56{\cdot}10^{-11}$	4.86	$1.10{\cdot}10^{-11}$	4.95

To test the accuracy of the time integration schemes, a uniform grid and the WENO35 scheme with a sufficiently fine grid were used to obtain a solution, which is independent of the grid size and convection discretisation scheme. The results of the accuracy tests are given in Table 3.5 and indeed al schemes have the expected order, already for quite large time steps. Obviously, the SDIRK33 scheme has the best performance.

Table 3.5: Accuracy test of SDIRK schemes.

Scheme	Δt	L_∞	L_∞ order	L_1	L_1 order
	$64{\cdot}10^{-3}$	$2.64{\cdot}10^{-1}$		$1.68{\cdot}10^{-1}$	
	$32{\cdot}10^{-3}$	$1.44{\cdot}10^{-1}$	0.88	$9.15{\cdot}10^{-2}$	0.88
	$16{\cdot}10^{-3}$	$7.54{\cdot}10^{-1}$	0.93	$4.80{\cdot}10^{-2}$	0.93
Euler	$8{\cdot}10^{-3}$	$3.85{\cdot}10^{-1}$	0.97	$2.45{\cdot}10^{-2}$	0.97
	$4{\cdot}10^{-3}$	$1.95{\cdot}10^{-2}$	0.98	$1.24{\cdot}10^{-2}$	0.98
	$2{\cdot}10^{-3}$	$9.82{\cdot}10^{-2}$	0.99	$6.25{\cdot}10^{-3}$	0.99
	$1{\cdot}10^{-3}$	$4.92{\cdot}10^{-2}$	1.00	$3.13{\cdot}10^{-3}$	1.00
	$64{\cdot}10^{-3}$	$4.94{\cdot}10^{-3}$		$3.14{\cdot}10^{-3}$	
	$32{\cdot}10^{-3}$	$1.32{\cdot}10^{-3}$	1.90	$8.41{\cdot}10^{-4}$	1.90
	$16{\cdot}10^{-3}$	$3.19{\cdot}10^{-4}$	2.05	$2.03{\cdot}10^{-4}$	2.05
SDIRK22	$8{\cdot}10^{-3}$	$7.98{\cdot}10^{-5}$	2.00	$5.08{\cdot}10^{-5}$	2.00
	$4{\cdot}10^{-3}$	$2.01{\cdot}10^{-5}$	1.99	$1.28{\cdot}10^{-5}$	1.99
	$2{\cdot}10^{-3}$	$5.02{\cdot}10^{-6}$	2.00	$3.19{\cdot}10^{-6}$	2.00
	$1{\cdot}10^{-3}$	$1.25{\cdot}10^{-6}$	2.00	$7.98{\cdot}10^{-7}$	2.00
	$64{\cdot}10^{-3}$	$6.23{\cdot}10^{-4}$		$3.96{\cdot}10^{-4}$	
	$32{\cdot}10^{-3}$	$7.99{\cdot}10^{-5}$	2.96	$5.09{\cdot}10^{-5}$	2.96
	$16{\cdot}10^{-3}$	$1.02{\cdot}10^{-5}$	2.96	$6.52{\cdot}10^{-6}$	2.96
SDIRK33	$8{\cdot}10^{-3}$	$1.28{\cdot}10^{-6}$	3.00	$8.17{\cdot}10^{-7}$	3.00
	$4{\cdot}10^{-3}$	$1.62{\cdot}10^{-7}$	2.98	$1.03{\cdot}10^{-7}$	2.98
	$2{\cdot}10^{-3}$	$2.15{\cdot}10^{-8}$	2.93	$1.35{\cdot}10^{-8}$	2.93
	$1{\cdot}10^{-3}$	$2.56{\cdot}10^{-9}$	3.06	$1.63{\cdot}10^{-9}$	3.06

3.5.2 1-D convection equation: moving front

To demonstrate the advantages of using automatic time stepping and local grid adaptation, the 1-D convection equation was solved with a steep front as initial profile. The PDE and the initial and boundary conditions are given in Table 3.6. To illustrate the effectiveness of the WENO schemes for capturing steep gradients, firstly results for a non-uniform grid without grid adaptation are discussed. For this purpose a similar grid as in given in Equation 3.28 was used:

$$\begin{aligned} x_{1/2} &= 0 \\ x_{3/2} &= 0.01 \\ x_{\mathrm{i}+1/2} &= x_{\mathrm{i}-3/2} + 0.05 \qquad i = 2 \ldots 40 \end{aligned} \tag{3.31}$$

Table 3.6: 1-D convection equation: moving front.

$\frac{\partial u}{\partial t} + \frac{\partial u}{\partial x}$	$= 0$		
$u\,(0, x)$	$= 0$	x_{interval}	$= 0 \ldots 1$ m
$u\,(t, 0)$	$= 1$	t_{interval}	$= 0 \ldots 0.5$ s
$u\,(t, x)$	$= H(t - x)$	ϵ	$= 1{\cdot}10^{-10}$

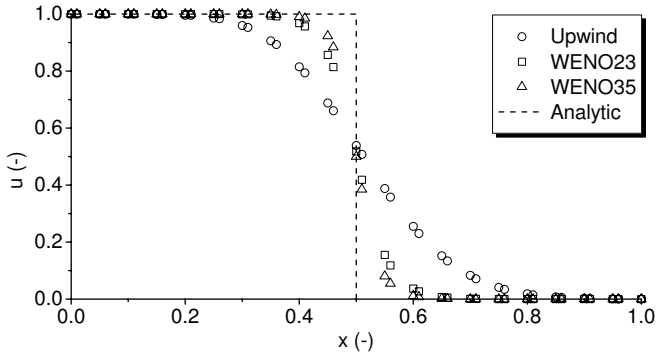

Figure 3.3: Numerical solution of the 1-D convection equation at $t = 0.5$ s on a non-uniform grid for different convection discretisation schemes. The computational grid consists of 40 cells.

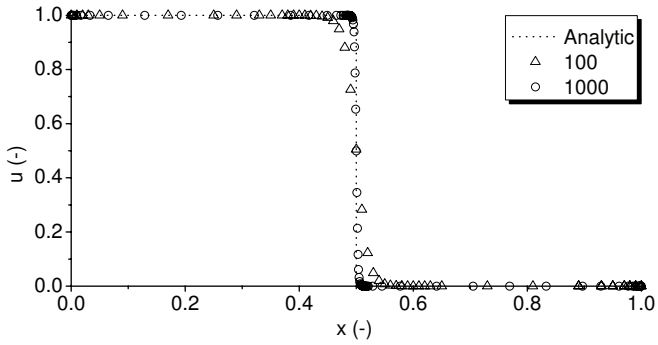

Figure 3.4: Numerical solution of the 1-D convection equation at $t = 0.5$ s with grid adaptation for 100 and 1000 grid cells initially.

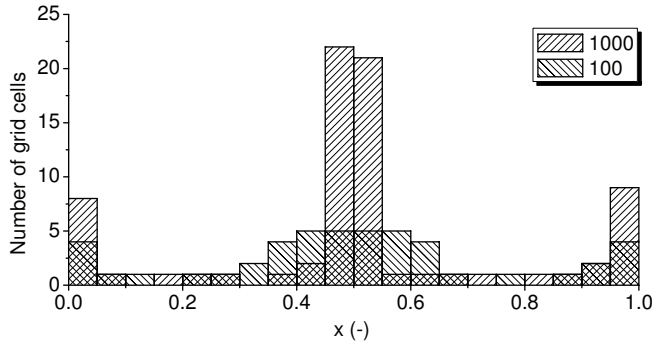

Figure 3.5: Distribution of the grid cells for the numerical solution of the 1-D convection equation at $t = 0.5$ s with grid adaptation for 100 and 1000 grid cells initially.

The numerical results obtained with the Upwind and WENO schemes for non-uniform grids as well as the analytic solution are presented in Figure 3.3. The markers indicate the cell faces. Indeed the WENO schemes for non-uniform grids are much more capable of accurately capturing steep gradients on a non-uniform grid compared to the 1^{st} order Upwind scheme.

To demonstrate the grid adaptation procedure, the 1-D convection equation with the moving front was solved using the WENO35 scheme with an initially uniform grid of 100 and 1000 cells and a sufficiently small time step. The minimal allowed grid cell size was equal to that of the initial grid size and the maximal allowed grid cell

size was 0.1 m. Again ϵ was taken as $1{\cdot}10^{-10}$. The grid was adapted with parameters $\Delta IS_{\max} = 1{\cdot}10^{-9}$ and $\Delta IS_{\min} = 1{\cdot}10^{-10}$. The cell-face values and the analytic solution are shown in Figure 3.4. The distribution of the grid cells is given in Figure 3.5. The numerical solutions correspond well to the case without grid adaptation and the maximal absolute difference between those solutions (*i.e.* L_∞) was smaller than $1{\cdot}10^{-4}$. For an initial grid of 100 cells, the number cells was only reduced to 47, but for an initial grid of 1000 cells the number of cells was reduced to 75, which clearly demonstrates that local grid adaptation can greatly reduce the the required CPU time when solving convection dominated PDE's. Obviously grid adaptation is most beneficial for very steep gradients and a fine initial grid.

To evaluate the different time integration schemes and the time-step adaptation procedure, the 1-D convection equation describing a moving front was again solved using the WENO35 scheme with the same parameters as discussed before, but now with an uniform grid of 1000 cells and without grid adaptation. The initial time step was set to $1{\cdot}10^{-6}$ s and different values of tol_{it} were used. Because the WENO schemes are non-linear, the convection term was discretised implicitly with the Upwind scheme and then iteratively corrected (semi-implicitly) with the WENO scheme in order to obtain a stable solution (*i.e.* deferred correction), following Ferziger and Perić (1996). In Table 3.7 the L_1-norm and the required CPU time are given. Here L_1 was calculated from the spatially averaged difference between the analytical and numerical solution and it is observed that for the SDIRK schemes L_1 converges to a value that is due to

Table 3.7: Benchmark of SDIRK schemes: moving front.

Scheme	tol_{it}	L_1	CPU time (s)
Euler	$1{\cdot}10^{-7}$	$4.88{\cdot}10^{-3}$	52
	$1{\cdot}10^{-8}$	$2.93{\cdot}10^{-3}$	193
	$1{\cdot}10^{-9}$	$2.32{\cdot}10^{-3}$	465
SDIRK22	$1{\cdot}10^{-7}$	$2.10{\cdot}10^{-3}$	15
	$1{\cdot}10^{-8}$	$2.09{\cdot}10^{-3}$	32
	$1{\cdot}10^{-9}$	$2.09{\cdot}10^{-3}$	56
SDIRK33	$1{\cdot}10^{-7}$	$2.09{\cdot}10^{-3}$	11
	$1{\cdot}10^{-8}$	$2.09{\cdot}10^{-3}$	20
	$1{\cdot}10^{-9}$	$2.09{\cdot}10^{-3}$	39

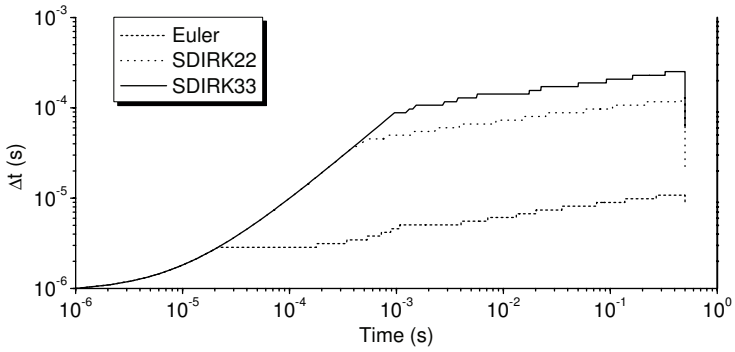

Figure 3.6: Time step as a function of the time for different time discretisation schemes for the solution of the 1-D convection equation ($tol_{\mathrm{it}} = 1{\cdot}10^{-9}$).

the error in the spatial discretisation. Only for the 1$^{\mathrm{st}}$ order accurate Euler scheme a significant contribution to the error as a result of the time discretisation was found. Inspecting the required CPU time, the SDIRK33 scheme has the best performance, which can be explained by the larger time steps that can be used with this scheme. This is illustrated in Figure 3.6, where the time step used is given as a function of the time. The difference in the time step between the SDIRK schemes and the Euler scheme is one order of magnitude.

3.5.3 Reverse flow reactor

Previously, the numerical algorithm was tested by solving the 1-D convection equation, which is only a single PDE. However, the main goal of this chapter is to develop a numerical algorithm to efficiently simulate reverse flow (catalytic membrane) reactors, which are described by a set of strongly coupled convection-dominated PDE's. Therefore, a conventional Reverse Flow Reactor (RFR) was simulated for the combustion of a small amount of CH_4 in air on a Pt/γ-Al_2O_3 catalyst consisting of porous spherical particles. Under certain conditions this RFR can be described with a mass conservation equation for CH_4 and a single heat balance (homogeneous model). As the initial condition a uniform temperature profile was selected and the usual Danckwerts-type boundary conditions were applied. For the reaction rate the kinetics determined by van Sint Annaland (2000) were used. The effective thermal conductivity λ_{eff} was calculated with a homogeneous axial heat dispersion model according to Vortmeyer

Table 3.8: Governing equations and constitutive relations that describe the RFR.

$$\varepsilon_{\mathrm{g}}\rho_{\mathrm{g}}\frac{\partial w_{\mathrm{CH_4,g}}}{\partial t} = -\rho_{\mathrm{g}}v_{\mathrm{g}}\frac{\partial w_{\mathrm{CH_4,g}}}{\partial x} - M_{\mathrm{CH_4}}\eta k_1 c_{\mathrm{CH_4,g}}$$

$$\left(\varepsilon_{\mathrm{g}}\rho_{\mathrm{g}}C_{\mathrm{p,g}} + (1-\varepsilon_{\mathrm{g}})\,\rho_{\mathrm{s}}C_{\mathrm{p,s}}\right)\frac{\partial T}{\partial t} = -\rho_{\mathrm{g}}v_{\mathrm{g}}C_{\mathrm{p,g}}\frac{\partial T}{\partial x} + \frac{\partial}{\partial x}\left(\lambda_{\mathrm{eff}}\frac{\partial T}{\partial x}\right) - \eta k_1 c_{\mathrm{CH_4,g}}\Delta H_{\mathrm{r}}$$

$$\eta = \frac{3\varphi - \tanh(3\varphi)}{3\varphi^2\tanh(3\varphi)} \qquad \varphi = \frac{d_{\mathrm{p}}}{6}\sqrt{\frac{\tau k_1}{\varepsilon_{\mathrm{s}}D_{\mathrm{CH_4,air}}}}$$

$$k_1 = a_{\mathrm{s}}k_{\mathrm{r}}c_{\mathrm{O_2,g}}exp\left(-\frac{E_{\mathrm{a}}}{R_{\mathrm{g}}T}\right) \qquad \lambda_{\mathrm{eff}} = \lambda_{\mathrm{bed}} + \frac{RePr\lambda_{\mathrm{g}}}{Pe_{\mathrm{ax}}} + \frac{Re^2Pr^2\lambda_{\mathrm{g}}}{6\,(1-\epsilon_{\mathrm{g}})\,Nu}$$

(1989) and Gunn and Misbah (1993). The set of equations equations that describe the RFR are given in Table 3.8. For a more detailed discussion on the reactor model and the assumptions, the interested reader is referred to Chapter 4. The kinetic parameters, physical properties and geometrical parameters that were used for the simulations are summarised in Table 3.9. Gas phase mixture properties were calculated according to Daubert and Danner (1985) and Reid et al. (1987).

The convection terms in the heat and mass balances were discretised using the WENO35 scheme for non-uniform grids and also the grid was adapted according to this scheme. The numerical parameters that were used are summarised in Table 3.10.

Table 3.9: Physical properties and geometrical parameters used for the simulation of the RFR.

a_{s}	$1{\cdot}10^7$	$\mathrm{m^2/m^3}$	T_{in}	300	K
$C_{\mathrm{p,s}}$	1000	J/kg/K	$w_{\mathrm{CH4,g,in}}$	0.002	
d_{p}	0.005	m	ϵ_{g}	0.4	
E_{a}	98.5	kJ/mol	ϵ_{s}	0.6	
k_{r}	0.1608	$\mathrm{m^4/mol/s}$	λ_{bed}	0.3	J/m/K/s
L	1	m	$\rho_{\mathrm{g}}v_{\mathrm{g}}$	1	$\mathrm{kg/m^2/s}$
p_{g}	$1{\cdot}10^5$	Pa	ρ_{s}	2000	$\mathrm{kg/m^3}$
t_{switch}	300	s	τ	2	

Table 3.10: Numerical parameters used for the simulation of the RFR.

	tol_{it}	ϵ	$\Delta IS_{\max}$	$\Delta IS_{\min}$
w_{CH_4}	$1{\cdot}10^{-7}$	$1{\cdot}10^{-14}$	$1{\cdot}10^{-10}$	$1{\cdot}10^{-11}$
T	$1{\cdot}10^{-3}$	$1{\cdot}10^{-6}$	10	1

The grid was initially uniform and consisted of 1000 grid cells. The minimal allowed grid cell size was set to 0.001 m, the maximal grid cell size to 0.1 m and the initial time step was $1{\cdot}10^{-5}$ s. To illustrate the typical movement of the axial temperature profile in the RFR, the profiles are presented in Figure 3.7 at different moments in time during a forward cycle in the cyclic stationary state. To illustrate the presence of the steep gradients and the advantage of using local grid adaptation to capture these gradients with minimal computational effort, the axial CH_4 weight fraction and temperature profiles in the RFR just after the beginning of a forward semi-cycle (0.05 s) in the cyclic stationary state are given in Figure 3.8 and the accompanying grid cell distribution in Figure 3.9. At this point in time the grid consists of only 211 grid cells. Calculations with the High Switching Frequency Model (see Chapter 4) showed that the required number of grid cells can be reduced by a factor of 50 to 100 compared to a case where the Upwind scheme is used without grid adaptation. This clearly demonstrates the efficiency of the numerical algorithm for simulating a RFR with respect to the grid adaptation and the higher order discretisation of the convection terms.

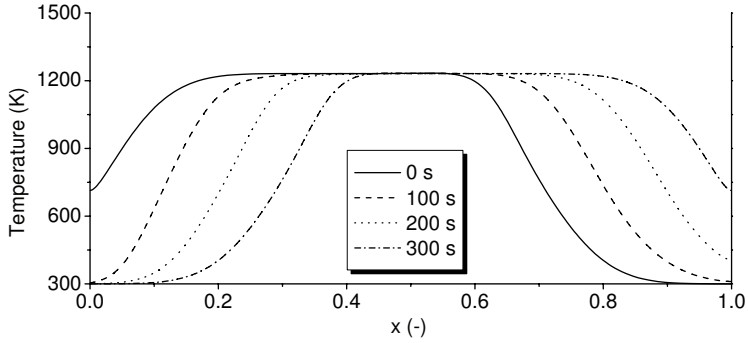

Figure 3.7: Axial temperature profiles in the RFR at several moments in time during a forward cycle.

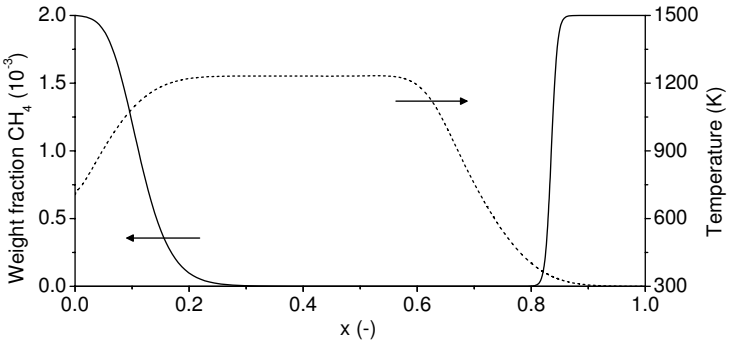

Figure 3.8: Axial CH_4 weight fraction and temperature profiles in the RFR just after the beginning of a forward semi-cycle (t = 0.05 s).

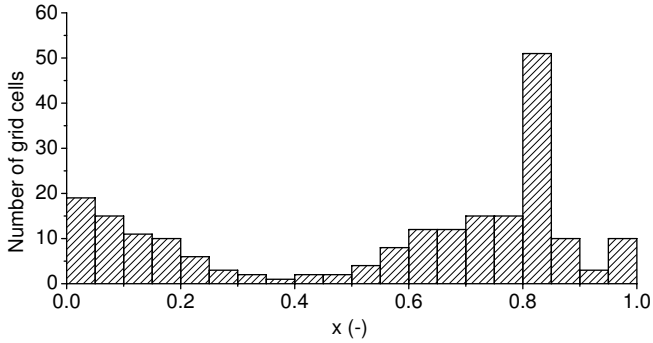

Figure 3.9: Distribution of grid cells in the simulation of the RFR just after the beginning of a forward semi-cycle (t = 0.05 s).

Comparing the different convection discretisation schemes, the choice of the optimal scheme is obvious: the WENO35 scheme is superior to the WENO23 and Upwind schemes and the additional CPU cost is small because a large part of the WENO35 scheme is only dependent on the geometry of the grid and has to be calculated only once per time step. For the time discretisation schemes, the choice is less obvious. This is because all stages in the SDIRK schemes have about the same CPU cost and therefore the additional accuracy obtained with an additional stage may not be worth the accompanying additional CPU cost. This is especially important when simulating reverse flow (catalytic membrane) reactors where the CPU cost per stage is substan-

tial due to the evaluation of the Jacobian of the source terms in the Newton-Rhapson procedure.

To select the most efficient time integration scheme, the RFR was simulated as above with the WENO35 scheme and grid adaptation, but with different time discretisation schemes and different values of tol_{it}. Again the numerical parameters in Table 3.10 were used. The grid was initially uniform and consisted of 1000 grid cells. The minimal allowed grid cell size was set to 0.001 m and the maximal grid cell size to 0.1 m. The initial temperature profile was 1200 K throughout the reactor and the initial time step was $1{\cdot}10^{-5}$ s. To evaluate the performance of the different schemes, in Table 3.11 the required CPU times to simulate the first 300 s are given. For lower accuracies the SDIRK22 and SDIRK33 schemes give a very comparable performance. This is because the time steps that are obtained with the time step adaptation using the SDIRK33 scheme are only slightly larger than those obtained using the SDIRK22 scheme. For higher accuracies the relative difference in time steps is larger and thus the SDIRK33 scheme is more efficient. This is illustrated in Figure 3.10, where the required time steps are plotted as a function of time. The differences in time steps are clearly observed on the left side of the figure, where the time step is determined by the moving CH_4 weight fraction profile and on the right side of the figure, where the time step is determined by the moving temperature profile (this is the most CPU demanding part). Furthermore, for the Euler scheme, the maximal temperature, $T_{\max}$ is lower than that of the SDIRK schemes, indicating a less accurate solution. When

Table 3.11: Benchmark of SDIRK schemes: RFR.

Scheme	tol_{it} $w_{\mathrm{CH_4}}$	tol_{it} T	$T_{\max}$	CPU time (s)
	$1{\cdot}10^{-5}$	$1{\cdot}10^{-1}$	1247.30	72
Euler	$1{\cdot}10^{-6}$	$1{\cdot}10^{-2}$	1248.62	225
	$1{\cdot}10^{-7}$	$1{\cdot}10^{-3}$	1249.04	757
	$1{\cdot}10^{-5}$	$1{\cdot}10^{-1}$	1249.10	39
SDIRK22	$1{\cdot}10^{-6}$	$1{\cdot}10^{-2}$	1249.20	77
	$1{\cdot}10^{-7}$	$1{\cdot}10^{-3}$	1249.23	213
	$1{\cdot}10^{-5}$	$1{\cdot}10^{-1}$	1249.19	40
SDIRK33	$1{\cdot}10^{-6}$	$1{\cdot}10^{-2}$	1249.21	75
	$1{\cdot}10^{-7}$	$1{\cdot}10^{-3}$	1249.22	166

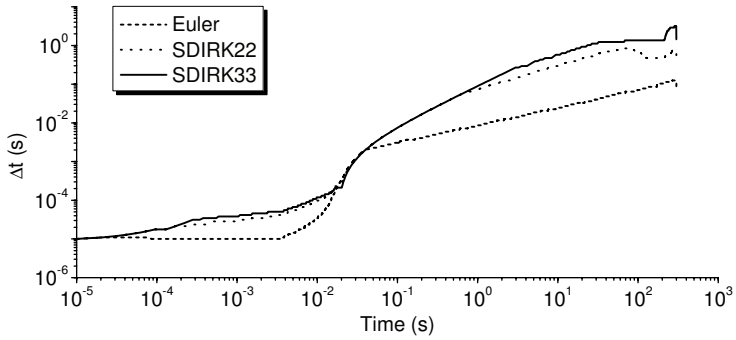

Figure 3.10: Time step as a function of the time for different time discretisation schemes for the simulation of the RFR ($tol_{\mathrm{it}}\ T = 1{\cdot}10^{-3}$, $tol_{\mathrm{it}}\ w_{\mathrm{CH_4}} = 1{\cdot}10^{-7}$).

high accuracies are required, the SDIRK33 is recommended, but when a large number of equations is involved (*e.g.* in the RFCMR), the SDIRK22 scheme is recommended, because the increased accuracy with an additional third stage is not worth the additional CPU cost.

3.6 Conclusions

In this chapter an efficient numerical algorithm was developed for the simulation of reverse flow (catalytic membrane) reactors, which are described by a system of strongly coupled convection dominated PDE's. This algorithm uses the method of lines for the discretisation of the PDE and includes higher order discretisation schemes for the accumulation and convection terms and also automatic time stepping and local grid adaptation.

For the time integration SDIRK schemes were used. SDIRK schemes are as stable as the first order Euler scheme, but can handle much larger time steps for a specified accuracy, which reduces the CPU time significantly. Using automatic time step adaptation, the time step is continuously maximised, while just meeting the accuracy requirements, thereby automatically minimising the required CPU time.

For the discretisation of the convection terms, explicit expressions for WENO schemes for non-uniform grids were derived analytically and it was shown that these schemes indeed show their accuracy orders for problems with smooth initial profiles

on non-uniform grids. Furthermore, a local grid adaptation technique was presented, which is based on the WENO principles. With this grid adaptation technique and the higher order discretisation schemes for the convection term, it was demonstrated that the number of grid cells that are required to accurately capture steep gradients can be greatly reduced, thereby greatly reducing the computational effort.

A conventional reverse flow reactor was simulated and it was shown that during a cycle, the time step could be increased with several orders of magnitude while keeping the desired accuracy because of the large difference in the time constants for mass and heat accumulation. With adaptive time stepping the required CPU time can be strongly reduced. When employing SDIRK schemes for the time integration, the CPU time could be even further reduced by a factor of 2-5, depending on the required accuracy. With respect to the WENO schemes and the local grid adaptation it was found that the required number of grid cells to accurately capture the concentration and temperature profiles can be reduced by a factor of 50-100 compared to a case where no local grid adaptation and the first order accurate Upwind convection discretisation scheme are used, which reduces the CPU time enormously. It might be argued that the equations of the WENO schemes for non-uniform grids are extensive and computational demanding. However, a large part of the equations is only dependent on the geometry of the grid and when simulating reverse flow (catalytic membrane) reactors, which require several Newton-Rhapson iterations per time step, these grid dependent coefficients have to be calculated only once per time step.

Acknowledgement

The financial support of the Dutch Technology Foundation STW, the Energy research Centre of the Netherlands ECN and the Association of Industrial Advisory Council Members of the Dutch Institute for Catalysis Research VIRAN is gratefully acknowledged.

Nomenclature

a_s	Catalyst specific surface area, m^2/m^3
$\mathbf{A}$	Matrix containing the implicit coefficients of a given linear system
$\mathbf{b}$	Vector containing the explicit terms of a given linear system

c	Concentration, mol/m^3
C	Coefficient used in the WENO scheme
C_p	Heat capacity, J/kg/K
d_p	Particle diameter, m
D	Diffusivity, m^2/s
E_a	Activation energy, J/mol
H	Heaviside function
ΔH_r	Reaction heat, J/mol
IS	Smoothness indicator
ΔIS_i	Maximal difference in smoothness indicators for a grid cell
k	Order of accuracy
k_1	Reaction rate constant, 1/s
k_r	Reaction rate constant, m^4/mol/s
L	Reactor length, m
L_1	L_1 norm
L_∞	L_∞ norm
M	Molar weight, mol/kg
N	Number of grid cells
Nu	Dimensionless Nusselt number, $\alpha_{\mathrm{g-s}}\ d_\mathrm{p}\ /\ \lambda_\mathrm{g}$
p	Pressure, Pa
p	Constant used in the WENO scheme
Pe_ax	Dimensionless Péclet number for axial heat dispersion, $\rho_\mathrm{g} v_\mathrm{g} d_\mathrm{p}\ C_{\mathrm{p,g}}/\lambda_\mathrm{ax}$
Pr	Dimensionless Prandtl number, $C_{\mathrm{p,g}}\eta_\mathrm{g}/\lambda_\mathrm{g}$
r	Indicates stencil in the WENO schemes
r	Reaction rate, mol/m^3/s
R_g	Gas constant, 8.314 J/mol/K
Re	Dimensionless Reynolds number, $\rho_\mathrm{g} v_\mathrm{g} d_\mathrm{p}/\eta_\mathrm{g}$
$S(u)$	source term, 1/s
t	Time, s
t_switch	Time between switching of the flow direction, s
t_interval	Time interval, s
Δt	Time step, s
T	Temperature, K
tol_it	Spatially averaged tolerance of the Newton-Rhapson iteration

tol_{t}	Spatially averaged tolerance of the time integration
u	A given variable u
$\hat{u}$	Point value of u
$\bar{u}$	Cell-averaged value of u
v	Velocity, m/s
w	Weight factor used in the WENO scheme
w	Weight fraction
x	Spatial coordinate, m
x_{interval}	Spatial domain, m
Δx	Grid cell size, m
$\mathbf{x}$	Vector containing the variables of a given linear system

Greek symbols

$\alpha_{\mathrm{g-s}}$	Gas-to-solid heat transfer coefficient, J/m^2/K/s
$\alpha, \beta, \gamma, \delta$	Parameters in the SDIRK schemes
ϵ	Constant used in the WENO scheme
ϵ	Constant used in linearisation of the source term
ϵ_{g}	Gas phase porosity
ϵ_{s}	Catalyst porosity
η	Effectiveness factor, dimensionless
η	Viscosity, kg/m^2/s
λ	A given constant in an ODE, 1/s
λ	Thermal conductivity, J/m/K/s
λ_{ax}	Axial thermal conductivity, J/m/K/s
λ_{bed}	Thermal conductivity of a quiescent packed bed, J/m/K/s
λ_{eff}	Effective thermal conductivity, J/m/K/s
ρ	Density, kg/m^3
τ	Tortuosity
φ	Thiele modulus

Subscripts

analytic	Analytical solution
i	Indicates grid cell i
in	Inlet

g	Gas
s	Solid
max	Maximal
min	Minimal
computed	Computed solution

Superscripts

*	Refers to new, adapted grid
m	Indicates iteration value
n	Indicates time level

Bibliography

Alexander, R., "Diagonal implicit Runge-Kutta methods for stiff O.D.E.'s", SIAM Journal om Numerical Analysis, 14(6), 1006–1021 (1977)

Ascher, U. M., Petzold, L. R., "Computer Methods for Ordinary Differential Equations and Differential Algebraic Equations", SIAM Press, Philadelphia (1998)

Aubé, F., Sapoundjiev, H., "Mathematical model and numerical simulations of catalytic flow reversal reactors for industrial applications", Computers & Chemical Engineering, 24(12), 2623–2632 (2000)

Courant, R., Friedrichs, K., Lewy, H., "Partial differential equations of mathematical physics", Mathematische Annalen, 100, 32–74 (1928)

Daubert, T. E., Danner, R. P., "Data Compilation Tables of Properties of Pure Compounds", American Institute of Chemical Engineers, New York (1985)

Ferziger, J. H., Perić, M., "Computational Methods for Fluid Dynamics", Springer, Berlin (1996)

Finlayson, B. A., "Numerical Methods for Problems with Moving Fronts", Ravenna Park Publishing, Inc., Seattle (1992)

Frank, R., Schneid, J., Ueberhuber, C. W., "Order results for implicit Runge-Kutta methods applied to stiff systems", SIAM Journal on Numerical Analysis, 22(3), 515–534 (1985)

Friedrich, O., "Weighted essentially non-oscillatory schemes for the interpolation of mean values on unstructured grids", Journal of Computational Physics, 144(1), 194–212 (1998)

Gunn, D. J., Misbah, M. M. A., "Bayesian estimation of heat transport parameters in fixed beds", International Journal of Heat and Mass Transfer, 36(8), 2209–2221 (1993)

Hairer, E., Wanner, G., "Solving Ordinary Differential Equations II: Stiff and Differential-Algebraic Problems", Springer-Verlag, Berlin (1991)

Hu, C., Shu, C.-W., "Weighted essentially non-oscillatory schemes on triangular meshes", Journal of Computational Physics, 150(1), 97–127 (1999)

Jiang, G.-S., Shu, C.-W., "Efficient implementation of weighted ENO schemes", Journal of Computational Physics, 126(1), 202–228 (1996)

Liu, X. D., Osher, S., Chan, T., "Weighted essentially non-oscillatory schemes", Journal of Computational Physics, 115(1), 200–212 (1994)

Reid, R. C., Prausnitz, J. M., Poling, B. E., "The Properties of Gases and Liquids", 4^{th} Edition, McGraw-Hill, Inc., New York (1987)

Schiesser, W. E., "The Numerical Method of Lines : Integration of Partial Differential Equations", Academic Press, San Diego (1991)

Shu, C.-W., "Essentially non-oscillatory and weighted essentially non-oscillatory schemes for hyperbolic conservation laws", in "Advanced Numerical Approximations of Nonlinear Hyperbolic Equations, Lecture Notes in Mathematics", Cockburn, B., Johnson, C., Shu, C.-W., Tadmore, E. Eds., Vol. 1697, Springer, 325–432 (1998)

van Sint Annaland, M., "A Novel Reverse Flow Reactor Coupling Endothermic and Exothermic Reactions", Ph.D. thesis, University of Twente, Enschede, The Netherlands (2000)

Vortmeyer, D., "Packed bed thermal dispersion models and consistent sets of coefficients", Chemical Engineering and Processing, 26(3), 263–268 (1989)

Wouwer, A. V., Saucez, P., Schiesser, W. E., "Some user-oriented comparisons of adaptive grid methods for partial differential equations in one space dimension", Applied Numerical Mathematics, 26(1-2), 49–62 (1998)

3.A WENO35 scheme for non-uniform grids

Explicit equations for the WENO35 scheme for uniform grids are given in Table 3.12 and those for non-uniform grids in Tables 3.13 and 3.14. Explicit equations for the grid adaptation procedure for the WENO35 scheme have been summarised in Table 3.15.

Table 3.12: WENO35 scheme for uniform grids

$\hat{u}^-_{\mathrm{i}+1/2,0}$	$= \frac{1}{3}\bar{u}_{\mathrm{i}} + \frac{5}{6}\bar{u}_{\mathrm{i}+1} - \frac{1}{6}\bar{u}_{\mathrm{i}+2}$	$C^-_{\mathrm{i}+1/2,0}$	$= \frac{3}{10}$
$\hat{u}^-_{\mathrm{i}+1/2,1}$	$= -\frac{1}{6}\bar{u}_{\mathrm{i}-1} + \frac{5}{6}\bar{u}_{\mathrm{i}} + \frac{1}{3}\bar{u}_{\mathrm{i}+1}$	$C^-_{\mathrm{i}+1/2,1}$	$= \frac{6}{10}$
$\hat{u}^-_{\mathrm{i}+1/2,2}$	$= \frac{1}{3}\bar{u}_{\mathrm{i}-2} - \frac{7}{6}\bar{u}_{\mathrm{i}-1} + \frac{11}{6}\bar{u}_{\mathrm{i}}$	$C^-_{\mathrm{i}+1/2,2}$	$= \frac{1}{10}$
$\hat{u}^+_{\mathrm{i}-1/2,0}$	$= \frac{11}{6}\bar{u}_{\mathrm{i}} - \frac{7}{6}\bar{u}_{\mathrm{i}+1} + \frac{1}{3}\bar{u}_{\mathrm{i}+2}$	$C^+_{\mathrm{i}-1/2,0}$	$= \frac{1}{10}$
$\hat{u}^+_{\mathrm{i}-1/2,1}$	$= \frac{1}{3}\bar{u}_{\mathrm{i}-1} + \frac{5}{6}\bar{u}_{\mathrm{i}} - \frac{1}{6}\bar{u}_{\mathrm{i}+1}$	$C^+_{\mathrm{i}-1/2,1}$	$= \frac{6}{10}$
$\hat{u}^+_{\mathrm{i}-1/2,2}$	$= -\frac{1}{6}\bar{u}_{\mathrm{i}-2} + \frac{5}{6}\bar{u}_{\mathrm{i}-1} + \frac{1}{3}\bar{u}_{\mathrm{i}}$	$C^+_{\mathrm{i}-1/2,2}$	$= \frac{3}{10}$
$IS_{\mathrm{i},0}$	$= \frac{4}{3}\left(\bar{u}_{\mathrm{i}+2} - \bar{u}_{\mathrm{i}+1}\right)^2 + \frac{11}{3}\left(\bar{u}_{\mathrm{i}+2} - \bar{u}_{\mathrm{i}+1}\right)\left(\bar{u}_{\mathrm{i}} - \bar{u}_{\mathrm{i}+1}\right) + \frac{10}{3}\left(\bar{u}_{\mathrm{i}} - \bar{u}_{\mathrm{i}+1}\right)^2$		
$IS_{\mathrm{i},1}$	$= \frac{4}{3}\left(\bar{u}_{\mathrm{i}-1} - \bar{u}_{\mathrm{i}}\right)^2 + \frac{5}{3}\left(\bar{u}_{\mathrm{i}+1} - \bar{u}_{\mathrm{i}}\right)\left(\bar{u}_{\mathrm{i}-1} - \bar{u}_{\mathrm{i}}\right) + \frac{4}{3}\left(\bar{u}_{\mathrm{i}+1} - \bar{u}_{\mathrm{i}}\right)^2$		
$IS_{\mathrm{i},2}$	$= \frac{4}{3}\left(\bar{u}_{\mathrm{i}-2} - \bar{u}_{\mathrm{i}-1}\right)^2 + \frac{11}{3}\left(\bar{u}_{\mathrm{i}} - \bar{u}_{\mathrm{i}-1}\right)\left(\bar{u}_{\mathrm{i}-2} - \bar{u}_{\mathrm{i}-1}\right) + \frac{10}{3}\left(\bar{u}_{\mathrm{i}} - \bar{u}_{\mathrm{i}-1}\right)^2$		

Table 3.13: WENO35 scheme for non-uniform grids

$$
\begin{aligned}
u^-_{\mathrm{i}+1/2,0} = \quad & \bar{u}_{\mathrm{i}+1} + \left(\frac{x_{\mathrm{i}+3/2} - x_{\mathrm{i}+1/2}}{x_{\mathrm{i}+5/2} - x_{\mathrm{i}-1/2}}\right)\left(\frac{x_{\mathrm{i}+5/2} - x_{\mathrm{i}+1/2}}{x_{\mathrm{i}+3/2} - x_{\mathrm{i}-1/2}}\right)\left(\bar{u}_{\mathrm{i}} - \bar{u}_{\mathrm{i}+1}\right) \\
& - \left(\frac{x_{\mathrm{i}+3/2} - x_{\mathrm{i}+1/2}}{x_{\mathrm{i}+5/2} - x_{\mathrm{i}-1/2}}\right)\left(\frac{x_{\mathrm{i}+1/2} - x_{\mathrm{i}-1/2}}{x_{\mathrm{i}+5/2} - x_{\mathrm{i}+1/2}}\right)\left(\bar{u}_{\mathrm{i}+2} - \bar{u}_{\mathrm{i}+1}\right)
\end{aligned}
$$

Table 3.13: *continued*

$$
\begin{aligned}
u^{-}_{\mathrm{i}+1/2,1} = \quad & \bar{u}_{\mathrm{i}} + \left(\frac{x_{\mathrm{i}+1/2} - x_{\mathrm{i}-1/2}}{x_{\mathrm{i}+3/2} - x_{\mathrm{i}-3/2}}\right)\left(\frac{x_{\mathrm{i}+1/2} - x_{\mathrm{i}-3/2}}{x_{\mathrm{i}+3/2} - x_{\mathrm{i}-1/2}}\right)(\bar{u}_{\mathrm{i}+1} - \bar{u}_{\mathrm{i}}) \\
& - \left(\frac{x_{\mathrm{i}+1/2} - x_{\mathrm{i}-1/2}}{x_{\mathrm{i}+3/2} - x_{\mathrm{i}-3/2}}\right)\left(\frac{x_{\mathrm{i}+3/2} - x_{\mathrm{i}+1/2}}{x_{\mathrm{i}+1/2} - x_{\mathrm{i}-3/2}}\right)(\bar{u}_{\mathrm{i}-1} - \bar{u}_{\mathrm{i}}) \\
u^{-}_{\mathrm{i}+1/2,2} = \quad & \bar{u}_{\mathrm{i}-1} + \left(\frac{x_{\mathrm{i}+1/2} - x_{\mathrm{i}-1/2}}{x_{\mathrm{i}-1/2} - x_{\mathrm{i}-5/2}}\right)\left(\frac{x_{\mathrm{i}+1/2} - x_{\mathrm{i}-3/2}}{x_{\mathrm{i}+1/2} - x_{\mathrm{i}-5/2}}\right)(\bar{u}_{\mathrm{i}-2} - \bar{u}_{\mathrm{i}-1}) \\
& + \left(1 + \frac{x_{\mathrm{i}+1/2} - x_{\mathrm{i}-1/2}}{x_{\mathrm{i}+1/2} - x_{\mathrm{i}-3/2}} + \frac{x_{\mathrm{i}+1/2} - x_{\mathrm{i}-1/2}}{x_{\mathrm{i}+1/2} - x_{\mathrm{i}-5/2}}\right)(\bar{u}_{\mathrm{i}} - \bar{u}_{\mathrm{i}-1}) \\
u^{+}_{\mathrm{i}-1/2,0} = \quad & \bar{u}_{\mathrm{i}+1} + \left(1 + \frac{x_{\mathrm{i}+1/2} - x_{\mathrm{i}-1/2}}{x_{\mathrm{i}+3/2} - x_{\mathrm{i}-1/2}} + \frac{x_{\mathrm{i}+1/2} - x_{\mathrm{i}-1/2}}{x_{\mathrm{i}+5/2} - x_{\mathrm{i}-1/2}}\right)(\bar{u}_{\mathrm{i}} - \bar{u}_{\mathrm{i}+1}) \\
& + \left(\frac{x_{\mathrm{i}+1/2} - x_{\mathrm{i}-1/2}}{x_{\mathrm{i}+5/2} - x_{\mathrm{i}-1/2}}\right)\left(\frac{x_{\mathrm{i}+3/2} - x_{\mathrm{i}-1/2}}{x_{\mathrm{i}+5/2} - x_{\mathrm{i}+1/2}}\right)(\bar{u}_{\mathrm{i}+2} - \bar{u}_{\mathrm{i}+1}) \\
u^{+}_{\mathrm{i}-1/2,1} = \quad & \bar{u}_{\mathrm{i}} + \left(\frac{x_{\mathrm{i}+1/2} - x_{\mathrm{i}-1/2}}{x_{\mathrm{i}+3/2} - x_{\mathrm{i}-3/2}}\right)\left(\frac{x_{\mathrm{i}+3/2} - x_{\mathrm{i}-1/2}}{x_{\mathrm{i}+1/2} - x_{\mathrm{i}-3/2}}\right)(\bar{u}_{\mathrm{i}-1} - \bar{u}_{\mathrm{i}}) \\
& - \left(\frac{x_{\mathrm{i}+1/2} - x_{\mathrm{i}-1/2}}{x_{\mathrm{i}+3/2} - x_{\mathrm{i}-3/2}}\right)\left(\frac{x_{\mathrm{i}-1/2} - x_{\mathrm{i}-3/2}}{x_{\mathrm{i}+3/2} - x_{\mathrm{i}-1/2}}\right)(\bar{u}_{\mathrm{i}+1} - \bar{u}_{\mathrm{i}}) \\
u^{+}_{\mathrm{i}-1/2,2} = \quad & \bar{u}_{\mathrm{i}-1} + \left(\frac{x_{\mathrm{i}-1/2} - x_{\mathrm{i}-3/2}}{x_{\mathrm{i}+1/2} - x_{\mathrm{i}-5/2}}\right)\left(\frac{x_{\mathrm{i}-1/2} - x_{\mathrm{i}-5/2}}{x_{\mathrm{i}+1/2} - x_{\mathrm{i}-3/2}}\right)(\bar{u}_{\mathrm{i}} - \bar{u}_{\mathrm{i}-1}) \\
& - \left(\frac{x_{\mathrm{i}-1/2} - x_{\mathrm{i}-3/2}}{x_{\mathrm{i}+1/2} - x_{\mathrm{i}-5/2}}\right)\left(\frac{x_{\mathrm{i}+1/2} - x_{\mathrm{i}-1/2}}{x_{\mathrm{i}-1/2} - x_{\mathrm{i}-5/2}}\right)(\bar{u}_{\mathrm{i}-2} - \bar{u}_{\mathrm{i}-1}) \\
C^{-}_{\mathrm{i}+1/2,0} = \quad & \left(\frac{x_{\mathrm{i}+1/2} - x_{\mathrm{i}-5/2}}{x_{\mathrm{i}+5/2} - x_{\mathrm{i}-5/2}}\right)\left(\frac{x_{\mathrm{i}+1/2} - x_{\mathrm{i}-3/2}}{x_{\mathrm{i}+5/2} - x_{\mathrm{i}-3/2}}\right) \\
C^{-}_{\mathrm{i}+1/2,1} = \quad & \left(\frac{x_{\mathrm{i}+1/2} - x_{\mathrm{i}-5/2}}{x_{\mathrm{i}+5/2} - x_{\mathrm{i}-5/2}}\right)\left(\frac{x_{\mathrm{i}+5/2} - x_{\mathrm{i}+1/2}}{x_{\mathrm{i}+5/2} - x_{\mathrm{i}-3/2}}\right)\left(\frac{x_{\mathrm{i}+5/2} - x_{\mathrm{i}-3/2}}{x_{\mathrm{i}+3/2} - x_{\mathrm{i}-5/2}} + 1\right) \\
C^{-}_{\mathrm{i}+1/2,2} = \quad & \left(\frac{x_{\mathrm{i}+3/2} - x_{\mathrm{i}+1/2}}{x_{\mathrm{i}+5/2} - x_{\mathrm{i}-5/2}}\right)\left(\frac{x_{\mathrm{i}+5/2} - x_{\mathrm{i}+1/2}}{x_{\mathrm{i}+3/2} - x_{\mathrm{i}-5/2}}\right) \\
C^{+}_{\mathrm{i}-1/2,0} = \quad & \left(\frac{x_{\mathrm{i}-1/2} - x_{\mathrm{i}-3/2}}{x_{\mathrm{i}+5/2} - x_{\mathrm{i}-5/2}}\right)\left(\frac{x_{\mathrm{i}-1/2} - x_{\mathrm{i}-5/2}}{x_{\mathrm{i}+5/2} - x_{\mathrm{i}-3/2}}\right) \\
C^{+}_{\mathrm{i}-1/2,1} = \quad & \left(\frac{x_{\mathrm{i}-1/2} - x_{\mathrm{i}-5/2}}{x_{\mathrm{i}+5/2} - x_{\mathrm{i}-5/2}}\right)\left(\frac{x_{\mathrm{i}+5/2} - x_{\mathrm{i}-1/2}}{x_{\mathrm{i}+5/2} - x_{\mathrm{i}-3/2}}\right)\left(\frac{x_{\mathrm{i}+5/2} - x_{\mathrm{i}-3/2}}{x_{\mathrm{i}+3/2} - x_{\mathrm{i}-5/2}} + 1\right) \\
C^{+}_{\mathrm{i}-1/2,2} = \quad & \left(\frac{x_{\mathrm{i}+3/2} - x_{\mathrm{i}-1/2}}{x_{\mathrm{i}+5/2} - x_{\mathrm{i}-5/2}}\right)\left(\frac{x_{\mathrm{i}+5/2} - x_{\mathrm{i}-1/2}}{x_{\mathrm{i}+3/2} - x_{\mathrm{i}-5/2}}\right)
\end{aligned}
$$

Table 3.14: WENO35 scheme for non-uniform grids, smoothness indicators

$$
\begin{aligned}
IS_{\mathrm{i},0} = \; & 4\left(\frac{x_{\mathrm{i}+1/2}-x_{\mathrm{i}-1/2}}{x_{\mathrm{i}+5/2}-x_{\mathrm{i}-1/2}}\right)^2 \\
& \times \left[\begin{array}{l}
\left(\dfrac{\bar{u}_{\mathrm{i}+2}-\bar{u}_{\mathrm{i}+1}}{x_{\mathrm{i}+5/2}-x_{\mathrm{i}+1/2}}\right)^2 \left(10\left(x_{\mathrm{i}+1/2}-x_{\mathrm{i}-1/2}\right)^2+\left(x_{\mathrm{i}+3/2}-x_{\mathrm{i}-1/2}\right)\left(x_{\mathrm{i}+3/2}-x_{\mathrm{i}+1/2}\right)\right) \\
+\dfrac{\left(\bar{u}_{\mathrm{i}+2}-\bar{u}_{\mathrm{i}+1}\right)\left(\bar{u}_{\mathrm{i}}-\bar{u}_{\mathrm{i}+1}\right)}{\left(x_{\mathrm{i}+5/2}-x_{\mathrm{i}+1/2}\right)\left(x_{\mathrm{i}+3/2}-x_{\mathrm{i}-1/2}\right)} \left[\begin{array}{l} 20\left(x_{\mathrm{i}+1/2}-x_{\mathrm{i}-1/2}\right)^2+2\left(x_{\mathrm{i}+3/2}-x_{\mathrm{i}-1/2}\right)\left(x_{\mathrm{i}+3/2}-x_{\mathrm{i}+1/2}\right) \\ +\left(x_{\mathrm{i}+5/2}-x_{\mathrm{i}-1/2}\right)\left(2x_{\mathrm{i}+3/2}-x_{\mathrm{i}+1/2}-x_{\mathrm{i}-1/2}\right) \end{array}\right] \\
+\left(\dfrac{\bar{u}_{\mathrm{i}}-\bar{u}_{\mathrm{i}+1}}{x_{\mathrm{i}+3/2}-x_{\mathrm{i}-1/2}}\right)^2 \left[10\left(x_{\mathrm{i}+1/2}-x_{\mathrm{i}-1/2}\right)^2+\left(x_{\mathrm{i}+5/2}+x_{\mathrm{i}+3/2}-2x_{\mathrm{i}-1/2}\right)\left(x_{\mathrm{i}+5/2}+x_{\mathrm{i}+3/2}-x_{\mathrm{i}+1/2}-x_{\mathrm{i}-1/2}\right)\right]
\end{array}\right] \\
IS_{\mathrm{i},1} = \; & 4\left(\frac{x_{\mathrm{i}+1/2}-x_{\mathrm{i}-1/2}}{x_{\mathrm{i}+3/2}-x_{\mathrm{i}-3/2}}\right)^2 \\
& \times \left[\begin{array}{l}
\left(\dfrac{\bar{u}_{\mathrm{i}-1}-\bar{u}_{\mathrm{i}}}{x_{\mathrm{i}+1/2}-x_{\mathrm{i}-3/2}}\right)^2 \left(10\left(x_{\mathrm{i}+1/2}-x_{\mathrm{i}-1/2}\right)^2+\left(x_{\mathrm{i}+3/2}-x_{\mathrm{i}-1/2}\right)\left(x_{\mathrm{i}+3/2}-x_{\mathrm{i}+1/2}\right)\right) \\
+\dfrac{\left(\bar{u}_{\mathrm{i}+1}-\bar{u}_{\mathrm{i}}\right)\left(\bar{u}_{\mathrm{i}-1}-\bar{u}_{\mathrm{i}}\right)}{\left(x_{\mathrm{i}+3/2}-x_{\mathrm{i}-1/2}\right)\left(x_{\mathrm{i}+1/2}-x_{\mathrm{i}-3/2}\right)} \left[\begin{array}{l} 20\left(x_{\mathrm{i}+1/2}-x_{\mathrm{i}-1/2}\right)^2-\left(x_{\mathrm{i}+3/2}-x_{\mathrm{i}+1/2}\right)\left(x_{\mathrm{i}-1/2}-x_{\mathrm{i}-3/2}\right) \\ -\left(x_{\mathrm{i}+3/2}-x_{\mathrm{i}-1/2}\right)\left(x_{\mathrm{i}+1/2}-x_{\mathrm{i}-3/2}\right) \end{array}\right] \\
+\left(\dfrac{\bar{u}_{\mathrm{i}+1}-\bar{u}_{\mathrm{i}}}{x_{\mathrm{i}+3/2}-x_{\mathrm{i}-1/2}}\right)^2 \left(10\left(x_{\mathrm{i}+1/2}-x_{\mathrm{i}-1/2}\right)^2+\left(x_{\mathrm{i}-1/2}-x_{\mathrm{i}-3/2}\right)\left(x_{\mathrm{i}+1/2}-x_{\mathrm{i}-3/2}\right)\right)
\end{array}\right] \\
IS_{\mathrm{i},2} = \; & 4\left(\frac{x_{\mathrm{i}+1/2}-x_{\mathrm{i}-1/2}}{x_{\mathrm{i}+1/2}-x_{\mathrm{i}-5/2}}\right)^2 \\
& \times \left[\begin{array}{l}
\left(\dfrac{\bar{u}_{\mathrm{i}-2}-\bar{u}_{\mathrm{i}-1}}{x_{\mathrm{i}-1/2}-x_{\mathrm{i}-5/2}}\right)^2 \left(10\left(x_{\mathrm{i}+1/2}-x_{\mathrm{i}-1/2}\right)^2+\left(x_{\mathrm{i}+1/2}-x_{\mathrm{i}-3/2}\right)\left(x_{\mathrm{i}-1/2}-x_{\mathrm{i}-3/2}\right)\right) \\
+\dfrac{\left(\bar{u}_{\mathrm{i}}-\bar{u}_{\mathrm{i}-1}\right)\left(\bar{u}_{\mathrm{i}-2}-\bar{u}_{\mathrm{i}-1}\right)}{\left(x_{\mathrm{i}+1/2}-x_{\mathrm{i}-3/2}\right)\left(x_{\mathrm{i}-1/2}-x_{\mathrm{i}-5/2}\right)} \left[\begin{array}{l} 20\left(x_{\mathrm{i}+1/2}-x_{\mathrm{i}-1/2}\right)^2+2\left(x_{\mathrm{i}+1/2}-x_{\mathrm{i}-3/2}\right)\left(x_{\mathrm{i}-1/2}-x_{\mathrm{i}-3/2}\right) \\ +\left(x_{\mathrm{i}+1/2}-x_{\mathrm{i}-5/2}\right)\left(x_{\mathrm{i}+1/2}+x_{\mathrm{i}-1/2}-2x_{\mathrm{i}-3/2}\right) \end{array}\right] \\
+\left(\dfrac{\bar{u}_{\mathrm{i}}-\bar{u}_{\mathrm{i}-1}}{x_{\mathrm{i}+1/2}-x_{\mathrm{i}-3/2}}\right)^2 \left[10\left(x_{\mathrm{i}+1/2}-x_{\mathrm{i}-1/2}\right)^2+\left(2x_{\mathrm{i}+1/2}-x_{\mathrm{i}-5/2}-x_{\mathrm{i}-3/2}\right)\left(x_{\mathrm{i}+1/2}+x_{\mathrm{i}-1/2}-x_{\mathrm{i}-3/2}-x_{\mathrm{i}-5/2}\right)\right]
\end{array}\right]
\end{aligned}
$$

Table 3.15: Grid adaptation for the WENO35 scheme

$$
\begin{aligned}
\bar{u}^*_{\mathrm{i},0} = \quad & \bar{u}_\mathrm{i} + \left(\frac{\bar{u}_{\mathrm{i}+2}}{4} - \frac{\bar{u}_{\mathrm{i}+1}}{4}\right)\left(\frac{x_{\mathrm{i}+1/2} - x_{\mathrm{i}-1/2}}{x_{\mathrm{i}+5/2} - x_{\mathrm{i}-1/2}}\right)\left(\frac{2x_{\mathrm{i}+3/2} - x_{\mathrm{i}+1/2} - x_{\mathrm{i}-1/2}}{x_{\mathrm{i}+5/2} - x_{\mathrm{i}+1/2}}\right) \\
& + \left(\frac{\bar{u}_\mathrm{i}}{4} - \frac{\bar{u}_{\mathrm{i}+1}}{4}\right)\left(\frac{x_{\mathrm{i}+1/2} - x_{\mathrm{i}-1/2}}{x_{\mathrm{i}+5/2} - x_{\mathrm{i}-1/2}}\right)\left(\frac{2x_{\mathrm{i}+5/2} - x_{\mathrm{i}+1/2} - x_{\mathrm{i}-1/2}}{x_{\mathrm{i}+3/2} - x_{\mathrm{i}-1/2}} + 2\right) \\
\bar{u}^*_{\mathrm{i},1} = \quad & \bar{u}_\mathrm{i} + \left(\frac{u_{\mathrm{i}-1}}{4} - \frac{\bar{u}_\mathrm{i}}{4}\right)\left(\frac{x_{\mathrm{i}+1/2} - x_{\mathrm{i}-1/2}}{x_{\mathrm{i}+3/2} - x_{\mathrm{i}-3/2}}\right)\left(\frac{2x_{\mathrm{i}+3/2} - x_{\mathrm{i}+1/2} - x_{\mathrm{i}-1/2}}{x_{\mathrm{i}+1/2} - x_{\mathrm{i}-3/2}}\right) \\
& + \left(\frac{\bar{u}_\mathrm{i}}{4} - \frac{\bar{u}_{\mathrm{i}+1}}{4}\right)\left(\frac{x_{\mathrm{i}+1/2} - x_{\mathrm{i}-1/2}}{x_{\mathrm{i}+3/2} - x_{\mathrm{i}-3/2}}\right)\left(\frac{x_{\mathrm{i}+1/2} + x_{\mathrm{i}-1/2} - 2x_{\mathrm{i}-3/2}}{x_{\mathrm{i}+3/2} - x_{\mathrm{i}-1/2}}\right) \\
\bar{u}^*_{\mathrm{i},2} = \quad & \bar{u}_{\mathrm{i}-1} + \left(\frac{\bar{u}_{\mathrm{i}-1}}{4} - \frac{\bar{u}_{\mathrm{i}-2}}{4}\right)\left(\frac{x_{\mathrm{i}+1/2} + x_{\mathrm{i}-1/2} - 2x_{\mathrm{i}-3/2}}{x_{\mathrm{i}+1/2} - x_{\mathrm{i}-5/2}}\right)\left(\frac{x_{\mathrm{i}+1/2} - x_{\mathrm{i}-1/2}}{x_{\mathrm{i}-1/2} - x_{\mathrm{i}-5/2}}\right) \\
& + \left(\frac{\bar{u}_\mathrm{i}}{4} - \frac{\bar{u}_{\mathrm{i}-1}}{4}\right)\left(\frac{x_{\mathrm{i}+1/2} + x_{\mathrm{i}-1/2} - 2x_{\mathrm{i}-3/2}}{x_{\mathrm{i}+1/2} - x_{\mathrm{i}-5/2}}\right)\left(\frac{x_{\mathrm{i}+1/2} + x_{\mathrm{i}-1/2} - 2x_{\mathrm{i}-5/2}}{x_{\mathrm{i}+1/2} - x_{\mathrm{i}-3/2}}\right) \\
\bar{u}^*_{\mathrm{i}+1,0} = \quad & \bar{u}_{\mathrm{i}+1} + \left(\frac{\bar{u}_{\mathrm{i}+1}}{4} - \frac{\bar{u}_{\mathrm{i}+2}}{4}\right)\left(\frac{2x_{\mathrm{i}+3/2} - x_{\mathrm{i}+1/2} - x_{\mathrm{i}-1/2}}{x_{\mathrm{i}+5/2} - x_{\mathrm{i}-1/2}}\right)\left(\frac{x_{\mathrm{i}+1/2} - x_{\mathrm{i}-1/2}}{x_{\mathrm{i}+5/2} - x_{\mathrm{i}+1/2}}\right) \\
& + \left(\frac{\bar{u}_\mathrm{i}}{4} - \frac{\bar{u}_{\mathrm{i}+1}}{4}\right)\left(\frac{2x_{\mathrm{i}+3/2} - x_{\mathrm{i}+1/2} - x_{\mathrm{i}-1/2}}{x_{\mathrm{i}+5/2} - x_{\mathrm{i}-1/2}}\right)\left(\frac{2x_{\mathrm{i}+5/2} - x_{\mathrm{i}+1/2} - x_{\mathrm{i}-1/2}}{x_{\mathrm{i}+3/2} - x_{\mathrm{i}-1/2}}\right) \\
\bar{u}^*_{\mathrm{i}+1,1} = \quad & \bar{u}_\mathrm{i} + \left(\frac{\bar{u}_\mathrm{i}}{4} - \frac{\bar{u}_{\mathrm{i}-1}}{4}\right)\left(\frac{x_{\mathrm{i}+1/2} - x_{\mathrm{i}-1/2}}{x_{\mathrm{i}+3/2} - x_{\mathrm{i}-3/2}}\right)\left(\frac{2x_{\mathrm{i}+3/2} - x_{\mathrm{i}+1/2} - x_{\mathrm{i}-1/2}}{x_{\mathrm{i}+1/2} - x_{\mathrm{i}-3/2}}\right) \\
& + \left(\frac{\bar{u}_{\mathrm{i}+1}}{4} - \frac{\bar{u}_\mathrm{i}}{4}\right)\left(\frac{x_{\mathrm{i}+1/2} - x_{\mathrm{i}-1/2}}{x_{\mathrm{i}+3/2} - x_{\mathrm{i}-3/2}}\right)\left(\frac{x_{\mathrm{i}+1/2} + x_{\mathrm{i}-1/2} - 2x_{\mathrm{i}-3/2}}{x_{\mathrm{i}+3/2} - x_{\mathrm{i}-1/2}}\right) \\
\bar{u}^*_{\mathrm{i}+1,2} = \quad & \bar{u}_\mathrm{i} + \left(\frac{\bar{u}_{\mathrm{i}-2}}{4} - \frac{\bar{u}_{\mathrm{i}-1}}{4}\right)\left(\frac{x_{\mathrm{i}+1/2} - x_{\mathrm{i}-1/2}}{x_{\mathrm{i}+1/2} - x_{\mathrm{i}-5/2}}\right)\left(\frac{x_{\mathrm{i}+1/2} + x_{\mathrm{i}-1/2} - 2x_{\mathrm{i}-3/2}}{x_{\mathrm{i}-1/2} - x_{\mathrm{i}-5/2}}\right) \\
& + \left(\frac{\bar{u}_\mathrm{i}}{4} - \frac{\bar{u}_{\mathrm{i}-1}}{4}\right)\left(\frac{x_{\mathrm{i}+1/2} - x_{\mathrm{i}-1/2}}{x_{\mathrm{i}+1/2} - x_{\mathrm{i}-5/2}}\right)\left(2 + \frac{x_{\mathrm{i}+1/2} + x_{\mathrm{i}-1/2} - 2x_{\mathrm{i}-5/2}}{x_{\mathrm{i}+1/2} - x_{\mathrm{i}-3/2}}\right) \\
C^*_{\mathrm{i},0} = \quad & \frac{1}{4}\left(\frac{x_{\mathrm{i}+1/2} + x_{\mathrm{i}-1/2} - 2x_{\mathrm{i}-5/2}}{x_{\mathrm{i}+5/2} - x_{\mathrm{i}-5/2}}\right)\left(\frac{x_{\mathrm{i}+1/2} + x_{\mathrm{i}-1/2} - 2x_{\mathrm{i}-3/2}}{x_{\mathrm{i}+5/2} - x_{\mathrm{i}-3/2}}\right) \\
C^*_{\mathrm{i},1} = \quad & \frac{1}{4}\left(\frac{2x_{\mathrm{i}+5/2} - x_{\mathrm{i}+1/2} - x_{\mathrm{i}-1/2}}{x_{\mathrm{i}+5/2} - x_{\mathrm{i}-3/2}}\right)\left(\frac{x_{\mathrm{i}+1/2} + x_{\mathrm{i}-1/2} - 2x_{\mathrm{i}-5/2}}{x_{\mathrm{i}+3/2} - x_{\mathrm{i}-5/2}}\right) \\
& \times \left(1 + \frac{x_{\mathrm{i}+3/2} - x_{\mathrm{i}-3/2}}{x_{\mathrm{i}+5/2} - x_{\mathrm{i}-5/2}}\right) \\
C^*_{\mathrm{i},2} = \quad & \frac{1}{4}\left(\frac{2x_{\mathrm{i}+5/2} - x_{\mathrm{i}+1/2} - x_{\mathrm{i}-1/2}}{x_{\mathrm{i}+5/2} - x_{\mathrm{i}-5/2}}\right)\left(\frac{2x_{\mathrm{i}+3/2} - x_{\mathrm{i}+1/2} - x_{\mathrm{i}-1/2}}{x_{\mathrm{i}+3/2} - x_{\mathrm{i}-5/2}}\right)
\end{aligned}
$$

3.B Grid adaptation algorithm

The grid adaptation algorithm is given in Table 3.16. k is a dummy integer used to keep track of the index number of the new grid cell and $\Delta x_{i-1}^{<}$, $\Delta x_{i-1}^{>}$, $\Delta x_{i}^{<}$ and $\Delta x_{i-1}^{>}$ are boolean variables indicating if a grid cell (Δx) is split ($^{<}$) or if two grid cells are merged ($^{>}$).

Table 3.16: Grid adaptation algorithm

$k = 0$, $\Delta x_{i-1}^{<}$ = FALSE, $\Delta x_{i-1}^{>}$ = FALSE
FOR $i = 1$ TO N DO
  $\Delta x_{i}^{<}$ = FALSE
  IF $\Delta IS_{i} > \Delta IS_{max}$ THEN
    $\Delta x_{i}^{<}$ = TRUE
  IF ($\Delta x_{i-1}^{>}$ = FALSE) AND ($\Delta x_{i-1}^{<}$ = FALSE) AND ($\Delta x_{i}^{<}$ = FALSE) THEN
    $\Delta x_{i}^{>}$ = TRUE
    IF ($\Delta x_{i}^{>}$ = TRUE) AND ($\Delta IS_{i} < \Delta IS_{min}$) AND ($\Delta IS_{i+1} < \Delta IS_{min}$) THEN
      $\Delta x_{i}^{>}$ = TRUE
    ELSE
      $\Delta x_{i}^{>}$ = FALSE
  IF ($\Delta x_{i}^{>}$ = FALSE) AND ($\Delta x_{i}^{<}$ = FALSE) THEN
    $x_{i+k+1/2}^{*} = x_{i+1/2}$
    $\bar{u}_{i+k}^{*} = \bar{u}_{i}$
    IF ($\Delta x_{i-1}^{>}$ = TRUE) THEN
      $\bar{u}_{i+k}^{*} = \bar{u}_{i}\left(\dfrac{x_{i+1/2} - x_{i-1/2}}{x_{i+1/2} - x_{i-3/2}}\right) + \bar{u}_{i-1}\left(\dfrac{x_{i-1/2} - x_{i-3/2}}{x_{i+1/2} - x_{i-3/2}}\right)$
    $\Delta x_{i-1}^{>}$ = FALSE, $\Delta x_{i-1}^{<}$ = FALSE
  IF $\Delta x_{i}^{<}$ = TRUE
    $x_{i+k+1/2}^{*} = \frac{1}{2}(x_{i+1/2} + x_{i-1/2})$, $x_{i+k+3/2}^{*} = x_{i+1/2}$
    $\bar{u}_{i+k}^{*} = \bar{u}_{i}^{*}$, $\bar{u}_{i+k+1}^{*} = \bar{u}_{i+1}^{*}$, with $\bar{u}_{i}^{*}$ and $\bar{u}_{i+1}^{*}$ according to Equation 3.26
    $k = k + 1$, $\Delta x_{i-1}^{>}$ = FALSE, $\Delta x_{i-1}^{<}$ = TRUE
  IF $\Delta x_{i}^{>}$ = TRUE
    $k = k - 1$, $\Delta x_{i-1}^{>}$ = TRUE, $\Delta x_{i-1}^{<}$ = FALSE

CHAPTER 4

Feasibility Study of the RFCMR Concept with Porous Membranes

Abstract

In this chapter the feasibility of the RFCMR concept with porous membranes for the partial oxidation of CH_4 to syngas is demonstrated for industrially relevant conditions. For this purpose 1-D reactor models, the HSFM (High Switching Frequency Model) and the DM (Dynamic Model), were developed, which include a detailed description of the prevailing heat and mass transfer processes and chemical kinetics of the relevant reactions. Firstly the design parameters related to the reverse flow section (*i.e.* the heat exchange section at the in- and outlet) were determined based on analytic relations from literature and HSFM simulations. With the HSFM it is also demonstrated that the addition of a small amount of H_2O to the O_2 feed is a crucial feature in the RFCMR concept to avoid runaways in the centre of the reactor. Subsequently, more detailed DM simulations were carried out to evaluate the reactor performance in terms of syngas selectivities for different CPO catalyst particle diameters, membrane lengths, switching times and tube diameters. It is shown that one of the major cost drivers of a conventional Gas-To-Liquid process, *i.e.* the cost associated with the production of pure O_2 via cryogenic distillation of air, can be decreased by 25 % and that very high syngas selectivities (> 98 %) can be achieved. Furthermore, it is demonstrated that hot spots can be avoided, while recuperative heat exchange is fully integrated.

This chapter is based on the paper:
Smit, J., van Sint Annaland, M., and Kuipers, J.A.M., Feasibility study of a Reverse Flow Catalytic Membrane Reactor with porous membranes for the production of syngas, Chemical Engineering Science, 60(24), 6971-6982 (2005)

4.1 Introduction

In this chapter the conceptual feasibility of the RFCMR concept with porous membranes is demonstrated by means of a simulation study using the efficient numerical algorithm developed in Chapter 3. To model a conventional reverse flow reactor commonly two approaches are used; a dynamic model (DM) and a High Switching Frequency Model (HSFM) (*e.g.* Nieken et al., 1995; van Sint Annaland et al., 2002). The DM consists of the unsteady-state continuity equations for total and species mass and energy (Bird et al., 2002) and provides detailed information about the dynamic behavior of the reactor. The HSFM considers the limiting case where the flow direction is switched infinitely fast, simplifying the mathematical description of the reactor behaviour. Because the HSFM reaches a static steady state whereas the DM reaches a periodic steady state, the HSFM results can be interpreted more easily and the model equations can be solved numerically much more efficient compared to the DM. As a result the HSFM is typically used for preliminary studies avoiding the additional complexity due to movement of the heat fronts. Subsequently, with DM simulations the results of the HSFM simulations can be verified and the effects of the movement of the heat fronts can be studied in detail. In this chapter, the RFCMR concept with porous membranes are studied with both the HSFM and DM using a detailed description of heat and mass transfer processes and reaction kinetics of the relevant reactions.

In a conventional reverse flow reactor the reaction heat is released just before the beginning of the temperature plateau, so that locally the heat convection is counterbalanced by heat conduction and energy production by the prevailing reactions. As a result temperature fronts with very steep gradients and low front velocities and high plateau temperatures can be obtained with a low adiabatic temperature rise. In the RFCMR concept, the reaction heat of the CPO reaction is released all along the membrane in the centre of the reactor, whereas a trapezoidal temperature profile with steep gradients outside the membrane section and a flat temperature plateau along the membrane is desired. Therefore, without making some conceptual adjustments, the RFCMR will not have the desired temperature profile and runaways are likely to occur in the centre of the reactor. In Chapter 2 it was already shown that by adding H_2O to the O_2 feed in a $CH_4/O_2/H_2O$ molar feed ratio of 1.13:0.5:0.13 all reaction heat produced by the CPO reaction can be effectively used for some additional

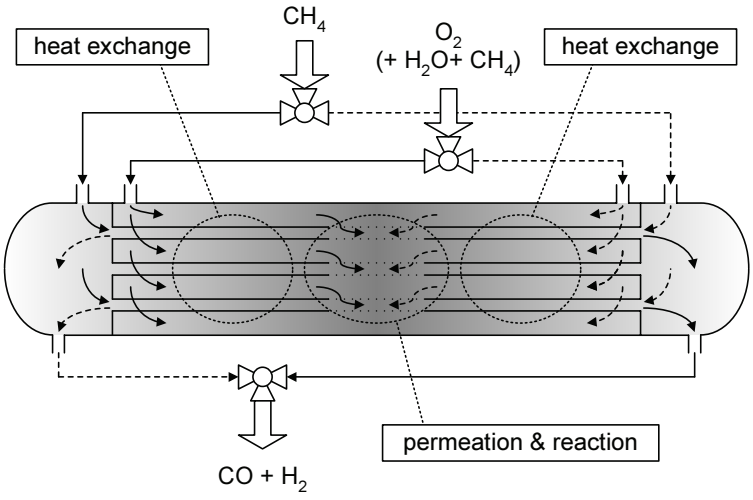

Figure 4.1: Schematic overview of the RFCMR concept with porous membranes in a shell-and-tube configuration. The colour gradient represents the axial temperature profile, a darker colour indicates a higher temperature.

syngas production via endothermic steam reforming, rendering the process overall auto-thermal. In case the H_2O would be co-fed with the CH_4, preliminary calculations have shown that this would lead to cold spots at the beginning of the membrane section, because all H_2O is converted at the very beginning of the membrane section via the fast endothermic steam reforming reaction. Therefore, the H_2O is fed distributively to the CH_4, together with the O_2. To establish the plateau temperature outside the membrane section, a small amount of CH_4 is added to the O_2 feed, which is combusted just before the membrane section over a combustion catalyst. Since the CO_2 and H_2O that are produced can be used for endothermic dry reforming and steam reforming in the membrane section, respectively, somewhat less H_2O has to be added to the O_2 feed, while no CH_4 is lost. In Figure 4.1 a schematic overview of the RFCMR concept is presented, in which the O_2 and syngas compartments are arranged in a shell-and-tube configuration. Obviously, also other configurations could be considered provided that a good heat transfer between the compartments can be achieved.

Firstly, the details of the reactor models used to study the theoretical feasibility of the RFCMR concept are described. Based on analytical expressions to estimate

the plateau temperature and the front velocity for conventional reverse flow reactors, the design parameters regarding the reverse flow section of the RFCMR are determined and verified with the HSFM. Subsequently, it is demonstrated with HSFM simulations that the addition of H_2O to the O_2 feed is crucial in the RFCMR concept to prevent runaways in the centre of the reactor. With the more detailed DM, design parameters such as the CPO catalyst diameter, membrane length, switching time and tube diameter are determined by evaluating them with respect to syngas selectivities, axial pressure and temperature profiles as well as the presence of mass transfer limitations. It is demonstrated that with an appropriate design and suitable operating conditions, very high syngas yields can be achieved at reduced O_2 consumption. Finally in this chapter, the validity of some model assumptions are addressed and concluding remarks are given.

4.2 Reactor model

In this section the selected reactor configuration and model assumptions are described and the model equations are presented. Furthermore, the constitutive relations for the heat and mass transfer processes, reaction kinetics and physical properties are given.

4.2.1 Reactor geometry

To study the feasibility of the RFCMR concept with porous membranes a reactor model was developed based on a shell-and-tube lay-out, see also Figure 4.1. A square pitch was selected as a possible configuration, which is illustrated in Figure 4.2. For the reactor model one unit cell is considered, which is assumed to represent the entire tube bank. The geometry of the unit cell is thus determined by its width, the length of the non-permeable walls, the length of the membrane and the inner and outer tube radii. The CH_4 is fed to the tube compartment and O_2 to the shell compartment. The membrane is filled with CPO catalyst particles, whereas the support tubes are filled with inert Al_2O_3 particles for additional heat capacity and to prevent back-reactions. The shell is filled with a Pt/Al_2O_3 combustion catalyst. Furthermore, in this study a ceramic membrane was considered with a macro-porous support and a micro-porous top layer on the inside of the membrane. However, also other types of distributors could be considered in practical applications such as sintered metal filters

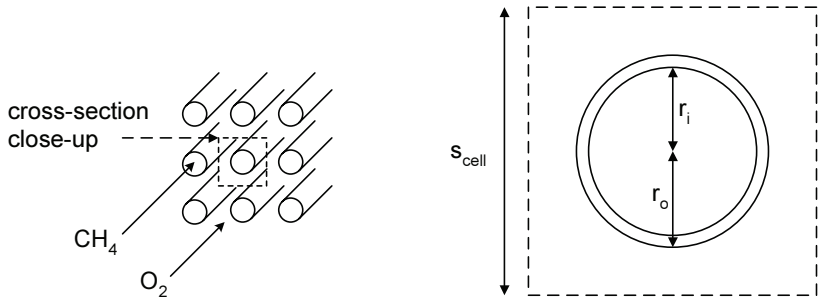

Figure 4.2: RFCMR geometry (left) and cross-section close-up (right).

or tubes with discrete holes. The only requirements of the porous membrane/filter are that it is resistant to very high temperatures at oxidising and reducing atmospheres and that it has a proper flow resistance and corresponding pressure drop over the membrane/filter to allow for a good distribution of the gas. The permeation rate through the ceramic membrane considered in this study was calculated according to the Dusty Gas Model (Mason and Malinauskas, 1983):

$$J = \frac{1}{R_{\mathrm{g}} T^{\mathrm{tw}}} \left(K_0 \frac{4}{3} \sqrt{\frac{8 R_{\mathrm{g}} T^{\mathrm{tw}}}{\pi \left\langle M^{\mathrm{s}} \right\rangle}} + B_0 \frac{p_{\mathrm{g}}^{\mathrm{s}} + p_{\mathrm{g}}^{\mathrm{t}}}{2 \eta_{\mathrm{g}}^{\mathrm{s}}} \right) \frac{\left(p_{\mathrm{g}}^{\mathrm{s}} - p_{\mathrm{g}}^{\mathrm{t}} \right)}{\left(r_{\mathrm{i}} + \delta_{\mathrm{m}} \right) \ln \left(\dfrac{r_{\mathrm{i}} + \delta_{\mathrm{m}}}{r_{\mathrm{i}}} \right)} \tag{4.1}$$

An explanation of the symbols used can be found in the nomenclature section at the end of this chapter.

4.2.2 Modelling assumptions and equations

The axial temperature and concentration profiles in the O_2 and syngas compartments were modelled with a 1-D axial dispersion model using the following general assumptions:

- Radial temperature and concentration gradients inside the compartments were ignored. In this study only the development of the axial temperature and concentration profiles were investigated to assess the over-all reactor performance. Radial temperature differences between the tube compartment, tube wall and shell compartment were accounted for via overall heat transfer coefficients.
- To reduce computational time a homogeneous model (Vortmeyer, 1989; Nieken

et al., 1995; van Sint Annaland et al., 2002) was adopted to describe the heat transfer processes in the tube and shell compartments of the reactor.

- The gas phase was assumed to be in pseudo stationary-state because of the small gas phase residence time compared to the switching times, *i.e.* the accumulation terms in the species conservation equations were neglected and therefore the switching losses.

Table 4.1: Conservations equations of the Dynamic Model (DM)

Mass conservation equations:

$$
\begin{aligned}
\frac{\partial\left(\rho_{\mathrm{g}}^{\mathrm{s}} v_{\mathrm{g}}^{\mathrm{s}}\right)}{\partial z} &= -\left\langle M^{\mathrm{s}}\right\rangle \frac{2\pi r_{\mathrm{i}}}{s_{\mathrm{cell}}^2-\pi r_{\mathrm{o}}^2} J \\
\frac{\partial\left(\rho_{\mathrm{g}}^{\mathrm{t}} v_{\mathrm{g}}^{\mathrm{t}}\right)}{\partial z} &= \left\langle M^{\mathrm{s}}\right\rangle \frac{2}{r_{\mathrm{i}}} J \\
\rho_{\mathrm{g}}^{\mathrm{s}} v_{\mathrm{g}}^{\mathrm{s}} \frac{\partial w_{\mathrm{j,g}}^{\mathrm{s}}}{\partial z} &= \frac{\partial}{\partial z}\left(\rho_{\mathrm{g}}^{\mathrm{s}} D_{\mathrm{ax,j}}^{\mathrm{s}} \frac{\partial w_{\mathrm{j,g}}^{\mathrm{s}}}{\partial z}\right)+r_{\mathrm{j,g}}^{\mathrm{s}} \\
\rho_{\mathrm{g}}^{\mathrm{t}} v_{\mathrm{g}}^{\mathrm{t}} \frac{\partial w_{\mathrm{j,g}}^{\mathrm{t}}}{\partial z} &= \frac{\partial}{\partial z}\left(\rho_{\mathrm{g}}^{\mathrm{t}} D_{\mathrm{ax,j}}^{\mathrm{t}} \frac{\partial w_{\mathrm{j,g}}^{\mathrm{t}}}{\partial z}\right)+\frac{6\left(1-\varepsilon_{\mathrm{g}}^{\mathrm{t}}\right)}{d_{\mathrm{p}}^{\mathrm{t}}} j_{\mathrm{j}}^{\mathrm{t}}+\left(1-w_{\mathrm{j,g}}^{\mathrm{s}}\right)\left\langle M^{\mathrm{s}}\right\rangle \frac{2}{r_{\mathrm{i}}} J \\
0 &= -\frac{6\left(1-\varepsilon_{\mathrm{g}}^{\mathrm{t}}\right)}{d_{\mathrm{p}}^{\mathrm{t}}} j_{\mathrm{j}}^{\mathrm{t}}+r_{\mathrm{j,s}}^{\mathrm{t}}
\end{aligned}
$$

Energy conservation equations:

$$
\begin{aligned}
\left(\varepsilon_{\mathrm{g}}^{\mathrm{s}} \rho_{\mathrm{g}}^{\mathrm{s}} C_{\mathrm{p,g}}^{\mathrm{s}}+\rho_{\mathrm{bulk}}^{\mathrm{s}} C_{\mathrm{p,s}}^{\mathrm{s}}\right) \frac{\partial T^{\mathrm{s}}}{\partial t} &= -\rho_{\mathrm{g}}^{\mathrm{s}} v_{\mathrm{g}}^{\mathrm{s}} C_{\mathrm{p,g}}^{\mathrm{s}} \frac{\partial T^{\mathrm{s}}}{\partial z}+\frac{\partial}{\partial z}\left(\lambda_{\mathrm{eff}}^{\mathrm{s}} \frac{\partial T^{\mathrm{s}}}{\partial z}\right) \\
&\quad -\sum_{\mathrm{j}}\left(\frac{r_{\mathrm{j,g}}^{\mathrm{s}}}{M_{\mathrm{j}}} H_{\mathrm{j,g}}^{\mathrm{s}}\right)+\frac{2\pi r_{\mathrm{o}} \alpha^{\mathrm{s-tw}}}{s_{\mathrm{cell}}^2-\pi r_{\mathrm{o}}^2}\left(T^{\mathrm{tw}}-T^{\mathrm{s}}\right) \\
\left(\varepsilon_{\mathrm{g}}^{\mathrm{t}} \rho_{\mathrm{g}}^{\mathrm{t}} C_{\mathrm{p,g}}^{\mathrm{t}}+\rho_{\mathrm{bulk}}^{\mathrm{t}} C_{\mathrm{p,s}}^{\mathrm{t}}\right) \frac{\partial T^{\mathrm{t}}}{\partial t} &= -\rho_{\mathrm{g}}^{\mathrm{t}} v_{\mathrm{g}}^{\mathrm{t}} C_{\mathrm{p,g}}^{\mathrm{t}} \frac{\partial T^{\mathrm{t}}}{\partial z}+\frac{\partial}{\partial z}\left(\lambda_{\mathrm{eff}}^{\mathrm{t}} \frac{\partial T^{\mathrm{t}}}{\partial z}\right) \\
&\quad -\sum_{\mathrm{j}}\left(\frac{r_{\mathrm{j,s}}^{\mathrm{t}}}{M_{\mathrm{j}}} H_{\mathrm{j,g}}^{\mathrm{t}}\right)+\frac{2\alpha^{\mathrm{t-tw}}}{r_{\mathrm{i}}}\left(T^{\mathrm{tw}}-T^{\mathrm{t}}\right) \\
\rho_{\mathrm{s}}^{\mathrm{tw}} C_{\mathrm{p,s}}^{\mathrm{tw}} \frac{\partial T^{\mathrm{tw}}}{\partial t} &= \frac{\partial}{\partial z}\left(\lambda^{\mathrm{tw}} \frac{\partial T^{\mathrm{tw}}}{\partial z}\right)+\frac{2 r_{\mathrm{o}} \alpha^{\mathrm{s-tw}}}{r_{\mathrm{o}}^2-r_{\mathrm{i}}^2}\left(T^{\mathrm{s}}-T^{\mathrm{tw}}\right) \\
&\quad +\frac{2 r_{\mathrm{i}} \alpha^{\mathrm{t-tw}}}{r_{\mathrm{o}}^2-r_{\mathrm{i}}^2}\left(T^{\mathrm{t}}-T^{\mathrm{tw}}\right)
\end{aligned}
$$

Table 4.2: Conservations equations of the High Switching Frequency Model (HSFM)

Mass conservation equations, forward direction ($\rightarrow$):

$$
\begin{aligned}
\frac{\partial\left(\rho^{\mathrm{s}}_{\mathrm{g},\rightarrow} v^{\mathrm{s}}_{\mathrm{g},\rightarrow}\right)}{\partial z} &= -\left\langle M^{\mathrm{s}}_{\rightarrow}\right\rangle \frac{2\pi r_{\mathrm{i}}}{s^2_{\mathrm{cell}} - \pi r^2_{\mathrm{o}}} J_{\rightarrow} \\
\frac{\partial\left(\rho^{\mathrm{t}}_{\mathrm{g},\rightarrow} v^{\mathrm{t}}_{\mathrm{g},\rightarrow}\right)}{\partial z} &= \left\langle M^{\mathrm{s}}_{\rightarrow}\right\rangle \frac{2}{r_{\mathrm{i}}} J_{\rightarrow} \\
\rho^{\mathrm{s}}_{\mathrm{g},\rightarrow} v^{\mathrm{s}}_{\mathrm{g},\rightarrow} \frac{\partial w^{\mathrm{s}}_{\mathrm{j,g},\rightarrow}}{\partial z} &= \frac{\partial}{\partial z}\left(\rho^{\mathrm{s}}_{\mathrm{g},\rightarrow} D^{\mathrm{s}}_{\mathrm{ax,j},\rightarrow} \frac{\partial w^{\mathrm{s}}_{\mathrm{j,g},\rightarrow}}{\partial z}\right) + r^{\mathrm{s}}_{\mathrm{j,g},\rightarrow} \\
\rho^{\mathrm{t}}_{\mathrm{g},\rightarrow} v^{\mathrm{t}}_{\mathrm{g},\rightarrow} \frac{\partial w^{\mathrm{t}}_{\mathrm{j,g},\rightarrow}}{\partial z} &= \frac{\partial}{\partial z}\left(\rho^{\mathrm{t}}_{\mathrm{g},\rightarrow} D^{\mathrm{t}}_{\mathrm{ax,j},\rightarrow} \frac{\partial w^{\mathrm{t}}_{\mathrm{j,g},\rightarrow}}{\partial z}\right) + \frac{6\left(1-\varepsilon^{\mathrm{t}}_{\mathrm{g}}\right)}{d^{\mathrm{t}}_{\mathrm{p}}} j^{\mathrm{t}}_{\mathrm{j},\rightarrow} \\
&\quad + \left(1 - w^{\mathrm{s}}_{\mathrm{j,g},\rightarrow}\right)\left\langle M^{\mathrm{s}}_{\rightarrow}\right\rangle \frac{2}{r_{\mathrm{i}}} J_{\rightarrow} \\
0 &= -\frac{6\left(1-\varepsilon^{\mathrm{t}}_{\mathrm{g}}\right)}{d^{\mathrm{t}}_{\mathrm{p}}} j^{\mathrm{t}}_{\mathrm{j},\rightarrow} + r^{\mathrm{t}}_{\mathrm{j,s},\rightarrow}
\end{aligned}
$$

For the backward direction similar equations apply, indicated with ($\leftarrow$).

Energy conservation equations:

$$
\begin{aligned}
&\left(\frac{1}{2}\varepsilon^{\mathrm{s}}_{\mathrm{g}}\left(\rho^{\mathrm{s}}_{\mathrm{g},\rightarrow} C^{\mathrm{s}}_{\mathrm{p,g},\rightarrow} + \rho^{\mathrm{s}}_{\mathrm{g},\leftarrow} C^{\mathrm{s}}_{\mathrm{p,g},\leftarrow}\right) + \rho^{\mathrm{s}}_{\mathrm{bulk}} C^{\mathrm{s}}_{\mathrm{p,s}}\right)\frac{\partial T^{\mathrm{s}}}{\partial t} = \\
&\quad -\frac{1}{2}\left(\rho^{\mathrm{s}}_{\mathrm{g},\rightarrow} v^{\mathrm{s}}_{\mathrm{g},\rightarrow} C^{\mathrm{s}}_{\mathrm{p,g},\rightarrow} + \rho^{\mathrm{s}}_{\mathrm{g},\leftarrow} v^{\mathrm{s}}_{\mathrm{g},\leftarrow} C^{\mathrm{s}}_{\mathrm{p,g},\leftarrow}\right)\frac{\partial T^{\mathrm{s}}}{\partial z} + \frac{1}{2}\frac{\partial}{\partial z}\left(\left(\lambda^{\mathrm{s}}_{\mathrm{eff},\rightarrow} + \lambda^{\mathrm{s}}_{\mathrm{eff},\leftarrow}\right)\frac{\partial T^{\mathrm{s}}}{\partial z}\right) \\
&\quad -\frac{1}{2}\sum_{\mathrm{j}}\left(\frac{r^{\mathrm{s}}_{\mathrm{j,g},\rightarrow}}{M_{\mathrm{j}}} H^{\mathrm{s}}_{\mathrm{j,g},\rightarrow} + \frac{r^{\mathrm{s}}_{\mathrm{j,g},\leftarrow}}{M_{\mathrm{j}}} H^{\mathrm{s}}_{\mathrm{j,g},\leftarrow}\right) + \frac{\pi r_{\mathrm{o}}\left(\alpha^{\mathrm{s-tw}}_{\rightarrow} + \alpha^{\mathrm{tw-s}}_{\leftarrow}\right)}{s^2_{\mathrm{cell}} - \pi r^2_{\mathrm{o}}}\left(T^{\mathrm{tw}} - T^{\mathrm{s}}\right) \\
&\left(\frac{1}{2}\varepsilon^{\mathrm{t}}_{\mathrm{g}}\left(\rho^{\mathrm{t}}_{\mathrm{g},\rightarrow} C^{\mathrm{t}}_{\mathrm{p,g},\rightarrow} + \rho^{\mathrm{t}}_{\mathrm{g},\leftarrow} C^{\mathrm{t}}_{\mathrm{p,g},\leftarrow}\right) + \rho^{\mathrm{t}}_{\mathrm{bulk}} C^{\mathrm{t}}_{\mathrm{p,s}}\right)\frac{\partial T^{\mathrm{t}}}{\partial t} = \\
&\quad -\frac{1}{2}\left(\rho^{\mathrm{t}}_{\mathrm{g},\rightarrow} v^{\mathrm{t}}_{\mathrm{g},\rightarrow} C^{\mathrm{t}}_{\mathrm{p,g},\rightarrow} + \rho^{\mathrm{t}}_{\mathrm{g},\leftarrow} v^{\mathrm{t}}_{\mathrm{g},\leftarrow} C^{\mathrm{t}}_{\mathrm{p,g},\leftarrow}\right)\frac{\partial T^{\mathrm{t}}}{\partial z} + \frac{1}{2}\frac{\partial}{\partial z}\left(\left(\lambda^{\mathrm{t}}_{\mathrm{eff},\rightarrow} + \lambda^{\mathrm{t}}_{\mathrm{eff},\leftarrow}\right)\frac{\partial T^{\mathrm{t}}}{\partial z}\right) \\
&\quad -\frac{1}{2}\sum_{\mathrm{j}}\left(\frac{r^{\mathrm{t}}_{\mathrm{j,s},\rightarrow}}{M_{\mathrm{j}}} H^{\mathrm{t}}_{\mathrm{j,g},\rightarrow} + \frac{r^{\mathrm{t}}_{\mathrm{j,s},\leftarrow}}{M_{\mathrm{j}}} H^{\mathrm{t}}_{\mathrm{j,g},\leftarrow}\right) + \frac{\left(\alpha^{\mathrm{t-tw}}_{\rightarrow} + \alpha^{\mathrm{t-tw}}_{\leftarrow}\right)}{r_{\mathrm{i}}}\left(T^{\mathrm{tw}} - T^{\mathrm{t}}\right) \\
&\rho^{\mathrm{tw}}_{\mathrm{s}} C^{\mathrm{tw}}_{\mathrm{p,s}}\frac{\partial T^{\mathrm{tw}}}{\partial t} = \frac{\partial}{\partial z}\left(\lambda^{\mathrm{tw}}\frac{\partial T^{\mathrm{tw}}}{\partial z}\right) + \frac{r_{\mathrm{o}}\left(\alpha^{\mathrm{s-tw}}_{\rightarrow} + \alpha^{\mathrm{s-tw}}_{\leftarrow}\right)}{r^2_{\mathrm{o}} - r^2_{\mathrm{i}}}\left(T^{\mathrm{s}} - T^{\mathrm{tw}}\right) \\
&\quad + \frac{r_{\mathrm{i}}\left(\alpha^{\mathrm{t-tw}}_{\rightarrow} + \alpha^{\mathrm{t-tw}}_{\leftarrow}\right)}{r^2_{\mathrm{o}} - r^2_{\mathrm{i}}}\left(T^{\mathrm{t}} - T^{\mathrm{tw}}\right)
\end{aligned}
$$

The mass and energy conservation equations of the DM and HSFM are listed in Tables 4.1 and 4.2, respectively. As initial condition a uniform temperature profile was taken at a temperature sufficiently high to assure reaction ignition and the usual Danckwerts-type boundary conditions were assumed. In both compartments all gaseous species that are likely to be present have been included, but possible formation of solid carbonaceous deposits has been ignored.

4.2.3 Reaction kinetics and constitutive relations

Syngas compartment

The following CPO reactions were considered: full combustion of CH_4, steam and dry reforming of CH_4 and the water-gas-shift reaction:

I	$CH_4 + 2O_2$	$\rightarrow$	$CO_2 + 2H_2O$
II	$CH_4 + H_2O$	$\rightleftharpoons$	$CO + 3H_2$
III	$CH_4 + CO_2$	$\rightleftharpoons$	$2CO + 2H_2$
IV	$CO + H_2O$	$\rightleftharpoons$	$CO_2 + H_2$

The intrinsic CPO reaction rates were calculated using kinetic data reported by Gosiewski et al. (1999), which are reproduced in Table 4.3. The accompanying ki-

Table 4.3: Kinetics of the combustion and CPO reactions (van Sint Annaland, 2000; Gosiewski et al., 1999).

$$
\begin{aligned}
R_{\mathrm{I}}^{\mathrm{s}} &= \rho_{\mathrm{bulk}}^{\mathrm{s}} k_{\mathrm{I},\infty}^{\mathrm{s}} \exp\left(-\frac{E_{\mathrm{a,I}}^{\mathrm{s}}}{R_{\mathrm{g}} T^{\mathrm{s}}}\right) c_{\mathrm{O_2,s}}^{\mathrm{s}} c_{\mathrm{CH_4,s}}^{\mathrm{s}} \\
R_{\mathrm{I}}^{\mathrm{t}} &= \rho_{\mathrm{bulk}}^{\mathrm{t}} k_{\mathrm{I},\infty}^{\mathrm{t}} \exp\left(-\frac{E_{\mathrm{a,I}}^{\mathrm{t}}}{R_{\mathrm{g}} T^{\mathrm{t}}}\right) c_{\mathrm{O_2,s}}^{\mathrm{t}} c_{\mathrm{CH_4,s}}^{\mathrm{t}} \\
R_{\mathrm{II}}^{\mathrm{t}} &= \rho_{\mathrm{bulk}}^{\mathrm{t}} k_{\mathrm{II},\infty}^{\mathrm{t}} \exp\left(-\frac{E_{\mathrm{a,II}}^{\mathrm{t}}}{R_{\mathrm{g}} T^{\mathrm{t}}}\right) c_{\mathrm{H_2O,s}}^{\mathrm{t}} c_{\mathrm{CH_4,s}}^{\mathrm{t}} \left(1 - \frac{\left(p_{\mathrm{H_2,s}}^{\mathrm{t}}\right)^3 p_{\mathrm{CO,s}}^{\mathrm{t}}}{p_{\mathrm{CH_4,s}}^{\mathrm{t}} p_{\mathrm{H_2O,s}}^{\mathrm{t}} \left(p_{\mathrm{g}}^{\ominus}\right)^2 K_{\mathrm{eq,II}}}\right) \\
R_{\mathrm{III}}^{\mathrm{t}} &= \rho_{\mathrm{bulk}}^{\mathrm{t}} k_{\mathrm{III},\infty}^{\mathrm{t}} \exp\left(-\frac{E_{\mathrm{a,III}}^{\mathrm{t}}}{R_{\mathrm{g}} T^{\mathrm{t}}}\right) c_{\mathrm{CO_2,s}}^{\mathrm{t}} c_{\mathrm{CH_4,s}}^{\mathrm{t}} \left(1 - \frac{\left(p_{\mathrm{H_2,s}}^{\mathrm{t}}\right)^2 \left(p_{\mathrm{CO,s}}^{\mathrm{t}}\right)^2}{p_{\mathrm{CH_4,s}}^{\mathrm{t}} p_{\mathrm{CO_2,s}}^{\mathrm{t}} \left(p_{\mathrm{g}}^{\ominus}\right)^2 K_{\mathrm{eq,III}}}\right) \\
R_{\mathrm{IV}}^{\mathrm{t}} &= \rho_{\mathrm{bulk}}^{\mathrm{t}} k_{\mathrm{IV},\infty}^{\mathrm{t}} \exp\left(-\frac{E_{\mathrm{a,IV}}^{\mathrm{t}}}{R_{\mathrm{g}} T^{\mathrm{t}}}\right) c_{\mathrm{CO,s}}^{\mathrm{t}} c_{\mathrm{H_2O,s}}^{\mathrm{t}} \left(1 - \frac{p_{\mathrm{H_2,s}}^{\mathrm{t}} p_{\mathrm{CO_2,s}}^{\mathrm{t}}}{p_{\mathrm{CO,s}}^{\mathrm{t}} p_{\mathrm{H_2O,s}}^{\mathrm{t}} K_{\mathrm{eq,IV}}}\right)
\end{aligned}
$$

Table 4.4: Kinetic parameters of the combustion and CPO reactions (van Sint Annaland, 2000; Gosiewski et al., 1999).

Reaction	$R_{\mathrm{I}}^{\mathrm{s}}$	$R_{\mathrm{I}}^{\mathrm{t}}$	$R_{\mathrm{II}}^{\mathrm{t}}$	$R_{\mathrm{III}}^{\mathrm{t}}$	$R_{\mathrm{IV}}^{\mathrm{t}}$
k_∞ (m^6/kg/s/mol)	$14.6 \cdot 10^3$	$15.07 \cdot 10^3$	$48.82 \cdot 10^3$	$6.804 \cdot 10^3$	$0.264 \cdot 10^3$
E_{a} (kJ/mol)	98.5	100.32	114.12	142.51	38.13

netic parameters are given in Table 4.4 and the the computation of the equilibrium constants is outlined in Appendix 4.C. For an accurate description of the effective conversion rate inside a catalyst particle where internal mass transfer limitations are fully accounted for, principally, the species and energy conservation equations have to be solved to obtain the concentration and temperature profiles inside the particles. Because this would require excessive computational efforts, the particle effectiveness factors were approximated with a linearisation approach following Gosiewski et al. (1999). In this approach the reaction rates in Table 4.3 are linearised with respect to the species that has the most significant influence on the reaction rate to obtain an apparent reaction rate constant that is used to calculate an effective reaction rate R_{eff} via:

$$R_{\mathrm{eff}} = R\eta \tag{4.2}$$

where the effectiveness factor η is calculated with:

$$\eta = \frac{3\varphi - \tanh(3\varphi)}{3\varphi^2 \tanh(3\varphi)} \tag{4.3}$$

and the Thiele modulus φ is given by:

$$\varphi = \frac{d_{\mathrm{p}}}{6}\sqrt{\frac{k_\eta}{D_{\mathrm{eff}}}} \tag{4.4}$$

The linearised reaction rate constants k_η were calculated following Gosiewski et al. (1999) and are given in Table 4.5. However, since CH_4 is present in excess for the most part of membrane section of the reactor, the reaction rate constants for reactions II and III were linearised with respect to H_2O and CO_2, respectively, instead of CH_4 (although it was found that this hardly affects the results). The effective diffusivity D_{eff} in Equation 4.4 is calculated via Blanc's law (Reid et al., 1987) and the Knudsen

Table 4.5: Linearised CPO reaction rate constants.

$$
\begin{aligned}
k^{\mathrm{s}}_{\eta,\mathrm{I}} &= \rho^{\mathrm{s}}_{\mathrm{bulk}} k^{\mathrm{s}}_{\mathrm{I},\infty} \exp\left(-\frac{E^{\mathrm{s}}_{\mathrm{a,I}}}{R_{\mathrm{g}} T^{\mathrm{s}}}\right) c^{\mathrm{s}}_{\mathrm{O_2,s}} \\
k^{\mathrm{t}}_{\eta,\mathrm{I}} &= 2\rho^{\mathrm{t}}_{\mathrm{bulk}} k^{\mathrm{t}}_{\mathrm{I},\infty} \exp\left(-\frac{E^{\mathrm{t}}_{\mathrm{a,I}}}{R_{\mathrm{g}} T^{\mathrm{t}}}\right) \left(c^{\mathrm{t}}_{\mathrm{CH_4,s}} + 0.5 c^{\mathrm{t}}_{\mathrm{O_2,s}}\right) \\
k^{\mathrm{t}}_{\eta,\mathrm{II}} &= \rho^{\mathrm{t}}_{\mathrm{bulk}} k^{\mathrm{t}}_{\mathrm{II},\infty} \exp\left(-\frac{E^{\mathrm{t}}_{\mathrm{a,II}}}{R_{\mathrm{g}} T^{\mathrm{t}}}\right) c^{\mathrm{t}}_{\mathrm{CH_4,s}} \\
k^{\mathrm{t}}_{\eta,\mathrm{III}} &= \rho^{\mathrm{t}}_{\mathrm{bulk}} k^{\mathrm{t}}_{\mathrm{III},\infty} \exp\left(-\frac{E^{\mathrm{t}}_{\mathrm{a,III}}}{R_{\mathrm{g}} T^{\mathrm{t}}}\right) c^{\mathrm{t}}_{\mathrm{CH_4,s}} \\
c^{\mathrm{t}}_{\mathrm{CO,s}} &> c^{\mathrm{t}}_{\mathrm{CO,s,eq,IV}} \qquad \Rightarrow \qquad k^{\mathrm{t}}_{\eta,\mathrm{IV}} = \frac{R^{\mathrm{t}}_{\mathrm{IV}}}{c^{\mathrm{t}}_{\mathrm{CO,s}} - c^{\mathrm{t}}_{\mathrm{CO,s,eq,IV}}} \\
c^{\mathrm{t}}_{\mathrm{CO,s}} &\leq c^{\mathrm{t}}_{\mathrm{CO,s,eq,IV}} \qquad \Rightarrow \qquad k^{\mathrm{t}}_{\eta,\mathrm{IV}} = \frac{R^{\mathrm{t}}_{\mathrm{IV}}}{c^{\mathrm{t}}_{\mathrm{CO_2,s}} - c^{\mathrm{t}}_{\mathrm{CO_2,s,eq,IV}}}
\end{aligned}
$$

diffusivity:

$$
\frac{\varepsilon_{\mathrm{s}}}{\tau D_{\mathrm{eff}}} = \frac{1}{\overline{D}_{\mathrm{j}}} + \frac{1}{D_{\mathrm{KN}}} = \frac{1}{\dfrac{1}{\sum\limits_{\mathrm{i}} \dfrac{x_{\mathrm{i}}}{D_{\mathrm{i,j}}}}} + \frac{1}{\dfrac{2}{3} r_{\mathrm{p}} \sqrt{\dfrac{8 R_{\mathrm{g}} T}{\pi \langle M \rangle}}} \tag{4.5}
$$

The different r_{j} in Tables 4.1 and 4.2 can be directly calculated from R_{eff} (Equation 4.2):

$$
\begin{aligned}
r_{\mathrm{CH_4}} &= M_{\mathrm{CH_4}} \left(-R_{\mathrm{eff,I}} - R_{\mathrm{eff,II}} - R_{\mathrm{eff,III}}\right) \\
r_{\mathrm{CO}} &= M_{\mathrm{CO}} \left(R_{\mathrm{eff,II}} + 2R_{\mathrm{eff,III}} - R_{\mathrm{eff,IV}}\right) \\
r_{\mathrm{CO_2}} &= M_{\mathrm{CO_2}} \left(R_{\mathrm{eff,I}} - R_{\mathrm{eff,III}} + R_{\mathrm{eff,IV}}\right) \\
r_{\mathrm{H_2}} &= M_{\mathrm{H_2}} \left(3R_{\mathrm{eff,II}} + 2R_{\mathrm{eff,III}} + R_{\mathrm{eff,IV}}\right) \\
r_{\mathrm{H_2O}} &= M_{\mathrm{H_2O}} \left(2R_{\mathrm{eff,I}} - R_{\mathrm{eff,II}} - R_{\mathrm{eff,IV}}\right) \\
r_{\mathrm{O_2}} &= M_{\mathrm{O_2}} \left(-2R_{\mathrm{eff,I}}\right)
\end{aligned} \tag{4.6}
$$

The effect of external mass transfer limitations from the gas bulk to the catalyst surface on the conversion rate by the CPO reactions was accounted for using the Maxwell-Stefan description. Details can be found in Appendix 4.A.

O_2 compartment

For the CH_4 combustion reaction rate for the shell compartment the kinetics determined in our lab were used (van Sint Annaland, 2000), which were adapted to the Pt loading (0.5 wt.%) and surface area (80 m^2/g) of a commercial Pt/Al_2O_3 catalyst (Engelhard), see Chapter 5. The kinetic data are very similar to that of the combustion kinetics in the syngas compartment, see also Table 4.4. Because only a small amount of CH_4 is combusted in air, the reaction rate can be considered to be pseudo first order with respect to CH_4 and also the diffusion coefficient in the calculation of the Thiele modulus can be considered constant, so that the effective reaction rate including internal and external mass transfer can be calculated analytically (Westerterp et al., 1984):

$$R_{\mathrm{j,eff}} = \frac{1}{\dfrac{d_\mathrm{p}}{6c_\mathrm{j}k_\mathrm{g}\left(1-\varepsilon_\mathrm{g}\right)} + \dfrac{1}{R_\mathrm{j}\eta}} \tag{4.7}$$

In Table 4.6 the correlations to compute the heat and mass transfer coefficients that were used in the simulations are summarised. The thermal conductivity of the stagnant packed bed was calculated according to Zehner and Schlünder (1970) and the wall-to-bed heat transfer coefficient was taken from Dixon and Creswell (1979), see Appendix 4.B for details. The axial pressure drops over the tube and shell compartments were calculated with the differential form of the Ergun-equation (Ergun, 1952):

$$-\frac{\partial p}{\partial z} = 150\left(\frac{\eta_\mathrm{g} v_\mathrm{g}}{d_\mathrm{p}^2}\right)\frac{\left(1-\varepsilon_\mathrm{g}\right)^2}{\varepsilon_\mathrm{g}^3} + 1.75\left(\frac{\rho v_\mathrm{g}^2}{d_\mathrm{p}}\right)\frac{1-\varepsilon_\mathrm{g}}{\varepsilon_\mathrm{g}^3} \tag{4.8}$$

The physical properties that were used for the simulations were set to typical values that would be selected for an industrial application and are summarised in Table 4.7. Other physical properties were calculated according to Reid et al. (1987), using the pure component data supplied by Daubert and Danner (1985), see appendices 2.A and 4.C.

Table 4.6: Heat and mass transfer coefficients.

Gas-to-particle heat transfer coefficient (Gunn, 1978):

$$Nu = \left(7 - 10\varepsilon_\mathrm{g} + 5\varepsilon_\mathrm{g}^2\right)\left(1 + 0.7Re^{0.2}Pr^{1/3}\right) + \left(1.33 - 2.4\varepsilon_\mathrm{g} + 1.2\varepsilon_\mathrm{g}^2\right)Re^{0.7}Pr^{1/3}$$

Axial heat dispersion (Gunn and Misbah, 1993):

$$\begin{aligned}\lambda_\mathrm{eff} &= \lambda_\mathrm{bed} + \frac{RePr\lambda_\mathrm{g}}{Pe_\mathrm{ax}} + \frac{Re^2Pr^2\lambda_\mathrm{g}}{6\left(1-\varepsilon_\mathrm{g}\right)Nu} \\ Pe_\mathrm{ax} &= \frac{2p}{1-p}, \qquad p = 0.17 + 0.33\exp\left(\frac{-24}{Re}\right)\end{aligned}$$

Gas-to-particle mass transfer coefficient (Thoenes and Kramers, 1958):

$$k_\mathrm{g} = \frac{0.81}{\varepsilon_\mathrm{g}} v_\mathrm{g} Re^{-0.5} Sc^{-2/3}$$

Axial mass dispersion coefficient (Edwards and Richardson, 1968):

$$\frac{D_\mathrm{ax}}{v_\mathrm{g} d_\mathrm{p}} = \frac{0.73}{ReSc} + \frac{0.5}{1 + 9.7\varepsilon_\mathrm{g} ReSc}$$

Table 4.7: Physical properties.

B_0	$6.9 \cdot 10^{-16}$ m^2	$\varepsilon_\mathrm{s}^\mathrm{s}, \varepsilon_\mathrm{s}^\mathrm{t}$	0.6
K_0	$2.24 \cdot 10^{-9}$ m	$\rho_{\mathrm{bulk,Al_2O_3}}$	2170 kg/m^3
r_p	$9.1 \cdot 10^{-9}$ m	$\rho_{\mathrm{bulk,CPO}}$, $\rho_{\mathrm{bulk,Pt/Al_2O_3}}$	677 kg/m^3
δ_m	$65 \cdot 10^{-6}$ m	$\tau_\mathrm{s}^\mathrm{s}, \tau_\mathrm{s}^\mathrm{t}$	2
$\varepsilon_\mathrm{g}^\mathrm{s}, \varepsilon_\mathrm{g}^\mathrm{t}$	0.4		

4.3 HSFM simulation results

In this section firstly the design parameters of the reverse flow section of the reactor are determined based on analytic expressions and HSFM simulations. Subsequently it will be demonstrated with HSFM simulations that it is indeed crucial in the RFCMR concept to add some H_2O to the O_2 feed to avoid runaways in the centre of the reactor.

4.3.1 Reverse flow section

A reactor with a shell-and-tube configuration with a square pitch (see Figure 4.2) has been selected for this study, where the ratio of the length of the unit cell, s_{cell}, and the tube outer diameter, d_{t}, has been set to 1.25:1 (quite similar results would be obtained with other ratios). With this design parameter fixed, the axial dimensions of the heat exchange sections of the reactor can be determined, *i.e.* length of the in- and outlet sections, here referred to as the "reverse flow" part of the reactor. The reactor will be designed to operate at elevated pressures so that very high temperatures are required for the CPO reactions in the membrane section. If a normal combustion catalyst is used in the in- and outlet section of the shell, it will be difficult to reach these very high plateau temperatures. This is because of the low ignition temperature of the CH_4 combustion and the increased reaction rates due to the elevated pressures. For conventional reverse flow reactors approximate relations for the plateau temperature (Nieken et al., 1995) and front velocity (Froment, 1990) were derived. For a reactor consisting of two separated compartments with co-current flow and with a reaction occurring in one of the compartments analogous expressions can be derived ignoring radial gradients. In case of a geometry similar to that of the RFCMR the plateau temperature can be estimated by the following implicit equation:

$$\int_{\mathrm{T_{feed}}+\Delta\mathrm{T_{ad}}}^{\mathrm{T_{plateau}}} \frac{M_{\mathrm{CH_4}} R^{\mathrm{s}}_{\mathrm{CH_4,eff}}}{w^{\mathrm{s}}_{\mathrm{CH_4,g,in}}} dT = \frac{\pi r_{\mathrm{i}}^2 \left(\rho^{\mathrm{s}}_{\mathrm{g,in}} v^{\mathrm{s}}_{\mathrm{g,in}}\right)^2}{s^2_{\mathrm{cell}} - \pi r_{\mathrm{o}}^2 + \pi r_{\mathrm{i}}^2} \frac{\left(-\Delta H^{\mathrm{s}}_{\mathrm{r}}\right) w^{\mathrm{s}}_{\mathrm{CH_4,g,in}}}{2 \left\langle \lambda_{\mathrm{eff}} \right\rangle M_{\mathrm{CH_4}}} \tag{4.9}$$

where ΔT_{ad} is given by:

$$\Delta T_{\mathrm{ad}} = \frac{\pi r_{\mathrm{i}}^2}{s^2_{\mathrm{cell}} - \pi r_{\mathrm{o}}^2 + \pi r_{\mathrm{i}}^2} \frac{\rho^{\mathrm{s}}_{\mathrm{g,in}} v^{\mathrm{s}}_{\mathrm{g,in}} \left(\Delta H^{\mathrm{s}}_{\mathrm{r}}\right) w^{\mathrm{s}}_{\mathrm{CH_4,g,in}}}{\left\langle \rho_{\mathrm{g,in}} v_{\mathrm{g,in}} C_{\mathrm{p,g}} \right\rangle M_{\mathrm{CH_4}}} \tag{4.10}$$

The front velocity can be estimated from:

$$v_{\mathrm{front}} = \frac{\langle \rho_{\mathrm{g,in}} v_{\mathrm{g,in}} C_{\mathrm{p,g}} \rangle}{\langle \rho_{\mathrm{p}} C_{\mathrm{p,s}} + \varepsilon_{\mathrm{g}} \rho_{\mathrm{g}} C_{\mathrm{p,g}} \rangle} \left(1 - \frac{\Delta T_{\mathrm{ad}}}{T_{\mathrm{plateau}} - T_{\mathrm{feed}}} \right) \tag{4.11}$$

where quantities in brackets can be calculated from:

$$\langle Y \rangle = \frac{\left(s_{\mathrm{cell}}^2 - \pi r_{\mathrm{o}}^2 \right) Y^{\mathrm{s}} + \pi r_{\mathrm{i}}^2 Y^{\mathrm{t}}}{s_{\mathrm{cell}}^2 - \pi r_{\mathrm{o}}^2 + \pi r_{\mathrm{i}}^2} \tag{4.12}$$

Using Equation 4.9 it can be calculated that the catalyst activity as listed in Table 4.4 has to be reduced with a factor of $1{\cdot}10^5$ (note that a possible and plausible contribution by homogeneous reactions has been ignored here) to reach a plateau temperature of 1500 K with a reasonable CH_4 weight fraction in the shell feed ($w^{\mathrm{s}}_{\mathrm{g,CH4}}$). Since this factor is impractical, use of inert sections is preferred. It is well known that inert sections can be used to increase the plateau temperature in a conventional reverse flow reactor (Nieken et al., 1994; Matros and Bunimovich, 1996). An advantage of using inert sections is that both the plateau temperature as well as the width of the plateau are independent of the reaction kinetics (as long as the reaction rate is sufficiently fast) so that the reactor can be more easily designed and operated. A disadvantage however, is that the plateau temperature decreases with increasing switching time (Nieken et al., 1994), so that the switching time and length of the inert section can no longer be selected separately. For a conventional reverse flow reactor with inert sections and assuming an infinitely fast reaction rate on the catalyst bed positioned downstream the inert section, the plateau temperature can be estimated from a relation given by Matros and Bunimovich (1996), here adapted for a reactor consisting of two separated compartments:

$$T_{\mathrm{plateau}} = T_{\mathrm{feed}} + \Delta T_{\mathrm{ad}} \left(1 + \frac{\langle \rho_{\mathrm{g}} v_{\mathrm{g}} \rangle \, L_{\mathrm{inert}}}{2 \, \langle \lambda_{\mathrm{eff}} \rangle} \right) \tag{4.13}$$

Again the quantities in brackets are calculated using Equation 4.12.

Selecting mass fluxes of 1.00 and 0.98 kg/m^2/s for feeds to the shell and tube compartments (based on an infinitely thin tube) corresponding to an overall stoichiometric feed, assuming that the adiabatic temperature rise is small ($\Delta T_{\mathrm{ad}}/(T_{\mathrm{plateau}} - T_{\mathrm{feed}}) \ll 1$) and approximating the physical properties with the inlet composition and a temperature of 900 K, a front velocity of about 0.0014 m/s is computed. For a reasonable switching time of 300 s, the front traverses 0.42 m each cycle and the length of the inert section should be considerably higher than this value in order to minimise the

Table 4.8: Parameters used in the simulation of the RFCMR.

$d_{p,Al_2O_3}, d_{p,Pt/Al_2O_3}$	$3 \cdot 10^{-3}$ m	s_{cell}	0.0313 m
d_t	0.025 m	T_{feed}	300 K
L_{inert}	2 m	$w^t_{g,CH4}$	1
$L_{reactor}$	6 m	$w^s_{g,H2O}$	0.13
p^s, p^t	20 bar	$w^s_{g,O2}$	0.87
r_o	0.0125 m	$\rho^s_g v^s_g$	1 kg/m^2/s
r_i	0.0105 m	$\rho^s_g v^t_g$	1.23 kg/m^2/s

influence of the switching time and to use the inert sections effectively. By selecting a value of 2 m for the length of the inert sections, a $w^s_{g,CH4}$ of only 0.0006 is required according to Equation 4.13 to reach a plateau temperature of 1420 K. To verify these results with a more accurate description of the physical properties, simulations were carried out with the HSFM for different values of $w^s_{g,CH4}$ and without permeation through the membrane. The simulation parameters are given in Table 4.8. The axial temperature profiles in the shell compartment in the stationary state are given in Figure 4.3 for different values of $w^s_{g,CH4}$. A flat temperature plateau is established between the inert sections and with $w^s_{g,CH4}$ equal to 0.0007 indeed a plateau temperature profile of about 1500 K can be accomplished. Nonetheless, the adiabatic temperature rise at the reactor outlet to achieve these very high plateau temperatures is very small (< 10 K). As discussed earlier, the required $w^s_{g,CH4}$ to reach a certain plateau temperature increases with increasing switching time. Since the HSFM assumes that this switching time is infinitely small, the actual $w^s_{g,CH4}$ that is required to achieve the desired temperature plateau for a given switching time is slightly higher than computed with the HSFM. The DM can be used to obtain a better estimate.

4.3.2 Membrane section

With the axial dimensions of the reverse flow section of the reactor more or less established, the design parameters of the membrane section of the RFCMR can be determined. The H_2O fraction in the shell feed ($w^s_{g,H2O}$) has to be selected in such a way that isothermal conditions are achieved along the membrane and that runaways in the centre are prevented. Furthermore, the required membrane length and the CPO catalyst diameter have to be selected simultaneously in such a way that the axial

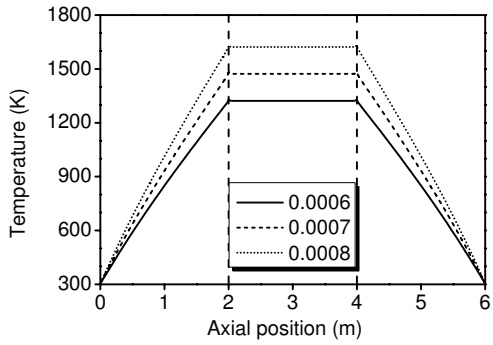

Figure 4.3: Axial temperature profiles in the shell compartment of the RFCMR simulated with the HSMF without membrane permeation for different values of $w^{\mathrm{s}}_{\mathrm{g,CH_4}}$ (simulation parameters are listed in Table 4.8). The combustion catalyst section is located between the dashed lines.

pressure drop over the tube side of the membrane is acceptable, while the particles are sufficiently small to avoid too strong influences of external and internal mass transfer limitations and the residence time is high enough to assure high conversion of the reactants via the CPO reactions. In this section only the optimal choice of $w^{\mathrm{s}}_{\mathrm{g,H2O}}$ will be discussed in detail. The optimal values for the membrane length and CPO catalyst diameter will be addressed in detail in the next section based on more detailed DM simulations, because the composition of the tube outlet is quite sensitive to the dynamic movement of the temperature profile.

To determine an appropriate value for $w^{\mathrm{s}}_{\mathrm{g,H2O}}$, HSFM simulations were performed where permeation through the membrane was incorporated. For the simulations again the parameters listed in Table 4.8 were used and, furthermore, the length of the membrane was set to 0.5 m. With respect to the mass fluxes of the shell and tube feeds, it was found that it is was numerically quite difficult to achieve exactly stoichiometric feeds of O_2 and CH_4 for the dead-end permeation configuration in the shell compartment. Dead-end permeation would imply two boundary conditions for the differential equation governing the shell mass flux (see Table 4.2): a fixed mass flux at the inlet and a zero mass flux at the end. Since this differential equation is only first order, only one boundary condition can be imposed. Thus the outlet mass flux has to be controlled with the shell inlet pressure, which requires an artificial by-pass to prevent the

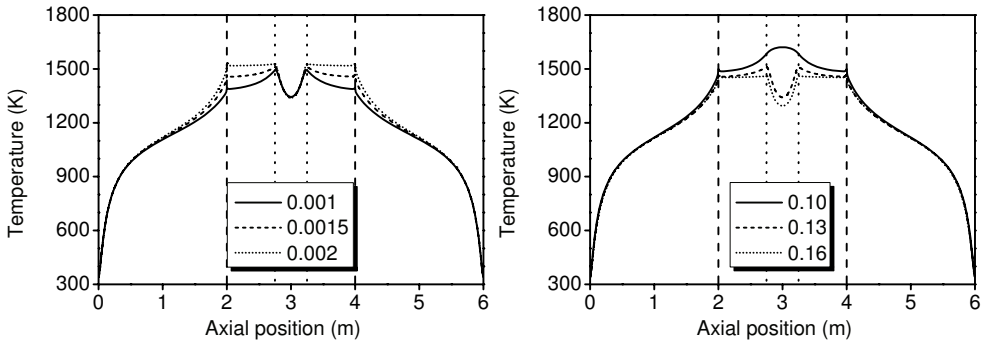

Figure 4.4: Axial temperature profiles in the shell compartment of the RFCMR with permeation simulated with the HSMF for different values for w^{s}_{g,CH_4} (left, $w^{s}_{g,H_2O} = 0.13$) and for w^{s}_{g,H_2O} (right, $w^{s}_{g,CH_4} = 0.0015$). The combustion catalyst section is located between the dashed lines and the membrane section between the dotted lines.

shell mass flux from becoming zero leading to numerical instabilities. Therefore, the tube mass flux was slightly decreased compared to the value that would be required for overall stoichiometric feeds, so that the shell by-pass was typically 0.1 kg/m/s^2 ($\approx$ 10 %). In practice the shell outlet can simply be closed so that the shell side pressure profile regulates itself.

In Figure 4.4 the axial temperature profiles are given for different values of $w^{s}_{g,CH4}$ and $w^{s}_{g,H2O}$. Remarkably, the temperature at the beginning of the temperature plateau is only dependent on $w^{s}_{g,CH4}$, whereas the temperature in the centre is totally controlled by $w^{s}_{g,H2O}$. From Figure 4.4 it is obvious that the addition of H_2O is essential in the RFCMR concept to prevent runaways in the centre. The plateau temperatures are not completely flat in the membrane section, which is caused by the changing equilibrium compositions along the membrane and the incomplete conversion of CH_4. At higher temperatures only syngas will be formed, as was shown in Chapter 2, by which the axial temperature gradients along the membrane can be reduced, but operation at higher temperatures is probably not feasible in view of membrane stability constraints. Another possibility to create a flatter temperature profile in the membrane section is via dynamic control of $w^{s}_{g,H2O}$ or a better tuning of the local H_2O and O_2 fluxes across the membranes by feeding the H_2O separately via a third compartment. Nevertheless, the HSFM simulations have shown that by

proper selection of the lengths of the inert sections and the shell feed composition the desired temperature profile can be attained.

4.4 DM simulation results

In the previous sections a number of design parameters were determined based on HSFM simulations. In this section the optimal CPO catalyst diameter, membrane length, switching time and tube diameter will be determined based on more detailed DM simulations by considering the syngas selectivities, the axial pressure drops and the influence of mass transfer limitations. Furthermore, also the influence of the dynamic movement of the temperature profile will be addressed.

4.4.1 Determination of the optimal CPO catalyst diameter and membrane length

To determine the optimal CPO catalyst particle diameter and membrane length, DM simulations were carried out for several cases listed in Table 4.9. Again the simulation parameters listed in Table 4.8 were used and furthermore a switching time of 300 s and $w^{\mathrm{s}}_{\mathrm{g,CH4}} = 0.003$. Typical axial temperature profiles at the end of a semi-cycle are given in Figure 4.5 for case B. It is observed that in the membrane section a temperature plateau of 1450 K is established whereas the maximal outlet temperature is limited to about 600 K demonstrating the very effective integrated recuperative heat exchange via the reverse flow concept. At the end of the inert sections small temperature spikes are observed in the shell compartment. These temperature excursions arise because of the combustion of the CH_4 added to the O_2 feed over the Pt/Al_2O_3 catalyst. In Figure 4.6 the corresponding CO and H_2 selectivities are given as a function of time and indeed very high syngas selectivities (> 98 %) are achieved throughout the entire semi-cycle. To evaluate all cases with respect to the syngas composition, in Table 4.9 the average outlet mole fractions, CO and H_2 selectivities and the accompanying inlet O_2/CH_4 and H_2O/CH_4 ratios (outlet composition based) are given for the different cases investigated. In this table also the equilibrium composition for stoichiometric conditions at 1500 K and 20 bar have been included for a $CH_4/H_2O/O_2$ feed ratio of 1.13:0.13:0.5 as a reference. Note that the small discrepancy in this ratio for the different cases is related to the combustion of a small amount of CH_4 in the shell compartment in the simulations. From these results it can be concluded that the dry

Table 4.9: Simulation results for different CPO catalyst particle diameters and membrane lengths.

	A	B	C	D	equilibrium
$d_{\mathrm{p,CPO}}$ $(\cdot 10^{-3}$ m)	1	3	1	3	
L_{membrane} (m)	0.25	0.25	0.5	0.5	
$\langle x^{\mathrm{t}}_{\mathrm{CH_4,g,out}} \rangle$	0.018	0.020	0.019	0.017	0.013
$\langle x^{\mathrm{t}}_{\mathrm{CO,g,out}} \rangle$	0.312	0.310	0.312	0.311	0.314
$\langle x^{\mathrm{t}}_{\mathrm{CO_2,g,out}} \rangle$	0.002	0.002	0.002	0.002	0.002
$\langle x^{\mathrm{t}}_{\mathrm{H_2,g,out}} \rangle$	0.655	0.652	0.656	0.653	0.659
$\langle x^{\mathrm{t}}_{\mathrm{H_2O,g,out}} \rangle$	0.011	0.012	0.010	0.012	0.011
$\langle x^{\mathrm{t}}_{\mathrm{O_2,g,out}} \rangle$	0.001	0.004	0.001	0.002	0
$\langle S_{\mathrm{CO}} \rangle$ (%)	99.3	99.3	99.4	99.3	99.4
$\langle S_{\mathrm{H_2}} \rangle$ (%)	98.3	98.2	98.5	98.2	98.4
$\langle \mathrm{O_2/CH_4} \rangle_{\mathrm{in}}$	0.438	0.444	0.443	0.444	0.442
$\langle \mathrm{H_2O/CH_4} \rangle_{\mathrm{in}}$	0.116	0.118	0.118	0.115	0.115

syngas content ($\langle x_{\mathrm{H_2,out}} \rangle + \langle x_{\mathrm{CO,out}} \rangle$) is above 98 % for each case, which is much higher than the values (< 95 %) reported for industrial processes (Brejc and Supp, 1989; Aasberg-Petersen et al., 2001). The CH_4 fraction in the reactor exhaust are quite dependent on the permeation rate through the membrane, since the permeation rate has to be controlled by the shell side pressure profile, which even changes in time as discussed previously. Therefore not too many conclusions can be drawn on the extent of CH_4 slip from these simulations, but it is small anyhow for all these cases. The feed O_2/CH_4 and H_2O/CH_4 ratios are typically about 0.44 and 0.12, respectively. Especially the consumption of the expensive O_2 is considerably lower (> 25 %) compared to industrial practice (Brejc and Supp, 1989; Aasberg-Petersen et al., 2001), where typically $O_2/CH_4 > 0.6$, demonstrating the great potential of the RFCMR concept. Regarding the influence of possible mass transfer limitations, even for case B having the shortest catalyst bed and largest CPO catalyst particle diameter the CO, CO_2, H_2 and H_2O fractions are close to the equilibrium values, although a small amount of O_2 is not converted. The extent and the influence of mass transfer limitations will be discussed in the next section. Obviously, when the length of the CPO catalyst bed is slightly larger than the catalyst bed, all O_2 could

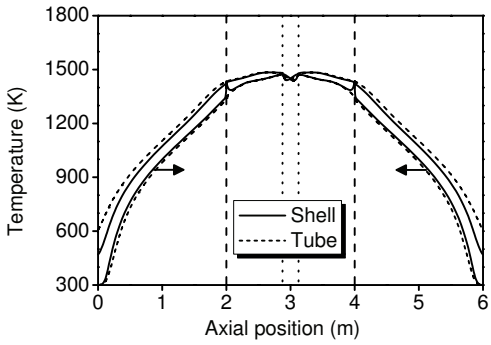

Figure 4.5: Axial temperature profiles in the RFCMR at the end of a forward (→) and backward (←) semi-cycle for case B. The combustion catalyst section is located between the dashed lines and the membrane section between the dotted lines.

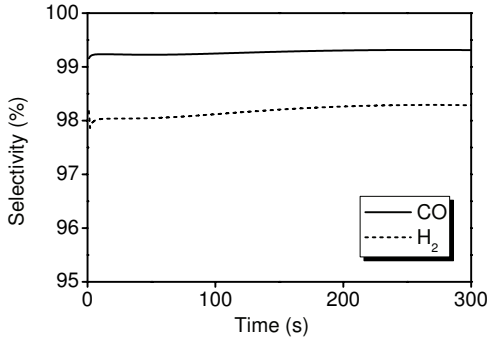

Figure 4.6: CO and H_2 selectivities of the tube outlet of the RFCMR as a function of time during a semi-cycle for case B.

be converted. In the simulations the length of the CPO catalyst bed was equal to that of the membrane.

As expected the highest syngas selectivities are obtained in the RFCMR for a large CPO catalyst bed of small particles, but this would lead to an unacceptably high pressure drop. To evaluate the influence of CPO catalyst particle diameters and membrane lengths of cases A-D with respect to the axial pressure drop, typical axial pressure profiles in the RFCMR are presented in Figure 4.7 for case B and C at the end of a forward cycle. The pressure drop on the tube side is the highest for case C, having the longest membrane and the smallest particle diameter, but the difference with case B is small, because the pressure drop is caused mainly in the outlet part of the tube. Nevertheless, in view of the very steep pressure gradient at the end of the membrane section for case C, it is concluded that particle diameters below 1 mm would lead to unacceptable pressure drops. In practice, the pressure drop that can be allowed and the particle diameter that is required for effective use of the expensive catalyst in view of possible external and internal mass transfer limitations will determine the reactor

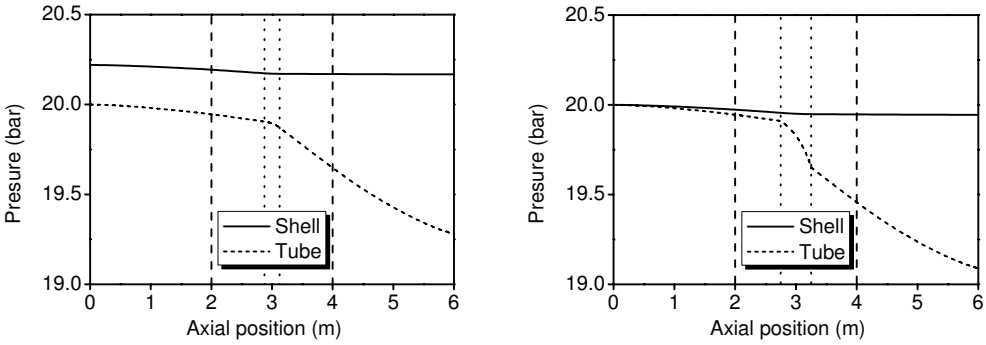

Figure 4.7: Axial pressure profiles in the RFCMR at the end of a forward semi-cycle for $d_{\mathrm{p}} = 3$ mm and $L_{\mathrm{membrane}} = 0.25$ m (case B, left) and for $d_{\mathrm{p}} = 1$ mm and $L_{\mathrm{membrane}} = 0.5$ m (case C, right). The combustion catalyst section is located between the dashed lines and the membrane section between the dotted lines.

throughput per unit cross-sectional area. Concluding, with a membrane length of 0.25-0.5 m and a CPO catalyst particle of about 1-3 mm excellent syngas selectivities can be obtained.

4.4.2 Presence of mass transfer limitations

In Table 4.9 average tube outlet compositions were presented and it was found that not all O_2 was converted indicating mass transfer limitations. To investigate the extent of mass transfer limitations in more detail, typical axial mole fraction profiles in the RFCMR are given in Figures 4.8 and 4.9 for case A and B with a particle diameter of 1 and 3 mm, respectively. These figures and in particular the axial profiles of the O_2 mole fraction indicate that there is indeed an influence of external mass transfer limitations, which are clearly smaller for smaller particles. Also internal mass transfer limitations play a role, confirmed by the low particle effectiveness factors (for reactions I-IV) presented in Figure 4.10. Despite the influence of both external and internal mass transfer limitations, the effect on the syngas yield is small, especially when considering the fact that gas phase reactions were not accounted for. When using a longer membrane (see Table 4.9, case C) or positioning some CPO catalyst outside the membrane section, equilibrium compositions could be easily achieved.

Since the outlet mole fractions are close to equilibrium (Table 4.9) and the influ-

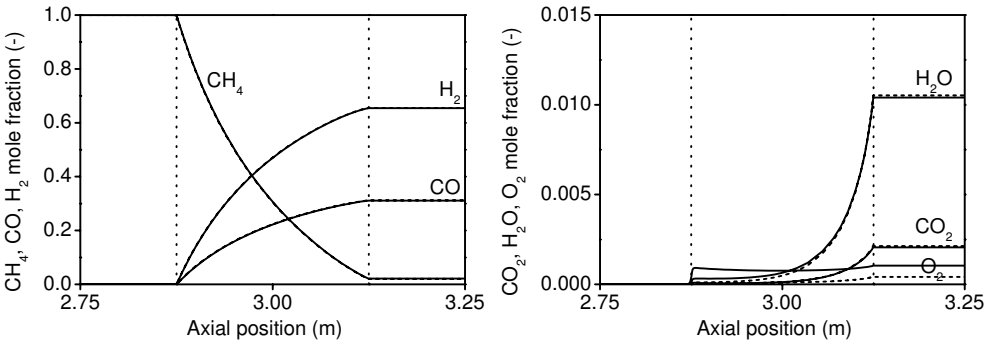

Figure 4.8: Axial gas phase (solid line) and catalyst surface (dashed line) mole fraction profiles in the RFCMR at the end of a forward semi-cycle with $d_\mathrm{p} = 1$ mm (case A). The membrane section is located between the dotted lines.

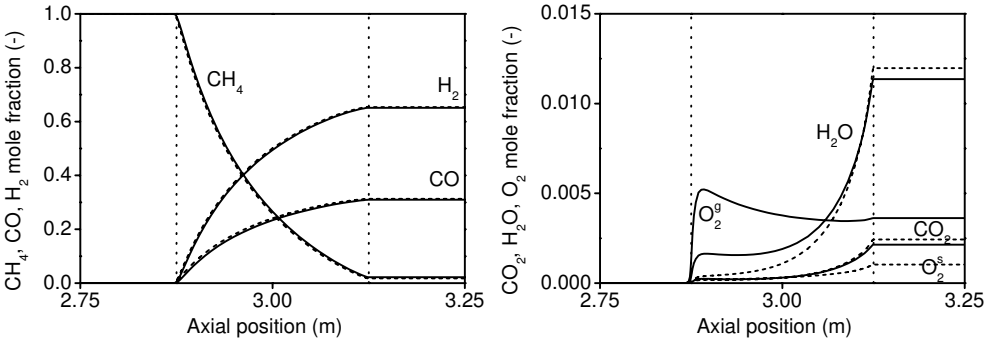

Figure 4.9: Axial gas phase (solid line) and catalyst surface (dashed line) mole fraction profiles in the RFCMR at the end of a forward semi-cycle with $d_\mathrm{p} = 3$ mm (case B). The membrane section is located between the dotted lines.

ence of mass transfer limitations on the syngas selectivities is very small as discussed above, the question arises wether it is really necessary to use a detailed description of the mass transfer from the gas bulk to the catalyst surface and inside the catalyst particle or that simply assuming local thermodynamic equilibrium in the gas bulk is already sufficiently accurate. This would reduce the number of equations to be solved considerably and thus the computational effort. Therefore, simulations were carried out for cases A and B in which it was assumed that the gas bulk is locally at equilibrium. In Figures 4.11 and 4.12 the axial profiles of the gas bulk mole fractions

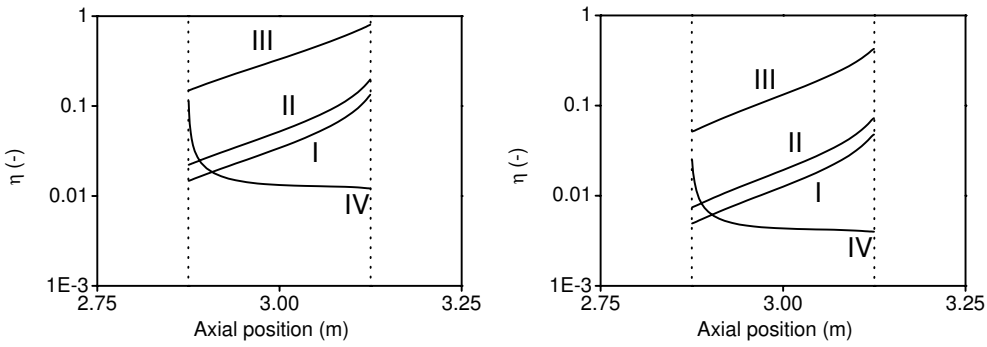

Figure 4.10: Axial profiles of the particle effectiveness factors of the CPO reaction rates in the RFCMR at the end of a forward semi-cycle with $d_p = 1$ mm (case A, left) and $d_p = 3$ mm (case B, right). The membrane section is located between the dotted lines.

are given for cases A and B, with and without mass transfer limitations. For case A, the gas bulk is indeed at local equilibrium due to the small particle diameters and a detailed description of the mass transfer is not required. For case B some differences can be discerned, but the gas bulk is still very close to local equilibrium and the differences are very small in view of the assumptions made in the modelling and the uncertainties in the kinetic rate expressions and with respect to the validity of a number of relations and physical properties used in the model.

4.4.3 Effect of the switching time and tube diameter

In the HSFM simulations discussed in section 4.3 it was found that the temperatures at the in- and outlet of the RFCMR are very low because of the assumed infinitely small switching times, but for longer switching times that are typically used in industrial practice and are required to minimise switching losses, the temperature at the outlet of the shell and tube might increase significantly during the semi-cycle. The increase in the outlet temperature should be small enough, to avoid the need for very expensive construction materials at the in- and outlets. For cases A-D (see Figure 4.5) the maximal tube outlet temperature was below about 600 K, which is still quite acceptable and also the (radial) differences between the tube and shell temperatures as well as the (axial) differences between the temperature profiles at the end of a

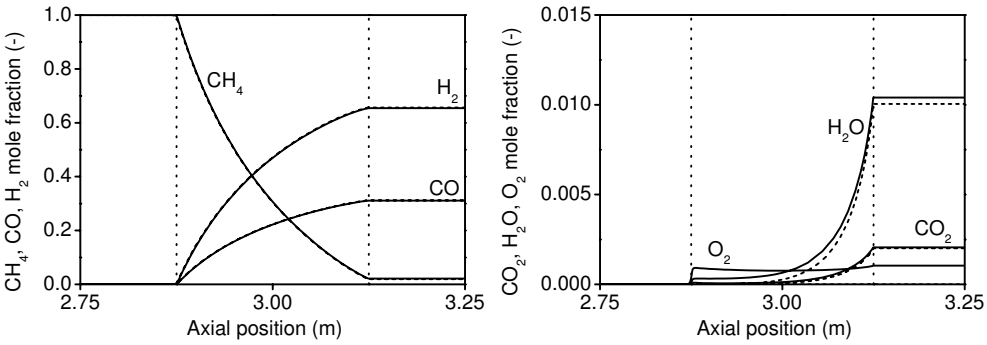

Figure 4.11: Axial gas bulk mole fraction profiles in the RFCMR at the end of a forward semi-cycle with (solid line) and without (dashed line) mass transfer limitations for case A. The membrane section is located between the dotted lines.

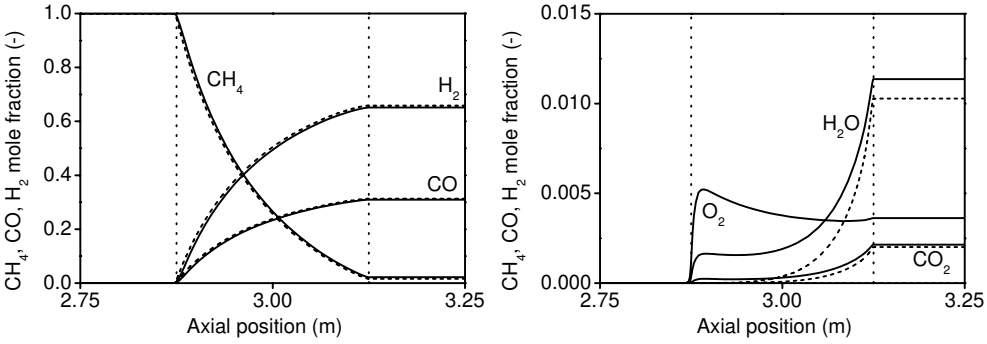

Figure 4.12: Axial gas bulk mole fraction profiles in the RFCMR at the end of a forward semi-cycle with (solid line) and without (dashed line) mass transfer limitations for case B. The membrane section is located between the dotted lines.

forward and backward semi-cycle were relatively small. The temperature profiles of cases A-D were obtained for a switching time of 300 s and a tube diameter of 2.5 cm. Obviously, when selecting longer switching times and/or larger tube diameters, the maximal tube outlet temperature will increase, because of the fact that the temperature profile is pushed further into the reactor and due to decreased heat transfer from the tube to the shell, respectively. This is illustrated in Figure 4.13 where the axial temperature profiles are shown for two cases similar to case B but with a switching time of 600 s and with a tube diameter of 5 cm. For both cases it is observed that

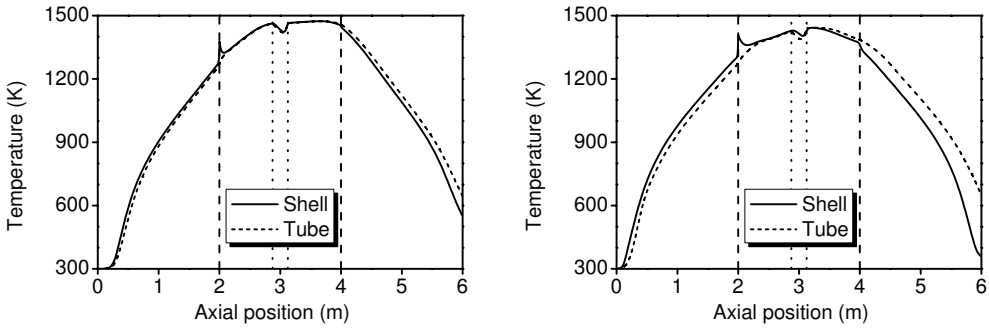

Figure 4.13: Axial temperature profiles in the RFCMR at the end of a forward cycle for case B with $d_t = 2.5$ cm and $t_{cycle} = 600$ s (left) and $d_t = 5$ cm and $t_{cycle} = 300$ s (right). The combustion catalyst section is located between the dashed lines and the membrane section between the dotted lines.

the tube outlet temperature is indeed higher, but still only about 700 K. Only when using even longer switching times and/or larger tube diameters, the maximal outlet temperature should be carefully considered.

4.4.4 Effect of CH_4 combustion in the O_2 compartment

For the HSFM simulations presented in the previous section it was observed that the temperature profile is not flat in the membrane section of the RFCMR, but that there are temperature peaks at the beginning and end of the membrane and a temperature drop in the centre. This can be explained by the changing gas composition along the axial direction of the the membrane and more specifically the CO_2 and H_2O mole fractions (see Figures 4.8 and 4.9), which indicate that in the centre of the membrane primarily CO and H_2 are produced and that locally heat is consumed, whereas at the end of the membrane section also significant amounts of CO_2 and H_2O are produced and therefore heat is released. In view of this heat release at the end of the membrane, the question arises if it is really necessary to combust some CH_4 in the O_2 compartment. Although in conventional reverse flow reactors the reaction heat is released at the beginning of the temperature plateau, whereas in the membrane section of the RFCMR reaction heat is released at the end of the plateau, the effect is more or less the same. Therefore, a simulation was performed with the operating conditions of case B, but without addition of CH_4 to the shell feed. The

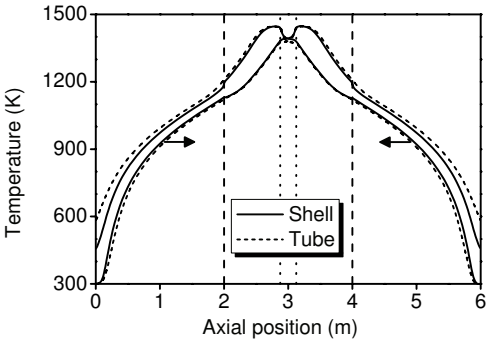

Figure 4.14: Axial temperature profiles in the RFCMR at the end of a forward (→) and backward (←) semi-cycle for case B with $w^{s}_{g,CH4} = 0$. The combustion catalyst section is located between the dashed lines and the membrane section between the dotted lines.

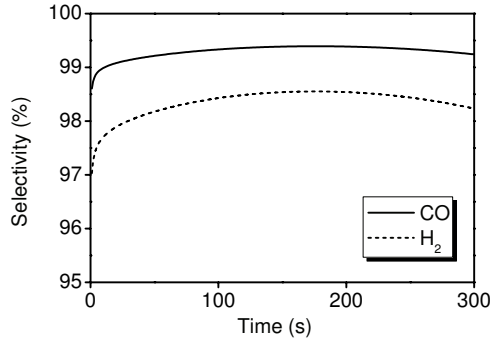

Figure 4.15: CO and H_2 selectivities at the tube outlet of the RFCMR as a function of time during a forward semi-cycle for case B with $w^{s}_{g,CH4} = 0$.

axial temperature profiles at the end of a semi-cycle are given in Figure 4.14 and the CO and H_2 selectivities are given in Figure 4.15 as a function of time. Indeed also without the addition of CH_4 to the O_2 feed, still a suitable temperature profile can be created and very high syngas selectivities can be achieved. Furthermore, if no CH_4 has to be combusted in the shell compartment, also no combustion catalyst is required, which might save on investment costs. However, high syngas selectivities will only be achieved if the temperature is high enough along the membrane and therefore not too high switching times can be allowed, depending on the membrane length and steepness of the temperature gradients, which limits the operation window. With the combustion of CH_4 in the O_2 compartment, the reverse flow section and the membrane section are separated, which simplifies both the design and operation. Also the combustion catalyst does not have to be very active (*i.e.* expensive), since the plateau temperature profile is primarily dependent on the length of the inert sections in the O_2 compartment. Concluding, combustion of a small amount of CH_4 in the O_2 compartment is preferred.

4.4.5 Evaluation of model assumptions

Finally the validity of two important modelling assumptions will be addressed, namely the neglect of gas phase accumulation terms (*i.e.* switching losses) and the 1-D modelling assuming negligible radial concentration gradients.

Switching losses

In the model equations the gas phase accumulation terms were neglected. For the cases considered in this work, the residence time in the tube compartment is about 13 s. So, for a switching time of 300 s, this means that about 4 % of the tube side output could be considered as switching losses due to unconverted CH_4 and combusted syngas. However, for a switching time of 600 s this already reduces to 2 %. The optimal switching time results from an economical optimisation balancing the switching losses and reactor volume.

1-D versus 2-D modelling

In this study a 1-D model was used, so that the effects of radial mass dispersion were not accounted for. To assess whether radial mass transfer limitations could affect the presented results, the modified Thiele modulus concept (Kuerten et al., 2004) was used. Furthermore, it was assumed that the CPO reaction rates are limited by the mass transfer rate from the gas bulk to the catalyst surface. In this case the modified Thiele modulus is given by:

$$\varphi = \frac{r_\mathrm{i}}{2}\sqrt{\frac{k_\mathrm{g}}{D_\mathrm{rad}}} \tag{4.14}$$

here, the radial mass dispersion is calculated according to Specchia et al. (1980):

$$D_\mathrm{rad} = \frac{d_\mathrm{p} v_\mathrm{g}}{8.65\left(1 + 19.4\left(\frac{d_\mathrm{p}}{2r_\mathrm{i}}\right)^2\right)} \tag{4.15}$$

From the correlation for the mass transfer coefficient proposed by Thoenes and Kramers (1958), see also Table 4.6, and using the simulation results of case B in Table 4.9, it was found that k_g has a typical value of about 0.1 and φ a typical value of 0.14. From Equation 4.3 it can then be calculated that $\eta = 0.99$, which indicates that there are hardly radial mass transfer limitations and that 1-D modelling constitutes a valid approach. For 1 mm particles the radial dispersion is smaller and thus the radial

mass transfer limitations become more pronounced, but still $\eta > 0.95$. Hence, for this study an extremely CPU demanding 2-D model, to accurately account for radial concentration gradients, is not required.

4.5 Conclusions

In this chapter the conceptual feasibility of the RFCMR concept with porous membranes for energy efficient syngas production was demonstrated. Detailed 1-D reactor models were developed with a detailed description of the heat and mass transfer processes and the relevant reaction kinetics involved. The reverse flow section of the RFCMR was designed with analytic relations from literature and HSFM simulations and it was shown that the addition of a small amount of H_2O to the O_2 feed is a key feature in the RFCMR concept to avoid runaways in the centre. Subsequently, simulations were carried out with the DM for different particle diameters, membrane lengths, tube diameters and switching times. It was found that by selecting the appropriate operating conditions the pure O_2 consumption can be reduced by at least 25 % compared to conventional processes and very high syngas selectivities (> 98 %) can be achieved, while fully integrating the recuperative heat exchange and avoiding hot spots and premixed feeds. Therefore, the RFCMR concept leads to a reduced number of smaller units via process intensification, making it a feasible and promising alternative to conventional processes.

Acknowledgement

The financial support of the Dutch Technology Foundation STW, the Energy research Centre of the Netherlands ECN and the Association of Industrial Advisory Council Members of the Dutch Institute for Catalysis Research VIRAN is gratefully acknowledged.

Nomenclature

A_j	Constant in the correlations for $\eta_\mathrm{j,g}$ and $\lambda_\mathrm{j,g}$
B	Parameter in the model of Zehner and Schlünder (1970)
B_0	Parameter in the Dusty Gas model, m^2
B_j	Constant in the correlations for $\eta_\mathrm{j,g}$ and $\lambda_\mathrm{j,g}$

B^{ou}	Parameter used in the Maxwell-Stefan description of multi-component mass transfer
Bi	Apparent Biot number, $\alpha_{\mathrm{w,eff}} r_{\mathrm{i}} / \lambda_{\mathrm{re}}$
Bi_{f}	Fluid-wall Biot number, $\alpha_{\mathrm{wf}} r_{\mathrm{i}} / \lambda_{\mathrm{rf}}$
Bi_{s}	Solid-wall Biot number, $\alpha_{\mathrm{ws}} r_{\mathrm{i}} / \lambda_{\mathrm{rs}}$
c_{j}	Concentration of species j, mol/m^3
C_{j}	Constant in the correlations for $\eta_{\mathrm{j,g}}$ and $\lambda_{\mathrm{j,g}}$
C_{p}	Heat capacity, J/kg/K
d_{p}	Particle diameter, m
d_{t}	Tube diameter, m
D_{j}	Constant in the correlations for $\eta_{\mathrm{j,g}}$ and $\lambda_{\mathrm{j,g}}$
$\hat{D}_{\mathrm{j}}$	Eigenvalues of the matrix of binary diffusion coefficients, m^2/s
$D_{\mathrm{i,j}}$	Binary diffusion coefficient in the molar average reference frame, m^2/s
$D^0_{\mathrm{i,j}}$	Binary diffusion coefficient in the mass average reference frame, m^2/s
$\overline{D}_{\mathrm{j}}$	Diffusivity of species j in a mixture, m^2/s
D_{ax}	Axial dispersion coefficient, m^2/s
D_{eff}	Effective diffusivity, m^2/s
D_{KN}	Knudsen diffusivity, m^2/s
D_{rad}	Radial diffusivity, m^2/s
e_{p}	Emissivity of a particle
e_{wall}	Emissivity of the wall
E_{a}	Activation energy, J/mol
E_{j}	Constant in the correlations for $\eta_{\mathrm{j,g}}$ and $\lambda_{\mathrm{j,g}}$
$\Delta g^{\ominus}_{\mathrm{f,j}}$	Gibbs' free energy of formation of species j, J/mol
$\Delta G^{\ominus}_{\mathrm{r}}$	Gibbs' free energy of reaction, J/mol
H_{j}	Enthalpy of species j, J/mol
ΔH_{r}	Reaction heat, J/mol
$\mathbf{I}$	Identity matrix
j_{j}	Mass flux of species j, kg/m^2/s
J	Permeation rate, mol/m^2/s
k_{∞}	Reaction rate constant, 1/s
$\hat{k}_{\mathrm{j}}$	Eigenvalues of the matrix of multi-component mass transfer coefficients, m/s
$k^{\bullet}$	Finite flux mass transfer coefficient, m/s

k_g	Gas-to-particle mass transfer coefficient, m/s
k_η	Linearised reaction rate constant, 1/s
K_0	Parameter in the Dusty Gas model, m
K_eq	Equilibrium constant
L_inert	Length inert section, m
L_membrane	Membrane length, m
L_reactor	Reactor length, m
M	Parameter in the model of Zehner and Schlünder (1970)
M_j	Molar weight of species j, kg/mol
$\langle M \rangle$	Average molar weight, kg/mol
N_f	Parameter in the model of Dixon and Creswell (1979)
N_s	Parameter in the model of Dixon and Creswell (1979)
Nu	Dimensionless Nusselt number, $\alpha_{\mathrm{g-s}} d_\mathrm{p}/\lambda_\mathrm{g}$
Nu_w	Apparent wall Nusselt number, $\alpha_{\mathrm{w,eff}} d_\mathrm{p}/\lambda_\mathrm{g}$
Nu_wf	Wall-to-fluid Nusselt number, $\alpha_\mathrm{wf} d_\mathrm{p}/\lambda_\mathrm{g}$
p	Parameter in axial heat dispersion coefficient of Gunn and Misbah (1993)
p	Pressure, Pa
p_j	Partial pressure of species j, Pa
Pe_ax	Dimensionless Péclet number for axial heat dispersion, $\rho_\mathrm{g} v_\mathrm{g} d_\mathrm{p} C_\mathrm{p,g}/\lambda_\mathrm{ax}$
Pe_er	Effective radial Péclet number, $\rho_\mathrm{g} v_\mathrm{g} r_\mathrm{i} C_\mathrm{p,g}/\lambda_\mathrm{er}$
Pe_rf	Radial fluid Péclet number, $\rho_\mathrm{g} v_\mathrm{g} r_\mathrm{i} C_\mathrm{p,g}/\lambda_\mathrm{rf}$
Pr	Dimensionless Prandtl number, $C_\mathrm{p,g}\eta_\mathrm{g}/\lambda_\mathrm{g}$
r_j	Reaction rate of species j, kg/m^3/s
r_i	Inner tube radius, m
r_o	Outer tube radius, m
r_p	Pore radius, m
R	Reaction rate, mol/m^3/s
R_eff	Effective reaction rate, mol/m^3/s
R_g	Gas constant, 8.314 J/mol/K
Re	Dimensionless Reynolds number, $\rho_\mathrm{g} v_\mathrm{g} d_\mathrm{p}/\eta_\mathrm{g}$
S	Selectivity
s_cell	Unit cell length, m
Sc	Dimensionless Schmidt number, $\eta_\mathrm{g}/\rho_\mathrm{g}/D$
t	Time, s

T	Temperature, K
T_{feed}	Feed temperature, K
ΔT_{ad}	Adiabatic temperature rise, K
T_{plateau}	Plateau temperature, K
Y	Dummy variable
v	Superficial velocity, m/s
v_{front}	Front velocity, m/s
w_{j}	Weight fraction of species j
x_{j}	Mole fraction of species j
z	Spatial coordinate, m

Greek symbols

$\alpha_{\text{bed-wall}}$	Overall wall-to-bed heat transfer coefficient, J/m^2/K/s
$\alpha_{\text{g-s}}$	Gas-to-solid heat transfer coefficient, J/m^2/K/s
α_{rad}	Wall-to-bed heat transfer coefficient due to radiation, J/m^2/K/s
$\alpha^{\text{s-tw}}$	Wall-to-shell heat transfer coefficient, J/m^2/K/s
$\alpha^{\text{t-tw}}$	Wall-to-tube heat transfer coefficient, J/m^2/K/s
$\alpha_{\text{w,eff}}$	Apparent wall heat transfer coefficient, J/m^2/K/s
α_{wf}	Wall-to-fluid heat transfer coefficient, J/m^2/K/s
α_{ws}	Wall-to-solid heat transfer coefficient, J/m^2/K/s
ϵ	Porosity
δ_{m}	Membrane toplayer thickness, m
η	Particle effectiveness factor
η	Viscosity, kg/m/s
κ_{r}	Parameter in the model of Zehner and Schlünder (1970)
κ_{s}	Parameter in the model of Zehner and Schlünder (1970)
λ	Thermal conductivity, J/m/K/s
λ_{ax}	Axial thermal conductivity, J/m/K/s
λ_{bed}	Thermal conductivity of a quiescent packed bed, J/m/K/s
λ_{eff}	Effective thermal conductivity, J/m/K/s
λ_{er}	Effective radial thermal conductivity, J/m/K/s
λ_{r}	Parameter in the model of Zehner and Schlünder (1970)
$\lambda_{\text{r,s}}$	Parameter in the model of Zehner and Schlünder (1970)
λ_{rf}	Radial thermal conductivity of the fluid, J/m/K/s

λ_{rs}	Radial thermal conductivity of the solid, J/m/K/s
ν_{j}	Molar volume of species j used in the calculation of binary diffusion coefficients
ν_{j}	Stoichiometric number of species j in a reaction
ρ	Density, kg/m^3
ρ_{bulk}	Packed bed bulk density, kg/m^3
σ	Stefan-Boltzmann constant, $5.67 \cdot 10^{-8}$ W/m^2/K^4
τ	Tortuosity
φ	Thiele modulus
$\varphi^{\eta}_{\mathrm{j,k}}$	Parameter used in the calculation of the mixture viscosity
$\varphi^{\lambda}_{\mathrm{j,k}}$	Parameter used in the calculation of the mixture thermal conductivity

Subscripts

I	CH_4 combustion
II	H_2O reforming of CH_4
III	CO_2 reforming of CH_4
IV	Water gas shift reaction
eq	At equilibrium
in	Inlet
g	Gas
out	Outlet
s	Solid

Superscripts

$\ominus$	At standard pressure (10^5 Pa)
s	Shell
t	Tube
tw	Tube wall

Bibliography

Aasberg-Petersen, K., Bak Hansen, J. H., Christensen, T. S., Dybkjaer, I., Seier Christensen, P., Stub Nielsen, C., Winter Madsen, S. E. L., Rostrup-Nielsen, J. R., "Technologies for large scale gas conversion", Applied Catalysis A: General, 221(1-2), 379–387 (2001)

Bird, R. B., Stewart, W. E., Lightfoot, E. N., "Transport Phenomena", 2nd Edition, John Wiley and Sons, New York (2002)

Brejc, M., Supp, E., "Non-catalytic partial oxidation and special gasification process for higher-boiling hydrocarbons", in "Ullmanns Encyclopedia of Industrial Chemistry", Elvers, B., Hawkins, S., Ravenscroft, M., Rounsaville, J. F., Shulz, G. Eds., 5th Edition, Vol. A12, VCH Verlagsgesellschaft, Weinheim, 204–214 (1989)

Daubert, T. E., Danner, R. P., "Data Compilation Tables of Properties of Pure Compounds", American Institute of Chemical Engineers, New York (1985)

Dixon, A. G., Creswell, D. L., "Theoretical prediction of effective heat-transfer parameters in packed-beds", AICHE Journal, 25(4), 663 (1979)

Edwards, M. F., Richardson, J. F., "Gas dispersion in packed beds", Chemical Engineering Science, 23(2), 109–123 (1968)

Ergun, S., "Fluid flow through packed columns", Chemical Engineering Progress, 48(2), 89–94 (1952)

Froment, G. F., "Reverse flow operation of fixed bed catalytic reactors", in "Unsteady State Processes in Catalysis", Matros, Y. S. Ed., VSP, Utrecht, 57–89 (1990)

Gosiewski, K., Bartmann, U., Moszcynski, M., Mleczko, L., "Effect of the intraparticle mass transport limitations on temperature profiles and catalytic performance of the reverse-flow reactor for the partial oxidation of methane to synthesis gas", Chemical Engineering Science, 54(20), 4589–4602 (1999)

Gunn, D. J., "Transfer of heat or mass to particles in fixed and fluidized beds", International Journal of Heat and Mass Transfer, 21(4), 467–476 (1978)

Gunn, D. J., Misbah, M. M. A., "Bayesian estimation of heat transport parameters in fixed beds", International Journal of Heat and Mass Transfer, 36(8), 2209–2221 (1993)

Kuerten, U., van Sint Annaland, M., Kuipers, J. A. M., "Oxygen distribution in packed bed membrane reactors for partial oxidation systems and its effect on product selectivity", International Journal of Chemical Reactor Engineering, 2, A24 (2004)

Mason, E. A., Malinauskas, A. P., "Gas Transport in Porous Media: The Dusty Gas Model", Elsevier, Amsterdam (1983)

Matros, Y. S., Bunimovich, G. A., "Reverse-flow operation in fixed bed catalytic reactors", Catalysis Reviews-Science and Engineering, 38(1), 1–68 (1996)

Nieken, U., Kolios, G., , Eigenberger, G., "Fixed-bed reactors with periodic flow reversal: experimental results for catalytic combustion", Catalysis Today, 20(3), 335–350 (1994)

Nieken, U., Kolios, G., Eigenberger, G., "Limiting cases and approximate solutions for fixed-bed reactors with periodic flow reversal", AIChE Journal, 41(8), 1915 (1995)

Reid, R. C., Prausnitz, J. M., Poling, B. E., "The Properties of Gases and Liquids", 4$^{\text{th}}$ Edition, McGraw-Hill, Inc., New York (1987)

Specchia, V., Baldi, G., Sicardi, S., "Heat transfer in packed bed reactors with one phase flow", Chemical Engineering Communications, 4(2-3), 361–380 (1980)

Stewart, W. E., Prober, R., "Matrix calculation of multicomponent mass transfer in isothermal systems", Industrial & Engineering Chemistry Fundamentals, 3(3), 224–235 (1964)

Taylor, R., Krishna, R., "Multicomponent Mass Transfer", Wiley Series in Chemical Engineering, New York (1993)

Thoenes, D., Kramers, H., "Mass transfer from spheres in various regular packings to a flowing fluid", Chemical Engineering Science, 8(3-4), 271–283 (1958)

Toor, H. L., "Solution of the linearized equations of multicomponent mass transfer: I", AIChE Journal, 10(4), 448–455 (1964a)

Toor, H. L., "Solution of the linearized equations of multicomponent mass transfer: II. matrix methods", AIChE Journal, 10(4), 460–465 (1964b)

van Sint Annaland, M., "A Novel Reverse Flow Reactor Coupling Endothermic and Exothermic Reactions", Ph.D. thesis, University of Twente, Enschede, The Netherlands (2000)

van Sint Annaland, M., Scholts, H. A. R., Kuipers, J. A. M., van Swaaij, W. P. M., "A novel reverse flow reactor coupling endothermic and exothermic reactions. Part I:

Comparison of reactor configurations for irreversible endothermic reactions", Chemical Engineering Science, 57(5), 833–854 (2002)

VDI Heat Atlas, VDI-Verlag (1993)

Vortmeyer, D., "Packed bed thermal dispersion models and consistent sets of coefficients", Chemical Engineering and Processing, 26(3), 263–268 (1989)

Westerterp, K. R., van Swaaij, W. P. M., Beenackers, A. A. C. M., "Chemical Reactor Design and Operation", John Wiley and Sons, New York (1984)

Zehner, P., Schlünder, E. U., "Wärmeleitfähigkeit von Schüttingen bei Mässigen Temperaturen", Chemie Ingenieur Technik, 42(14), 933–941 (1970)

4.A Maxwell-Stefan description of gas-to-particle mass transfer

The mass transfer rates (j) from the gas bulk to the catalyst surface appearing in the mass conservation equations in Tables 4.1 and 4.2 have been calculated via the method of Toor (1964a,b) and Stewart and Prober (1964), see also Taylor and Krishna (1993, p214-215).

$$(j) = \left[k_{\mathrm{g}}^{\bullet}\right](c_{\mathrm{g}} - c_{\mathrm{s}}) \tag{4.16}$$

The matrix of finite flux mass transfer coefficients $\left[k_{\mathrm{g}}^{\bullet}\right]$ is calculated with Sylvesters' expansion formula (Taylor and Krishna, 1993, p188)

$$\left[k_{\mathrm{g}}^{\bullet}\right] = \sum_{\mathrm{i}=1}^{\mathrm{m}} \hat{k}_{\mathrm{g,i}} \left(\prod_{\substack{\mathrm{j}=1 \\ \mathrm{j}\neq\mathrm{i}}}^{\mathrm{m}} \left([D] - \hat{D}_{\mathrm{j}}\mathbf{I} \right) \Big/ \prod_{\substack{\mathrm{j}=1 \\ \mathrm{j}\neq\mathrm{i}}}^{\mathrm{m}} \left(\hat{D}_{\mathrm{i}} - \hat{D}_{\mathrm{j}} \right) \right) \tag{4.17}$$

$\hat{k}_{\mathrm{g,i}}$ are the Eigenvalues containing the matrix of multi-component mass transfer coefficients $[k_{\mathrm{g}}]$, which have been calculated with the correlation by Thoenes and Kramers (1958).

$$[k_{\mathrm{g}}] = \frac{0.81}{\varepsilon_{\mathrm{g}}} v_{\mathrm{g}} Re^{-1/2} [Sc]^{-2/3} \tag{4.18}$$

The matrix of Schmidt numbers $[Sc]$ is calculated from the inverse of the matrix with the multicomponent diffusion coefficients in the mass average reference frame $[D^{\mathrm{o}}]$:

$$[Sc] = \frac{\eta_{\mathrm{g}}}{\rho_{\mathrm{g}}} [D^{\mathrm{o}}]^{-1} \tag{4.19}$$

$[D^{\mathrm{o}}]$ is calculated from the matrix with the binary diffusion coefficients in the molar average reference frame $[D]$ (Taylor and Krishna, 1993, p56), which are estimated according to Reid et al. (1987):

$$[D^{\mathrm{o}}] = [B^{\mathrm{ou}}]\,[w]\,[x]^{-1}\,[D]\,[x]\,[w]^{-1}\,[B^{\mathrm{ou}}]^{-1} \tag{4.20}$$

where

$$B^{\mathrm{ou}}_{\mathrm{i,k}} = \mathbf{I}_{\mathrm{i,k}} - \mathrm{w_i}\left(1 - \frac{\mathrm{w_n x_k}}{\mathrm{w_k x_n}}\right) \tag{4.21}$$

4.B Heat transfer models

The thermal conductivity of the stagnant packed bed is calculated according to the model of Zehner and Schlünder (1970) given in Table 4.10. The wall-to-bed heat transfer was calculated using the correlations proposed by Dixon and Creswell (1979) detailed in Table 4.11.

Table 4.10: Thermal conductivity of a stagnant packed bed according to Zehner and Schlünder (1970).

$$\lambda_{\mathrm{bed}} = \lambda_{\mathrm{r,s}}\sqrt{1-\varepsilon_{\mathrm{g}}} + \lambda_{\mathrm{g}}\left(1-\sqrt{1-\varepsilon_{\mathrm{g}}}\right)\left(1+\varepsilon_{\mathrm{g}}\kappa_{\mathrm{r}}\right)$$

$$\lambda_{\mathrm{r,s}} = \frac{2\lambda_{\mathrm{g}}}{M}\left(\frac{B\left(\kappa_{\mathrm{s}}+\kappa_{\mathrm{r}}-1\right)}{M^2\kappa_{\mathrm{s}}}\ln\left(\kappa_{\mathrm{s}}+\frac{\kappa_{\mathrm{r}}}{B}\right)+\frac{(B+1)}{2B}\left(\kappa_{\mathrm{r}}-B\right)-\frac{(B-1)}{M}\right)$$

$$M = \frac{\kappa_{\mathrm{s}}+\kappa_{\mathrm{r}}-B}{\kappa_{\mathrm{s}}} \qquad B = 1.25\left(\frac{1-\varepsilon_{\mathrm{g}}}{\varepsilon_{\mathrm{g}}}\right)^{\frac{10}{9}}$$

$$\kappa_{\mathrm{s}} = \frac{\lambda_{\mathrm{s}}}{\lambda_{\mathrm{g}}} \qquad \kappa_{\mathrm{r}} = \frac{\lambda_{\mathrm{r}}}{\lambda_{\mathrm{g}}}$$

$$\lambda_{\mathrm{r}} = \frac{4e_{\mathrm{p}}}{2-e_{\mathrm{p}}}\sigma T^3 d_{\mathrm{p}}$$

Table 4.11: Wall-to-bed heat transfer according to Dixon and Creswell (1979).

$$\frac{1}{\alpha_{\mathrm{bed-wall}}} = \frac{1}{\frac{Nu_{\mathrm{w}}\lambda_{\mathrm{g}}}{d_{\mathrm{p}}} + \alpha_{\mathrm{rad}}} + \frac{r_{\mathrm{i}}Pe_{\mathrm{er}}}{3RePr\lambda_{\mathrm{g}}}\frac{Bi+3}{Bi+4} \qquad \alpha_{\mathrm{rad}} = \frac{4\sigma T^3}{\frac{1}{e_{\mathrm{wall}}} + \frac{1}{e_{\mathrm{p}}} - 1}$$

$$Bi_{\mathrm{f}} = \frac{Nu_{\mathrm{wf}}r_{\mathrm{i}}Pe_{\mathrm{rf}}}{d_{\mathrm{p}}RePr} \qquad Bi_{\mathrm{s}} = 2.41 + 0.156\left(\frac{2r_{\mathrm{i}}}{d_{\mathrm{p}}} - 1\right)^2$$

$$Bi = \frac{r_{\mathrm{i}}Nu_{\mathrm{w}}Pe_{\mathrm{er}}}{d_{\mathrm{p}}RePr} \qquad Pe_{\mathrm{rf}} = \frac{12}{1 + 8\frac{\varepsilon_{\mathrm{g}}}{RePr}}$$

$$Nu_{\mathrm{wf}} = \left(1 - \frac{d_{\mathrm{p}}}{2r_{\mathrm{i}}}\right)Re^{0.6}Pr^{1/3} \qquad Nu = \text{see Table 4.6}$$

If $Re > 50$:

$$Nu_{\mathrm{w}} = \frac{Bi_{\mathrm{f}}d_{\mathrm{p}}RePr}{r_{\mathrm{i}}Pe_{\mathrm{er}}}$$

$$Pe_{\mathrm{er}} = \frac{1}{\frac{1}{Pe_{\mathrm{rf}}} + \frac{\lambda_{\mathrm{bed}}}{\lambda_{\mathrm{g}}RePr}\frac{(Bi_{\mathrm{f}}+4)}{Bi_{\mathrm{f}}\left(\frac{8}{N_{\mathrm{s}}} + \frac{Bi_{\mathrm{s}}+4}{Bi_{\mathrm{s}}}\right)}}$$

$$N_{\mathrm{s}} = 1.5\left(1-\varepsilon_{\mathrm{g}}\right)\left(\frac{2r_{\mathrm{i}}}{d_{\mathrm{p}}}\right)^2\frac{\lambda_{\mathrm{g}}}{\lambda_{\mathrm{bed}}}\frac{1}{\frac{1}{Nu} + \frac{\lambda_{\mathrm{g}}}{10\lambda_{\mathrm{s}}}}$$

If $Re < 50$:

$$Nu_{\mathrm{w}} = \frac{Bi_{\mathrm{s}}d_{\mathrm{p}}RePr}{r_{\mathrm{i}}Pe_{\mathrm{er}}}$$

$$Pe_{\mathrm{er}} = \frac{1}{\frac{1}{Pe_{\mathrm{rf}}Bi_{\mathrm{s}}}\frac{(Bi_{\mathrm{s}}+4)}{\left(\frac{8}{N_{\mathrm{f}}} + \frac{Bi_{\mathrm{f}}+4}{Bi_{\mathrm{f}}}\right)} + \frac{\lambda_{\mathrm{bed}}}{\lambda_{\mathrm{g}}RePr}}$$

$$N_{\mathrm{f}} = 1.5\left(1-\varepsilon_{\mathrm{g}}\right)\left(\frac{2r_{\mathrm{i}}}{d_{\mathrm{p}}}\right)^2\frac{Pe_{\mathrm{rf}}}{RePr}\frac{1}{\frac{1}{Nu} + \frac{\lambda_{\mathrm{g}}}{10\lambda_{\mathrm{s}}}}$$

4.C Physical properties: equilibrium constants, viscosity, thermal conductivity, heat capacity and diffusivity

The equilibrium constants of the steam and dry reforming of CH_4 and the water-gas-shift reactions in Table 4.3 were calculated from the Gibbs' free energy of reaction:

$$K_{\mathrm{eq}} = exp\left(-\frac{\Delta G_{\mathrm{r}}^{\ominus}}{RT}\right) \tag{4.22}$$

The Gibbs' free energy of reaction was calculated from the Gibbs' free energy of formation of the reacting species (see Chapter 2):

$$\Delta G_{\mathrm{r}}^{\ominus} = \sum_{\mathrm{j}} \nu_{\mathrm{j}} \Delta g_{\mathrm{f,j}}^{\ominus} \tag{4.23}$$

Because the Gibbs' free energy of reactions II-IV have an almost linear dependence on temperature and to reduce computational efforts, they were fitted as a function of temperature:

$$\begin{aligned} \Delta G_{\mathrm{r,II}}^{\ominus} &= -2.5317 \cdot 10^2 T + 2.2569 \cdot 10^5 \\ \Delta G_{\mathrm{r,III}}^{\ominus} &= -2.8117 \cdot 10^2 T + 2.5639 \cdot 10^5 \\ \Delta G_{\mathrm{r,IV}}^{\ominus} &= 2.8000 \cdot 10^1 T - 3.0699 \cdot 10^4 \end{aligned} \tag{4.24}$$

The mixture viscosity was calculated according to Wilke's method (Reid et al., 1987):

$$\eta_{\mathrm{g}} = \sum_{\mathrm{j=1}}^{\mathrm{N}} \frac{x_{\mathrm{j,g}} \eta_{\mathrm{j,g}}}{\sum\limits_{\mathrm{k=1}}^{\mathrm{N}} x_{\mathrm{k,g}} \varphi_{\mathrm{j,k}}^{\eta}} \tag{4.25}$$

where:

$$\varphi_{\mathrm{j,k}}^{\eta} = \frac{\left(1 + \sqrt{\frac{\eta_{\mathrm{j}}}{\eta_{\mathrm{k}}}} \left(\frac{M_{\mathrm{k}}}{M_{\mathrm{j}}}\right)^{0.25}\right)^2}{\sqrt{8 + 8\frac{M_{\mathrm{j}}}{M_{\mathrm{k}}}}} \tag{4.26}$$

The component viscosities were calculated using the data provided by Daubert and Danner (1985):

$$\eta_{\mathrm{j,g}} = \frac{A_{\mathrm{j}} T^{\mathrm{B_j}}}{1 + \frac{C_{\mathrm{j}}}{T} + \frac{D_{\mathrm{j}}}{T^2}} \tag{4.27}$$

Table 4.12: Constants used in the calculation of the component viscosity taken from Daubert and Danner (1985).

	A_j	B_j	C_j	D_j
$CH_{4,g}$	$5.2546 \cdot 10^{-7}$	$5.9006 \cdot 10^{-1}$	$1.0567 \cdot 10^{2}$	0
CO_g	$1.1127 \cdot 10^{-6}$	$5.3380 \cdot 10^{-1}$	$9.4700 \cdot 10^{1}$	0
$CO_{2,g}$	$2.1480 \cdot 10^{-6}$	$4.6000 \cdot 10^{-1}$	$2.9000 \cdot 10^{2}$	0
$H_{2,g}$	$1.5600 \cdot 10^{-7}$	$7.0600 \cdot 10^{-1}$	$-5.8700 \cdot 10^{0}$	$2.1000 \cdot 10^{2}$
H_2O_g	$6.1839 \cdot 10^{-7}$	$6.7779 \cdot 10^{-1}$	$8.4723 \cdot 10^{2}$	$-7.3930 \cdot 10^{4}$
$N_{2,g}$	$6.5592 \cdot 10^{-7}$	$6.0810 \cdot 10^{-1}$	$5.4714 \cdot 10^{1}$	0
$O_{2,g}$	$8.0380 \cdot 10^{-7}$	$6.0478 \cdot 10^{-1}$	$7.0300 \cdot 10^{1}$	0

The related coefficients have been reproduced in Table 4.12.

The mixture thermal conductivity was also calculated with Wilke's method (Reid et al., 1987):

$$\lambda_g = \sum_{j=1}^{N} \frac{x_{j,g} \lambda_{j,g}}{\sum_{k=1}^{N} x_{k,g} \varphi_{j,k}^{\lambda}} \tag{4.28}$$

where:

$$\varphi_{j,k}^{\lambda} = \frac{\left(1 + \sqrt{\frac{\lambda_j}{\lambda_k}} \left(\frac{M_k}{M_j}\right)^{0.25}\right)^2}{\sqrt{8 + 8\frac{M_j}{M_k}}} \tag{4.29}$$

The component thermal conductivities were again calculated according to Daubert and Danner (1985):

$$\lambda_{j,g} = \frac{A_j T^{B_j}}{1 + \frac{C_j}{T} + \frac{D_j}{T^2}} \tag{4.30}$$

The related coefficients have been summarised in Table 4.13.

The mixture heat capacity was calculated via:

$$C_{p,g} = \sum_{j=1}^{N} w_{j,g} C_{p,j,g} \tag{4.31}$$

Table 4.13: Constants used in the calculation of the component thermal conductivity taken from Daubert and Danner (1985).

	A_j	B_j	C_j	D_j
$CH_{4,g}$	$6.3252 \cdot 10^{3}$	$4.3041 \cdot 10^{-1}$	$7.7040 \cdot 10^{8}$	$-3.8725 \cdot 10^{10}$
CO_g	$8.3900 \cdot 10^{-4}$	$6.4090 \cdot 10^{-1}$	$8.6050 \cdot 10^{1}$	0
$CO_{2,g}$	$3.6900 \cdot 10^{0}$	$-3.8380 \cdot 10^{-1}$	$9.6400 \cdot 10^{2}$	$1.8600 \cdot 10^{6}$
$H_{2,g}$	$2.4570 \cdot 10^{-3}$	$7.4440 \cdot 10^{-1}$	$9.0000 \cdot 10^{0}$	0
H_2O_g	$2.1606 \cdot 10^{-3}$	$7.6839 \cdot 10^{-1}$	$3.9405 \cdot 10^{3}$	$-4.4534 \cdot 10^{5}$
$N_{2,g}$	$3.3143 \cdot 10^{-4}$	$7.7220 \cdot 10^{-1}$	$1.6323 \cdot 10^{1}$	0
$O_{2,g}$	$4.9430 \cdot 10^{-4}$	$7.3400 \cdot 10^{-1}$	$7.0000 \cdot 10^{1}$	0

The component heat capacities were calculated as a function of temperature via (Daubert and Danner, 1985):

$$C_{p,j} = \frac{1}{1000 M_j} \left[A_j + B_j \left(\frac{C_j}{T \sinh\left(\frac{C_j}{T}\right)} \right)^2 + D_j \left(\frac{E_j}{T \cosh\left(\frac{E_j}{T}\right)} \right)^2 \right] \tag{4.32}$$

The related coefficients are identical to those used for the calculation of the component enthalpies and entropies, see Chapter 2, Appendix 2.A, Table 2.2.

The binary diffusion coefficients were estimated via Fuller's method (Reid et al., 1987):

$$D_{j,k} = \frac{1}{\sqrt{\frac{2000}{\frac{1}{M_j} + \frac{1}{M_k}}}} \frac{0.0143 T^{1.75}}{p \left(\nu_j^{1/3} + \nu_k^{1/3} \right)^2} \tag{4.33}$$

The molar volumes ν_j of the relevant species have been listed in Table 4.14.

Table 4.14: Molar volumes used in the calculation of the binary diffusion coefficients (Reid et al., 1987).

ν_{CH_4}	ν_{CO}	ν_{CO_2}	ν_{H_2}	ν_{H_2O}	ν_{O_2}
25.14	18	26.9	6.12	13.1	16.3

The physical properties of Al_2O_3 were used to represent the inert Al_2O_3 particles and the Pt/Al_2O_3 combustion and CPO catalyst and are given in Table 4.15.

Table 4.15: Physical properties of Al_2O_3.

$C_{p,s}$	$4.33 \cdot 10^2 + 1.94T - 1.71 \cdot 10^{-3}T^2$	
	$+6.94 \cdot 10^{-7}T^3 - 1.03 \cdot 10^{-10}T^4$	Daubert and Danner (1985)
e_p	$6.34 \cdot 10^{-4}T + 1.14$	VDI Heat Atlas (1993)
λ_s	$33.2\exp(-1.3310^{-3})$	Daubert and Danner (1985)

CHAPTER 5

Experimental Demonstration of the RFCMR Concept with Porous Membranes

Abstract

To demonstrate the technical feasibility of the Reverse Flow Catalytic Membrane Reactor concept with porous membranes, a demonstration unit was constructed. Prior to testing this demonstration unit, different CPO catalysts and ceramic porous membranes were tested in an isothermal membrane reactor in order to find the most optimal catalyst and membrane to be used in the demonstration unit. Furthermore, a gas tight sealing between the ceramic membrane and ceramic support tubes was developed, which could withstand sufficiently high pressure differences and temperatures. In the isothermal membrane reactor experiments were performed with different catalysts and different operating conditions and it was shown that with a Rh/Al_2O_3 catalyst very high syngas selectivities could be achieved, which were very close to equilibrium. The demonstration unit was first tested as a conventional reverse flow reactor to determine the optimal operating conditions of the air compartment (air was used instead of O_2 for safety reasons) of the RFCMR with respect to the air flow rate and CH_4 inlet fraction. It was found that radial heat losses greatly affect the reactor behaviour, as expected, and that as a result significantly higher flow rates and CH_4 inlet fractions had to be used than would be required for an industrial scale reactor to establish the desired trapezoidal temperature profile. A reactor model was developed that included a detailed description of the insulation layer with which the axial temperature profiles could be very well described, without using any fitting parameters. Because of the fragility and rigidness of the Al_2O_3 support tubes and ceramic porous membranes it was very difficult to implement these in the demonstration unit, especially because of the length of the membrane and the two supporting tubes and the corresponding mechanical stresses. Therefore, as an alternative, a metal filter was used, consisting of a tube in which a number of holes were made by a laser. In the demonstration unit experiments were carried out at different operating conditions and it was shown that without using any compensatory heating to counteract radial heat losses very high syngas selectivities (up to 95 %) could be achieved, higher than typically encountered in industrial practice for conventional processes. Furthermore, no hot spots were observed in the axial temperature profiles, indicating safe reactor

Parts of this chapter are based on the paper:
Smit, J., Bekink, G.J, van Sint Annaland, M., and Kuipers, J.A.M., A Reverse Flow Catalytic Membrane Reactor for the production of syngas: an experimental study, International Journal of Chemical Reactor Engineering, 3, A12 (2005)

operation. The experimental results could be very well described with the developed reactor model, although the measured syngas selectivities were slightly lower than predicted by the model. The experimental results clearly demonstrate the technical feasibility and great potential of the RFCMR concept for energy efficient syngas production, despite the fact that the on-stream time of the demonstration unit was limited to about 12 hours due to cokes formation on the Al_2O_3 particles in the support tubes and because of fouling of the filter.

5.1 Introduction

In previous chapters the Reverse Flow Catalytic Membrane Reactor (RFCMR) concept with porous membranes was developed and its conceptual feasibility was demonstrated for industrially relevant conditions via a simulation study. In this chapter the technical feasibility of the RFCMR concept with porous membranes will be demonstrated by an experimental study.

Before a demonstration unit for the RFCMR concept with porous membranes could be constructed, firstly a suitable CPO catalyst and porous membrane had to be selected and also a gas tight sealing between the membrane and the support tubes needed to be developed that can withstand high temperatures and reasonable pressure differences. In order to test different catalysts, porous membranes and sealing procedures an isothermal membrane reactor was constructed, which will be discussed in detail in this chapter. A novel sealing procedure will be presented and experimental results obtained with different catalysts will be discussed. Based on the measured syngas compositions and other evaluation criteria such as durability and cokes formation the most suitable catalyst for the demonstration unit is selected.

To demonstrate the technical feasibility of the RFCMR concept with porous membranes, a demonstration unit was constructed, which was designed for a CH_4 consumption of 4 l/min (STP) equivalent to one 50 l gas bottle (200 bar) per work week (40 hours). The construction and operating procedures of the demonstration unit will be discussed in detail.

The demonstration unit was first tested as a conventional reverse flow reactor to determine the required operating conditions of the air compartment (air was used instead of O_2 for safety reasons) of the RFCMR with porous membranes and also to

assess the importance and influence of the radial heat losses. The axial temperature profiles that were measured in the demonstration unit for different operating conditions will be discussed based on which the optimal operating conditions to create the desired trapezoidal temperature profile are determined. Furthermore, a reactor model was developed, based on the reactor model that was used in the feasibility study in Chapter 4, in order to accurately describe and interpret the experimental observations.

Finally in this chapter, an experimental proof-of-principle of the RFCMR concept with porous membranes will be provided. The demonstration unit was tested at different operating conditions and it will be shown that, by selecting appropriate operating conditions, very high syngas selectivities can be obtained without using any external heating. Furthermore, the reactor model used to describe the conventional reverse flow reactor was further extended to accurately describe the axial temperature profiles and syngas compositions that were measured with the demonstration unit.

5.2 Isothermal membrane reactor

In this section firstly the experimental set-up is described, which has been used to test different CPO catalysts and porous membranes. Furthermore, the CPO catalysts and their preparation are addressed and a novel gas tight sealing, to connect the membrane to the support tubes, is presented. Finally, syngas compositions that were measured with the most optimal CPO catalyst and membrane are presented and compared with equilibrium values.

5.2.1 Experimental set-up & procedures

A shell-and-tube membrane reactor was constructed, consisting of an Al_2O_3 shell (ODxIDxL = 26x18x500 mm) and a ceramic porous membrane, which was filled with a CPO catalyst and connected to two Al_2O_3 support tubes (ODxIDxL = 12x9x400 mm) that were filled with dense Al_2O_3 particles (3 mm spheres). A detailed flow-sheet of the experimental set-up is given in Figure 5.1. The shell was placed in a special 3-zone oven (Elicra, 2 kW) with a very flat temperature profile in the central zone. CH_4 was fed to the tube and air to the shell compartment. Air was used instead of pure O_2 for safety reasons, but the dilution by inert N_2 does not affect the conclusions

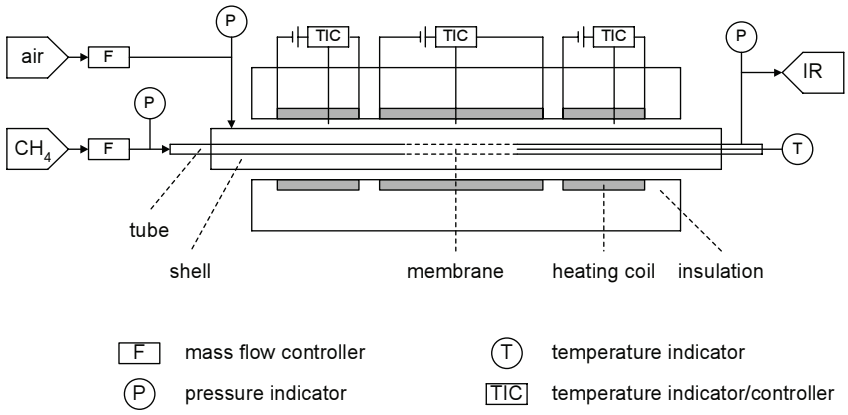

Figure 5.1: Flow-sheet of the isothermal membrane reactor experimental set-up.

drawn from the experimental results in qualitative sense. The gas feed flow rates were controlled with mass flow controllers (Brooks Instruments, 5850s; Bronkhorst, F201). To measure the temperature at the end of the catalyst bed, a thermocouple (Rössel, k-type, ODxL = 1.6x500 mm) was placed inside the tube. Pressures were measured with analog transmitters (Econosto) and the pressure at the tube outlet was regulated at about 1.3 bar in order to provide for a sufficient flow rate to the gas analysis equipment. The gas composition was analysed with an IR/TCD-analyser (Sick-Maihak, s710) equipped with two modules. The first module was a Multor (IR) and was used to measure the CH_4 (0-5 %), CO (0-20 %) and CO_2 (0-5 %) mole fractions. The analysis time of this module was about 24 s (non-synchronous). The second module was a Thermor (TCD), which enabled the measurement of the H_2 concentration virtually instantaneously. Between the tube outlet and the IR/TCD analyser the syngas was passed through an ice-cooled condenser to prevent water condensation in the IR/TCD analyser.

To distributively feed the air to the CH_4, a porous Al_2O_3 membrane provided by Membraflow was used, consisting of a macro-porous support (ODxIDxL = 11x6.5x120 mm) coated with a micro-porous layer (thickness of 23 μm, average pore size of 150 nm) on the inside. This membrane was selected due to its excellent resistance to high temperatures. The micro-porous layer provided for a reasonable but not too high pressure difference over the membrane (relative to the axial pressure drop in the shell compartment), so that the air could indeed be fed distributively to the CH_4.

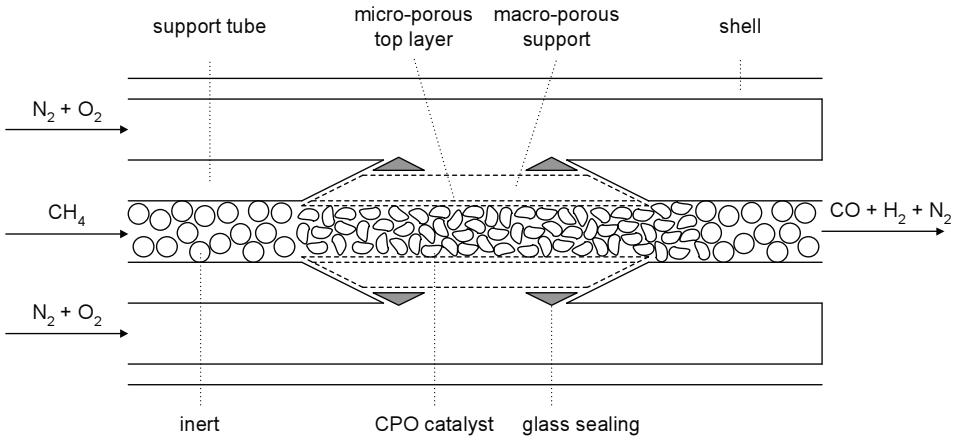

Figure 5.2: Detailed drawing of the isothermal membrane reactor.

The permeability as specified by Membraflow is 300000 l/h/bar/m^2 (STP), which was confirmed with permeability experiments. To establish a gas-tight connection between the support tube and the membrane a special sealing technique was developed. The ends of the support tube and membrane were conically polished and in the spare space between the membrane and the support tube a special glass sealing with a high melting temperature (Schott, 8252) was applied (see Figure 5.2). The principle of the sealing technique is that when an over-pressure is applied in the shell compartment, the viscous glass will be pushed into the very small space between the membrane and the support tube. Because this space is very small and due to the conically polished ends, no glass can slip through, thereby effectively preventing gas leakage. In the sealing procedure, firstly the glass was crushed and milled to a powder with an average particle size of 64 μm, which was suspended in alcohol. The suspension was then applied into the spare space between the membrane and the support tube. The membrane and support tube were placed in an oven, which was heated up slowly (5 °C/min) to 1100 °C. After heating for one hour the oven was cooled down again. The sealing was found to be gas tight for temperatures up to 1000 °C and a pressure difference of 1.5 bar for several hours (longer periods of time were not investigated).

As discussed in Chapter 1, CPO catalysts have been extensively researched in the last decades, but not many CPO catalysts in the form of spherical particles (or pellets) are offered commercially. At the scale at which CPO is carried out in this study

(undiluted feeds, high flow rates), it is essential that, besides a high activity and high selectivities towards CO and H_2, the CPO catalyst also has a sufficient mechanical strength and high temperature resistance to prevent fracture of the particles. Furthermore, cokes formation on the catalyst should be very limited to avoid blocking of the reactor. To select a suitable CPO catalyst, several catalysts were investigated in this study. Firstly, a commercial Ni/Al_2O_3 catalyst (3 mm spheres) from Süd Chemie was tested with which very high syngas selectivities were obtained, but this catalyst also showed excessive cokes formation leading to particle fracture and blocking of the reactor. Secondly, a commercial Pt/Al_2O_3 combustion catalyst (3 mm spheres) from Engelhard (Escat 26) was tested. According to the specifications, the Pt loading is 0.5 wt.% and the specific surface area 80 m^2/g. This catalyst was found to have a good mechanical strength, high temperature resistance and minimal cokes formation, but the CO and H_2 selectivities were unacceptably low. Therefore, a CPO catalyst was made by impregnating an Y_2O_3 stabilised ZrO_2 powder (Tosoh, TZ8Y) with an aqueous $RhCl_3$ solution. The resulting powder had a Rh loading of 1 wt.% and the specific area was 15 m^2/g. To obtain particles, the powder was first compressed to pellets, which were subsequently crushed and sieved. This Rh/YsZ catalyst gave high CO and H_2 selectivities as well as minimal cokes formation, but the mechanical strength of this catalyst was not sufficient leading to particle break-up. Therefore, the maximal on-stream time was limited and also it was very difficult to obtain reproducible results. The reason for the poor mechanical strength is probably due to the fact that the powder was first calcined before compressing it to pellets. Calcining the pellets rather than the powder could yield particles with better mechanical strength. Finally, to combine the high CO and H_2 selectivities of the Rh/YsZ catalyst and the good mechanical strength of the Pt/Al_2O_3 catalyst from Engelhard, Pt/Al_2O_3 particles were crushed and sieved to obtain particles of 1.4-2 mm, which were then impregnated with an aqueous $RhCl_3$ solution. Again the Rh loading was 1 wt.%. This catalyst gave very satisfactory results, as will be discussed later in this section. It might be argued that by impregnation of the particles the Rh might not be as well distributed inside the particles as in the powder based particles of the Rh/YsZ catalyst and that the Rh is mainly located on the particle surface. However, this is not necessarily a disadvantage, but rather an advantage, because of the generally very low particle effectiveness factors of CPO catalysts due to intra-particle diffusion limitations, as discussed in Chapter 4, so that only the active sites close the catalyst outer surface can be used.

5.2.2 Experimental results

With the isothermal membrane reactor experiments were carried out to study the performance of the $Rh/Pt/Al_2O_3$ catalyst at different feed flow rates of air and CH_4 (maintaining overall stoichiometric feed) and different temperature set-points in the central zone in the oven. In Figure 5.3 the dry syngas composition normalised to the CH_4, CO, CO_2 and H_2 mole fractions (thus excluding N_2) is given as a function of the measured temperature at the end of the catalyst bed for CH_4 feed flow rates of 0.5 and 1 l/min (STP). Also included in this figure are the equilibrium compositions calculated with the Gibb's free energy minimisation method discussed in Chapter 2. Because air was used instead of pure O_2, also N_2 was taken into account in these calculations. However, solid carbon was not taken into account, because in the experiments with the selected catalyst hardly any cokes formation was observed as will be discussed in more detail later. The CO and H_2 mole fractions in Figure 5.3 are very close to the equilibrium values for both flow rates and the CO_2 mole fractions are slightly below the equilibrium values. This is also reflected in the CO selectivity defined as $S_{CO} = x_{CO}/\left(x_{CO} + x_{CO2}\right)$ given in Figure 5.4 as a function of the temperature measured at the end of the catalyst bed, which is above the equilibrium value for all temperatures and even exceeds 95 % already at 1000 K. The H_2/CO ratio is slightly above 2 and very close to the equilibrium value (Figure 5.4), indicating that also the H_2 selectivity, defined as $S_{H2} = x_{H2}/(x_{H2}+x_{H2O})$, is at least as high as the CO selectivity. The CH_4 mole fraction is above the equilibrium value (Figure 5.3) and accordingly the conversion of CH_4, defined as $\zeta_{CH4} = \left(x_{CO} + x_{CO2}\right) / \left(x_{CH4} + x_{CO} + x_{CO2}\right)$, is lower than the equilibrium value (Figure 5.4), but this is attributed mainly to a small mismatch in the CH_4 and air feed flow rates, since the differences between the measured and equilibrium values are almost constant and independent of temperature. This mismatch is confirmed by calculating the O_2/CH_4 ratio from the overall C, H and O mass balances at the tube outlet. In these calculations it is assumed that pure CH_4 is fed to the tube, all CH_4 is converted to CO and CO_2 and also it is assumed that all O_2 is converted. These assumptions were verified by an analysis of the syngas composition with a micro-GC. For the CH_4 feed flow rate of 0.5 l/min (STP) the calculated O_2/CH_4 ratio was about 0.46-0.47 and for 1 l/min (STP) the calculated O_2/CH_4 ratio was typically 0.47-0.48, which explains why the CH_4 conversions are somewhat higher for the flow rate of 1 l/min (STP). Concluding, the reactor effluent was very close to equilibrium.

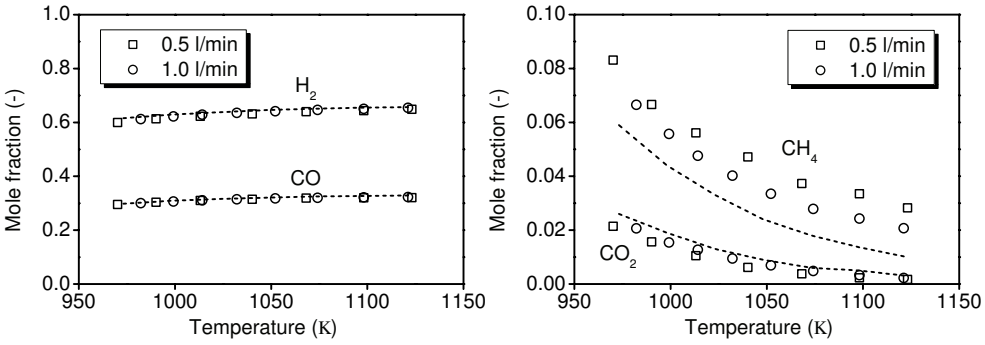

Figure 5.3: Measured (markers) and equilibrium (dashed line) dry outlet mole fractions (excluding N_2) of CO, H_2 (left) and CH_4, CO_2 as a function of the temperature at the end of the catalyst bed in the isothermal membrane reactor for different CH_4 flow rates.

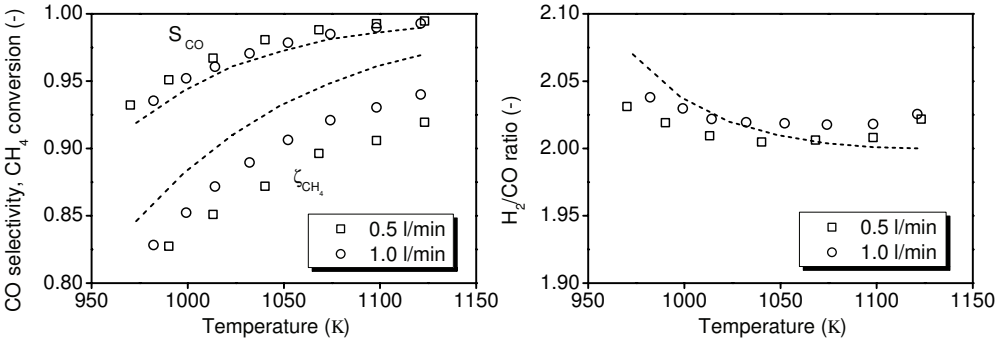

Figure 5.4: Measured (markers) and equilibrium (dashed line) CO selectivity, CH_4 conversion (left) and H_2/CO ratio (right) as a function of the temperature at the end of the catalyst bed in the isothermal membrane reactor for different CH_4 flow rates.

In the experiments a maximal CH_4 feed flow rate of 1 l/min (STP) was used whereas the catalyst mass was 3.86 gram. This yields a gas hourly space velocity (GHSV), defined as the volumetric flow rate of reactants divided by the catalyst volume, of $1.5{\cdot}10^4$ h^{-1}. Hohn and Schmidt (2001) obtained reasonably high H_2 and CO selectivities with Rh/Al_2O_3 spheres for a GHSV as high as $1{\cdot}10^6$ h^{-1}, but their Rh loading was more than a factor of 10 higher and moreover in their experiments equilibrium compositions were not yet reached. Since the syngas compositions ob-

tained in this study are virtually at equilibrium, probably even higher flow rates and GHSV's could have been used while retaining the high CO and H_2 selectivities, but this was not possible due to the pressure limitations of the experimental set-up. To increase the GHSV without increasing the pressure drop and pressure difference bigger particles and membranes with higher permeabilities should be used, respectively. Obviously the optimal Rh loading, catalyst geometry and membrane permeability have eventually to be optimised for industrial applications.

The experimental set-up was operated continuously for over 7 hours with negligible increases in the pressure difference over the membrane and the pressure drop over the catalyst bed, demonstrating the high temperature resistance and mechanical strength of the catalyst, porous membrane and sealing. Also the obtained syngas compositions were very reproducible. Obviously longer on-stream times are required to fully assess the technical feasibility. Some minor cokes formation was observed on the CPO catalyst at the beginning of the catalyst bed, probably due to CH_4 cracking:

$$CH_4 \rightarrow C_s + 2H_2 \tag{5.1}$$

Also on the "inert" Al_2O_3 particles some cokes formation was observed just after the end of the catalyst bed, which is probably due to the Boudouard reaction:

$$2CO \rightarrow C_s + CO_2 \tag{5.2}$$

To prevent this cokes formation the inert Al_2O_3 could be replaced by SiC particles, whereas YsZ might be used as support for the CPO catalyst. Alternatively, the cokes could be burned off periodically.

5.3 Conventional reverse flow reactor

To show the technical feasibility of the RFCMR concept with porous membranes a demonstration unit was constructed. To determine the optimal operating conditions related to the shell compartment of the RFCMR with porous membranes, this demonstration unit was first tested as a conventional revere flow reactor (RFR). In this section firstly the construction and operation of the demonstration unit are discussed. Subsequently, axial temperature profiles are presented that were measured at different operating conditions, based on which optimal operating conditions for the current set-up to achieve the desired trapezoidal temperature profile were selected.

To describe the reactor behaviour a reactor model was developed, which is validated with the experimental results.

5.3.1 Experimental set-up & procedures

The demonstration unit of the conventional reverse flow reactor consisted of a shell (ODxIDxL = 30x26x1500 mm) made from a high-temperature resistant steel (AISI 310), to which 48 small tubes (ODxIDxL = 4x2x25 mm) were welded (manufactured by SRI). In these tubes thermocouples (Rössel, k-type, ODxL = 1.6x250 mm) were inserted to measure the axial temperature profile in the radial centre of the reactor. Because the thermocouples were inserted inside the tubes, rubber rings could be employed at the cold ends of the tubes to make a gas tight connection. The thermocouples were connected to a data acquisition card (Advantech PCL-818HD with PCLD-789D daughterboards). The pressure was measured with digital transmitters (Drück, PTX 1400) connected to a multi-function I/O card (National Instruments PCI-6014 with 68E wiring terminal) at the in- and outlets of the shell and tube. To minimise radial heat losses, the shell was placed in a box (HxWxL= 400x400x1000 mm) filled with an insulation material (vermiculite). Electrical heating coils (3x600 Watt) were winded around the shell to start-up the reactor and also to provide for compensatory heating. The gas feed flow rates were controlled with automated mass flow controllers (Brooks Instruments, 5850s/5851s). The shell inlet and outlet were connected to an automated 4-way valve (Joucomatic), to achieve the periodic switching of the flow direction. The reactor operation and data-acquisition were fully automated in LabView. To guarantee safe operation, a stand-alone hard-ware alarm system was used with temperature controllers (Eurotherm 2132), gas detectors (Dräger) and a PC-watchdog system. A schematic overview of the experimental set-up is given in Figure 5.5.

5.3.2 Experimental results

Because of the relatively large specific external surface area of the shell, radial heat losses will greatly influence the axial temperatures obtained in the demonstration unit, despite the usage of an insulation box. As a result the required operating conditions, such as the shell CH_4 inlet fraction, the shell inlet gas flow rate etc., to establish the desired trapezoidal temperature profile in the demonstration unit could

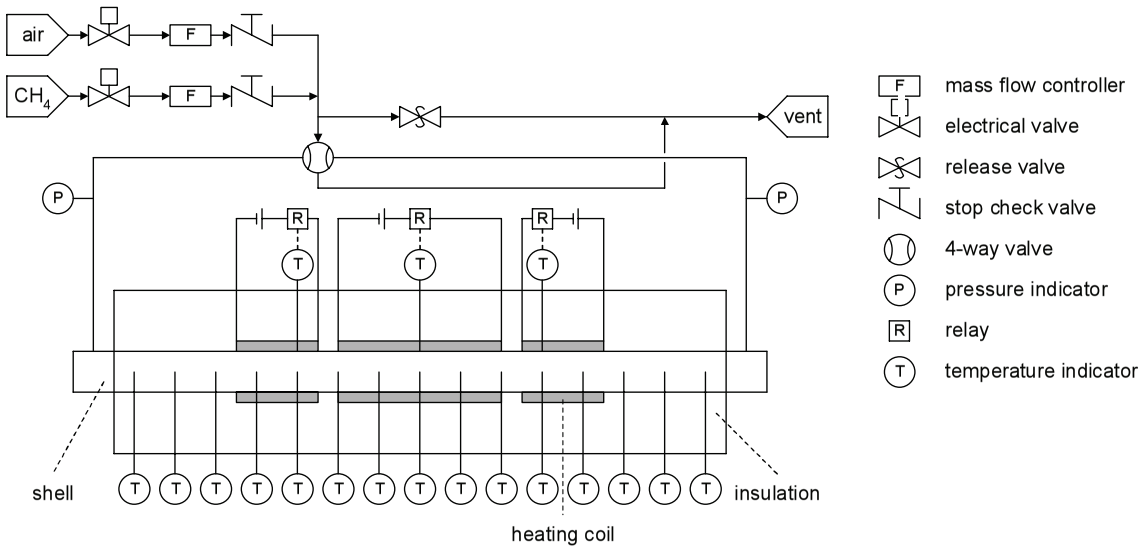

Figure 5.5: Flow-sheet of the RFR experimental set-up.

Table 5.1: Operating conditions used in RFR demonstration unit for cases A-E.

	A	B	C	D	E
L_{Pt/Al_2O_3} (m)	0.3	0.3	0.3	0.5	0.3
t_{switch} (s)	120	240	120	120	120
T_{feed} (K)	298	298	298	298	298
$\phi^s_{v,total,in}$ (l/min, STP)	30	30	30	30	20
$x^s_{CH_4,in}$	0.018	0.018	0.014	0.018	0.018

not be estimated directly from the analytic relations discussed in Chapter 4, but had to be determined experimentally. Therefore, the demonstration unit was operated as a conventional reverse flow reactor for the combustion of a small amount of CH_4 in air, considering only the shell side of the RFCMR. As combustion catalyst the commercial Pt/Al_2O_3 catalyst from Engelhard was used (see the previous section for the specifications). Because this catalyst is already very active at low temperatures ($\approx$ 900 K), inert sections had to be used to increase the plateau temperature in the centre of the reactor to the desired level of 1000-1100 K, which is required in the membrane section of the RFCMR to obtain high syngas yields and selectivities as reported in the previous section. See Chapter 4 for a more detailed discussion on inert sections in reverse flow reactors.

In Figure 5.6 axial temperature profiles measured in the demonstration unit at the end of a forward and backward semi-cycle are given for a number of cases with different lengths of the inert sections, flow rates, switching times and CH_4 inlet fractions. The operating conditions for these cases are summarised in Table 5.1. The axial temperature profiles were obtained in the cyclic steady-state (after at least 10000 s) and without using any compensatory heating from the heating coils. Indeed very high temperatures (up to 1300 K) can be obtained, which are self-sustaining, but only when employing large flow rates and relatively high CH_4 inlet fractions (cases A and B) due to the large radial heat losses in the lab-scale reactor used in this work. For a reactor with a sufficiently large diameter (*i.e.* industrial scale) the influence of radial heat losses are negligible and much smaller flow rates and CH_4 fractions are already sufficient to obtain similar plateau temperatures. For such a reactor with inert sections, the plateau temperature can be predicted with the expression given by

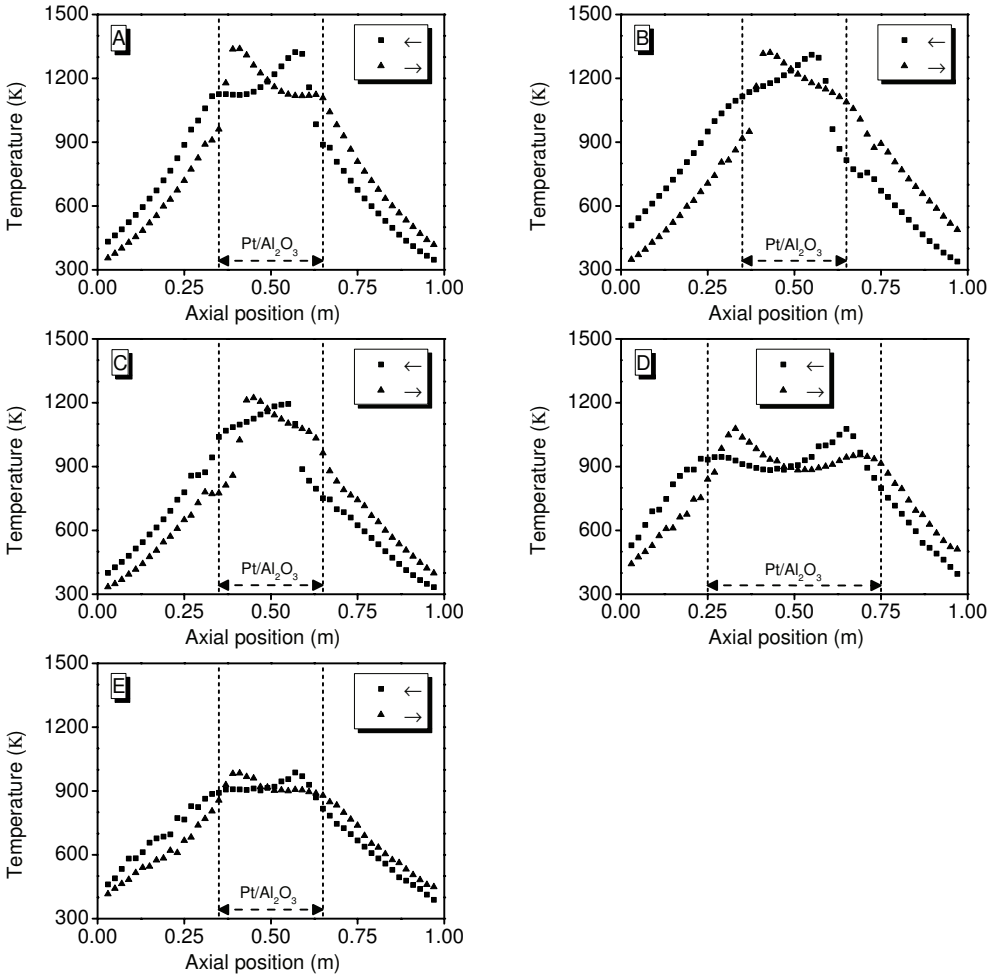

Figure 5.6: Axial temperature profiles in the RFR demonstration unit in the cyclic steady-state after a forward (→) and backward (←) semi-cycle for different cases. See Table 5.1 for the related operating conditions.

Matros and Bunimovich (1996):

$$T_{\text{plateau}} = T_{\text{feed}} + \Delta T_{\text{ad}} \left(1 + \frac{\rho_{\text{g}} v_{\text{g}} L_{\text{inert}}}{2\lambda_{\text{eff}}} \right) \tag{5.3}$$

where ΔT_{ad} is given by:

$$\Delta T_{\text{ad}} = \frac{(-\Delta H_{\text{r}})\, w^{\text{s}}_{\text{CH}_4,\text{in}}}{C_{\text{p,g}} M_{\text{CH}_4}} \tag{5.4}$$

With Equations 5.3-5.4 and calculating physical properties and λ_{eff} according to Chapter 4, it can be calculated that a plateau temperature of 1100 K can already be achieved with a flow rate of 5 l/min (STP) and a CH_4 inlet fraction as low as 0.0018. These values are at least a factor of 4 and 6 lower, respectively, than the values reported in Table 5.1. This clearly illustrates the large effect of radial heat losses on the axial temperature profiles. Nevertheless, the desired trapezoidal temperature profile with a plateau temperature of 1000-1100 K could be established.

With respect to the inert sections, it was observed that the plateau temperature was established exactly at the beginning of the combustion catalyst bed. Therefore, the length of the combustion catalyst bed in the RFCMR should be slightly larger (depending on the switching time) than the length of the membrane/filter.

5.3.3 Development of a reactor model and validation with experimental results

To describe the experimental results of the RFR demonstration unit, a detailed reactor model was developed, which is based on the reactor model used for the feasibility study in Chapter 4. Because of the relatively large specific external surface area and the accompanying large radial heat losses of the RFR demonstration unit and also the buffering effect of the insulation box, it was found that it is essential to include the radial heat losses into the model. Therefore, the reactor model was extended with a detailed description of the heat transport in the insulation layer. It was assumed that the box filled with the vermiculite can be represented by a cylinder with a diameter equal to the height of the box. This approximation can be justified, since the main resistance for the heat transport and hence the largest temperature gradients are located close to the shell wall, whereas the temperature gradients at the surface of the insulation box are very flat. The insulation layer could thus be described by a 2-D model (cylindrical coordinates), which was solved explicitly in the radial direction

and implicitly in the axial direction to allow for local grid adaptation in the axial direction.

The mass and energy conservation equations of the RFR model are given in Table 5.2. The constitutive relations and physical properties were already given in Chapter 4. The heat transfer coefficient from the insulation box to the air was calculated via a Nusselt correlation for laminar natural convection near a hot vertical plate (Bird et al., 2002):

$$\alpha^{\mathrm{i-air}} = 0.515 \frac{\lambda_{\mathrm{g,air}}}{h^{\mathrm{i}}} \left(Ra^{\mathrm{i-air}}\right)^{1/4} \tag{5.5}$$

where the Rayleigh number is given by:

$$Ra^{\mathrm{i-air}} = gPr \left(h^{\mathrm{i}}\right)^3 \frac{T^{\mathrm{i}} - T^{\mathrm{air}}}{T^{\mathrm{air}}} \left(\frac{\rho_{\mathrm{g,air}}}{\eta_{\mathrm{g,air}}}\right)^2 \tag{5.6}$$

The heat transfer coefficient from the shell to the air (outside the insulation box) was calculated via the Rayleigh number for laminar natural convection around a hot horizontally placed cylinder (Bird et al., 2002):

$$\alpha^{\mathrm{sw-air}} = 0.398 \frac{\lambda_{\mathrm{g,air}}}{2R_{\mathrm{o}}^{\mathrm{s}}} \left(Ra^{\mathrm{sw-air}}\right)^{1/4} \tag{5.7}$$

$$Ra^{\mathrm{sw-air}} = gPr \left(2R_{\mathrm{o}}^{\mathrm{s}}\right)^3 \frac{T^{\mathrm{sw}} - T^{\mathrm{air}}}{T^{\mathrm{air}}} \left(\frac{\rho_{\mathrm{g,air}}}{\eta_{\mathrm{g,air}}}\right)^2 \tag{5.8}$$

The physical properties of the insulation material and stainless steel have been summarised in Table 5.3. In the calculation of the thermal conductivity of the vermiculite, the heat transport due to radiation was super-imposed.

Regarding the kinetics of the Pt/Al_2O_3 combustion catalyst (see Chapter 4), it was found that the kinetic data obtained by van Sint Annaland (2000) could accurately describe the reaction rates of the fresh catalyst. However, because of the relatively high temperatures in the RFR demonstration unit, it was found that the activity of the catalyst quickly decreased because of sintering and loss of Pt due to vaporisation until a relatively constant activity was achieved. For the aged catalyst the Pt loading was 0.4 % and the specific surface area had decreased to 44 m^2/g. Therefore, the lumped kinetics of the combustion reaction were determined for the aged catalyst. See Appendix 5.A for details.

Table 5.2: Conservations equations of the reactor model of the RFR demonstration unit.

Mass conservation equations:

$$\begin{aligned}
\frac{\partial\left(\rho_{\mathrm{g}}^{\mathrm{s}} v_{\mathrm{g}}^{\mathrm{s}}\right)}{\partial z} &= 0 \\
\rho_{\mathrm{g}}^{\mathrm{s}} v_{\mathrm{g}}^{\mathrm{s}} \frac{\partial w_{\mathrm{CH_4,g}}^{\mathrm{s}}}{\partial z} &= \frac{\partial}{\partial z}\left(\rho_{\mathrm{g}}^{\mathrm{s}} D_{\mathrm{ax}}^{\mathrm{s}} \frac{\partial w_{\mathrm{CH4,g}}^{\mathrm{s}}}{\partial z}\right) + r_{\mathrm{CH_4,g}}^{\mathrm{s}}
\end{aligned}$$

Energy conservation equations:

Shell

$$\begin{aligned}
\left(\varepsilon_{\mathrm{g}}^{\mathrm{s}} \rho_{\mathrm{g}}^{\mathrm{s}} C_{\mathrm{p,g}}^{\mathrm{s}} + \rho_{\mathrm{bulk}}^{\mathrm{s}} C_{\mathrm{p,s}}^{\mathrm{s}}\right) \frac{\partial T^{\mathrm{s}}}{\partial t} &= -\rho_{\mathrm{g}}^{\mathrm{s}} v_{\mathrm{g}}^{\mathrm{s}} C_{\mathrm{p,g}}^{\mathrm{s}} \frac{\partial T^{\mathrm{s}}}{\partial z} + \frac{\partial}{\partial z}\left(\lambda_{\mathrm{eff}}^{\mathrm{s}} \frac{\partial T^{\mathrm{s}}}{\partial z}\right) \\
&\quad - \sum_{\mathrm{j}} \frac{r_{\mathrm{j,g}}^{\mathrm{s}}}{M_{\mathrm{j}}} H_{\mathrm{j,g}}^{\mathrm{s}} + \frac{2\pi}{R_{\mathrm{i}}^{\mathrm{s}}} \alpha^{\mathrm{s-sw}} \left(T^{\mathrm{sw}} - T^{\mathrm{s}}\right)
\end{aligned}$$

Shell wall inside the insulation box

$$\begin{aligned}
\rho_{\mathrm{s}}^{\mathrm{sw}} C_{\mathrm{p,s}}^{\mathrm{sw}} \frac{\partial T^{\mathrm{sw}}}{\partial t} &= \frac{\partial}{\partial z}\left(\lambda_{\mathrm{s}}^{\mathrm{sw}} \frac{\partial T^{\mathrm{sw}}}{\partial z}\right) + \frac{2R_{\mathrm{i}}^{\mathrm{s}} \alpha^{\mathrm{s-sw}}}{\left(R_{\mathrm{o}}^{\mathrm{s}}\right)^2 - \left(R_{\mathrm{i}}^{\mathrm{s}}\right)^2} \left(T^{\mathrm{s}} - T^{\mathrm{sw}}\right) \\
&\quad + \frac{2R_{\mathrm{o}}^{\mathrm{s}} \alpha^{\mathrm{sw-i}}}{\left(R_{\mathrm{o}}^{\mathrm{s}}\right)^2 - \left(R_{\mathrm{i}}^{\mathrm{s}}\right)^2} \left(T_{\mathrm{z,r=R_o^i}}^{\mathrm{i}} - T^{\mathrm{sw}}\right)
\end{aligned}$$

Shell wall outside the insulation box

$$\begin{aligned}
\rho_{\mathrm{s}}^{\mathrm{sw}} C_{\mathrm{p,s}}^{\mathrm{sw}} \frac{\partial T^{\mathrm{sw}}}{\partial t} &= \frac{\partial}{\partial z}\left(\lambda_{\mathrm{s}}^{\mathrm{sw}} \frac{\partial T^{\mathrm{sw}}}{\partial z}\right) + \frac{2R_{\mathrm{i}}^{\mathrm{s}} \alpha^{\mathrm{s-sw}}}{\left(R_{\mathrm{o}}^{\mathrm{s}}\right)^2 - \left(R_{\mathrm{i}}^{\mathrm{s}}\right)^2} \left(T^{\mathrm{s}} - T^{\mathrm{sw}}\right) \\
&\quad + \frac{2R_{\mathrm{o}}^{\mathrm{s}} \alpha^{\mathrm{sw-air}}}{\left(R_{\mathrm{o}}^{\mathrm{s}}\right)^2 - \left(R_{\mathrm{i}}^{\mathrm{s}}\right)^2} \left(T^{\mathrm{air}} - T^{\mathrm{sw}}\right)
\end{aligned}$$

Insulation layer

$$\rho_{\mathrm{s}}^{\mathrm{i}} C_{\mathrm{p,s}}^{\mathrm{i}} \frac{\partial T^{\mathrm{i}}}{\partial t} = \frac{\partial}{\partial z}\left(\lambda_{\mathrm{s}}^{\mathrm{i}} \frac{\partial T^{\mathrm{i}}}{\partial z}\right) + \frac{1}{r} \frac{\partial}{\partial r}\left(r \lambda_{\mathrm{s}}^{\mathrm{i}} \frac{\partial T^{\mathrm{i}}}{\partial r}\right)$$

Insulation boundary conditions

$$\lambda_{\mathrm{s}}^{\mathrm{i}} \left.\frac{\partial T^{\mathrm{i}}}{\partial r}\right|_{\mathrm{z,r=R_o^s}} = \alpha^{\mathrm{sw-i}} \left(T^{\mathrm{sw}} - T^{\mathrm{i}}\right)\big|_{\mathrm{z,r=R_o^s}} \quad \lambda_{\mathrm{s}}^{\mathrm{i}} \left.\frac{\partial T^{\mathrm{i}}}{\partial r}\right|_{\mathrm{z,r=R_o^i}} = \alpha^{\mathrm{i-air}} \left(T^{\mathrm{air}} - T^{\mathrm{i}}\right)\big|_{\mathrm{z,r=R_o^i}}$$

$$\lambda_{\mathrm{s}}^{\mathrm{i}} \left.\frac{\partial T^{\mathrm{i}}}{\partial z}\right|_{\mathrm{z=Z_0^i,r}} = \alpha^{\mathrm{i-air}} \left(T^{\mathrm{air}} - T^{\mathrm{i}}\right)\big|_{\mathrm{z=Z_0^i,r}} \quad \lambda_{\mathrm{s}}^{\mathrm{i}} \left.\frac{\partial T^{\mathrm{i}}}{\partial z}\right|_{\mathrm{z=Z_L^i,r}} = \alpha^{\mathrm{i-air}} \left(T^{\mathrm{air}} - T^{\mathrm{i}}\right)\big|_{\mathrm{z=Z_L^i,r}}$$

Table 5.3: Physical properties of vermiculite and stainless steel

	vermiculite[1]	stainless steel[2]
$C_{p,s}$ (J/kg/K)	960	$-1.73 \cdot 10^{-4}T^2 + 0.406T + 365$
$d_{p,s}$ (m)	$3.5 \cdot 10^{-3}$	
e_s	0.65	0.65
λ_s (J/m/K/s)	$1.40{\cdot}10^{-4}T - 1.12 \cdot 10^{-2}$ $+2.27 \cdot 10^{-7}\frac{e_s^i}{2-e_s^i}T^3 d_s^i$	$1.53{\cdot}10^{-2}T + 9.02$
ρ_s (kg/m^3)	182	7750

[1]Data from manufacturer

[2]Karditsas and Baptiste (2005)

With the reactor model of the RFR demonstration unit simulations were carried out for the cases A, B and E listed in Table 5.1. The measured axial temperature profile at the beginning of the experiment (after heating-up) was taken as initial condition for the temperature profile in the shell to speed up the computations. Furthermore, the insulation layer in the reactor model was allowed to heat up for 7200 s before applying the gas flows, in order to establish a temperature profile in the insulation layer very similar to the actual temperature profile in the insulation box in the experimental set-up. It was found that the axial temperature profile in the experimental set-up could be very well described by the reactor model. This is illustrated for case B in Figure 5.7, where the measured and simulated axial temperature profiles in the RFR demonstration unit are given at several moments in time. In Figure 5.8 the measured and predicted axial temperature profiles after 9600 s are given for cases A and E. Also for case A the model corresponds very well with the measured temperature profiles, but for case E the agreement is somewhat less, although the temperature plateaus and front velocities are still very similar. The discrepancy for case E may have been caused by the lower flow rate used in case E, so that radial heat losses and an accurate description of these heat losses become more important. Another reason could be related to presence of radial concentration profiles, because of which the ignition of the CH_4 combustion is postponed. Nevertheless, in view of the uncertainties in the physical properties, constitutive relations and reaction kinetics, the reactor model is able to describe the experiments very well, without using any fitting parameters.

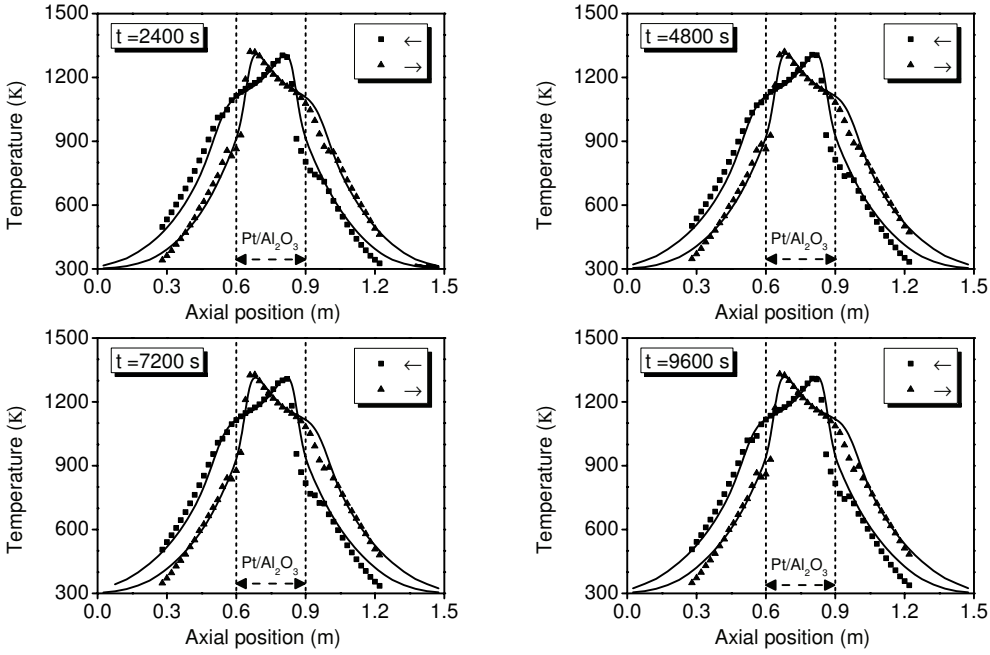

Figure 5.7: Measured (markers) and predicted (solid lines) axial temperature profiles in the RFR demonstration unit after a forward (→) and backward (←) semi-cycle at several points in time (case B).

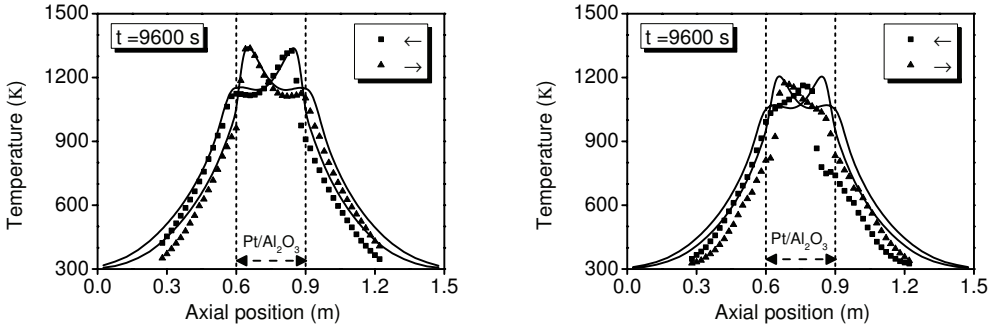

Figure 5.8: Measured (markers) and predicted (solid lines) axial temperature profiles in the RFR demonstration unit after a forward (→) and backward (←) semi-cycle after 9600 s for cases A (left) and E (right).

5.4 RFCMR with porous membranes

In the previous sections, it was shown that syngas could be produced with very high selectivities in the isothermal membrane reactor and that the demonstration unit was successfully tested as a conventional reverse flow reactor. In this section the RFCMR concept with porous membranes is tested in the demonstration unit. Firstly, the experimental set-up and operating procedures are described. Then, axial temperature profiles and tube outlet compositions are presented that were measured with the demonstration unit at different operating conditions. Finally, a reactor model is developed to describe the behaviour of the RFCMR demonstration unit, which is validated with the experimental results.

5.4.1 Experimental set-up & procedures

To demonstrate the RFCMR concept with porous membranes a tube compartment was inserted into the shell of the RFR demonstration unit. Furthermore, mass flow controllers, a 4-way valve, pressure indicators and condensers were added. The thermocouples used for measuring the axial temperature profile were positioned just outside the tube wall. A flow-sheet of the RFCMR demonstration unit is provided in Figure 5.9. Although in section 5.2 porous Al_2O_3 membranes were successfully applied in the isothermal membrane reactor, it proved to be very difficult to implement these membranes and the Al_2O_3 support tubes in the RFCMR demonstration unit. This is because Al_2O_3 is very rigid and also quite fragile, so that the tube has to placed very precisely into the shell to avoid any stresses. Furthermore, the presence of particles (inert particles and combustion catalyst particles) in the shell compartment leads to additional radial stresses. To circumvent these mechanical problems, steel filters were used as an alternative because of their superior mechanical strength and flexibility. Furthermore, they do not require a high temperature sealing but can simply be welded to stainless steel (AISI 316) support tubes, which greatly simplifies the assembly. Firstly, sintered metal filters made from high temperature resistant steel (Inconel 600, Hastelloy X; purchased from GKN-filters) were tested. However, these filters sintered over time, resulting in a continuously increasing pressure difference over the filter. As a result the on-stream time was limited to only a few hours before the maximal allowed pressure in the shell compartment was reached. To avoid sintering problems, a filter was developed consisting of a high temperature resistant

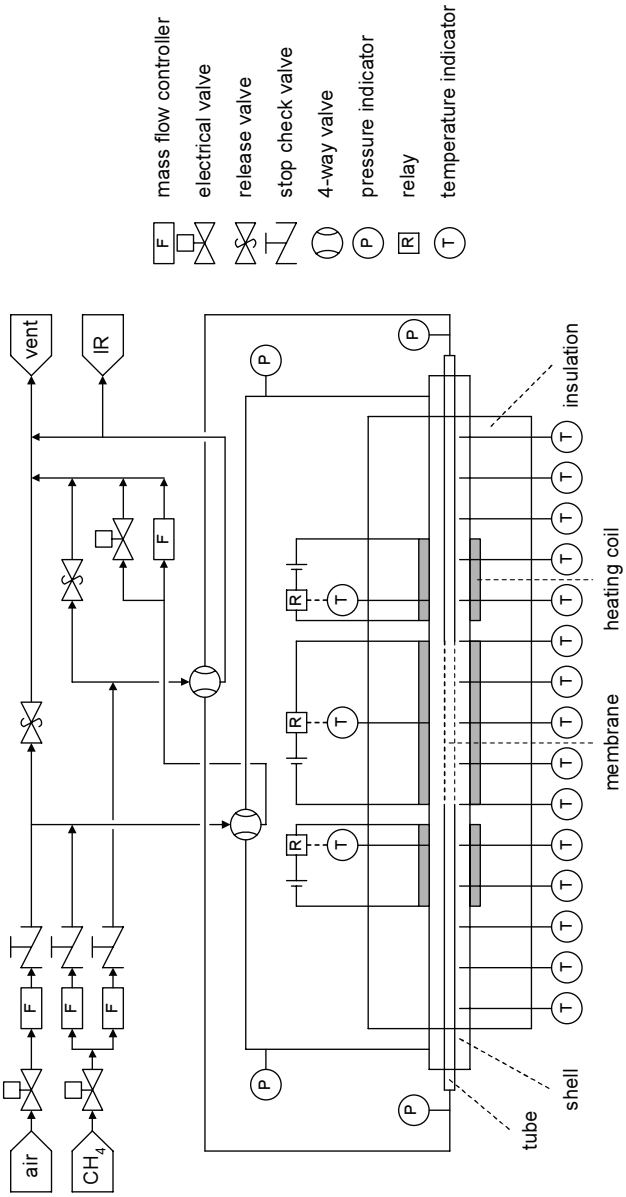

Figure 5.9: Flow-sheet of the RFCMR demonstration unit.

steel tube (Inconel 600, ODxIDxL = 10x8x200 mm) in which a number (96) of tiny holes (diameter of 0.2 mm) were made with a laser. With these filters experiments could be carried out for over 12 hours, as will be discussed later in this section. The filter was filled with the Rh/Al_2O_3 catalyst particles described in section 5.2 and the steel support tubes were filled with inert particles (3 mm Al_2O_3 spheres). Similarly to the RFR experiments, the shell compartment was filled with inert particles (3 mm Al_2O_3 spheres) at the in- and outlet and Pt/Al_2O_3 combustion catalyst particles (3 mm spheres) in the centre. The syngas composition was again analysed with the IR/TCD-analyser described in section 5.2 and the pressure at the tube outlet was regulated at about 1.7 bar in order to provide for a sufficiently large flow rate to the analyser.

Because of the large radial heat losses much larger air feed flow rates are required to create the desired trapezoidal temperature profile in the RFCMR demonstration unit than would be required for an industrial scale reactor as discussed in the previous section for the RFR demonstration unit. Due to pressure drop limitations in the tube compartment, it was not possible to increase the CH_4 feed flow rate to the tube compartment accordingly and therefore it was necessary to use a by-pass flow at the shell outlet. Since air is used instead of pure O_2 for safety reasons, the mismatch in the shell and tube flow rates is even larger, because the steepness of the temperature fronts and the height of the plateau temperature in the reverse flow section of the reactor are related to the total flow rate in the shell. At industrial scale dead-end permeation can be used, as was demonstrated in Chapter 4. The by-pass flow rate was controlled by a separate mass flow controller at the outlet of the shell.

Although in principle the CPO reaction is slightly exothermic, the released reaction heat is small compared to the radial heat losses. Furthermore, since a relatively large amount of CH_4 is combusted in the shell compartment to compensate the radial heat losses, considerable amounts of CO_2 and H_2O permeate through the filter to the tube compartment, so that the heat produced by the partial oxidation is counterbalanced by the endothermic CO_2 and H_2O reforming of CH_4 and additional syngas is produced. For isothermal operation at industrial scale, a molar H_2O/O_2 ratio of about 0.25 is required in the shell feed (see Chapter 4). With the CH_4 mole fraction in the air feed required to create the trapezoidal temperature profile, the molar $(CO_2+H_2O)/O_2$ ratio in the shell compartment just after the combustion section is

also about 0.25. Therefore, it was not necessary to add any H_2O to the air feed in the cases studied in this work. Regarding the self-sustainability of the RFCMR demonstration unit it was found that for a sufficiently large permeation rate through the filter of 10 l/min (STP) and an accompanying feed flow rate of CH_4 to the tube of about 4 l/min (STP), no compensatory heating was required to achieve high syngas selectivities.

Finally, because the H_2 mole fraction is measured practically instantaneously with the IR/TCD-analyser, it can be plotted with a high resolution as a function of time. Each time the flow direction is switched dips in the H_2 mole fraction are observed (see the next sub-section), which are caused by combustion of part of the produced syngas at the moment of switching of the flow direction and also by unconverted CH_4. The amounts of H_2 (and CO) that are lost because of the switching of the flow direction are referred to as switching losses. Because of dead volumes between the reactor and the IR/TCD-analyser (piping, condenser), the switching losses are smeared out in time. The CH_4, CO and CO_2 mole fractions can only be measured with intervals of 24 s (asynchronous). As a result, dips and peaks in these mole fractions might or might not be present around the switching of the flow direction. To avoid misinterpretation the measured values for CH_4, CO and CO_2 during the first 40 s of the semi-cycle have been omitted from the figures presented in the next sub-section.

5.4.2 Experimental results

With the RFCMR demonstration unit numerous experiments were carried out at different operating conditions, varying the switching time, the length of the combustion catalyst section, the CH_4 fraction in the air feed and the total air feed flow rate. Furthermore, the influence of compensatory heating was investigated. In all cases a permeation rate through the filter of 10 l/min (STP) was imposed and the CH_4 feed flow rate to the tube compartment was adjusted accordingly to obtain stoichiometric feed flow rates with an overall O_2/CH_4 ratio of 0.5. The operating conditions of the cases studied are listed in Table 5.4.

The dry syngas compositions that were measured at the tube outlet of the demonstration unit in the cyclic steady-state (after at least 7200 s) for cases F-K are given as a function of time during several semi-cycles in Figure 5.10. In Figure 5.11 the accompanying axial temperature profiles that were measured in the demonstration

Table 5.4: Operating conditions used in RFCMR demonstration unit for cases F-K.

Case	F	G	H	I	J	K
t_{switch}	240	120	240	240	120	240
$\phi^{\text{t}}_{\text{v,CH}_4\text{,in}}$ (l/min, STP)	4.0	4.0	3.8	4.0	4.0	4.2
$\phi^{\text{s}}_{\text{v,total,in}}$ (l/min, STP)	25	25	25	25	25	10
$\phi^{\text{s}}_{\text{v,bypass}}$ (l/min, STP)	15	15	15	15	15	0
$L_{\text{Pt/Al}_2\text{O}_3}$ (m)	0.42	0.42	0.42	0.42	0.30	0.30
T_{feed} (K)	298	298	298	298	298	298
T_{heating} (K)	off	off	off	1023	off	off
$x^{\text{s}}_{\text{CH}_4\text{,in}}$	0.01	0.01	0.02	0.01	0.01	0

Table 5.5: Dry, normalised syngas compositions and related quantities measured in the RFCMR demonstration unit for cases F-K.

Case	F	G	H	I	J	K
$x^{\text{t}}_{\text{CH}_4\text{,out}}$	0.049	0.045	0.058	0.038	0.027	0.042
$x^{\text{t}}_{\text{CO,out}}$	0.308	0.309	0.293	0.315	0.315	0.315
$x^{\text{t}}_{\text{CO}_2\text{,out}}$	0.021	0.019	0.029	0.015	0.016	0.018
$x^{\text{t}}_{\text{H}_2\text{,out}}$	0.614	0.612	0.619	0.625	0.643	0.625
$S^{\text{t}}_{\text{CO,out}}(\%)$	93.6	94.2	91.1	95.3	95.3	94.6
$S^{\text{t}}_{\text{H2,out}}(\%)$[1]	94.3	95.5	96.4	95.5	96.8	93.7
$R^{\text{t}}_{\text{O}_2/\text{CH}_4\text{,out}}$[1]	0.513	0.504	0.492	0.510	0.508	0.524
$R^{\text{t}}_{\text{H}_2/\text{CO,out}}$	2.02	2.03	2.12	2.00	2.04	1.98
$\zeta^{\text{t}}_{\text{CH}_4\text{,out}}(\%)$	87.1	87.9	84.6	89.8	92.6	88.7
H_2 loss (%)	1.26	2.27	0.08	1.04	2.19	1.65

[1]Calculated from the element mass balances at the tube outlet

unit are presented at the end of a forward and backward semi-cycle. The CH_4, CO, CO_2 and H_2 mole fractions were again normalised by excluding N_2. In Table 5.5 the time-averaged CH_4, CO, CO_2 and H_2 mole fractions are given for each case. The mole fractions were time-averaged over multiple semi-cycles, but the first 40 s of every semi-cycle were not included, thus excluding switching losses. Furthermore, also the CO and H_2 selectivities, the overall O_2/CH_4 ratios in the feeds, the H_2/CO ratios, the CH_4 conversions and the switching losses have been included in Table 5.5. The

CO selectivities, H_2/CO ratios and CH_4 conversions were directly calculated from the measured tube outlet compositions, whereas the H_2 selectivities and O_2/CH_4 ratios in the feeds were calculated from the element mass balances at the tube outlet (see section 5.2). The switching losses were calculated by comparing the time-averaged H_2 mole fraction of the entire semi-cycle and the time-averaged H_2 mole fraction of the entire semi-cycle minus the first 40 s.

From Table 5.5 and Figures 5.10-5.11 it can be concluded that for almost every case very high syngas selectivities, high CH_4 conversions and ideal H_2/CO ratios can be achieved even with plateau temperatures as low as 1000 K. Furthermore, no hot spots were observed in the filter section, while steep temperature gradients are located outside the filter section, resulting in low temperatures at the in- and outlet. The influence of the different operating conditions on the obtained results will now be discussed in more detail below.

Comparing cases F and G, it is observed that a shorter switching time gives somewhat higher CO and H_2 selectivities and a higher CH_4 conversion because of the somewhat higher plateau temperature, but the differences are small. More importantly, shorter switching times give higher switching losses. For a switching time of 120 s (case G) the switching losses are 2.27 %, but for a switching time of 240 s (case F), the switching losses reduce to 1.26 %. Since the movement of the temperature profile is relatively small, even longer switching times could be used with even lower switching losses. Also two 3-way valves could be used instead of one 4-way valve to switch the flow direction in the tube compartment, so that the dead volumes between the tube in- and outlet and the 4-way valve are eliminated.

With respect to the influence of the CH_4 fraction in the air feed, it is observed that a higher CH_4 fraction (case H) gives much higher temperature peaks just before the beginning of the filter, leading to significantly higher H_2 fractions at the beginning of a semi-cycle compared to the remainder of the semi-cycle, which explains the very low switching losses that were calculated. Surprisingly, the CO selectivity and CH_4 conversion measured for case H are the lowest of all cases studied, whereas the H_2/CO ratio is the highest and also the H_2 selectivity is very high. The most likely explanation for these observations is that inside the filter CH_4 and O_2 are primarily converted via the very fast CPO reaction, whereas the CO_2 and H_2O produced during the CH_4 combustion in the air compartment are converted via CO_2 and H_2O reforming of

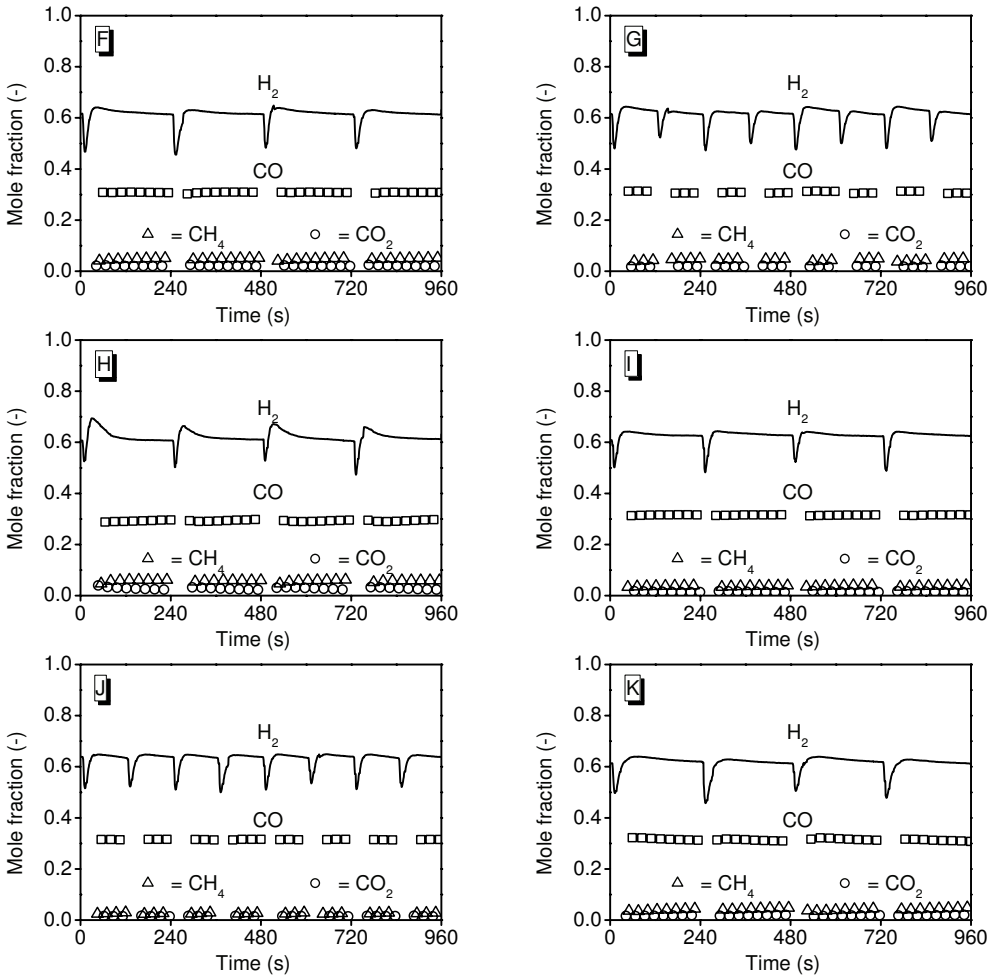

Figure 5.10: Measured (dry), normalised mole fractions at the tube outlet as a function of the time for cases F-K. See Table 5.4 for the operating conditions.

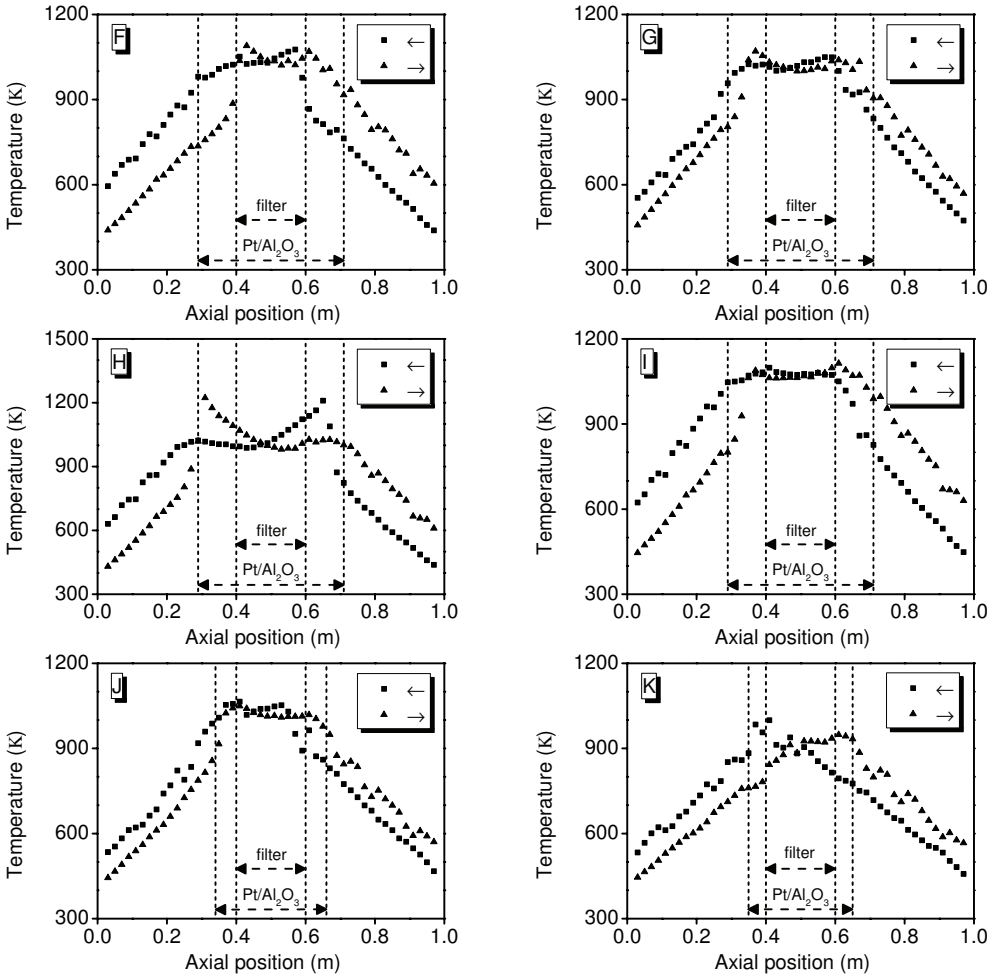

Figure 5.11: Measured axial temperature profiles in the RFCMR demonstration unit at the end of forward (→) and backward (←) semi-cycle for cases F-K. See Table 5.4 for the operating conditions.

CH_4, respectively. CO_2 reforming is much slower than the CPO and H_2O reforming reactions, see Chapter 4, and apparently the residence time in the filter was too short to convert all CO_2.

As discussed earlier, the radial heat losses in the demonstration unit severely affect the reverse flow behaviour of the reactor. However, in Chapter 4 it was found that the temperature profiles in the reverse flow section and the membrane section are established relatively independently. To assess the importance of the radial heat losses in the filter section, also an experiment was carried out in which compensatory heating along the filter was used. For case F the temperature measured just outside the shell wall in the (axial) centre of the reactor was typically about 925 K, which is considerably lower than the plateau temperature at the tube wall (about 1050 K), indicating quite steep radial temperature gradients. In case I identical operating conditions to those in case F were used, but the central heating coil was controlled in such a way that a temperature of 1025 K was established just outside the shell wall in the (axial) centre of the reactor. The resulting temperature plateau observed for case I is about 100 K higher than for case F and accordingly also the CO and H_2 selectivities and CH_4 conversion are higher. Obviously, additional compensatory heating or absence of radial heat losses in the case of an industrial scale reactor would lead to even higher plateau temperatures and thus higher selectivities and conversions, but then H_2O should be added to the air feed to prevent runaways.

To study the effect of the length of the combustion catalyst section, an experiment was performed with a somewhat shorter length (case J). Comparing cases G and J, the axial temperature profile for case J is narrower and the temperature peaks due to the CH_4 combustion are located inside the filter section resulting in higher temperatures in this section because the radial heat losses are counterbalanced by the combustion reaction. As a result also the syngas selectivities and CH_4 conversion are significantly higher for case J. The switching time that was used for case J is relatively short (120 s) and accordingly the switching losses are relatively high (2.19 %). Longer switching times might lead to lower switching losses for case J, but the overall syngas yield does not necessarily increase. For longer switching times the combustion of CH_4 in the shell compartment occurs well within the filter section at the end of the semi-cycle, leading to significantly lower temperatures at the beginning of the filter section, so that at the beginning of the next semi-cycle the temperatures at that location will still

be relatively low and accordingly also the syngas selectivities and CH_4 conversions will be significantly lower.

In Chapter 4 it was found that it is desirable to add a small amount of CH_4 to the air feed to create the trapezoidal temperature profile and to separate the reverse flow and membrane sections, but also that this was not strictly essential to achieve high syngas selectivities. To confirm these findings, also an experiment (case K) was carried out in which dead-end permeation (thus no by-pass at the outlet of the shell compartment) was used and furthermore no CH_4 was added to the shell feed. Indeed still very high CO and H_2 selectivities and CH_4 conversions can be achieved despite very low temperatures at the beginning of the filter section, because for this case the maximum temperature was established at the end of the filter section. A similar axial temperature profile was calculated in Chapter 4 for the case where no CH_4 was added to the O_2 feed. The high selectivities and conversions also result from the fact that no CO_2 has to be converted by the relatively slow CO_2 reforming reaction, since no CH_4 is combusted in the shell compartment. This is reflected by the relatively low H_2/CO ratio measured for case K. The switching losses are somewhat higher compared to other cases with a switching time of 240 s, because of the low temperatures at the end of the filter at the beginning of the semi-cycle and as a result the H_2 mole fraction reaches its semi-stationary value relatively slowly. Longer switching times are probably not possible for this case though, because a blow-out could occur.

Concluding, the results presented in Table 5.5 and figures 5.10-5.11 have shown that with the RFCMR demonstration unit very high syngas selectivities and CH_4 conversions can be achieved, higher than typical values encountered in industrial practice (Brejc and Supp, 1989; Aasberg-Petersen et al., 2001), without using any heating and even despite the radial heat losses. This clearly demonstrates the technical feasibility and potential of the RFCMR concept for energy efficient syngas production. However, the maximal on-stream time of the RFCMR demonstration unit was limited to about 12 hours for two reasons:

One limiting factor was cokes formation in the support tubes, resulting in a slowly increasing axial pressure drop over time. The cokes could be (partially) burned of by temporarily shutting off the CH_4 feed to the tube compartment, so that the tube compartment was flushed with air. This resulted in significant temperature peaks at the in- and outlet of the reactor. Similar to the isothermal membrane reactor, the

cokes formation is probably caused by the Boudouard reaction occurring on the Al_2O_3 particles. Therefore, particles made of a different material such as SiC are preferred, which makes operation with longer on-stream times possible. Alternatively the cokes has to be burned off periodically.

The second reason for the limited on-stream time was fouling of the filters. Inspection with a microscope revealed that apparently very small pieces of the combustion catalyst accumulated inside the tiny holes of the filter, which resulted in a gradually increasing pressure difference over the filter. To circumvent this problem, a glass wool blanket was wound around the filter. This effectively prevented the fouling by small pieces of combustion catalyst, but instead fouling by small threads of glass wool was observed, so that the maximal on-stream time was increased but still limited. Clearly fouling of the filter is a serious problem that has to be solved. A possible solution could be periodic back-flushing to clean the holes. Alternatively, filters have to be used with much smaller pore sizes (*i.e.* porous membranes).

5.4.3 Development of a reactor model and validation with experimental results

To describe the experimental results of the RFCMR demonstration unit, the reactor model of the RFR demonstration unit was extended with a detailed description of the tube compartment, very similar to that used in Chapter 4. The mass and energy conservation equations describing the shell and tube compartments and the tube wall are given in Table 5.6. Again the constitutive relations and correlations to describe the physical properties were given in Chapter 4. For the CPO reactions local, instantaneous equilibrium was assumed inside the filter, but solid carbon (*i.e.* cokes formation) was not taken into account. The total permeation rate through the holes in the filter was simply approximated with the well-known Hagen-Poiseuille equation (Bird et al., 2002) by considering a single hole as a tube:

$$J = \frac{p^{\mathrm{t}} + p^{\mathrm{s}}}{2R_{\mathrm{g}}T^{\mathrm{tw}}} \frac{n_{\mathrm{h}} R_{\mathrm{h}}^4 \left(p^{\mathrm{s}} - p^{\mathrm{t}}\right)}{16 R_{\mathrm{i}}^{\mathrm{t}} L_{\mathrm{filter}} \eta_{\mathrm{g}}^{\mathrm{s}} L_{\mathrm{h}}} \tag{5.9}$$

However, the permeation rate through the filter was greatly over-predicted by this equation. This is probably caused by the roughness of the steel and also by additional friction at the in- and outlet of the holes. To account for the additional friction and to calculate pressure differences with the reactor model, which correspond with the

Table 5.6: Conservations equations for the tube and shell compartments and the tube wall in the reactor model of the RFCMR demonstration unit.

Mass conservation equations:

$$\begin{aligned}
\frac{\partial\left(\rho_{\mathrm{g}}^{\mathrm{s}} v_{\mathrm{g}}^{\mathrm{s}}\right)}{\partial z} &= -\left\langle M^{\mathrm{s}}\right\rangle \frac{2 R_{\mathrm{i}}^{\mathrm{t}}}{\left(R_{\mathrm{i}}^{\mathrm{s}}\right)^2-\left(R_{\mathrm{o}}^{\mathrm{t}}\right)^2} J \\
\frac{\partial\left(\rho_{\mathrm{g}}^{\mathrm{t}} v_{\mathrm{g}}^{\mathrm{t}}\right)}{\partial z} &= \left\langle M^{\mathrm{s}}\right\rangle \frac{2}{R_{\mathrm{i}}^{\mathrm{t}}} J \\
\rho_{\mathrm{g}}^{\mathrm{s}} v_{\mathrm{g}}^{\mathrm{s}} \frac{\partial w_{\mathrm{j,g}}^{\mathrm{s}}}{\partial z} &= \frac{\partial}{\partial z}\left(\rho_{\mathrm{g}}^{\mathrm{s}} D_{\mathrm{ax}}^{\mathrm{s}} \frac{\partial w_{\mathrm{j,g}}^{\mathrm{s}}}{\partial z}\right)+r_{\mathrm{j,g}}^{\mathrm{s}} \\
\rho_{\mathrm{g}}^{\mathrm{t}} v_{\mathrm{g}}^{\mathrm{t}} \frac{\partial w_{\mathrm{j,g}}^{\mathrm{t}}}{\partial z} &= \frac{\partial}{\partial z}\left(\rho_{\mathrm{g}}^{\mathrm{t}} D_{\mathrm{ax}}^{\mathrm{t}} \frac{\partial w_{\mathrm{j,g}}^{\mathrm{t}}}{\partial z}\right)+r_{\mathrm{j,g}}^{\mathrm{t}}+\left(1-w_{\mathrm{j,g}}^{\mathrm{s}}\right)\left\langle M^{\mathrm{s}}\right\rangle \frac{2}{R_{\mathrm{i}}^{\mathrm{t}}} J
\end{aligned}$$

Energy conservation equations:

$$\begin{aligned}
\left(\varepsilon_{\mathrm{g}}^{\mathrm{s}} \rho_{\mathrm{g}}^{\mathrm{s}} C_{\mathrm{p,g}}^{\mathrm{s}}+\rho_{\mathrm{bulk}}^{\mathrm{s}} C_{\mathrm{p,s}}^{\mathrm{s}}\right) \frac{\partial T^{\mathrm{s}}}{\partial t} &= -\rho_{\mathrm{g}}^{\mathrm{s}} v_{\mathrm{g}}^{\mathrm{s}} C_{\mathrm{p,g}}^{\mathrm{s}} \frac{\partial T^{\mathrm{s}}}{\partial z}+\frac{\partial}{\partial z}\left(\lambda_{\mathrm{eff}}^{\mathrm{s}} \frac{\partial T^{\mathrm{s}}}{\partial z}\right) \\
&\quad -\sum_{\mathrm{j}} \frac{r_{\mathrm{j,g}}^{\mathrm{s}}}{M_{\mathrm{j}}} H_{\mathrm{j,g}}^{\mathrm{s}}+\frac{2 R_{\mathrm{o}}^{\mathrm{t}} \alpha^{\mathrm{s-tw}}}{\left(R_{\mathrm{i}}^{\mathrm{s}}\right)^2-\left(R_{\mathrm{o}}^{\mathrm{t}}\right)^2}\left(T^{\mathrm{tw}}-T^{\mathrm{s}}\right) \\
&\quad +\frac{2 R_{\mathrm{i}}^{\mathrm{s}} \alpha^{\mathrm{s-sw}}}{\left(R_{\mathrm{i}}^{\mathrm{s}}\right)^2-\left(R_{\mathrm{o}}^{\mathrm{t}}\right)^2}\left(T^{\mathrm{sw}}-T^{\mathrm{s}}\right) \\
\left(\varepsilon_{\mathrm{g}}^{\mathrm{t}} \rho_{\mathrm{g}}^{\mathrm{t}} C_{\mathrm{p,g}}^{\mathrm{t}}+\rho_{\mathrm{bulk}}^{\mathrm{t}} C_{\mathrm{p,s}}^{\mathrm{t}}\right) \frac{\partial T^{\mathrm{t}}}{\partial t} &= -\rho_{\mathrm{g}}^{\mathrm{t}} v_{\mathrm{g}}^{\mathrm{t}} C_{\mathrm{p,g}}^{\mathrm{t}} \frac{\partial T^{\mathrm{t}}}{\partial z}+\frac{\partial}{\partial z}\left(\lambda_{\mathrm{eff}}^{\mathrm{t}} \frac{\partial T^{\mathrm{t}}}{\partial z}\right) \\
&\quad -\sum_{\mathrm{j}} \frac{r_{\mathrm{j,s}}^{\mathrm{t}}}{M_{\mathrm{j}}} H_{\mathrm{j,g}}^{\mathrm{t}}+\frac{2 \alpha^{\mathrm{t-tw}}}{R_{\mathrm{i}}^{\mathrm{t}}}\left(T^{\mathrm{tw}}-T^{\mathrm{t}}\right) \\
\rho_{\mathrm{s}}^{\mathrm{tw}} C_{\mathrm{p,s}}^{\mathrm{tw}} \frac{\partial T^{\mathrm{tw}}}{\partial t} &= \frac{\partial}{\partial z}\left(\lambda^{\mathrm{tw}} \frac{\partial T^{\mathrm{tw}}}{\partial z}\right)+\frac{2 R_{\mathrm{o}}^{\mathrm{t}} \alpha^{\mathrm{s-tw}}}{\left(R_{\mathrm{o}}^{\mathrm{t}}\right)^2-\left(R_{\mathrm{i}}^{\mathrm{t}}\right)^2}\left(T^{\mathrm{s}}-T^{\mathrm{tw}}\right) \\
&\quad +\frac{2 R_{\mathrm{i}}^{\mathrm{t}} \alpha^{\mathrm{t-tw}}}{\left(R_{\mathrm{o}}^{\mathrm{t}}\right)^2-\left(R_{\mathrm{i}}^{\mathrm{t}}\right)^2}\left(T^{\mathrm{t}}-T^{\mathrm{tw}}\right)
\end{aligned}$$

measured pressure differences, the friction factor was increased by a factor of 16.

During the simulation study, it was found that the axial pressure drop in the tube compartment calculated with the reactor model was considerably larger than observed in the experiments, very likely because of the very low tube diameter to particle diameter ratio (about 2) in the demonstration unit. In the reactor model the axial pressure drop was computed with the Ergun equation, which is not valid for these low ratios. To account for the low tube diameter to particle diameter ratio and to calculate axial pressured drops with the reactor model, which are similar to those measured in the demonstration unit, the friction factors were reduced, which corresponded to selecting a particle diameter twice as large.

With the reactor model of the RFCMR demonstration unit simulations were carried out selecting the operating conditions of cases F, H and K listed in Table 5.4. Again the axial temperature profile measured at the beginning of the experiment was taken as initial condition for the simulation and before applying the gas flows, the insulation layer was allowed to heat up for 7200 s. In Figure 5.12 the measured axial temperature profiles in the demonstration unit and the simulated axial temperature profiles in the shell and tube compartments are given at the end of a forward and backward semi-cycle in the cyclic steady-state (after 7200 s) for cases F, H and K. Because the temperatures are measured just outside the tube wall in the demonstration unit, the measured values should lie between the simulated values of the shell and tube compartments, but closer to those of the shell compartment. As shown in Figure 5.12, the simulated temperature profiles correspond very well with the measured temperature profiles, especially the temperature fronts, the front velocities and the plateau temperatures, and indeed the measured values are closer to those simulated in the shell compartment than to those simulated in the tube compartment.

For case F pronounced temperature peaks due to the CH_4 combustion in the shell compartment were observed in the measured axial temperature profiles at the end of a semi-cycle, but these peaks were not predicted by the reactor model. However, just after the beginning of a semi-cycle also temperature peaks were observed in the simulation, which followed the measured peaks quite closely. About half-way the semi-cycle the temperature peaks started to decrease in the simulations and at the end of the semi-cycle the peaks had completely disappeared. In the experiments it was observed that the temperature peaks maintained more or less the same height

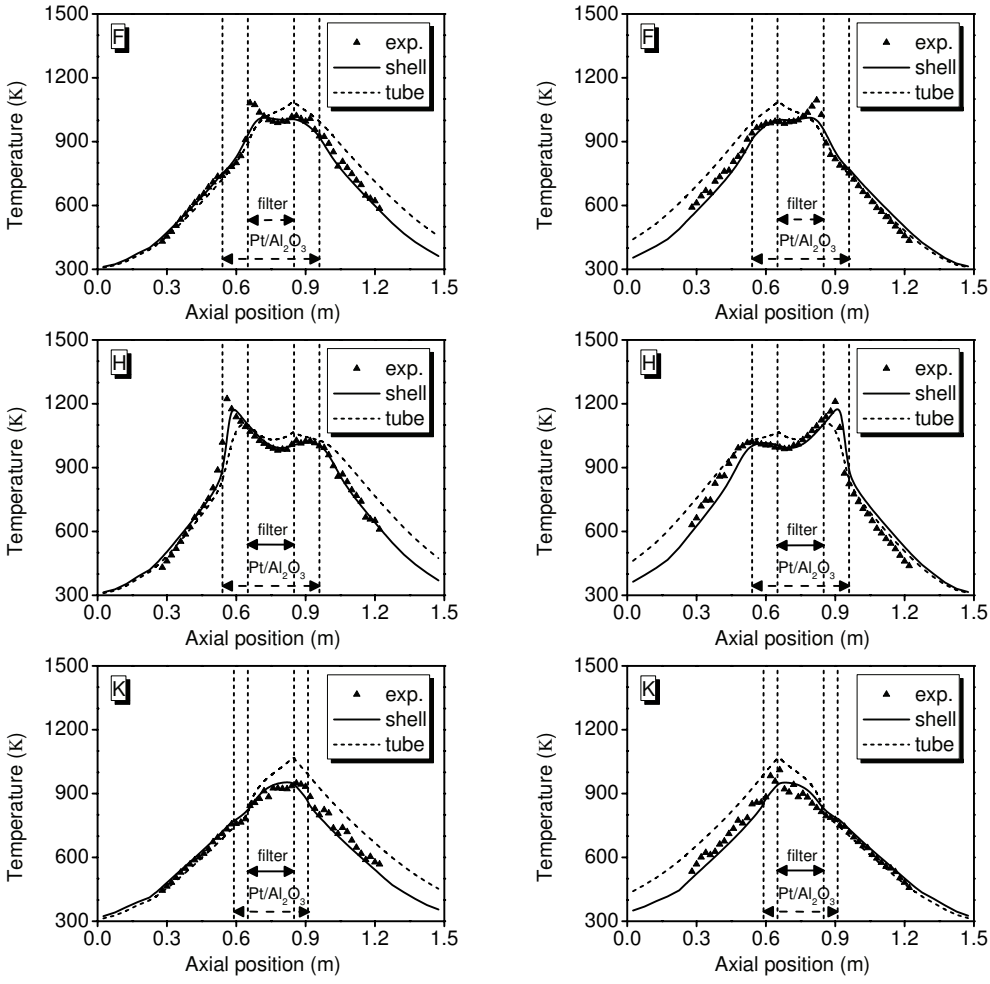

Figure 5.12: Measured (markers) and simulated (lines) axial temperature profiles in the RFCMR demonstration unit at the end of forward (left) and backward (right) semi-cycle after 7200 s for cases F, H and K.

during the entire semi-cycle and traversed into the combustion catalyst bed. The disagreement between the simulation and experimental results is probably caused by the presence of radial temperature gradients in the shell compartment, which are not taken into account in the reactor model. In the simulation the temperature at the beginning of the combustion catalyst bed was too low in the second half of the semi-cycle to maintain a temperature peak at the beginning of the combustion catalyst bed because not enough heat was produced to counterbalance the heat convection. Nevertheless, the temperature was still high enough to convert some CH_4. In the experiments the temperature close to the shell wall at the beginning of the combustion catalyst bed might have become so low due to radial heat losses that no CH_4 was converted anymore in this part of the shell compartment. Instead, the ignition of the CH_4 combustion was postponed so that still a temperature peak could be formed further on in the catalyst bed. To verify this explanation, simulations with a full 2-D description of the tube and shell compartments is required, but this type of simulation is extremely CPU demanding and hence not included in this work. For case H and also for the cases studied with the conventional reverse flow reactor the agreement between the simulated and measured axial temperature profile is much better. Apparently for these cases sufficient heat was produced at the beginning of the combustion catalyst bed to maintain a temperature peak at the beginning of the combustion catalyst bed in the simulations.

In Table 5.7 the measured and simulated syngas compositions at the tube outlet of the demonstration unit are compared. The CH_4, CO, CO_2 and H_2 mole fractions were again normalised by excluding N_2 and time-averaged over multiple semi-cycles, excluding the first 40 s of every semi-cycle. Furthermore, also the CO and H_2 selectivities, the O_2/CH_4 and H_2/CO ratios and the CH_4 conversions have been included in Table 5.7. The simulation results agree reasonably well with the experimental data, although for cases F and H the measured CO selectivity is 3-5% lower than the simulated value. This is most likely because of the slow CO_2 reforming of CH_4 as discussed earlier and accordingly also the CH_4 conversions are slightly lower. For case K, in which no CH_4 is added to the air feed, the difference between the measured and calculated CO selectivity is only about 1 %. For an industrial scale reactor the amount of CH_4 that has to be added to the air feed to create the desired trapezoidal temperature profile is much smaller than for the lab-scale reactor used in this study and therefore the CO selectivity will be even higher, since much less CO_2 from the

Table 5.7: Measured and simulated dry, normalised syngas compositions and related quantities for cases F, H and K.

	F		H		K	
	exp.	model	exp.	model	exp.	model
$x^{t}_{CH_4,out}$	0.049	0.035	0.058	0.046	0.042	0.041
$x^{t}_{CO,out}$	0.308	0.317	0.293	0.312	0.315	0.313
$x^{t}_{CO_2,out}$	0.021	0.012	0.029	0.015	0.018	0.015
$x^{t}_{H_2,out}$	0.614	0.636	0.619	0.627	0.625	0.630
$S^{t}_{CO,out}(\%)$	93.6	96.4	91.1	95.5	94.6	95.5
$S^{t}_{H2,out}(\%)$[1]	94.3	96.5	96.4	95.9	93.7	95.8
$R^{t}_{O_2/CH_4,out}$[1]	0.513	0.499	0.492	0.494	0.524	0.502
$R^{t}_{H_2/CO,out}$	2.02	2.00	2.12	2.01	1.98	2.01
$\zeta^{t}_{CH_4,out}(\%)$	87.1	90.3	84.6	87.7	88.7	88.9

[1]Calculated from the overall mass balance

air compartment has to be converted via slow dry reforming. The differences between the measured and calculated H_2 selectivities are only about 2 % and for case H the measured value is in fact higher than the calculated value. In view of the strong temperature dependency of the equilibrium compositions at the temperatures studied and the steep radial temperature gradients, it is questionable if a more detailed description of the mass transfer and more detailed reaction kinetics would give a better agreement between the experimental and simulated results. Because of the extremely high CPO reaction rates on Rh-based catalysts, it is very difficult to determine detailed reaction kinetics experimentally and up till now very few, if any, reaction kinetics of CPO reactions on Rh-based catalysts have been reported in the literature. For a large scale reactor radial heat losses will be much smaller and much higher plateau temperatures can be established at which the equilibrium compositions are less dependent on the temperature, so the agreement between measured and predicted syngas selectivities should be better.

Concluding, it was shown that the measured axial temperature profiles in the demonstration unit could be predicted really well with a reactor model that is based on the model that was used in the conceptual feasibility study in Chapter 4 and also the syngas compositions could be predicted reasonably well. Therefore, it can be con-

cluded that the model that was used in Chapter 4 gives a very realistic representation of an industrial scale reactor and that the very high syngas selectivities that were calculated can indeed be achieved in practice.

5.5 Summary and conclusions

In this chapter an experimental proof of principle of the RFCMR concept with porous membranes was provided. Firstly, CPO was studied in an isothermal membrane reactor. A novel sealing technique was presented, which enables a gas tight connection between a porous Al_2O_3 membrane and Al_2O_3 support tubes at very high temperatures and reasonable pressure differences. The porous Al_2O_3 membrane was filled with a CPO catalyst that was made by crushing a commercial Pt/Al_2O_3 catalyst to smaller particles, which were subsequently impregnated with an aqueous $RhCl_3$ solution. With the isothermal membrane reactor it was shown that very high syngas selectivities close to equilibrium could be achieved. The catalyst showed a very good mechanical strength and also the results could be reproduced very well.

To demonstrate the RFCMR concept with porous membranes, a demonstration unit was constructed. This demonstration unit was firstly operated as a conventional reverse flow reactor for the combustion of CH_4 in air in order to determine the optimal operating conditions related to the air compartment in the RFCMR. It was found that radial heat losses had a major influence on the axial temperature profiles, as expected, so that much higher air feed flow rates and CH_4 mole fractions in the air feed were required to achieve the desired trapezoidal temperature plateau than would be needed for an industrial scale reactor. By employing a reactor model extending the reactor model used for the feasibility study in Chapter 4 with a detailed description of the insulation layer around the reactor, it was found that the measured axial temperature profiles could be very well described.

Subsequently, the RFCMR concept was tested in the demonstration unit by inserting a tube compartment, consisting of a steel filter welded to support tubes, into the shell. Steel filters were used in the demonstration unit instead of porous Al_2O_3 membranes, because of their superior mechanical strength and flexibility. The steel filters consisted of high temperature resistant steel tubes in which a number of small holes were made with a laser. The demonstration unit was tested for different operating conditions and design parameters such as the switching time, the weight fraction

of CH_4 in the air feed, the length of the combustion catalyst section and the influence of using compensatory heating. Syngas with high very high CO and H_2 selectivities (up to 95 %) could be produced from undiluted CH_4 feeds, despite the radial heat losses and without using any compensatory heating. These selectivities are higher than the typical values of about 90 % encountered in industry (Brejc and Supp, 1989; Aasberg-Petersen et al., 2001) because of the lower O_2/CH_4 ratio that can be used with the RFCMR concept. Furthermore, a flat temperature plateau without any hot spots was observed in the filter section, demonstrating the advantage of distributive feeding of O_2. The maximal on-stream time was about 12 hours and was limited by cokes formation in the support tubes and by fouling of the filter. Further optimisation of the type of inert particles and the type of filter may solve these problems. The axial temperature profiles could be very well described with a reactor model based on the reactor model used in the feasibility study in Chapter 4 and also the syngas selectivities could be predicted reasonably well by simply assuming local, instantaneous equilibrium inside the filter.

The experimental results presented in this chapter clearly demonstrate the technical feasibility and the great potential of the RFCMR concept for energy efficient syngas production. Furthermore, the very good agreement between the experimentally measured and simulated axial temperature profiles and syngas compositions show that the model that was used in the feasibility study in Chapter 4 gives a very realistic representation of an industrial scale reactor, so that the computed very high syngas selectivities can indeed be achieved in practice.

Acknowledgement

G.J. Bekink is gratefully acknowledged for his experimental and modelling work on the conventional reverse flow reactor. G. Schorfhaar, R.L. Brouwer and B. Knaken are gratefully acknowledged for the building of the experimental set-ups and for their technical assistance. Also the financial support of the Dutch Technology Foundation STW, the Energy research Centre of the Netherlands ECN and the Association of Industrial Advisory Council Members of the Dutch Institute for Catalysis Research VIRAN is gratefully acknowledged.

Nomenclature

A	Pre-exponential factor, $m^6/kg/s/mol$
c_j	Concentration of species j, mol/m^3
C_p	Heat capacity, J/kg/K
d_p	Particle diameter, m
D_{ax}	Axial dispersion coefficient, m^2/s
e	Emissivity
E_a	Activation energy, J/mol
H_j	Enthalpy of species j, J/mol
ΔH_r	Reaction heat, J/mol
ID	Inner diameter, m
g	Acceleration by gravity, m/s^2
h^i	Height insulation box, m
J	Permeation rate, $mol/m^2/s$
k_1	Reaction rate constant, $m^6/kg/s/mol$
L	length, m
L_{filter}	Length of the filter, m
L_{inert}	Length inert section, m
L_{Pt/Al_2O_3}	Length of the combustion catalyst section, m
m_{sample}	Mass of catalyst sample, kg
M	Molar weight, kg/mol
n_h	Number of holes
OD	Outer diameter m
p	Pressure, Pa
Pr	Dimensionless Prandtl number, $C_{p,g}\eta_g/\lambda_g$
r	Radial coordinate, m
r_j	Reaction rate of species j, $kg/m^3/s$
R	Radius, m
R_g	Gas constant, 8.314 J/mol/K
$R_{j,k}$	Molar ratio of species j to k
Ra	Dimensionless Rayleigh number
t_{switch}	Switching time, s
T	Temperature, K
T_{feed}	Feed temperature, K

T_{heating}	Temperature at the outside of the shell wall in the axial centre of the reactor controlled with the heating coil, K
T_{plateau}	Plateau temperature, K
ΔT_{ad}	Adiabatic temperature rise, K
v	Superficial gas velocity, m/s
x	Mole fraction
w	Weight fraction
z	Axial coordinate, m
Z_0	Axial coordinate at the beginning of the insulation box, m
Z_{L}	Axial coordinate at the end of the insulation box, m

Greek symbols

α	Heat transfer coefficient, J/m^2/K/s
ϵ	Porosity
ζ	Conversion
η	Viscosity, kg/m/s
λ	Thermal conductivity, J/m/K/s
λ_{eff}	Effective thermal conductivity, J/m/K/s
ρ	Density, kg/m^3
ρ_{bulk}	Bulk density of the packed bed, kg/m^3
τ	Residence time, s
ϕ_{v}	Flow rate, l/min (STP)

Subscripts

air	Air
by-pass	By-pass
g	Gas phase
h	Hole
i	Inner
o	Outer
out	At the outlet
s	Solid
total	Total flow

Superscripts

i	Insulation layer
i-air	From the insulation layer to the air
s	Shell
s-sw	From the shell to the shell wall
sw	Shell wall
sw-i	From the shell wall to the insulation layer
sw-air	From the shell wall to the air
t	Tube
tw	Tube wall

Bibliography

Aasberg-Petersen, K., Bak Hansen, J. H., Christensen, T. S., Dybkjaer, I., Seier Christensen, P., Stub Nielsen, C., Winter Madsen, S. E. L., Rostrup-Nielsen, J. R., "Technologies for large scale gas conversion", Applied Catalysis A: General, 221(1-2), 379–387 (2001)

Bird, R. B., Stewart, W. E., Lightfoot, E. N., "Transport Phenomena", 2nd Edition, John Wiley and Sons, New York (2002)

Brejc, M., Supp, E., "Non-catalytic partial oxidation and special gasification process for higher-boiling hydrocarbons", in "Ullmanns Encyclopedia of Industrial Chemistry", Elvers, B., Hawkins, S., Ravenscroft, M., Rounsaville, J. F., Shulz, G. Eds., 5th Edition, Vol. A12, VCH Verlagsgesellschaft, Weinheim, 204–214 (1989)

Hohn, K. L., Schmidt, L. D., "Partial oxidation of methane to syngas at high space velocities over Rh-coated spheres", Applied Catalysis A: General, 211(1), 53–68 (2001)

Karditsas, P. J., Baptiste, M. J., "Thermal and Structural Properties of Fusion related Materials", (2005)
URL `http://www-ferp.ucsd.edu/LIB/PROPS/PANOS/`

Matros, Y. S., Bunimovich, G. A., "Reverse-flow operation in fixed bed catalytic reactors", Catalysis Reviews-Science and Engineering, 38(1), 1–68 (1996)

Trimm, D. L., Lam, C.-W., "The combustion of methane on platinum-alumina fibre catalysts-1: kinetics and mechanism", Chemical Engineering Science, 35(6), 1405–1413 (1980)

van Sint Annaland, M., "A Novel Reverse Flow Reactor Coupling Endothermic and Exothermic Reactions", Ph.D. thesis, University of Twente, Enschede, The Netherlands (2000)

5.A Reaction kinetics of CH_4 combustion over a Pt/Al_2O_3 combustion catalyst

In the feasibility study in Chapter 4 the reaction kinetics determined by van Sint Annaland (2000) were used to model the combustion of CH_4 in the air compartment. Although in this study very similar reaction rates were observed for fresh catalyst particles, a significant decrease in catalyst activity was observed during the experiments until a relatively steady state was reached. This decrease in activity is caused by the very high temperatures at which the RFR and RFCMR demonstration units were operated, which resulted in Pt losses and sintering and hence deactivation of the catalyst. Therefore, also the reaction kinetics of the aged catalyst were determined experimentally. The experimental set-up, operating procedures and experimental results are shortly described in this appendix.

5.A.1 Experimental set-up & procedures

To determine the reaction kinetics of CH_4 combustion in excess air on a Pt/Al_2O_3 catalyst an experimental set-up was used, which was specifically designed to measure reaction kinetics. It consists of a quartz glass U-shaped tube, which is placed inside a heated fluidised bed to keep the catalyst bed at constant temperature (measured with a thermocouple). The gas feed flows to the U-shape tube were controlled with mass-flow controllers. The outlet composition was analysed with a Micro-GC (Varian, CP-4900), which has three separate columns. The first column was a Molsieve 5Å column with He as carrier gas and was used to measure the O_2, N_2, CH_4 and CO mole fractions. The second column was also a Molsieve 5Å column but with N_2 as carrier gas to measure the H_2 mole fraction. The third column was a PoraPlot Q column with He as carrier gas to measure the CO_2 and H_2O mole fractions. The

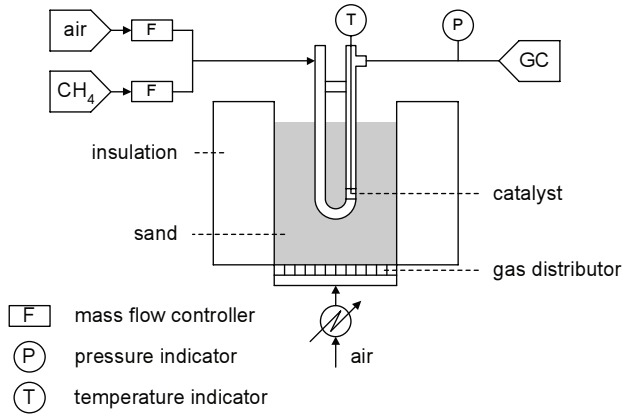

Figure 5.13: Flow-sheet of the kinetics set-up.

Micro-GC has a very high sensitivity (to the ppm level) and the relative error in the measured concentration was typically 1-2 %. A flow-sheet of the kinetics set-up is given in Figure 5.13. The Pt/Al_2O_3 particles were crushed and sieved to obtain particles with a size of 212-500 μm. Prior to the experiments a sample of catalyst was weighed (about $\pm$0.04 g) and placed inside the U-shape tube. Subsequently, the sample was heated up in the fluidised bed under inert conditions (N_2) and was kept at a temperature of about 1100 K for about 15 hours before the measurements were started.

As was shown by van Sint Annaland (2000), the CH_4 reaction rate is linearly proportional to the CH_4 concentration for very low CH_4 fractions in excess air. Because O_2 is present in large excess, the O_2 concentration can be considered constant. Assuming ideal plug flow behaviour in the catalyst bed, the CH_4 mass balance can be written as:

$$\phi_{\mathrm{v}} \frac{\partial c_{\mathrm{CH_4}}}{\partial z} = -\rho_{\mathrm{Pt/Al_2O_3,bulk}} k_1 c_{\mathrm{O_2,in}} c_{\mathrm{CH_4}} \tag{5.10}$$

Integration over the catalyst bed yields:

$$c_{\mathrm{CH_4,out}} = c_{\mathrm{CH_4,in}} \exp\left(-\rho_{\mathrm{Pt/Al_2O_3,bulk}} k_1 c_{\mathrm{O_2,in}} \tau\right) \tag{5.11}$$

where:

$$\tau = \frac{m_{\mathrm{Pt/Al_2O_3,sample}}}{\phi_{\mathrm{v}} \rho_{\mathrm{Pt/Al_2O_3,bulk}}} \tag{5.12}$$

Rewriting the equation in terms of the CH_4 conversion:

$$k_1 = \frac{-\ln\left(1-\zeta_{CH_4}\right)}{\tau \rho_{Pt/Al_2O_3,bulk} c_{O_2,in}} \tag{5.13}$$

From this equation the CH_4 reaction rate constant, k_1, be determined by measuring the CH_4 conversion. For the temperature dependency of the reaction rate constant an Arrhenius type expression was assumed:

$$k_1 = A \exp\left(-\frac{E_a}{R_g T}\right) \tag{5.14}$$

By plotting $\ln(k_1)$ versus $1/T$ the activation energy, E_a, and pre-exponential factor, A, can be determined.

5.A.2 Experimental results

In Figure 5.14 the reaction rate of the CH_4 combustion in air on the aged Pt/Al_2O_3 catalyst is given as function of the temperature for CH_4 inlet fractions of 0.005 and 0.01. The CH_4 conversion was less than 15 % for all measurements so the influence of back-mixing and axial temperature profiles should be relatively small. From the slope and intercept of the trend line through the measured data points in Figure 5.14 the activation energy and pre-exponential factor were calculated as 168 kJ/mol and $1.071 \cdot 10^7$ $m^6/kg/s/mol$, respectively. Also included in Figure 5.14 is the reaction rate that was extrapolated from the reaction kinetics measured by van Sint Annaland (2000). The reaction rates measured in this study are about a factor 1.5-3 lower than those extrapolated from the kinetic parameters determined by van Sint Annaland (2000), while the activation energy was much higher than the 98.5 kJ/mol measured by van Sint Annaland (2000). An explanation for the discrepancy in the activation energy could be that the reaction rates were measured in a different temperature range (1000-1100 K) in this study compared to the range (700-900 K) studied by van Sint Annaland (2000). Trimm and Lam (1980) also observed different activation energies for different temperature ranges at lower temperatures. Another explanation is that at higher temperatures also homogeneous gas phase reactions contributed to the observed reaction rate resulting in a higher apparent activation energy. Furthermore, also aging of the catalyst (sintering, loss of certain active sites etc.) could have altered the apparent activation energy.

To verify the assumption that the CH_4 reaction rate is linearly proportional to

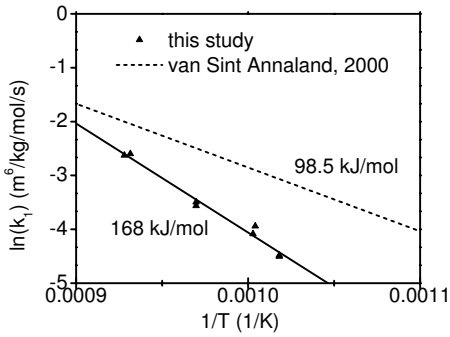

Figure 5.14: Reaction rate as a function of the temperature measured in this study (markers) and determined by van Sint Annaland (2000) (dashed line).

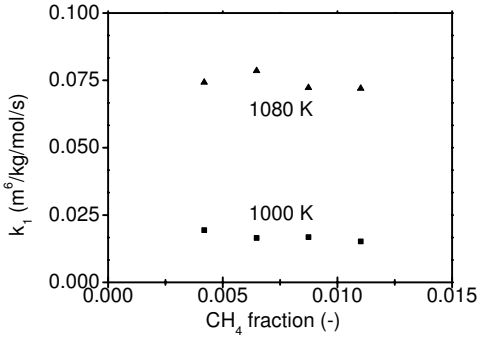

Figure 5.15: Reaction rate as a function of the CH_4 inlet fraction for different temperatures.

the CH_4 concentration, the CH_4 conversion was measured as a function of the CH_4 inlet fraction for different temperatures. As is shown in Figure 5.15, the reaction rate constant is indeed independent of the CH_4 concentration for low CH_4 inlet fractions. Finally, note that the contribution of homogeneous gas phase reactions is implicitly taken into account in the lumped kinetics.

CHAPTER 6

Feasibility Study of the RFCMR Concept with Perovskite Membranes

Abstract

In this chapter the conceptual feasibility of the RFCMR concept with perovskite membranes for energy efficient syngas production was investigated for industrially relevant conditions by means of a simulation study. In order to capture the influences of the operating conditions and the local syngas compositions on the O_2 permeation rate in the simulation study, the O_2 permeation rate through a perovskite membrane with composition $(LaCa)(CoFe)O_{3-\delta}$ was studied experimentally in an isothermal membrane reactor. In these experiments, non-reducing and reducing gasses were used as sweeping gas and also the flow rate, the composition of the sweeping gas, the membrane thickness and the temperature were varied. It was found that the O_2 permeation rate was greatly enhanced when sweeping with reducing gasses and also a higher temperature and a smaller membrane thickness increased the O_2 permeation rate. From the experimental results it was concluded that under both non-reducing and reducing atmospheres, the O_2 permeation rate was controlled by bulk diffusion and could be described with the Wagner equation. Furthermore, it was found that for the O_2 transport under reducing atmospheres the O_2 partial pressure at the membrane surface could be calculated by assuming local chemical equilibrium of the CO and H_2 combustion reactions. With the experimentally determined permeation expression, HSFM simulations were performed to study the behaviour of the RFCMR with perovskite membranes. From these simulations it was found that the local heat production/consumption varies enormously along the membrane. Because the O_2 permeation rate strongly depends on the temperature, sharp temperature peaks reflecting runaways were calculated and the $CH_4/H_2O/O_2$ feed ratio, which determines the total nett heat production inside the reactor, could not be controlled. To circumvent these runaway problems, a porous support is proposed that acts as an additional mass transfer resistance, which renders the O_2 transport rate almost independent of the temperature and provides for a relatively constant O_2 permeation flux. Therefore, DM simulations were performed where a constant O_2 permeation flux was assumed and it was demonstrated very high syngas selectivities could be achieved while fully integrating air separation and recuperative heat exchange.

Parts of this chapter are based on the paper:
Smit, J., van Sint Annaland, M., and Kuipers, J.A.M., "Modelling of a Reverse Flow Catalytic Membrane Reactor for the Partial Oxidation of Methane", International Journal of Chemical Reactor Engineering, 1, A54 (2003)

6.1 Introduction

In this chapter the conceptual feasibility of the RFCMR concept with perovskite membranes is investigated by means of a simulation study, using an experimentally determined expression for the O_2 permeation through the perovskite membrane.

Conceptually, the RFCMR with perovskite membranes is very similar to the RFCMR with porous membranes. The air and CH_4 feed streams are fed to two different compartments, which are separated by impermeable walls at the in- and outlets. In the centre of the reactor, the compartments are separated by a perovskite membrane, which is 100 % perm-selective for O_2 and through which the O_2 is fed distributively to the CH_4 compartment, while the N_2 (or O_2 depleted air) exits the air compartment as retentate. Both compartments are filled with inert particles at the in- and outlet of the reactor for additional heat capacity. In the centre of the air compartment a combustion catalyst is positioned to convert a small amount of CH_4 co-fed with the air feed, in order to obtain the desired trapezoidal temperature profile (see Chapter 4). Because the perovskite membrane is perm-selective for O_2, the H_2O, required to maintain the centre of the reactor at isothermal conditions, cannot be co-fed with the air feed. Therefore, H_2O is injected via a third compartment. The H_2O compartment could consist of a small tube located inside the syngas compartment, which is porous along the perovskite membrane. Alternatively, the H_2O could be fed via tubes positioned perpendicularly to the air and syngas compartments, thereby allowing for an axial H_2O injection profile. In Figure 6.1 a schematic overview of the RFCMR concept with perovskite membranes is presented, in which the air, H_2O and syngas compartments are arranged in a shell-and-tube configuration. Obviously, also other configurations could be considered.

Perovskite membranes have been researched extensively in the last two decades, see Bouwmeester (2003) for a review. However, in most studies inert gasses were used on the permeate side of the membrane and few researchers (Van Hassel et al., 1994; Ten Elshof et al., 1996; Xu and Thomson, 1998; Balachandran et al., 1995; Ran et al., 2000; Stephens et al., 2000; Diethelm et al., 2003) reported experimental results for the O_2 permeation rate in the presence of reducing gasses, such as CH_4, CO and H_2. In the syngas compartment of the RFCMR with perovskite membranes these components will be present, which will have a profound influence on the O_2 permeation rate through the perovskite membrane. In most of the mentioned exper-

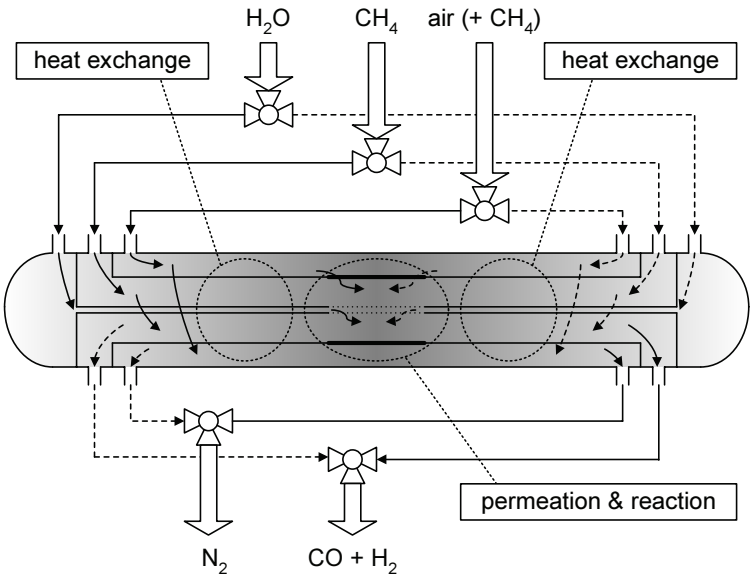

Figure 6.1: Schematic overview of the RFCMR concept with perovskite membranes in a shell-and-tube configuration. The colour gradient represents the axial temperature profile, a darker colour indicates a higher temperature.

imental studies disk-shaped membranes were used. The main disadvantage of using an experimental set-up with disk-shaped membranes is the fact that local concentration gradients and velocity profiles close to the membrane surface are not well known, causing serious difficulties in the interpretation of the experimental results and hence the derivation of expressions to describe the O_2 permeation rate. Also when tubular membranes are used the O_2 permeation rate can be influenced by radial velocity and concentration gradients. However, for tubular geometries detailed models that account for these axial and radial velocity and concentration gradients are available. Using such a model, permeation expressions that have been derived from differential measurements with small axial concentration gradients can be validated with other experiments with larger axial concentration gradients. Because of the different geometries, different sweeping flow rates and different materials used in the experimental studies reported in the literature, also different transport mechanisms have been suggested to dominate the overall O_2 permeation rate. However, the question arises if in some of these studies, the measured O_2 permeation rate was actually in-

fluenced by mass transfer limitations from the membrane surface to the gas bulk, due to the particular geometries and flow rates that were selected, rather than by bulk diffusion through the membrane or by reactions prevailing on the membrane surface. Therefore, it was decided to carry out an experimental study to develop an accurate expression for the O_2 permeation rate through a perovskite membrane under non-reducing and reducing conditions. Tubular perovskite membranes with composition $(LaCa)(CoFe)O_{3-\delta}$ were purchased from HTCeramix, which proved to have sufficient mechanical strength and chemical stability. Based on the experimentally determined O_2 permeation rates, an expression for the O_2 permeation rate was derived for both non-reducing and reducing atmospheres on the permeate side, which was subsequently used in a conceptual feasibility study. The obtained expression will be verified with a detailed model accounting for mass transport limitations inside the membrane tube, *i.e.* the influence of axial and radial velocity and concentration gradients in the gas bulk.

Based on the reactor models developed in Chapter 4 to demonstrate the conceptual feasibility of the RFCMR concept with porous membranes, reactor models for the RFCMR with perovskite membranes have been developed based on a detailed description of the heat and mass transfer processes, reaction kinetics of the relevant reactions, and the experimentally determined expression for the O_2 permeation rate through the perovskite membrane. For this purpose, again the dynamic model (DM) and the High Switching Frequency Model (HSFM) have been employed, which were solved with the efficient numerical algorithm discussed in Chapter 3. Firstly, the results of the HSFM simulations will be discussed to determine the optimal values for a number of design parameters such as the membrane length and plateau temperature. Subsequently, the influence of axial concentration gradients and the apparent activation energy of the O_2 permeation rate on the heat management of the reactor will be addressed. With DM simulations, it will be demonstrated that with an appropriate design and suitable operating conditions, very high syngas yields can be achieved while integrating the air separation, the heat integration and the CPO reaction into a single apparatus, provided that a reasonably uniform O_2 permeation flux can be accomplished. Finally in this chapter, some concluding remarks are given and the advantages and disadvantages of the two RFCMR concepts will be discussed.

6.2 Experimental study of the O_2 permeation rate through perovskite membranes under reducing and non-reducing atmospheres

In this section firstly the O_2 permeation through perovskite membranes is discussed theoretically to identify the different transport mechanisms that might play a role and to design experiments with which the rate determining step(s) can be elucidated. In order to study the O_2 permeation rate under different atmospheres on the permeate side, an experimental set-up was constructed, which is described in detail. Subsequently experimental results will be presented to pinpoint the rate determining step under both reducing and non-reducing atmospheres. Based on these experimental results expressions for the permeation rate will be derived, which are validated with a detailed model which accounts for axial and radial velocity and concentration gradients in the gas bulk.

6.2.1 Theory of O_2 permeation through perovskite membranes

O_2 permeation through perovskite membranes is a complex process that involves a number of different steps, which are schematically depicted in Figure 6.2. From the air bulk, O_2 is first transported to the membrane surface (A). At the membrane surface the O_2 dissociates (B) into the perovskite lattice and diffuses to the other side of the membrane (C). On the permeate side, either gaseous O_2 is formed at the membrane surface (B) or, in a reducing atmosphere, lattice oxygen might also directly react with gaseous or adsorbed species such as CH_4, CO and H_2. Finally, the O_2 and/or oxidation products diffuse from the membrane surface to the permeate bulk (E). General consensus has been reached that the overall permeation rate is either controlled by bulk diffusion through the perovskite (C) or by surface exchange on the permeate side of the membrane (D), provided that mass transfer limitations from the gas bulk to the membrane surface can be excluded.

In case the O_2 permeation rate is determined by bulk diffusion (C), the O_2 permeation rate can be described by the Wagner equation, see Bouwmeester and Burggraaf (1997) for a detailed discussion. Considering a shell-and-tube geometry with air flow-

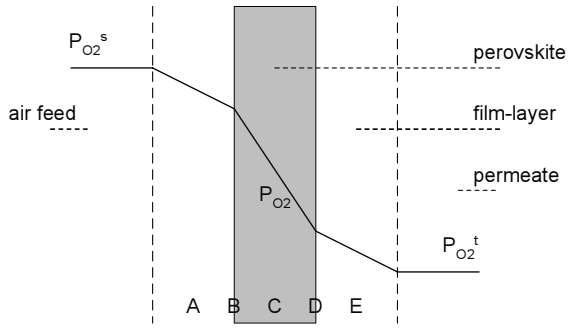

Figure 6.2: Simplified representation of O_2 transport through perovskite membranes.

ing through the shell compartment, the Wagner equation is represented by:

$$J_{\mathrm{O_2}} = \frac{D_{\mathrm{v}}}{4V_{\mathrm{m}}\Delta r_{\mathrm{m}}} \int_{\ln P^{\mathrm{s}}_{\mathrm{O_2}}}^{\ln P^{\mathrm{t}}_{\mathrm{O_2}}} (\delta)\, d\ln P_{\mathrm{O_2}} \tag{6.1}$$

where the relative partial pressure, P_{j}, is defined as:

$$P_{\mathrm{j}} = \frac{x_{\mathrm{j,g}} p_{\mathrm{g}}}{p_{\mathrm{STP}}} \tag{6.2}$$

Usually it is assumed that the non-stoichiometry δ is related to the relative O_2 partial pressure via a simple power law:

$$\delta = \delta_0 \left(P_{\mathrm{O_2}}\right)^{\mathrm{n}} \tag{6.3}$$

Using this relation Equation 6.1 can be integrated, yielding:

$$J_{\mathrm{O_2}} = \frac{D_{\mathrm{v}}\delta_0}{4V_{\mathrm{m}}\Delta r_{\mathrm{m}} n} \left[\left(P^{\mathrm{s}}_{\mathrm{O_2}}\right)^{\mathrm{n}} - \left(P^{\mathrm{t}}_{\mathrm{O_2}}\right)^{\mathrm{n}}\right] \tag{6.4}$$

showing that under these conditions the O_2 permeation rate is inversely proportional to the membrane thickness. If the O_2 permeation rate is completely controlled by bulk diffusion even when the permeate side of the membrane is exposed to a reducing atmosphere, the actual O_2 partial pressure at the permeate side is determined by the rate at which O_2 is converted near the membrane surface and in the limiting case that this reaction rate is infinitely fast, the O_2 permeation rate can be calculated directly from the partial pressures of all other species present by assuming local equilibrium.

In case the O_2 permeation rate is determined by the surface exchange rate on the permeate side, two situations can be distinguished. In a non-reducing atmosphere gaseous O_2 is formed from lattice oxygen:

$$O_O^x + 2h^{\cdot} \rightleftharpoons \frac{1}{2}O_2 + V_O^{\cdot\cdot} \tag{6.5}$$

The surface exchange mechanism at the membrane surface is generally considered to consist of a series of reactions, however the actual process is not yet very well understood (Bouwmeester and Burggraaf, 1997). What is clear, however, is that when the membrane thickness is relatively small and the O_2 permeation rate is no longer controlled by bulk diffusion, the O_2 permeation rate will no longer be inversely proportional to the membrane thickness (hence decreasing the membrane thickness will not result in higher O_2 permeation rates). More of interest for the present study is the influence of the presence of reducing species such as CH_4, CO and H_2 on the permeate side, since these species might directly react with lattice oxygen. Ten Elshof et al. (1996) studied the O_2 permeation through a perovskite membrane with composition $La_{1-x}Sr_xFeO_{3-\delta}$ while sweeping with a CO/CO_2 mixture. Based on their experimental results, the authors proposed that CO attacks the oxygen vacancy and lattice oxygen pair $V_O^{\cdot\cdot} - O_O^x$ on the membrane surface represented by the reaction:

$$CO + V_O^{\cdot\cdot} - O_O^x \rightarrow CO_2 + V_O^{\cdot\cdot} - V_O^{\cdot\cdot} + 2e' \tag{6.6}$$

Because $V_O^{\cdot\cdot}$ is smaller than O_O^x and therefore $V_O^{\cdot\cdot} - O_O^x \approx V_O^{\cdot\cdot}$, the reaction rate of gaseous CO and lattice oxygen can be expressed by (assuming 1^{st} order reaction orders):

$$J_{O_2} = \frac{1}{2}k_O^0 \left[V_O^{\cdot\cdot}\right] P_{CO}^s \tag{6.7}$$

According to this expression, the permeation rate is linearly proportional to the CO partial pressure, but independent of the membrane thickness and the partial pressure of CO_2. When sweeping with CH_4 and H_2 similar reaction mechanisms could apply.

Concluding, if the O_2 permeation rate through the perovskite membrane is completely determined by bulk diffusion, the permeation rate is inversely proportional to the membrane thickness and dependent on the partial pressure of O_2 on the permeate side, which for reducing atmospheres is related to the partial pressures of the reducing species and oxidation products. However, if the permeation rate is determined by surface exchange on the permeate side, the permeation rate is independent

of the membrane thickness and, in the presence of a reducing atmosphere on the permeate side, linearly proportional the CO (and/or CH_4, H_2) partial pressure, but independent of the partial pressures of the oxidation products. To elucidate the rate determining transport mechanism, differential measurements are required to minimise the obscuring influence of radial and axial concentration gradients on the observed O_2 permeation rates.

6.2.2 Experimental set-up & procedures

The experimental set-up that was used to study the perovskite membranes was very similar to the isothermal membrane reactor described in Chapter 5, see Figure 6.3 for a detailed flow sheet. Perovskite membranes were purchased from HTCeramix, which had an inner diameter of 9 mm and a wall thickness of 0.4 and 0.8 mm. To allow for differential measurements, assuring that axial concentration gradients are small, membranes with a length of 10 mm were used, which were positioned between two Al_2O_3 support tubes. To enable a gas-tight connection between the Al_2O_3 support tubes and the perovskite membrane, a special sealing technique was developed. Glass rings were produced from a glass with high melting point (Schott, 8252), which were positioned between the support tubes and the membrane. At the temperatures at which the experiments were performed, the glass becomes somewhat viscous and acts as a glue. This provided for a gas-tight sealing with negligible leakage as verified with experiments, however only for relatively small pressure differences between the shell and the tube compartments. Tubings and mass flow controllers for additional gas feed streams (CO, CO_2, H_2, He and N_2) were added to the tube feed section to study the O_2 permeation rate under reducing atmospheres and a Micro-GC was used to analyse the tube outlet composition, see Appendix 5.A for further specifications.

During the experiments it was observed that the perovskite membrane underwent an activation process when it was exposed to either inert or reducing atmospheres after heating up. This activation process was characterised by a slowly increasing O_2 permeation rate, which reached a steady state after about 5-10 hours. When the steady state was reached, the permeation rate responded instantly to changes in operating conditions such as the temperature and gas flow rate. Xu and Thomson (1998) reported a similar activation period with an increasing O_2 permeation rate for a perovskite membrane with composition $La_{0.6}Sr_{0.4}Co_{0.2}Fe_{0.8}O_{3-\delta}$ and attributed

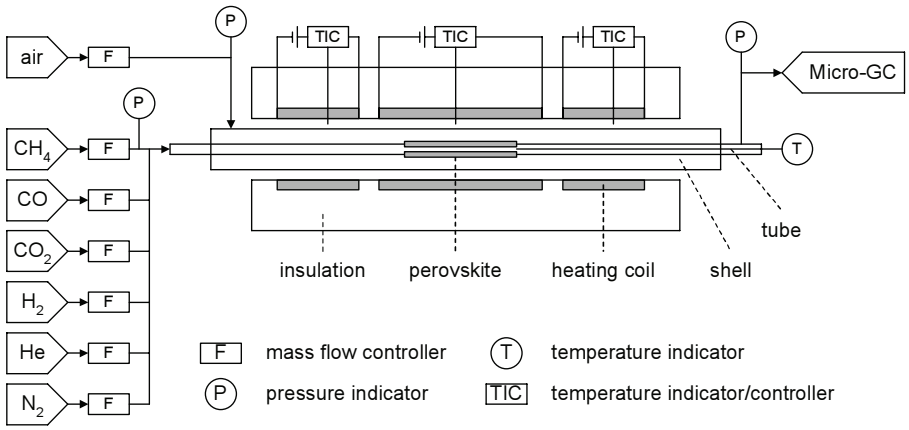

Figure 6.3: Flow sheet of the isothermal membrane reactor set-up with perovskite membranes.

this increase to a gradual facilitation of the movement of oxygen vacancies. However, Tsai et al. (1997) and Kruidhof et al. (1993) reported decreasing O_2 permeation rates before a steady state was reached for perovskite membranes with compositions $La_{0.2}Ba_{0.8}Fe_{0.8}CO_{0.2}O_{3-\delta}$ and $La_{0.6}Sr_{0.4}CoO_{3-\delta}$, respectively. These authors attributed the decreasing permeation rate to a gradual development of an ordered structure, which could be unfavourable for oxygen transport. The explanation for the observed different behaviour is not yet clear, but is most likely related to the particular perovskite compositions that were studied.

6.2.3 Experimental results: non-reducing atmosphere

The O_2 permeation rate through the perovskite membrane was first studied for non-reducing atmospheres on the permeate side by sweeping with He. As discussed previously, under non-reducing atmospheres the O_2 transport is either controlled by surface exchange processes or by bulk diffusion. Only in the latter case the O_2 permeation rate is inversely proportional to the membrane thickness. To discriminate between the two mechanisms, experiments were carried out using membranes with a wall thickness of 0.4 and 0.8 mm. Also the He flow rate was varied to establish different O_2 partial pressure profiles on the permeate side, thus varying the overall driving force for O_2 transport. During the experiments the temperature of the oven was kept at 1223

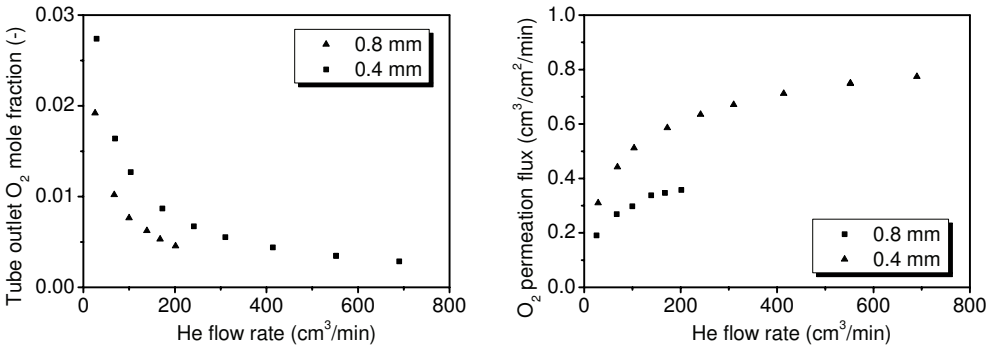

Figure 6.4: Measured tube outlet O_2 mole fraction (left) and O_2 permeation flux (right) as a function of the He flow rate for a membrane thickness of 0.4 and 0.8 mm ($T = 1223$ K).

K and the air flow rate through the shell compartment was kept sufficiently high to avoid O_2 depletion. In Figure 6.4 the measured tube outlet O_2 mole fractions (mole fractions are considered in the remainder of this section because the operating pressures used were always atmospheric) and the accompanying O_2 permeation fluxes are given as a function of the He sweeping flow rate for both membranes. Generally, it is observed that the O_2 permeation flux increases when the He flow rate is increased, but with a continuously decreasing slope. For the thicker membrane (0.8 mm) the permeation rate is about a factor 2 lower than for the thinner membrane (0.4 mm), which indicates that the O_2 permeation rate is inversely proportional to the membrane thickness and that the O_2 permeation rate is controlled by bulk diffusion.

When the O_2 transport through the perovskite membrane is controlled by bulk diffusion, the O_2 permeation rate can be described by Equation 6.4. By lumping the parameters D_v, δ_0, n and $4V_m$ into a single permeability coefficient, this equation can be simplified to (note that the relative partial pressures have been replaced by mole fractions):

$$J_{O_2} = \frac{P}{\Delta r_m} \left[\left(x^t_{O_2} \right)^n - \left(x^s_{O_2} \right)^n \right] \tag{6.8}$$

The determination of P and n from the experimental data is not very straightforward, because of the power-law dependency of the permeation rate on the O_2 mole fractions at both the permeate and retentate side, and especially because of axial and radial

concentration gradients resulting from the laminar flow conditions ($Re < 100$) as discussed in the introduction section.

If a sweep gas with a known O_2 concentration is used and if the permeated amount of O_2 is small compared to the amount that is present in the sweeping gas, the O_2 concentration gradient along the membrane could be neglected, so that P and n could in principle be determined easily. Unfortunately, such differential measurements could not be performed for low O_2 mole fractions at the permeate side because of experimental limitations. Since the permeation rate increases with a decreasing O_2 mole fraction at the permeate side, very high sweeping flow rates would be required to maintain low O_2 mole fractions and differential conditions. These high flow rates could not be realised in the experimental set-up used in this work. Moreover, the small differences between the O_2 mole fractions in the inlet and outlet streams result in relatively large experimental errors in the O_2 permeation flux.

Because of radial concentration gradients, the O_2 mole fraction at the membrane surface, which determines the permeation rate, could be be significantly higher than the mole fraction in the gas bulk. In order to interpret the measured data, it was first assumed that radial and axial concentration gradients could be neglected inside the small membrane tube so that the O_2 mole fraction along the membrane surface could be assumed equal to the measured outlet mole fraction. This assumption can be justified if the absolute difference between the O_2 mole fraction at the membrane surface and the O_2 mole fraction in the gas bulk is relatively small (*i.e.* well within an order of magnitude) compared to the relative difference between the O_2 mole fraction in the gas bulk in the tube compartment and that in the gas bulk in the shell compartment. A similar argument applies for radial concentration gradients in the shell compartment. The validity of neglecting the radial and axial concentration gradients inside the membrane tube will be verified later with a detailed model. Using the assumption of an ideally mixed gas inside the membrane tube, the constants P and n were determined by plotting the permeation flux multiplied with the membrane thickness versus the measured tube outlet O_2 mole fraction (see Figure 6.5). By fitting a flux expression of the form of Equation 6.8 through the measured data points by linear regression, P and n were determined as 0.094 $cm^4/cm^2/min$ and -0.063, respectively.

The diffusion of lattice oxygen through the bulk of the perovskite membrane is

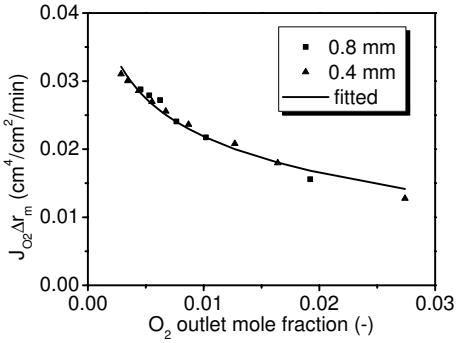

Figure 6.5: Measured (markers) and fitted (solid line) normalised O_2 permeation flux as a function of the O_2 mole fraction at the tube outlet for a membrane thickness of 0.4 and 0.8 mm (T = 1223 K)

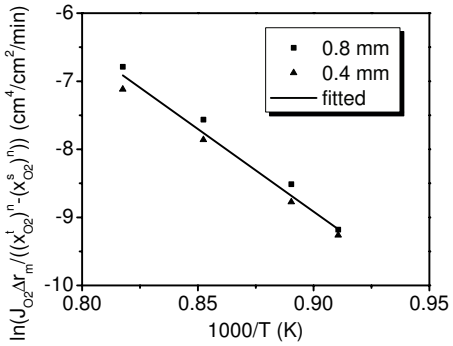

Figure 6.6: Measured (markers) and fitted (solid line) normalised O_2 permeation flux as function of the temperature for a membrane thickness of 0.4 and 0.8 mm ($\Phi_{v,He}$ = 140 cm^3/min).

a temperature activated process and usually the permeability coefficient in Equation 6.8 is assumed to exhibit an Arrhenius type temperature dependence:

$$J_{O_2} = \frac{P_0}{\Delta r_m} \exp\left(-\frac{E_a}{R_g T}\right) \left[\left(x^t_{O_2}\right)^n - \left(x^s_{O_2}\right)^n\right] \tag{6.9}$$

To determine the pre-exponential factor and the apparent activation energy, the O_2 permeation rate was studied at different temperatures and a fixed He sweeping flow rate. Because the permeation rate is higher at higher temperatures, the O_2 mole fraction along the membrane will be higher reducing the overall driving force. To account for the influence of the O_2 mole fractions, $\ln\left[J_{O2}\Delta r_m / \left(\left(x^t_{O2,out}\right)^n - \left(x^s_{O2}\right)^n\right)\right]$ was plotted versus $1/T$ in Figure 6.6. By linear regression, P_0 and E_a were determined as 202 kJ/mol and $4.140{\cdot}10^7$ cm^4/cm^2/min, respectively.

6.2.4 Validation of permeation expression for non-reducing atmospheres

Radial velocity and concentration profiles may prevail in the membrane tube due to the laminar flow conditions. These radial concentration gradients could affect the derived expression for the permeation rate through the perovskite membrane significantly. Because the O_2 mole fraction at the membrane surface may be much higher than the mole fraction measured at the tube outlet, the obtained permeation expression could underestimate the actual O_2 permeation rate. To verify the assumption of

Table 6.1: Model of O_2 transport in an empty perovskite tube.

Total mass conservation equation:

$$\frac{\partial\left(\rho_{\mathrm{g}}^{\mathrm{t}} v_{\mathrm{t}}^{\mathrm{t}}\right)}{\partial z} = \frac{2}{r_{\mathrm{i}}} M_{\mathrm{O_2}} J_{\mathrm{O_2}}$$

Component mass balance in gas bulk:

$$\rho_{\mathrm{g}}^{\mathrm{t}} v_{\mathrm{g}}^{\mathrm{t}} \frac{\partial w_{\mathrm{j,g}}^{\mathrm{t}}}{\partial z} = \frac{\partial}{\partial z}\left(\rho_{\mathrm{g}}^{\mathrm{t}} D_{\mathrm{ax,j}}^{\mathrm{t}} \frac{\partial w_{\mathrm{j,g}}^{\mathrm{t}}}{\partial z}\right) + \frac{2}{r_{\mathrm{i}}} j_{\mathrm{j,g}}^{\mathrm{t}}$$

Taylor dispersion coefficient (Bird et al., 2002):

$$D_{\mathrm{ax,j}}^{\mathrm{t}} = D_{\mathrm{j}}^{\mathrm{t}} + \frac{1}{48 D_{\mathrm{j}}^{\mathrm{t}}}\left(\frac{r_{\mathrm{i}}^{\mathrm{t}} v_{\mathrm{g}}^{\mathrm{t}}}{48}\right)^2$$

Component mass balances at the tube surface:

$$0 = r_{\mathrm{j,g}}^{\mathrm{t}} - \frac{2}{r_{\mathrm{i}}} j_{\mathrm{j,g}}^{\mathrm{t}} - w_{\mathrm{j,m}}^{\mathrm{t}} J_{\mathrm{O_2}} M_{\mathrm{O_2}}$$

$$0 = r_{\mathrm{O_2,g}}^{\mathrm{t}} - \frac{2}{r_{\mathrm{i}}} j_{\mathrm{O_2,g}}^{\mathrm{t}} + \left(1 - w_{\mathrm{O_2,m}}^{\mathrm{t}}\right) J_{\mathrm{O_2}} M_{\mathrm{O_2}}$$

Wall-to-fluid mass transfer coefficient (Bird et al., 2002):

$$k_{\mathrm{w}} = \frac{ShD}{2r_{\mathrm{i}}} \qquad \text{where:} \qquad Sh = \max\left(3.66, 1.08\left(\frac{Dz}{4r_{\mathrm{i}}^2 v_{\mathrm{g}}}\right)^{-1/3}\right)$$

neglecting concentration gradients inside the membrane tube, which was used to determine the parameters in the permeation expression, a model was developed, where the influences of axial and radial velocity and concentration profiles were accounted for. In this model, it is assumed that the flow at the beginning of the membrane tube is hydrodynamically fully developed. Furthermore, radial dispersion due to radial velocity and concentration profiles is accounted for via the Taylor dispersion coefficient (Bird et al., 2002), whereas mass transfer from the gas bulk to the membrane surface is calculated using the Maxwell-Stefan description, see Appendix 4.A. The model equations are listed in Table 6.1.

With the model firstly simulations using the derived expression for the O_2 permeation rate were carried out, where the He flow rate was varied keeping the temperature constant (1223 K), similar to the experimental conditions presented in Figure 6.4. In Figure 6.7 the calculated and measured O_2 permeation fluxes are given as a function

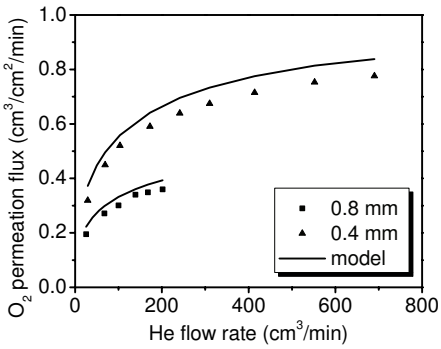

Figure 6.7: Measured (markers) and predicted (lines) O_2 permeation fluxes as a function of the He flow rate for a membrane thickness of 0.4 and 0.8 mm (T = 1223 K).

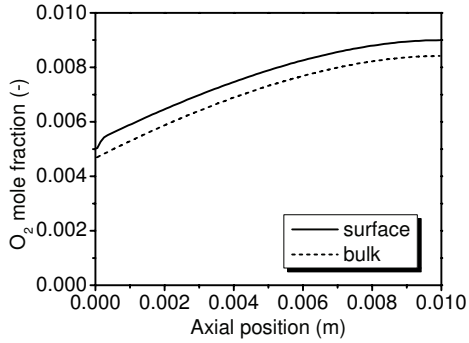

Figure 6.8: Predicted axial O_2 mole fraction profiles at the membrane surface (solid line) and in the gas bulk (dashed line) ($\Phi_{v,He}$ = 100 cm^3/min, Δr_m = 0.8 mm, T = 1223 K).

of the He sweeping flow rate. For all measurements the O_2 permeation flux is slightly over-predicted by the model, but the deviation is less than 15 % for all measurements. The deviation can be explained by examination of the axial profiles of the O_2 mole fractions at the membrane surface and in the gas bulk, which are presented in Figure 6.8 for a He flow rate of 100 cm^3/cm^2/min and a membrane thickness of 0.8 mm. As expected, the O_2 mole fractions at the membrane surface are somewhat higher than those in the gas bulk, but the differences are small. On average the O_2 mole fraction at the membrane surface is slightly lower than that in the bulk at the outlet of the membrane tube and as a result the O_2 permeation flux is slightly over-predicted. The largest deviation is found for low He sweeping flow rates, because for relatively large O_2 mole fractions the relative difference between the O_2 mole fraction at the membrane surface and that in the gas bulk is more significant compared to the relative difference between the O_2 mole fraction at the membrane surface and that in the shell compartment, which determines the permeation flux.

To verify the values obtained for the pre-exponential factor and the apparent activation energy regarding the temperature dependency of the O_2 permeation rate, simulations were carried out for different temperatures with a fixed He sweeping flow rate of 140 cm^3/cm^2/min, similar to the experimental conditions of the results presented in Figure 6.6. In Figure 6.9 the measured and predicted O_2 permeation

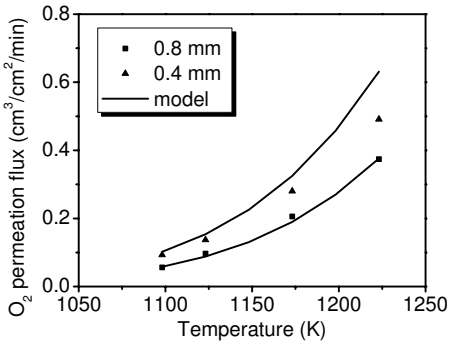

Figure 6.9: Measured (markers) and predicted (lines) O_2 permeation fluxes as a function of the temperature for a membrane thickness of 0.4 and 0.8 mm ($\Phi_{v,He}$ =140 cm^3/min).

fluxes are given as a function of the temperature. The measured and calculated O_2 permeation fluxes correspond quite well, especially for the membrane with a thickness of 0.8 mm, where the deviation is less than 10 %. For the membrane with a thickness of 0.4 mm the deviation is somewhat larger for higher temperatures, up to 25-30 %. This can be explained by the way the pre-exponential factor and the activation energy were determined. From Figure 6.6 it can be observed that the normalised O_2 permeation flux is generally somewhat higher for the thicker membrane than for the thinner membrane. Since the pre-exponential factor and activation energy were fitted using the measured O_2 permeation fluxes for both membranes, the permeation flux of the thicker membrane will be slightly under-predicted and that of the thinner membrane slightly over-predicted. As discussed earlier, the O_2 permeation fluxes are typically over-predicted by about 10 % because of axial and radial concentration profiles. For the thicker membrane the over-prediction due to axial and radial concentration profiles is thus balanced by the under-prediction due to the temperature dependence, which explains the small deviations between the measured and calculated O_2 permeation rates. For the thinner membrane the expected over-prediction due to the radial concentration gradients is increased by the over-prediction due to the temperature dependence.

Based on the good agreement between the the measured and predicted O_2 permeation fluxes in Figures 6.7 and 6.9, it can be concluded that the assumption of

negligible influence of radial and axial concentration gradients inside the membrane tube on the determined parameters in Equation 6.9 is very reasonable (because of the differential operation), so that the derived flux expression can be confidently used for design purposes when a non-reducing atmosphere is applied on the permeate side.

6.2.5 Experimental results: reducing atmosphere

The integration of the partial oxidation of CH_4 and air separation into a membrane reactor such as the RFCMR with perovskite membranes has the major advantage that the O_2 partial pressure in the syngas compartment is greatly reduced by the O_2 consumption via partial oxidation reactions and accordingly the driving force for the O_2 permeation is increased enormously. Lattice oxygen could also react directly with reducing gasses such as CH_4, CO and H_2, which might enhance the O_2 permeation rate even further.

To determine to what extent the O_2 permeation rate is enhanced when a reducing atmosphere is present on the permeate side of the perovskite membrane, experiments were performed in which CH_4/N_2, CO/N_2 and H_2/N_2 mixtures were used as sweeping gas. In Figure 6.10 the measured O_2 permeation fluxes are compared as a function of the inlet mole fractions of CH_4, CO and H_2. During these experiments, the oven temperature set-point was kept at 1223 K. Furthermore, no O_2 was detected in the tube outlet, indicating that all permeated O_2 was converted to other species and therefore the O_2 permeation fluxes were back-calculated from the measured tube outlet compositions. When CH_4/N_2 mixtures were used as sweeping gas, the increase in the O_2 permeation flux was found to be relatively small compared to sweeping with He (*cf.* Figure 6.4), although some CH_4 was converted and combustion products such as CO, CO_2, H_2, H_2O and also minor amounts of C_2H_2 and C_2H_4 were detected. Apparently the reaction between CH_4 and (lattice) O_2 is too slow to enhance the permeation rate significantly. However, when CO/N_2 and H_2/N_2 mixtures were used as sweeping gas, it was found that the O_2 permeation flux increased with a factor of about 30 compared to sweeping with He. For a membrane thickness of 0.8 mm O_2 permeation fluxes up to 10 $cm^3/cm^2/min$ were measured. This value has been reported (Bredesen and Sogge, 1996) as a minimal permeation flux required for membrane reactors with integrated air separation to become economically feasible. For a thinner membrane (0.4 mm), the O_2 permeation flux is even higher (up to almost

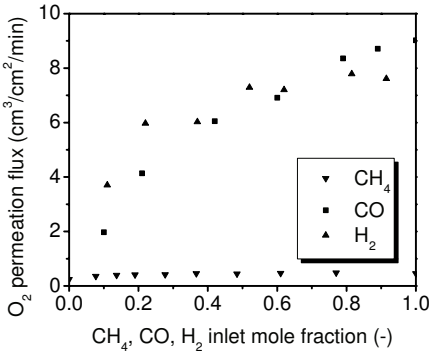

Figure 6.10: Measured O_2 permeation flux as a function of the inlet mole fractions of CH_4, CO and H_2 while sweeping with CH_4/N_2 ($\Phi_{v,tot} = 60$ cm^3/min), CO/N_2 ($\Phi_{v,tot} = 200$ cm^3/min) and H_2/N_2 ($\Phi_{v,tot} = 250$ cm^3/min) mixtures ($\Delta r_m = 0.8$ mm, $T = 1223$ K).

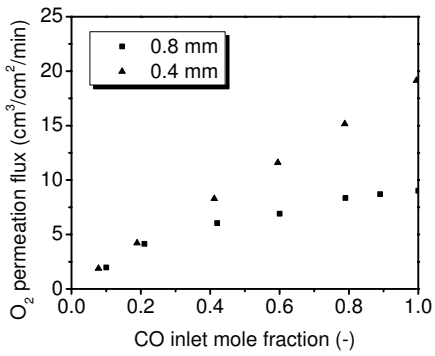

Figure 6.11: Measured O_2 permeation flux as a function of the inlet mole fraction of CO while sweeping with CO/N_2 mixtures for a membrane thickness of 0.4 and 0.8 mm ($\Phi_{v,tot} = 200$ cm^3/min, $T = 1223$ K).

20 cm^3/cm^2/min) as is illustrated in Figure 6.11, showing the O_2 permeation flux as a function of the CO inlet mole fraction while sweeping with CO/N_2 mixtures for a membrane thickness of 0.4 and 0.8 mm. Since identical operating conditions were used, the higher O_2 permeation fluxes measured for the thinner membrane compared to those measured for the thicker membrane further indicate that when a reducing atmosphere is present on the permeate side of the perovskite membrane studied in this work, the O_2 permeation rate is still strongly influenced by the membrane thickness and that the O_2 permeation rate is thus primarily determined by bulk diffusion.

As discussed in the beginning of this section, if the O_2 transport through the perovskite membrane is governed by bulk diffusion while a reducing atmosphere is present on the permeate side of the membrane, the O_2 permeation rate will be determined by the reaction rate between O_2 at the membrane surface, or lattice oxygen, and the reducing species. If this surface reaction proceeds extremely fast, a local equilibrium at the membrane surface could be reached and the mole fraction of O_2 close to the membrane surface can be computed from the mole fractions of the reducing species and their oxidation products using thermodynamics. For the CO and H_2 combustion

reactions, the equilibrium constants are given by:

$$CO + \tfrac{1}{2}O_2 \rightleftharpoons CO_2 \qquad K_{eq,I} = \frac{x_{CO_2}}{x_{CO}\sqrt{x_{O2}}} \tag{6.10}$$

$$H_2 + \tfrac{1}{2}O_2 \rightleftharpoons H_2O \qquad K_{eq,II} = \frac{x_{H_2O}}{x_{H_2}\sqrt{x_{O_2}}} \tag{6.11}$$

Inspecting these equilibrium constants, one can directly deduce that the O_2 mole fractions will be higher if CO_2 and H_2O are present and therefore the O_2 permeation flux will decrease. On the other hand, if the CO/CO_2 and H_2/H_2O ratios are kept constant while their mole fractions are varied (*e.g.* by dilution), the O_2 mole fraction and therefore the permeation flux should remain the same. To investigate wether local equilibrium prevails at the membrane surface, experiments were carried out, where different CO/CO_2 mixtures were used as sweeping gas and additionally experiments where a constant CO/CO_2 feed was diluted with He. In Figure 6.12 the O_2 permeation flux is given as a function of the inlet mole fraction of CO while sweeping with different CO/CO_2 mixtures. Although the O_2 permeation flux is still very high compared to sweeping with He, it is not as high as measured for CO/N_2 mixtures, see Figure 6.10, which indicates that CO_2 has an inhibiting effect. In Figure 6.13 the measured O_2 permeation flux is given as a function of the inlet mole fraction of CO while sweeping with a constant CO/CO_2 (3:2) feed, to which a He flow was added. Remarkably, the O_2 permeation flux remains almost constant, which indicates that the O_2 permeation rate is determined by the CO/CO_2 ratio rather than by the CO mole fraction. These observations strongly suggest that the O_2 mole fraction and thus the O_2 permeation flux is indeed determined by the local CO and CO_2 mole fractions and that thus indeed local equilibrium is reached and that the O_2 permeation is still determined by bulk diffusion.

Neglecting axial and radial concentration gradients inside the membrane tube and assuming that the O_2 mole fraction can be directly calculated from the CO and CO_2 mole fractions via Equation 6.10 (*i.e.* local thermodynamical equilibrium), the parameters n and P in the O_2 permeation flux expression (Equation 6.8) can be obtained by plotting the normalised O_2 permeation flux (normalised with respect to the membrane thickness) as a function of the calculated O_2 mole fraction at the tube outlet. For the the experimental results presented here, the temperature increase due to the released reaction heat was relatively small (10-30 K) and, as will be discussed later, the temperature dependency on the O_2 permeation rate is much smaller than for

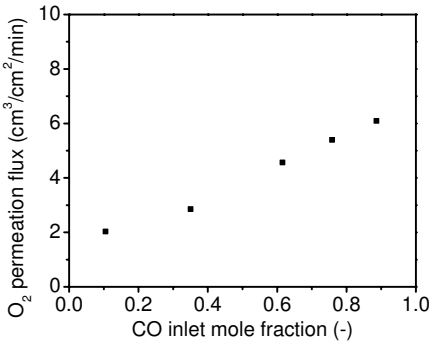

Figure 6.12: Measured O_2 permeation flux as a function of the inlet mole fraction of CO while sweeping with different CO/CO_2 mixtures ($\Phi_{v,tot}$ = 325 cm^3/min, Δr_m = 0.8 mm, T = 1223 K).

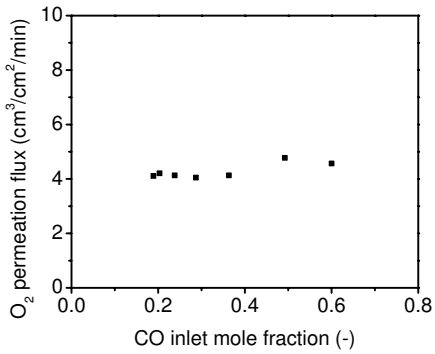

Figure 6.13: Measured O_2 permeation flux as a function of the inlet mole fraction of CO while adding He to a constant CO/CO_2 (3:2) feed ($\Phi_{v,CO/CO2}$ = 325 cm^3/min, Δr_m = 0.8 mm, T = 1223 K).

the experiments with the non-reducing sweeping gasses. Therefore, n and P were determined by plotting the normalised O_2 permeation flux as a function of the O_2 mole fraction calculated from the measured CO and CO_2 mole fractions for the case in which different CO/CO_2 mixtures were used as sweeping gas (see Figure 6.12 for the operating conditions). These measurements were selected because the differences in the CO and CO_2 mole fractions between the in- and outlet were relatively small, so that differential conditions were assured. Furthermore, because of the different CO/CO_2 inlet compositions in these experiments, also the variation in the O_2 mole fraction was largest for these experiments. In Figure 6.14 the measured, normalised O_2 permeation flux is given as a function of the calculated O_2 mole fraction at the tube outlet and also the fitted line by linear regression is included. The values that were obtained for P and n are $1.90 \cdot 10^{-3}$ cm^4/cm^2/min and -0.153, respectively. The value for n is considerably larger than the value that was found non-reducing atmospheres, showing that relatively small changes in the O_2 mole fraction in case of a reducing atmosphere have a more pronounced effect than would be expected from the permeation expression that was determined for non-reducing atmospheres. An explanation for this behaviour could be that the transport mechanism of lattice oxygen and electrons through the perovskite membrane becomes different at very low O_2

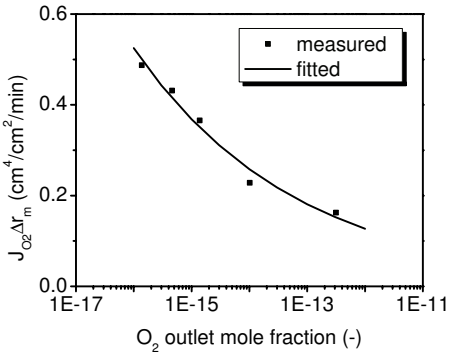

Figure 6.14: Measured (markers) and fitted (solid line) normalised permeation rate as a function of the O_2 mole fraction at the tube outlet while sweeping with different CO/CO_2 mixtures, see Figure 6.12 for the operating conditions.

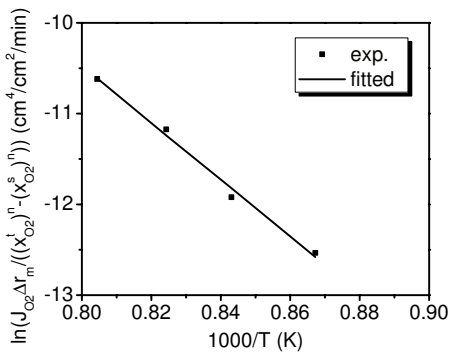

Figure 6.15: Measured (markers) and fitted (solid line) normalised O_2 permeation flux as function of temperature while sweeping with a CO/CO_2 mixture (3:2) ($\Delta r_m = 0.8$ mm, $\Phi_{v,tot} = 317$ cm^3/min).

mole fractions on the permeate side.

Finally, the temperature dependency of the O_2 permeation rate was investigated. In the presence of non-reducing atmospheres at the permeate side of the perovskite membrane, the temperature dependency of the O_2 permeation rate can be accounted for via an (apparent) activation energy. In the presence of reducing atmospheres at the permeate side of the membrane, the operating temperature will also influence the O_2 mole fraction at the membrane surface via the effect of the temperature on the local thermodynamic equilibrium. For CO and H_2 combustion the equilibrium constants decrease with increasing temperature and therefore the O_2 mole fraction increases, so that the O_2 permeation flux decreases. Consequently, the overall apparent activation energy can be significantly lower. To measure the temperature dependency of the O_2 rate, experiments were carried out where the oven temperature was raised in steps while sweeping with a constant CO_2/CO (3:2) feed. To determine the apparent activation energy the normalised O_2 permeation flux, $\ln\left[J_{O2}\Delta r_m/\left(\left(x^t_{O2,out}\right)^n - x^s_{O2}\right)^n\right]$, was plotted versus the inverse of the temperature in Figure 6.15 in order to account for the influence of the O_2 mole fraction along the membrane surface. Because of the relatively small increase in the CO_2 mole fraction, differential conditions were assured and therefore the O_2 mole fraction along the membrane surface was approximated

from the CO and CO_2 mole fractions at the tube outlet by assuming thermodynamic equilibrium. Via linear regression P_0 and E_a were determined as 260 kJ/mol and $2.01{\cdot}10^8$ $cm^4/cm^2/min$, respectively. The apparent activation energy differs somewhat from that measured for the non-reducing experiments, however, in view of the uncertainties in the interpretation because the local O_2 mole fractions at the membrane surface were not known exactly for both cases, the agreement is reasonably good.

6.2.6 Validation of permeation expression for reducing atmospheres

To validate the values that were obtained for n and P for the case when a reducing atmosphere is present at the permeate side of the perovskite membrane, a model very similar to that used before for the non-reducing case was employed, see Table 6.1 for the relevant equations. The CO and H_2 combustion reactions at the membrane surface were accounted for by assuming local thermodynamic equilibrium. Thermodynamic equilibrium was calculated in the model by implementing infinitely fast reaction kinetics according to:

$$R_{\mathrm{I}} = k_\infty x_{\mathrm{CO}} \left(x_{\mathrm{O_2}}\right)^{0.1} \left(1 - \frac{x_{\mathrm{CO_2}}}{x_{\mathrm{CO}}\sqrt{x_{\mathrm{O_2}}}K_{\mathrm{eq,I}}}\right) \tag{6.12}$$

$$R_{\mathrm{II}} = k_\infty x_{\mathrm{H_2}} \left(x_{\mathrm{O_2}}\right)^{0.1} \left(1 - \frac{x_{\mathrm{H_2O}}}{x_{\mathrm{H_2}}\sqrt{x_{\mathrm{O_2}}}K_{\mathrm{eq,II}}}\right) \tag{6.13}$$

The artificial reaction order in the O_2 mole fraction of 0.1 was included only to accelerate numerical convergence. For k_∞ a very high value was used so that eventually the term between the brackets in Equations 6.12-6.13 approaches zero and local equilibrium is obtained. The different r_j in Table 6.1 can thus be computed from:

$$\begin{aligned} r_{\mathrm{CO}} &= M_{\mathrm{CO}} \left(-R_{\mathrm{I}}\right) \\ r_{\mathrm{CO_2}} &= M_{\mathrm{CO_2}} \left(R_{\mathrm{I}}\right) \\ r_{\mathrm{H_2}} &= M_{\mathrm{H_2}} \left(-R_{\mathrm{II}}\right) \\ r_{\mathrm{H_2O}} &= M_{\mathrm{H_2O}} \left(R_{\mathrm{II}}\right) \\ r_{\mathrm{O_2}} &= M_{\mathrm{O_2}} \left(-\tfrac{1}{2}R_{\mathrm{I}} - \tfrac{1}{2}R_{\mathrm{II}}\right) \end{aligned} \tag{6.14}$$

With the model firstly simulations were carried out to verify the values for n, P_0 and E_a for the experimental data with which they were fitted, thereby again assessing the influence of axial and radial concentration gradients in the differential

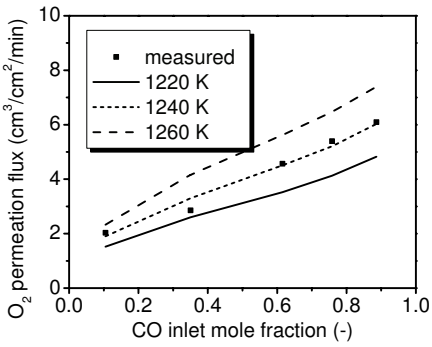

Figure 6.16: Measured (markers) O_2 permeation flux as a function of the CO mole fraction while sweeping different CO/CO_2 mixtures, see Figure 6.12 for the operating conditions. Included are the predicted O_2 permeation fluxes for different temperatures (lines).

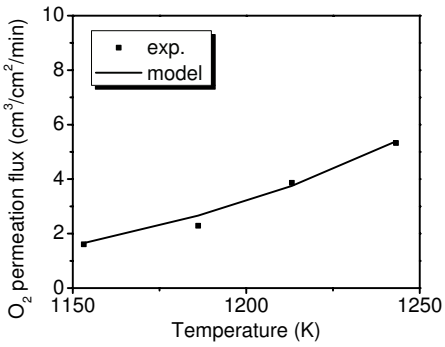

Figure 6.17: Measured (markers) and predicted (lines) O_2 permeation flux as a function of the temperature while sweeping with a CO/CO_2 (3:2) mixture, see Figure 6.15 for the operating conditions.

experiments. In Figure 6.16 the measured and predicted O_2 permeation fluxes are given as a function of the CO inlet mole fraction for different temperatures, while sweeping with different CO/CO_2 mixtures (see Figure 6.12 for the operating conditions), showing that the derived O_2 permeation expression describes the experiments very well. Subsequently, simulations were performed for different temperatures using the experimentally determined activation energy of 260 kJ/mol to assess the temperature sensitivity of the results. The influence of the temperature on the calculated O_2 permeation rate is remarkably small and the apparent activation energy, obtained by plotting $\ln(J_{O2})$ versus $1/T$, is only about 150 kJ/mol. This is explained by the decreasing equilibrium constant of the combustion reaction when the temperature is increased. Moreover, the assumption that the influence of the temperature was small with respect to the O_2 permeation data used to determine the values of n and P, was indeed justified. In Figure 6.17 the measured and predicted O_2 permeation fluxes are given as a function of the temperature while sweeping with a CO/CO_2 mixture (see Figure 6.15 for the operating conditions). Also for this case the measured and predicted O_2 fluxes correspond very well.

The good agreement between the measured and predicted O_2 permeation fluxes

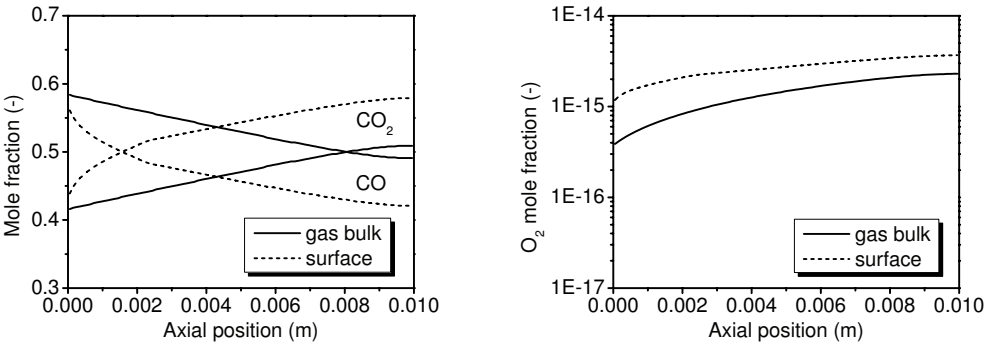

Figure 6.18: Predicted axial CO, CO_2 (left) and O_2 (right) mole fractions while sweeping with a CO/CO2 (3:2) mixture ($\Phi_{v,tot}$ = 325 cm^3/min, Δr_m = 0.8 mm, T = 1223 K).

can be understood from the axial profiles of the O_2 mole fractions at the membrane surface and in the gas bulk, presented in Figure 6.18. As expected, the CO_2 and O_2 mole fractions at the membrane surface are somewhat higher than those in the gas bulk and *viceversa* for the CO mole fraction, but the differences are small. On average the O_2 mole fraction at the membrane surface is very similar to that in the gas bulk at the end of the membrane tube and as a result the O_2 permeation fluxes are very well predicted.

In Figure 6.13 it was observed that the O_2 permeation flux hardly changes when a CO/CO_2 feed is diluted with He. To verify this observation, simulations were performed taking the same operating conditions. In Figure 6.19 the simulation results are compared with the measurements. Indeed the same trend is observed and the permeation fluxes are predicted extremely well.

To validate the permeation expression for experiments where large axial concentration gradients prevailed, simulations were carried out for the case where CO/N_2 mixtures were used as a sweeping gas and a membrane thickness of 0.4 and 0.8 mm, taking the same operating conditions of the experimental results presented in Figure 6.11. The measured and predicted O_2 permeation fluxes are given as a function of the inlet mole fraction of CO in Figure 6.20. Generally the model predicts lower fluxes than the measured fluxes, although the trends are in good agreement. The deviation might be attributed to temperature effects, especially for the thinner membrane at

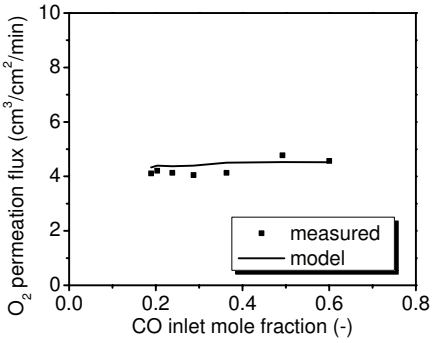

Figure 6.19: Measured (markers) and predicted (line) O_2 permeation flux as a function of the inlet mole fraction of CO while adding He to a constant CO/CO_2 (3:2) feed, see Figure 6.13 for the operating conditions.

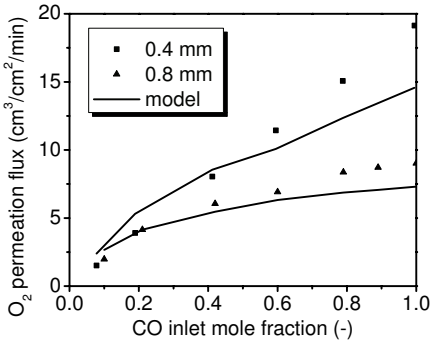

Figure 6.20: Measured (markers) and predicted (lines) O_2 permeation flux as a function of the CO inlet mole fraction for a membrane thickness of 0.4 and 0.8 mm while sweeping with CO/N_2 mixtures, see Figure 6.11 for the operating conditions.

high CO inlet fractions for which the permeation rate is highest. Another reason for the deviation could be related to the larger axial concentration gradients, so that an accurate prediction of the axial profile of the O_2 mole fractions at the membrane surface becomes much more important. In Figure 6.21 the axial concentration profiles are given for a typical case. The difference between the O_2 mole fractions at the beginning and at the end of the membrane is more than a factor of 10, both at the membrane surface and in the gas bulk, whereas for the experiments with a CO/CO_2 sweeping mixture this difference was less than a factor of 2 (*cf.* Figure 6.18).

Finally, the model was used to interpret the experiments where H_2/N_2 mixtures were used as sweeping gas. Due to experimental limitations (H_2O condensation) it was not possible to determine values for P and n based on measurements with H_2/H_2O mixtures, but principally those values should be very similar to those determined from the experiments with CO/CO_2 mixtures, because these parameters were determined from the equilibrium O_2 mole fractions. In Figure 6.22 the measured and predicted O_2 permeation fluxes are given as a function of the H_2 mole fraction and, remarkably, the agreement is very well. This confirms once more that for the perovskite studied in this work, the O_2 permeation rate is indeed determined by bulk diffusion and that

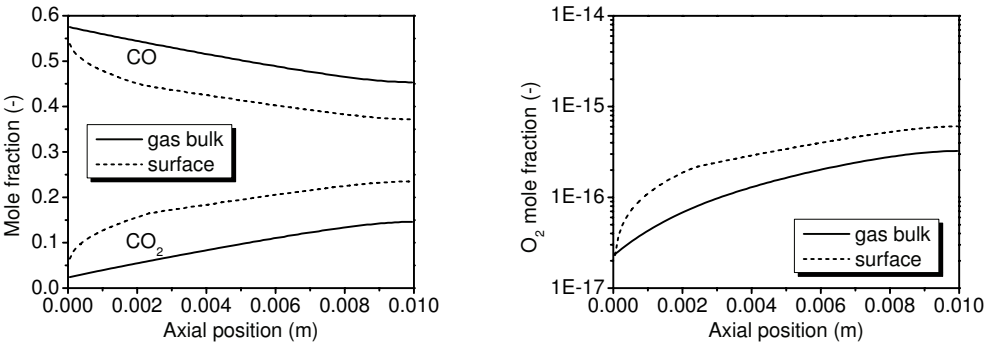

Figure 6.21: Predicted axial CO, CO_2 (left) and O_2 (right) mole fractions while sweeping with a CO/N_2 (3:2) mixture ($\Phi_{v,tot} = 200$ cm^3/min, $\Delta r_m = 0.8$ mm, T = 1223 K).

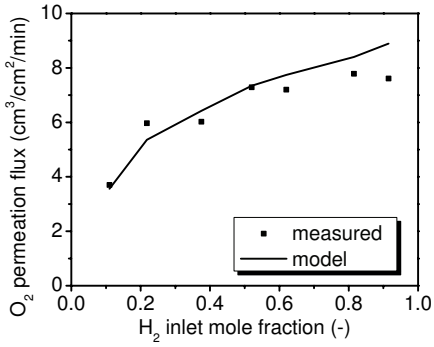

Figure 6.22: Measured (markers) and predicted (line) O_2 permeation flux as a function of the H_2 inlet mole fraction while sweeping with different H_2/N_2 mixtures ($\Phi_{v,tot} = 250$ cm^3/min, $\Delta r_m = 0.8$ mm, $T = 1223$ K).

the O_2 mole fractions on the permeate side of the membrane can simply be calculated by assuming local thermodynamic equilibrium.

6.3 Simulation study of the RFCMR concept with perovskite membranes

In the previous section the O_2 permeation through a perovskite membrane was studied experimentally as a function of the temperature and gas composition at the permeate side of the membrane and a correlation to predict the O_2 permeation rate for these conditions was determined. In this section the conceptual feasibility of the RFCMR concept with perovskite membranes is investigated by means of a simulation study using a model in which the experimentally determined expression for the O_2 permeation rate has been incorporated. Because the RFCMR is an adiabatic reactor and because the O_2 permeation rate strongly depends on the temperature and O_2 partial pressure on the permeate side, runaways may occur if no precautions are taken to control the axial temperature profile. Therefore, firstly the influence of axial concentration gradients on the O_2 permeation rate and on the reactor behaviour will be investigated with HSFM simulations in which the temperature dependency of the O_2 permeation rate is ignored. With these simulations also the influence of a number of design parameters such as the membrane length and plateau temperature will be investigated. Subsequently, the influence of the apparent activation energy of the O_2 permeation rate on the reactor behaviour will addressed with HSFM simulations. Finally, the conceptual feasibility of the RFCMR concept with perovskite membranes will be demonstrated with DM simulations, in which the dynamic behaviour of the reactor is fully accounted for.

6.3.1 Reactor model

To simulate the RFCMR concept with perovskite membranes, a model very similar to that used in Chapter 4 was employed and the same shell-and-tube geometry was considered. In the syngas compartment possible radial mass transfer limitations between the gas bulk, the membrane surface and the catalyst surface have been taken into account. The H_2O injection flux was assumed to be constant along the perovskite membrane and was calculated in such a way that all H_2O is injected to the syngas compartment (*i.e.* no H_2O by-pass). Furthermore, it was assumed that the H_2O is injected via a porous membrane inside the syngas compartment, where temperature differences between the H_2O and syngas compartments were neglected in view of the small diameter of the porous membranes and support tubes. The mass

Table 6.2: Mass conservations equations of the DM and HSFM.

Shell compartment:

$$\begin{aligned}
\frac{\partial\left(\rho_{\mathrm{g}}^{\mathrm{s}} v_{\mathrm{g}}^{\mathrm{s}}\right)}{\partial z} &= -\frac{2\pi r_{\mathrm{i}}}{s_{\mathrm{cell}}^2 - \pi r_{\mathrm{o}}^2} M_{\mathrm{O_2}} J_{\mathrm{O_2}} \\
\rho_{\mathrm{g}}^{\mathrm{s}} v_{\mathrm{g}}^{\mathrm{s}} \frac{\partial w_{\mathrm{j,g}}^{\mathrm{s}}}{\partial z} &= \frac{\partial}{\partial z}\left(\rho_{\mathrm{g}}^{\mathrm{s}} D_{\mathrm{ax,j}}^{\mathrm{s}} \frac{\partial w_{\mathrm{j,g}}^{\mathrm{s}}}{\partial z}\right) + r_{\mathrm{j,g}}^{\mathrm{s}} + \frac{2\pi r_{\mathrm{i}}}{s_{\mathrm{cell}}^2 - \pi r_{\mathrm{o}}^2} w_{\mathrm{j,g}}^{\mathrm{s}} M_{\mathrm{O_2}} J_{\mathrm{O_2}} \\
\rho_{\mathrm{g}}^{\mathrm{s}} v_{\mathrm{g}}^{\mathrm{s}} \frac{\partial w_{\mathrm{O_2,g}}^{\mathrm{s}}}{\partial z} &= \frac{\partial}{\partial z}\left(\rho_{\mathrm{g}}^{\mathrm{s}} D_{\mathrm{ax,j}}^{\mathrm{s}} \frac{\partial w_{\mathrm{O_2,g}}^{\mathrm{s}}}{\partial z}\right) + r_{\mathrm{O_2,g}}^{\mathrm{s}} + \frac{2\pi r_{\mathrm{i}}}{s_{\mathrm{cell}}^2 - \pi r_{\mathrm{o}}^2} \left(w_{\mathrm{O_2,g}}^{\mathrm{s}} - 1\right) M_{\mathrm{O_2}} J_{\mathrm{O_2}}
\end{aligned}$$

Tube compartment, total mass:

$$\begin{aligned}
\frac{\partial\left(\rho_{\mathrm{g}}^{\mathrm{t}} v_{\mathrm{g}}^{\mathrm{t}}\right)}{\partial z} &= \frac{2}{r_{\mathrm{i}}}\left(M_{\mathrm{O_2}} J_{\mathrm{O_2}} + M_{\mathrm{H_2O}} J_{\mathrm{H_2O}}\right) \\
\frac{\partial\left(\rho_{\mathrm{H_2O}}^{\mathrm{t}} v_{\mathrm{H_2O}}^{\mathrm{t}}\right)}{\partial z} &= -\frac{2}{r_{\mathrm{i}}}\left(M_{\mathrm{H_2O}} J_{\mathrm{H_2O}}\right)
\end{aligned}$$

Tube compartment, gas bulk:

$$\begin{aligned}
\rho_{\mathrm{g}}^{\mathrm{t}} v_{\mathrm{g}}^{\mathrm{t}} \frac{\partial w_{\mathrm{j,g}}^{\mathrm{t}}}{\partial z} &= \frac{\partial}{\partial z}\left(\rho_{\mathrm{g}}^{\mathrm{t}} D_{\mathrm{ax,j}}^{\mathrm{t}} \frac{\partial w_{\mathrm{j,g}}^{\mathrm{t}}}{\partial z}\right) + \frac{6\left(1-\varepsilon_{\mathrm{g}}^{\mathrm{t}}\right)}{d_{\mathrm{p}}^{\mathrm{t}}} j_{\mathrm{j,g-s}}^{\mathrm{t}} + \frac{2}{r_{\mathrm{i}}} j_{\mathrm{j,g-m}}^{\mathrm{t}} \\
&\quad - w_{\mathrm{j,g}}^{\mathrm{t}} \frac{2}{r_{\mathrm{i}}} J_{\mathrm{H_2O}} M_{\mathrm{H_2O}} \\
\rho_{\mathrm{g}}^{\mathrm{t}} v_{\mathrm{g}}^{\mathrm{t}} \frac{\partial w_{\mathrm{H_2O,g}}^{\mathrm{t}}}{\partial z} &= \frac{\partial}{\partial z}\left(\rho_{\mathrm{g}}^{\mathrm{t}} D_{\mathrm{ax,H_2O}}^{\mathrm{t}} \frac{\partial w_{\mathrm{H_2O,g}}^{\mathrm{t}}}{\partial z}\right) + \frac{6\left(1-\varepsilon_{\mathrm{g}}^{\mathrm{t}}\right)}{d_{\mathrm{p}}^{\mathrm{t}}} j_{\mathrm{H_2O,g-s}}^{\mathrm{t}} + \frac{2}{r_{\mathrm{i}}} j_{\mathrm{H_2O,g-m}}^{\mathrm{t}} \\
&\quad + \left(1 - w_{\mathrm{H_2O,g}}^{\mathrm{t}}\right) \frac{2}{r_{\mathrm{i}}} J_{\mathrm{H_2O}} M_{\mathrm{H_2O}}
\end{aligned}$$

Tube compartment, membrane surface:

$$\begin{aligned}
0 &= -\frac{2}{r_{\mathrm{i}}} j_{\mathrm{j,g-m}}^{\mathrm{t}} + r_{\mathrm{j,m}}^{\mathrm{t}} - \frac{2}{r_{\mathrm{i}}} w_{\mathrm{j,m}}^{\mathrm{t}} J_{\mathrm{O_2}} M_{\mathrm{O_2}} \\
0 &= -\frac{2}{r_{\mathrm{i}}} j_{\mathrm{O_2,g-m}}^{\mathrm{t}} + r_{\mathrm{O_2,m}}^{\mathrm{t}} + \frac{2}{r_{\mathrm{i}}}\left(1 - w_{\mathrm{O_2,m}}^{\mathrm{t}}\right) J_{\mathrm{O_2}} M_{\mathrm{O_2}}
\end{aligned}$$

Tube compartment, catalyst surface:

$$0 = -\frac{6\left(1-\varepsilon_{\mathrm{g}}^{\mathrm{t}}\right)}{d_{\mathrm{p}}^{\mathrm{t}}} j_{\mathrm{j,g-s}}^{\mathrm{t}} + r_{\mathrm{j,s}}^{\mathrm{t}}$$

Table 6.3: Energy conservation equations of the DM.

$$\left(\varepsilon_{\mathrm{g}}^{\mathrm{s}}\rho_{\mathrm{g}}^{\mathrm{s}}C_{\mathrm{p,g}}^{\mathrm{s}}+\rho_{\mathrm{bulk}}^{\mathrm{s}}C_{\mathrm{p,s}}^{\mathrm{s}}\right)\frac{\partial T^{\mathrm{s}}}{\partial t}=-\rho_{\mathrm{g}}^{\mathrm{s}}v_{\mathrm{g}}^{\mathrm{s}}C_{\mathrm{p,g}}^{\mathrm{s}}\frac{\partial T^{\mathrm{s}}}{\partial z}+\frac{\partial}{\partial z}\left(\lambda_{\mathrm{eff}}^{\mathrm{s}}\frac{\partial T^{\mathrm{s}}}{\partial z}\right)$$
$$-\sum_{\mathrm{j}}\left(\frac{r_{\mathrm{j,g}}^{\mathrm{s}}}{M_{\mathrm{j}}}H_{\mathrm{j,g}}^{\mathrm{s}}\right)+\frac{2\pi r_{\mathrm{o}}\alpha^{\mathrm{s-tw}}}{s_{\mathrm{cell}}^{2}-\pi r_{\mathrm{o}}^{2}}\left(T^{\mathrm{tw}}-T^{\mathrm{s}}\right)$$

$$\left(\varepsilon_{\mathrm{g}}^{\mathrm{t}}\left(\rho_{\mathrm{g}}^{\mathrm{t}}C_{\mathrm{p,g}}^{\mathrm{t}}+\rho_{\mathrm{H_2O}}^{\mathrm{t}}C_{\mathrm{p,H_2O}}^{\mathrm{t}}\right)+\rho_{\mathrm{bulk}}^{\mathrm{t}}C_{\mathrm{p,s}}^{\mathrm{t}}\right)\frac{\partial T^{\mathrm{t}}}{\partial t}=$$
$$-\left(\rho_{\mathrm{g}}^{\mathrm{t}}v_{\mathrm{g}}^{\mathrm{t}}C_{\mathrm{p,g}}^{\mathrm{t}}+\rho_{\mathrm{H_2O}}^{\mathrm{t}}v_{\mathrm{H_2O}}^{\mathrm{t}}C_{\mathrm{p,H_2O}}^{\mathrm{t}}\right)\frac{\partial T^{\mathrm{t}}}{\partial z}+\frac{\partial}{\partial z}\left(\lambda_{\mathrm{eff}}^{\mathrm{t}}\frac{\partial T^{\mathrm{t}}}{\partial z}\right)$$
$$-\sum_{\mathrm{j}}\left(\frac{r_{\mathrm{j,s}}^{\mathrm{t}}+r_{\mathrm{j,m}}^{\mathrm{t}}}{M_{\mathrm{j}}}H_{\mathrm{j,g}}^{\mathrm{t}}\right)+\frac{2\alpha^{\mathrm{t-tw}}}{r_{\mathrm{i}}}\left(T^{\mathrm{tw}}-T^{\mathrm{t}}\right)$$

$$\rho_{\mathrm{s}}^{\mathrm{tw}}C_{\mathrm{p,s}}^{\mathrm{tw}}\frac{\partial T^{\mathrm{tw}}}{\partial t}=\frac{\partial}{\partial z}\left(\lambda^{\mathrm{tw}}\frac{\partial T^{\mathrm{tw}}}{\partial z}\right)+\frac{2r_{\mathrm{o}}\alpha^{\mathrm{s-tw}}}{r_{\mathrm{o}}^{2}-r_{\mathrm{i}}^{2}}\left(T^{\mathrm{s}}-T^{\mathrm{tw}}\right)+\frac{2r_{\mathrm{i}}\alpha^{\mathrm{t-tw}}}{r_{\mathrm{o}}^{2}-r_{\mathrm{i}}^{2}}\left(T^{\mathrm{t}}-T^{\mathrm{tw}}\right)$$

conservation equations for the DM are given in Table 6.2. For the HSFM, two sets of these equations are solved: once for each direction (see also Chapter 4). The energy conservation equations for the DM are listed in Table 6.3 and those for the HSFM in Table 6.4. The initial and boundary conditions, the reaction rates in the catalyst particles for both the shell and tube compartments and also the constitutive relations for the different mass and heat transport processes and the correlations to describe the physical properties were calculated as described in Chapter 4. The mass transfer from the membrane surface to the gas bulk was calculated according to the Maxwell-Stefan description (see Appendix 4.A) and the wall-to-fluid mass transfer coefficient was calculated from the correlation of Yagi and Wakao (1959):

$$\begin{aligned} Re<40 \qquad & k_{\mathrm{g}}=\frac{0.6}{\varepsilon_{\mathrm{g}}}v_{\mathrm{g}}Re^{-0.5}Sc^{-2/3} \\ Re>40 \qquad & k_{\mathrm{g}}=\frac{0.2}{\varepsilon_{\mathrm{g}}}v_{\mathrm{g}}Re^{-0.2}Sc^{-2/3} \end{aligned} \tag{6.15}$$

The O_2 permeation rate through the perovskite membrane was described with the expression that was derived in the previous section, but now based on relative partial pressures rather than mole fractions (see also Equation 6.2):

$$J_{\mathrm{O_2}}=\frac{P_0}{\Delta r_{\mathrm{m}}}\exp\left(-\frac{E_{\mathrm{a}}}{R_{\mathrm{g}}T}\right)\left[\left(P_{\mathrm{O_2,m}}^{\mathrm{t}}\right)^{\mathrm{n}}-\left(P_{\mathrm{O_2}}^{\mathrm{s}}\right)^{\mathrm{n}}\right] \tag{6.16}$$

Table 6.4: Energy conservation equations of the HSFM.

$$\left(\frac{1}{2}\varepsilon_{\mathrm{g}}^{\mathrm{s}}\left(\rho_{\mathrm{g},\rightarrow}^{\mathrm{s}}C_{\mathrm{p,g},\rightarrow}^{\mathrm{s}}+\rho_{\mathrm{g},\leftarrow}^{\mathrm{s}}C_{\mathrm{p,g},\leftarrow}^{\mathrm{s}}\right)+\rho_{\mathrm{bulk}}^{\mathrm{s}}C_{\mathrm{p,s}}^{\mathrm{s}}\right)\frac{\partial T^{\mathrm{s}}}{\partial t}=-\frac{1}{2}\left(\rho_{\mathrm{g},\rightarrow}^{\mathrm{s}}v_{\mathrm{g},\rightarrow}^{\mathrm{s}}C_{\mathrm{p,g},\rightarrow}^{\mathrm{s}}+\rho_{\mathrm{g},\leftarrow}^{\mathrm{s}}v_{\mathrm{g},\leftarrow}^{\mathrm{s}}C_{\mathrm{p,g},\leftarrow}^{\mathrm{s}}\right)\frac{\partial T^{\mathrm{s}}}{\partial z}$$

$$+\frac{1}{2}\frac{\partial}{\partial z}\left(\left(\lambda_{\mathrm{eff},\rightarrow}^{\mathrm{s}}+\lambda_{\mathrm{eff},\leftarrow}^{\mathrm{s}}\right)\frac{\partial T^{\mathrm{s}}}{\partial z}\right)-\frac{1}{2}\sum_{\mathrm{j}}\left(\frac{r_{\mathrm{j,g},\rightarrow}^{\mathrm{s}}}{M_{\mathrm{j}}}H_{\mathrm{j,g},\rightarrow}^{\mathrm{s}}+\frac{r_{\mathrm{j,g},\leftarrow}^{\mathrm{s}}}{M_{\mathrm{j}}}H_{\mathrm{j,g},\leftarrow}^{\mathrm{s}}\right)+\frac{\pi r_{\mathrm{o}}\left(\alpha_{\rightarrow}^{\mathrm{s-tw}}+\alpha_{\leftarrow}^{\mathrm{s-tw}}\right)}{s_{\mathrm{cell}}^{2}-\pi r_{\mathrm{o}}^{2}}\left(T^{\mathrm{tw}}-T^{\mathrm{s}}\right)$$

$$\left(\frac{1}{2}\varepsilon_{\mathrm{g}}^{\mathrm{t}}\left(\rho_{\mathrm{g},\rightarrow}^{\mathrm{t}}C_{\mathrm{p,g},\rightarrow}^{\mathrm{t}}+\rho_{\mathrm{g},\leftarrow}^{\mathrm{t}}C_{\mathrm{p,g},\leftarrow}^{\mathrm{t}}+\rho_{\mathrm{H_2O},\rightarrow}^{\mathrm{t}}C_{\mathrm{p,H_2O},\rightarrow}^{\mathrm{t}}+\rho_{\mathrm{H_2O},\leftarrow}^{\mathrm{t}}C_{\mathrm{p,H_2O},\leftarrow}^{\mathrm{t}}\right)+\rho_{\mathrm{bulk}}^{\mathrm{t}}C_{\mathrm{p,s}}^{\mathrm{t}}\right)\frac{\partial T^{\mathrm{t}}}{\partial t}=$$

$$-\frac{1}{2}\left(\rho_{\mathrm{g},\rightarrow}^{\mathrm{t}}v_{\mathrm{g},\rightarrow}^{\mathrm{t}}C_{\mathrm{p,g},\rightarrow}^{\mathrm{t}}+\rho_{\mathrm{g},\leftarrow}^{\mathrm{t}}v_{\mathrm{g},\leftarrow}^{\mathrm{t}}C_{\mathrm{p,g},\leftarrow}^{\mathrm{t}}+\rho_{\mathrm{H_2O},\rightarrow}^{\mathrm{t}}v_{\mathrm{H_2O},\rightarrow}^{\mathrm{t}}C_{\mathrm{p,H_2O},\rightarrow}^{\mathrm{t}}+\rho_{\mathrm{H_2O},\leftarrow}^{\mathrm{t}}v_{\mathrm{H_2O},\leftarrow}^{\mathrm{t}}C_{\mathrm{p,H_2O},\leftarrow}^{\mathrm{t}}\right)\frac{\partial T^{\mathrm{t}}}{\partial z}$$

$$+\frac{1}{2}\frac{\partial}{\partial z}\left(\left(\lambda_{\mathrm{eff},\rightarrow}^{\mathrm{t}}+\lambda_{\mathrm{eff},\leftarrow}^{\mathrm{t}}\right)\frac{\partial T^{\mathrm{t}}}{\partial z}\right)-\frac{1}{2}\sum_{\mathrm{j}}\left(\frac{r_{\mathrm{j,s},\rightarrow}^{\mathrm{t}}+r_{\mathrm{j,m},\rightarrow}^{\mathrm{t}}}{M_{\mathrm{j}}}H_{\mathrm{j,g},\rightarrow}^{\mathrm{t}}+\frac{r_{\mathrm{j,s},\leftarrow}^{\mathrm{t}}+r_{\mathrm{j,m},\leftarrow}^{\mathrm{t}}}{M_{\mathrm{j}}}H_{\mathrm{j,g},\leftarrow}^{\mathrm{t}}\right)+\frac{\left(\alpha_{\rightarrow}^{\mathrm{t-tw}}+\alpha_{\leftarrow}^{\mathrm{t-tw}}\right)}{r_{\mathrm{i}}}\left(T^{\mathrm{tw}}-T^{\mathrm{t}}\right)$$

$$\rho_{\mathrm{s}}^{\mathrm{tw}}C_{\mathrm{p,s}}^{\mathrm{tw}}\frac{\partial T^{\mathrm{tw}}}{\partial t}=\frac{\partial}{\partial z}\left(\lambda^{\mathrm{tw}}\frac{\partial T^{\mathrm{tw}}}{\partial z}\right)+\frac{r_{\mathrm{o}}\left(\alpha_{\rightarrow}^{\mathrm{s-tw}}+\alpha_{\leftarrow}^{\mathrm{s-tw}}\right)}{r_{\mathrm{o}}^{2}-r_{\mathrm{i}}^{2}}\left(T^{\mathrm{s}}-T^{\mathrm{tw}}\right)+\frac{r_{\mathrm{i}}\left(\alpha_{\rightarrow}^{\mathrm{t-tw}}+\alpha_{\leftarrow}^{\mathrm{t-tw}}\right)}{r_{\mathrm{o}}^{2}-r_{\mathrm{i}}^{2}}\left(T^{\mathrm{t}}-T^{\mathrm{tw}}\right)$$

To calculate the O_2 partial pressures at the membrane surface from the CO/CO_2 and H_2/H_2O mole fractions via the equilibrium constants, the equilibrium kinetics given in Equations 6.12-6.14 were adopted. The model equations were solved with the very efficient numerical method described in Chapter 3.

6.3.2 HSFM simulation results: influence of axial concentration gradients

In the RFCMR concept with porous membranes, the O_2 is fed with a dead-end construction, so that a stoichiometric feed of CH_4 and O_2 can be easily established. The experimental results presented in the previous section revealed that the O_2 permeation rate through perovskite membranes strongly depends on the temperature and the O_2 partial pressures at the membrane surface. Therefore, to obtain a stoichiometric feed of CH_4 and O_2 for the RFCMR concept with perovskite membranes, the plateau temperature and membrane length have to be selected simultaneously.

To determine for which plateau temperatures and membrane lengths stoichiometric O_2/CH_4 feeds can be achieved, HSFM simulations were performed. In these simulations the value for T in Equation 6.16 was kept at a constant value to eliminate the temperature dependency of the O_2 permeation rate to avoid runaways. The influence of this assumption will be examined in the next subsection. The simulation parameters were very similar to those used in Chapter 4 and the most important parameters are listed in Table 6.5. An air inlet pressure of 6 bar was required to overcome the axial pressure drop in the air compartment, which is significantly larger than the pressure drop in the O_2 compartment in the RFCMR with porous membranes

Table 6.5: Parameters used in the HSFM simulations of the RFCMR concept with perovskite membranes.

d_p	$3 \cdot 10^{-3}$ m	P_0	$2.01{\cdot}10^8$ cm^4/cm^2/min
E_a	260 kJ/mol	r_i	0.0121 m
$L_{\mathrm{Pt/Al_2O_3}}$	2 m	r_o	0.0125 m
L_reactor	6 m	s_cell	0.0313 m
n	-0.153	$w^\mathrm{t}_{\mathrm{g,CH4,in}}$	1
p^s_in	6 bar	$w^\mathrm{s}_{\mathrm{g,O2,in}}$	0.232
p^t_in	20 bar	$\rho^\mathrm{s}_{\mathrm{g,in}} v^\mathrm{s}_{\mathrm{g,in}}$	4.07 kg/m^2/s

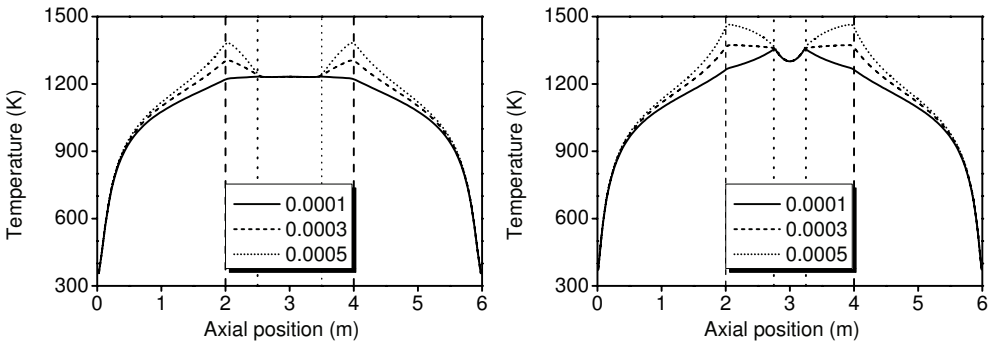

Figure 6.23: Axial temperature profiles in the RFCMR with perovskite membranes calculated with the HSFM for different values of $w^{\mathrm{s}}_{\mathrm{g,CH4,in}}$. Left: T = 1243 K, L_{membrane} = 1 m, $R_{\mathrm{H2O/O2}}$ = 0.348. Right: T = 1323 K, L_{membrane} = 0.5 m, $R_{\mathrm{H2O/O2}}$ = 0.200. The combustion catalyst section is located between the dashed lines and the membrane section between the dotted lines.

because of the larger flow rate due to the N_2 dilution and lower pressure. Obviously lower axial pressure drops can be achieved when larger particles are used in the air compartment.

To use the excess reaction heat of the CPO reaction for additional syngas production via steam reforming and to maintain the centre of the reactor at a plateau temperature close to the desired temperature T, H_2O is injected and the CH_4 feed flow rate is increased. To relate the H_2O and CH_4 feed flow rates to the air feed flow rate to achieve overall autothermal reforming, the parameter $R_{\mathrm{H2O/O2}}$ is introduced, which is defined as the ratio of the molar amount of CH_4 that is to be converted via steam reforming and the total amount that is to be converted. With this parameter, the desired feed mass fluxes of CH_4 and H_2O can be expressed as:

$$\begin{aligned}\rho^{\mathrm{t}}_{\mathrm{g}} v^{\mathrm{t}}_{\mathrm{g}} &= \rho^{\mathrm{s}}_{\mathrm{g}} v^{\mathrm{s}}_{\mathrm{g}} w^{\mathrm{s}}_{\mathrm{g,O_2}} \frac{s^2_{\mathrm{cell}} - \pi r^2_{\mathrm{i}}}{\pi r^2_{\mathrm{o}}} \frac{2M_{\mathrm{CH_4}}}{M_{\mathrm{O_2}}} \left(1 + R_{\mathrm{H_2O/O_2}}\right) \\ \rho^{\mathrm{t}}_{\mathrm{H_2O}} v^{\mathrm{t}}_{\mathrm{H_2O}} &= \rho^{\mathrm{s}}_{\mathrm{g}} v^{\mathrm{s}}_{\mathrm{g}} w^{\mathrm{s}}_{\mathrm{g,O_2}} \frac{s^2_{\mathrm{cell}} - \pi r^2_{\mathrm{o}}}{\pi r^2_{\mathrm{i}}} \frac{2M_{\mathrm{CH_4}}}{M_{\mathrm{O_2}}} R_{\mathrm{H_2O/O_2}}\end{aligned} \tag{6.17}$$

Using the simulation parameters listed in Table 6.5, it was found that when using T = 1243 K (the temperature at which most experiments were performed in the previous section) in Equation 6.16, a membrane length of 1 m and a $R_{\mathrm{H2O/O2}}$ of 0.348

are required to achieve a stoichiometric feed and to obtain a plateau temperature of about 1243 K. Similarly, for $T = 1323$ K, a membrane length of 0.5 m and a $R_{\mathrm{H2O/O2}}$ of 0.200 are required. This is illustrated in Figure 6.23 where the axial temperature profiles in the tube compartment are given for both cases for different values of $w^{\mathrm{s}}_{\mathrm{g,CH4,in}}$ (the amount of CH_4 that is added to the air feed). It is observed that a very flat temperature plateau is established in the centre of reactor for $T = 1243$ K, whereas for $T = 1323$ K a small temperature dip is observed in the centre of the membrane section, which was also observed in the HSFM simulations of the RFCMR with porous membranes (Chapter 4).

Also similar to the RFCMR with porous membranes, the value for $w^{\mathrm{s}}_{\mathrm{g,CH4,in}}$ hardly affects the temperature in the membrane section of the reactor and, moreover, a value as low as 0.0003 is already sufficient to establish the desired temperature plateau. This value is a factor of 3 lower than the values reported for the RFCMR with porous membranes, because of the the larger flow rate of the air feed in the RFCMR with perovskite membranes (the pure O_2 feed flow rate was 1 kg/m/s^2 for both cases).

The dip in the axial temperature profile that is observed in Figure 6.23 in the centre of the membrane section for $T = 1323$ K may suggest that for this case the O_2 permeation rate is smaller in the centre of the membrane section than at the beginning and at the end of this section. Surprisingly, the O_2 partial pressure is actually the lowest in the centre of the membrane section and accordingly the O_2 permeation flux the largest. This is illustrated in Figure 6.24 where the O_2 partial pressure and the O_2 permeation flux are given as a function of the relative axial position along the membrane for both cases studied. The discrepancy between the observed and expected axial temperature profiles is caused by complex interactions between local temperatures, concentrations and equilibrium constants, which will be discussed below in more detail.

As is illustrated in Figure 6.25, large axial concentration gradients prevail along the membrane for all species, which are caused by the distributive feeding of H_2O and O_2, causing large differences in the reaction rates of the combustion and reforming reactions. As a result also the reaction heat that is produced or consumed varies enormously along the membrane. In Figure 6.26 the reaction heat that is produced/consumed locally is given as a function of the relative axial position along the membrane for the forward and backward direction. For the forward direction, heat

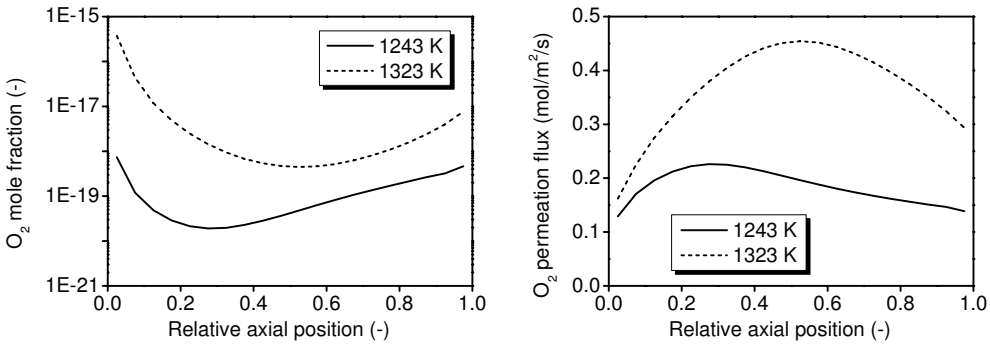

Figure 6.24: O_2 mole fraction at the membrane surface (left) and O_2 permeation flux (right) as a function of the relative axial position along the membrane in the RFCMR with perovskite membranes calculated with the HSFM (forward direction) for T = 1243 K and T = 1323 K ($w^{\mathrm{s}}_{\mathrm{g,CH4,in}} = 0.0003$).

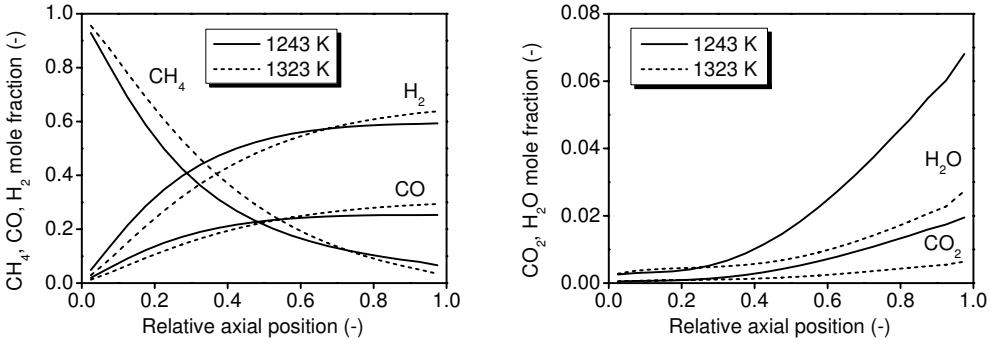

Figure 6.25: CH_4, CO, H_2 (left) and CO_2, H_2O (right) mole fractions in the bulk as a function of the relative axial position along the membrane in the RFCMR with perovskite membranes calculated with the HSFM (forward direction) for T = 1243 K and T = 1323 K ($w^{\mathrm{s}}_{\mathrm{g,CH4,in}} = 0.0003$).

is consumed in the first half of the membrane section and heat is produced in the second half. For the backward direction the exact opposite can be observed. In the HSFM the sum of the reaction heats of both directions, also included in Figure 6.26, determines the local temperature in the tube compartment (see Table 6.4). For the case with T = 1243, the sum of the reaction heats is practically zero all along the

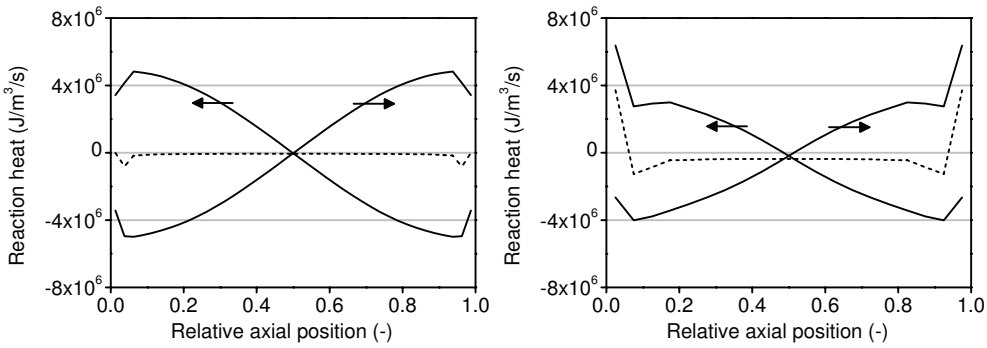

Figure 6.26: Axial reaction heat profiles in the RFCMR with perovskite membranes for the forward (→) and backward (←) directions (solid lines) calculated with the HSFM for $T = 1243$ K (left) and $T = 1323$ K (right). Also included is the sum of the reactions heats of the forward and backward direction (dashed line).

membrane, which explains the very flat temperature profile in Figure 6.23. However, for $T = 1323$ K, the sum of the reaction heats is slightly negative in the centre of the membrane section, which explains the temperature dip for this case despite the maximum in the O_2 permeation flux in the centre of the membrane section.

The large axial differences in the reaction heats for the forward and backward directions can be explained by inspecting the axial profiles of the CO_2 and H_2O mole fractions in the bulk (Figure 6.25) and the axial profiles of the CO and H_2 selectivities in the bulk, which are given in Figure 6.27. For the forward direction, hardly any CO_2 or H_2O is produced in the beginning of the membrane section and accordingly the CO and H_2 selectivities are very high. This indicates that almost all CO_2 and H_2O are converted to CO and H_2 via endothermic reforming reactions and as a result heat is consumed. At the end of the membrane section, significant amounts of CO_2 and H_2O are produced leading to much lower CO and H_2 selectivities. Apparently, in this part of the membrane section exothermic combustion reactions play an important role and nett heat is produced.

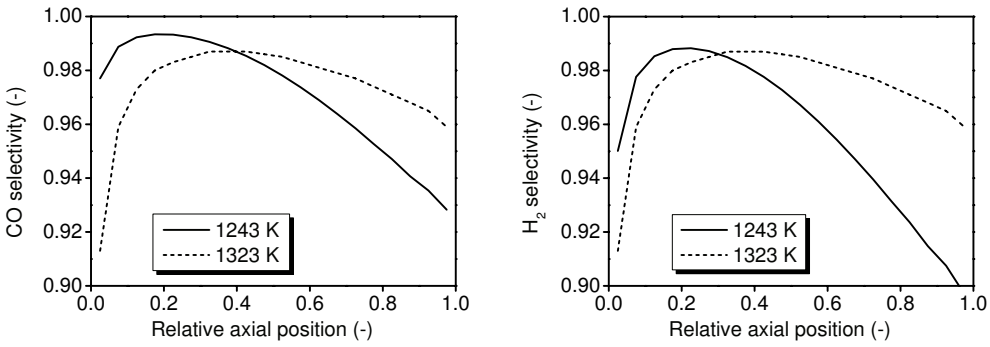

Figure 6.27: CO (left) and H_2 (right) selectivities in the bulk as a function of the relative axial position along the membrane in the RFCMR with perovskite membranes calculated with the HSFM (forward direction) for $T = 1243$ K and $T = 1323$ K ($w^{\mathrm{s}}_{\mathrm{g,CH4,in}} = 0.0003$).

6.3.3 HSFM simulation results: influence of temperature dependency of the O_2 permeation rate

The most important conclusion to be drawn from the HSFM simulation results presented previously is that the heat production at the end of the membrane section for the forward direction has to be matched very closely with the heat consumption at the same location for the backward direction (and *viceversa*) in order to avoid runaways and to establish the desired flat temperature plateau. When a constant permeability coefficient is assumed in the expression for the O_2 permeation rate and the activation energy is neglected, this can be achieved as was shown in Figure 6.23.

To investigate whether runaways can indeed be avoided, even when the activation energy of the O_2 permeation rate is accounted for, HSFM simulations were carried out, where the plateau temperature was controlled by continuously adjusting the amount of H_2O that is injected (analogous to a PID controller). It was found that for a relatively low plateau temperature of about 1243 K and a membrane length of 1 m, indeed a relatively flat temperature could be established and runaways could be avoided, as is demonstrated in Figure 6.28. At higher temperatures, no flat temperature plateaus could be established and runaways were observed at the beginning and end of the membrane section. When the simulations were initiated with a flat

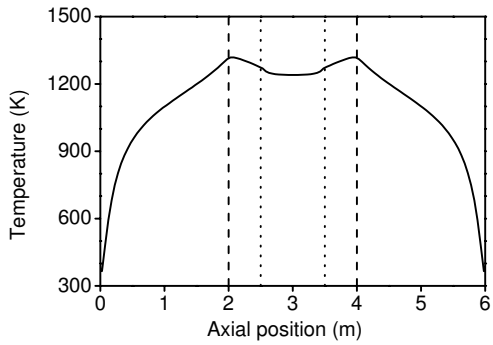

Figure 6.28: Axial temperature profile in the tube compartment of the RFCMR with perovskite membranes calculated with the HSFM while accounting for the temperature dependency of the O_2 permeation rate ($L_{\mathrm{membrane}} = 1$ m, $R_{\mathrm{H2O/O2}} = 0.345$, $w^{\mathrm{s}}_{\mathrm{CH4,g,in}} = 0.0003$). The combustion catalyst section is located between the dashed lines and the membrane section between the dotted lines.

temperature profile along the membrane section for these cases, the temperature at the beginning and at the end of the membrane section started to increase and the temperature in the centre started to decrease. The increased temperatures led to higher O_2 permeation rates so that locally even more reaction heat was produced due to the exothermic combustion reactions, which could no longer be balanced by the endothermic reforming reactions. This resulted in even higher temperatures and after some time very high temperature peaks were observed at the beginning and end of the membrane section. The decreasing temperature in the centre resulted in lower O_2 permeation rates and thus a locally reduced heat production so that the heat consumption of the endothermic reforming reactions could no longer be balanced by the heat production via exothermic combustion reactions and eventually temperature dips were observed in the centre.

It was investigated whether co-feeding of a part of the H_2O with the CH_4 could be a possible solution to prevent runaways at the beginning and end of the membrane section. For these cases the HSFM simulations showed a large temperature drop at the beginning of the membrane section, caused by the very fast steam reforming reaction, followed by a sharp temperature peak due to combustion reactions (and *viceversa* at the end of the membrane section) and still runaways were observed. Another solution

to avoid the large temperature peaks could be via imposing an axial H_2O injection profile. However, many different injection points would be required and the axial and radial temperature profiles would have to be monitored very closely, which is probably not economically feasible.

The runway problems caused by the relatively high temperature dependency of the O_2 transport rate through perovskite membranes might be solved by introducing a mass transfer limitation outside the membrane. This could be achieved by depositing the perovskite material on a porous support, which is designed in such a way that it acts as a mass transfer resistance. Because the activation energy of molecular diffusion is much smaller than that of the O_2 transport through the perovskite membrane, runaways could be effectively avoided. Use of a porous support has the additional advantage that it can provide for additional mechanical strength and so that the perovskite membrane can be made much thinner and higher O_2 permeation fluxes can be achieved. This principle of a porous support for the perovskite membrane, which acts as a mass transfer resistance that is almost independent of the temperature, was recently proposed by Air Products in the ITM-syngas project (Chen, 2005).

6.3.4 DM simulation results

For the HSFM simulations where the activation energy of the O_2 permeation rate was accounted for, only for low plateau temperatures runaways could be avoided by carefully matching the axial reaction heat profiles of the forward and backward flow directions. For the DM this matching of the axial reaction heat profiles is much more difficult, because in the DM the heat that is produced locally by the combustion reactions cannot be removed instantaneously by the reforming reactions as was the case for the HSFM, but only in the next semi-cycle. For very short switching times and low plateau temperatures a stable operation mode might be established, but these operating conditions are detrimental for the reactor performance.

As proposed earlier, a porous support which acts as an additional mass transfer resistance in order to provide for a relatively constant O_2 permeation flux along the membrane to the syngas compartment could avoid the occurrence of runaways. Therefore, to demonstrate the conceptual feasibility of the RFCMR concept with perovskite membranes in dynamic operation, a DM simulation was performed in which a constant O_2 permeation flux of 0.37 $mol/m^2/s$ was assumed. This value is equal to the

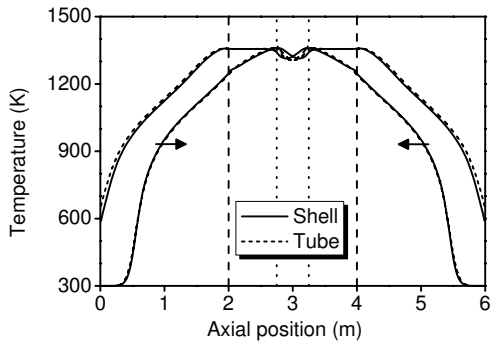

Figure 6.29: Axial temperature profiles in the shell and tube compartments of the RFCMR with perovskite membranes at the end of a forward (→) and backward (←) semi-cycle calculated with the DM (J_{O2} = 0.37 mol/m^2/s, t_{cycle} = 300 s, $R_{H2O/O2}$ = 0.2, $w^{s}_{CH4,g,in}$ = 0.0005). The combustion catalyst section is located between the dashed lines and the membrane section between the dotted lines.

spatially averaged O_2 permeation flux that was calculated for the HSFM simulation with T = 1323 K (see Figure 6.23). In Figure 6.29 the simulated axial temperature profiles in the shell and tube compartments at the end of a forward and backward semi-cycle in the cyclic steady state are presented. It is observed that a relatively flat temperature plateau is established in the membrane section, although still a temperature dip is observed, indicating that in the very centre of the membrane section some heat is consumed on average. However, this temperature dip does not affect the overall reactor performance. With respect to the heat exchange section, it is observed that the temperature gradients are very similar to those observed for the RFCMR with porous membranes (Chapter 4). An important difference is that the front velocity is twice as high, because of the higher flow rate of air compared to that of pure O_2. Therefore, the length of the heat exchange section needs to be twice as large for the RFCMR with perovskite membranes in order to achieve the same switching losses as for the RFCMR with porous membranes.

In Figure 6.30 the CO and H_2 selectivity, the CH_4 conversion and the H_2/CO ratio are given as a function of time during a semi-cycle. Besides some minor fluctuations at the beginning of the semi-cycle related to temperature changes at the end of the membrane section, the selectivities and conversion remain very constant during the

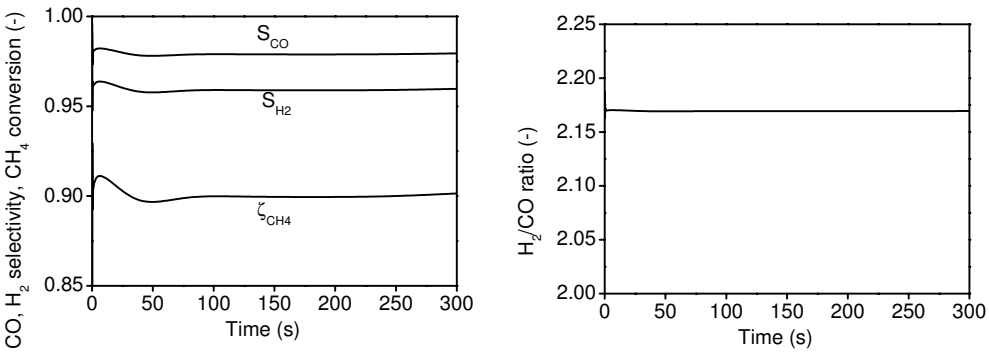

Figure 6.30: CO and H_2 selectivity, CH_4 conversion (left) and H_2/CO ratio (right) at the tube outlet as a function of time during a semi-cycle calculated with the DM ($J_{O2} = 0.37$ mol/m^2/s, $t_{cycle} = 300$ s, $R_{H2O/O2} = 0.2$, $w^{s}_{CH4,g,in} = 0.0005$).

semi-cycle. The time-averaged CO and H_2 selectivities are very high, 97.9 % and 95.9 %, respectively, and also the CH_4 conversion is high (89.7 %). Note that the CH_4 is somewhat lower because the air in the shell compartment was not fully depleted. Due to the relatively large amount of H_2O that had to be added to maintain isothermal conditions, also the H_2/CO ratio is relatively high (2.17). Although the selectivities and conversions are already very high and above values reported for industrial processes (Brejc and Supp, 1989; Aasberg-Petersen et al., 2001), they can be increased even further by selecting higher plateau temperatures. Therefore, a DM simulation was performed in which the O_2 permeation flux was set to 0.61 mol/m^2/s, the membrane length was decreased to 0.3 m and furthermore $R_{H2O/CO}$ was decreased to a value of 0.16. In Figure 6.31 the simulated axial temperature profiles in the shell and tube compartments at the end of a forward and backward semi-cycle are presented for this case and in Figure 6.32 the accompanying CO and H_2 selectivities, CH_4 conversion and H_2/CO ratio as a function of time during a semi-cycle. With the higher plateau temperature, CO and H_2 selectivities of 99.2 % and 98.0 % could be achieved, respectively, whereas the CH_4 conversion was increased to 92.2 %. The H_2/CO ratio is somewhat lower (2.14), due to the lower $R_{H2O/CO}$. These values are quite comparable with the values reported in Chapter 4 for the RFCMR with porous membranes. Therefore, it can be concluded that the DM simulation results have clearly demonstrated the conceptual feasibility of the RFCMR with perovskite membranes and its great potential for energy efficient syngas production with integrated air separation

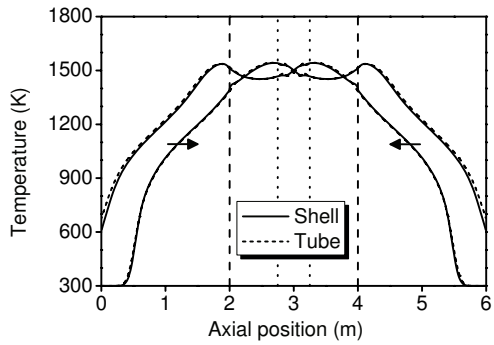

Figure 6.31: Axial temperature profiles in the shell and tube compartments of the RFCMR with perovskite membranes at the end of a forward (→) and backward (←) semi-cycle calculated with the DM (J_{O2} = 0.61 mol/m^2/s, t_{cycle} = 300 s, $R_{H2O/O2}$ = 0.16, $w^{s}_{CH4,g,in}$ = 0.001). The combustion catalyst section is located between the dashed lines and the membrane section between the dotted lines.

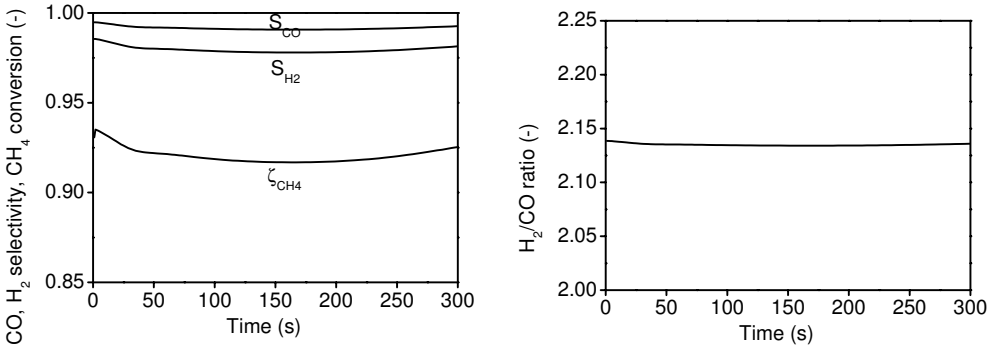

Figure 6.32: CO and H_2 selectivity, CH_4 conversion (left) and H_2/CO ratio (right) at the tube outlet as a function of time during a semi-cycle calculated with the DM (J_{O2} = 0.61 mol/m^2/s, t_{cycle} = 300 s, $R_{H2O/O2}$ = 0.16, $w^{s}_{CH4,g,in}$ = 0.001).

and integrated recuperative heat exchange, provided that a constant O_2 permeation flux along the membrane is realised.

6.4 Summary and conclusions

In this chapter the conceptual feasibility of the RFCMR concept with perovskite membranes for energy efficient syngas production with integrated air separation was investigated by means of a simulation study. In this study, a reactor model was employed that accounted for the strong influences of the temperature and the O_2 partial pressure at the membrane surface on the O_2 permeation rate via an experimentally determined permeation expression.

In order to capture the influences of the operating conditions and the syngas compositions on the O_2 permeation behaviour in the reactor model, the O_2 permeation rate through a perovskite membrane with composition $(LaCa)(CoFe)O_{3-\delta}$ was studied experimentally while sweeping with inert gasses and reducing gasses, including CH_4, CO and H_2. To elucidate the rate determining transport mechanism and to derive a permeation rate expression, the flow rates, the composition of the sweeping gas, the membrane thickness and the operating temperature were varied. It was found that under both non-reducing and reducing atmospheres, the O_2 permeation rate was controlled by bulk diffusion and that the permeation rate could be well described with the Wagner equation. Furthermore, it was found that when employing reducing sweeping gasses the O_2 partial pressure at the permeate side of the membrane can be calculated by assuming local thermodynamic equilibrium of the CO and H_2 combustion reactions at the membrane surface. In Table 6.6 the parameters of the Wagner equation that were determined for non-reducing and reducing sweeping gasses are summarised. The most noteworthy difference between these parameters is the difference in the exponent n. In the derivation of the Wagner equation a power law dependency of the non-stoichiometry on the relative O_2 partial pressure was assumed with a single value for n, which cannot describe the observed experimental results. With more detailed information on the oxygen dependency of the non-stoichiometry, the O_2 permeation rate might be expressed with a single correlation for both non-reducing and reducing atmospheres.

With the experimentally determined permeation expression, HSFM simulations were performed to study the behaviour of the RFCMR with perovskite membranes. It was found that when the temperature dependency of the O_2 permeation rate was ignored, trapezoidal temperature profiles, stoichiometric feeds and high syngas selectivities could be achieved by selecting appropriate design parameters. A very important

Table 6.6: Expressions for the O_2 permeation rate through a perovskite membrane with composition (LaCa)(CoFe)$O_{3-\delta}$ under non-reducing and reducing atmospheres on the permeate side of the membrane.

	non reducing	reducing
J_{O_2}	$\frac{P_0}{\Delta r_m}\exp\left(-\frac{E_a}{R_g T}\right)$ $\times\left[\left(P^t_{O_2,m}\right)^n-\left(P^s_{O_2}\right)^n\right]$	$\frac{P_0}{\Delta r_m}\exp\left(-\frac{E_a}{R_g T}\right)$ $\times\left[\left(P^t_{O_2,m}\right)^n-\left(P^s_{O_2}\right)^n\right]$
n	-0.063	-0.153
P_0 ($cm^4/cm^2/min$)	$4.140{\cdot}10^7$	$2.01{\cdot}10^8$
E_a (kJmol)	202	260

observation deduced from these simulation results was that the nett heat production or consumption changes enormously along the membrane and that in the beginning of the membrane section heat is consumed, whereas at the end heat is produced. For a relatively low plateau temperature the local heat consumption at the beginning of the membrane section during the forward semi-cycle could be balanced with the local heat production during the backward semi-cycle and *viceversa* at the end of the membrane section. Thus isothermal operation could be accomplished, despite the large axial differences in the local reaction heat production rate. However, when the temperature dependency of the O_2 permeation rate was accounted for, it was found that in the beginning and end of the membrane section the O_2 permeation flux increased strongly due to increasing temperatures and in the centre of this section the O_2 permeation flux decreased due decreasing temperatures. As a result the total reaction heat production and consumption could no longer be matched, which led to unstable operation and runaways. To circumvent the runaway problems caused by the relatively large activation energy of the O_2 transport rate, use of a porous support was proposed that acts as an additional mass transfer resistance (moderator), which renders the overall O_2 transport rate almost independent of the temperature and provides for a constant O_2 permeation flux. Finally, DM simulations were performed where a constant O_2 permeation flux was assumed. It was demonstrated that also with the RFCMR with perovskite membranes very high syngas selectivities could be achieved, higher than

typically encountered in industrial practice (Brejc and Supp, 1989; Aasberg-Petersen et al., 2001) while fully integrating air separation and recuperative heat exchange into a single apparatus.

6.5 Outlook

Finally in this thesis, a qualitative comparison is made between the RFCMR concept with porous membranes and the RFCMR concept with perovskite membranes to provide for an outlook on both reactor concepts. This comparison is based on the simulation and experimental results presented in Chapters 4-5 and this chapter. The different advantages and disadvantages have been summarised in Table 6.7 and are discussed in more detail below.

An important advantage of the RFCMR with perovskite membranes is that the air separation is integrated inside the reactor, circumventing the expensive separate air separation unit, which is especially attractive for small-scale applications. The penalty, however, is that to accomplish the *in situ* air separation, expensive and stable perovskite membranes are required, which also need a high temperature/high pressure difference resistant sealing. Another important aspect of the investment costs is related to the size of the reactors. In this respect the RFCMR with porous membranes has a clear advantage. This is because for this concept the required length of the heat exchange section is shorter due to the lower flow rates and furthermore the required membrane surface area is much lower, because the porous membranes only need to provide for distributive feeding of the O_2. Nonetheless, only a detailed cost analysis can reveal which reactor concept is most beneficial for a particular scale of operation.

Regarding the operation of both reactors, fouling proved to be a major problem for the RFCMR with porous membranes, whereas a good temperature control is probably the most important challenge for the RFCMR with perovskite membranes. For both issues solutions have been suggested, but these need to be studied in more detail. As discussed in Chapter 2, the syngas selectivities are primarily determined by the temperature and for the RFCMR concepts thus by the plateau temperature. For the RFCMR with porous membranes, high temperatures may not pose any problems as long as the membranes/filters retain their structural integrity. For the perovskite membranes very high temperatures might be detrimental for the chemical and thermal

Table 6.7: Qualitative comparison of the advantages (+) and disadvantages (–) of the RFCMR concepts with porous and perovskite membranes.

	RFCMR with porous membranes	RFCMR with perovskite membranes
Air separation costs	–	+
Construction material demands	+	–
Fouling	–	+
Length heat exchange section	+	–
Length membrane section	+	–
Maximal temperature	+	–
Temperature control	+	–

stability. However, the maximal operating temperature of both reactor concepts might also be limited by the stability/performance of the CPO catalyst.

Based on the comparison of the advantages and disadvantages of both reactor concepts, the RFCMR with porous membranes may be the concept of choice for large-scale syngas production and probably this concept can also be developed to pilot-plant scale within a relatively short period of time. Intrinsically, the RFCMR concept with perovskite membranes has a higher cost saving potential, but for this concept still further research is required with respect to the performance and stability of the perovskite membranes and the heat management of the reactor.

Acknowledgement

W. Zhang is gratefully acknowledged for having performed all the experimental work described in this chapter. G. Schorfhaar and R.L. Brouwer are gratefully acknowledged for the building of the experimental set-up and for their technical assistance. Also the financial support of the Dutch Technology Foundation STW, the Energy research Centre of the Netherlands ECN and the Association of Industrial Advisory Council Members of the Dutch Institute for Catalysis Research VIRAN is gratefully acknowledged.

Nomenclature

C_p	Heat capacity, J/kg/K
d_p	Particle diameter, m
$D_\mathrm{ax,j}$	Axial dispersion coefficient of species j, m^2/s
D_j	Diffusivity of species j in a mixture, m^2/s
D_V	Vacancy diffusivity, m^2/s
e'	Electron
E_a	Activation energy, J/mol
$h^{\cdot}$	Electron hole
H_j	Enthalpy of species j, J/mol
j_j	Mass flux of species j, $\mathrm{kg}/\mathrm{m}^2/\mathrm{s}$
J	Permeation rate, $\mathrm{mol}/\mathrm{m}^2/\mathrm{s}$
k_∞	Reaction rate constant, 1/s
k_O^0	Reaction rate constant
k_w	Wall-to-fluid mass transfer coefficient, m/s
K_eq	Equilibrium constant
L_inert	Length inert section, m
L_membrane	Membrane length, m
L_reactor	Reactor length, m
M_j	Molar weight of species j, kg/mol
$\langle M \rangle$	Average molar weight, kg/mol
n	Exponent in the power-law correlation of the non-stoichiometry number
O_O^x	Lattice oxygen
p	Pressure, Pa
p_STP	Standard pressure, $1{\cdot}10^5$ Pa
P_j	Relative partial pressure of species j
P	Permeability coefficient, mol/m/s
P_0	Pre-exponential factor in the permeability coefficient, mol/m/s
Pr	Dimensionless Prandtl number, $C_\mathrm{p,g}\eta_\mathrm{g}/\lambda_\mathrm{g}$
r_i	Inner tube radius, m
r_j	Reaction rate of species j, $\mathrm{kg}/\mathrm{m}^3/\mathrm{s}$
Δr_m	Membrane thickness, m
r_o	Outer tube radius, m
R_g	Gas constant, 8.314 J/mol/K

R_j	Reaction rate of species j, mol/m^3/s
Re	Dimensionless Reynolds number, $\rho_\mathrm{g} v_\mathrm{g} d_\mathrm{p}/\eta_\mathrm{g}$
S	Selectivity
s_cell	Unit cell length, m
Sc	Dimensionless Schmidt number, $\eta_\mathrm{g}/\rho_\mathrm{g}/D$
t	Time, s
t_cycle	Switching time, s
T	Temperature, K
v	Superficial velocity, m/s
V_m	Molar volume, m^3/mol
$V_\mathrm{O}^{\cdot\cdot}$	Oxygen vacancy in the perovskite
w_j	Weight fraction of species j
x_j	Mole fraction of species j
z	Spatial coordinate, m

Greek symbols

$\alpha^{\mathrm{s-tw}}$	Wall-to-shell heat transfer coefficient, J/m^2/K/s
$\alpha^{\mathrm{t-tw}}$	Wall-to-tube heat transfer coefficient, J/m^2/K/s
ϵ	Porosity
δ	Non-stoichiometry number
δ_0	Coefficient in the non-stoichiometry number
η	Viscosity, kg/m/s
λ	Thermal conductivity, J/m/K/s
λ_eff	Effective thermal conductivity, J/m/K/s
ρ	Density, kg/m^3
ρ_bulk	Packed bed bulk density, kg/m^3
Φ_v	Flow rate, cm^3/min

Subscripts

I	CO combustion
II	H_2 combustion
in	Inlet
g	Gas
m	At the membrane surface

out	Outlet
s	Solid

Superscripts

s	Shell
t	Tube
tw	Tube wall

Bibliography

Aasberg-Petersen, K., Bak Hansen, J. H., Christensen, T. S., Dybkjaer, I., Seier Christensen, P., Stub Nielsen, C., Winter Madsen, S. E. L., Rostrup-Nielsen, J. R., "Technologies for large scale gas conversion", Applied Catalysis A: General, 221(1-2), 379–387 (2001)

Balachandran, U., Dusek, J. T., Mieville, R. L., Poeppel, R. B., Kleefisch, M. S., Pei, S., Kobylinski, T. P., Udovich, C. A., Bose, A. C., "Dense ceramic membranes for partial oxidation of methane to syngas", Applied Catalysis A: General, 133(1), 19–29 (1995)

Bird, R. B., Stewart, W. E., Lightfoot, E. N., "Transport Phenomena", 2nd Edition, John Wiley and Sons, New York (2002)

Bouwmeester, H. J. M., "Dense ceramic membranes for methane conversion", Catalysis Today, 82(1-4), 141–150 (2003)

Bouwmeester, H. J. M., Burggraaf, A. J., "Dense ceramic membranes for oxygen separation", in "The CRCR Handbook of Solid State Electrochemistry", Gellings, P. J., Bouwmeester, H. J. M. Eds., CRC Press, London, 481–553 (1997)

Bredesen, R., Sogge, J., "A Technical and Economic Assessment of Membrane Reactors for Hydrogen and Syngas Production", Seminar on the Ecological Applications of Innovative Membrane Technology in the Chemical Industry, Cetraro, Italy, (1996)

Brejc, M., Supp, E., "Non-catalytic partial oxidation and special gasification process for higher-boiling hydrocarbons", in "Ullmanns Encyclopedia of Industrial Chemistry", Elvers, B., Hawkins, S., Ravenscroft, M., Rounsaville, J. F., Shulz, G. Eds., 5th Edition, Vol. A12, VCH Verlagsgesellschaft, Weinheim, 204–214 (1989)

Chen, C. M., "Ceramic membrane reactor systems for converting natural gas to hydrogen (ITM syngas)", US Department of Energy (2005)
URL `http://www.eere.energy.gov`

Diethelm, S., Van herle, J., Middleton, P. H., Favrat, D., "Oxygen permeation and stability of $La_{0.4}Ca_{0.6}Fe_{1-x}Co_xO_{3-d}$ (x = 0, 0.25, 0.5) membranes", Journal of Power Sources, 118(1-2), 270–275 (2003)

Kruidhof, H., Bouwmeester, H. J. M., van Doorn, R. H. E., Burggraaf, A. J., "Influence of order-disorder transitons on oxygen permeability through selected nonstoichiometric perovskite-type oxides", Solid State Ionics, 63-65, 816–822 (1993)

Ran, S., Zhang, X., Yang, P. H., Jiang, M., Peng, D. K., Chen, C. S., "Oxygen transport through $SrFe_{1.125}CO_{0.375}O_y$ coupled with oxidation of carbon monoxide", Solid State Ionics, 135(1-4), 681–685 (2000)

Stephens, W. T., Mazanec, T. J., Anderson, H. U., "Influence of gas flow rate on oxygen flux measurements for dense oxygen conducting membranes", Solid State Ionics, 129(1-4), 271–284 (2000)

Ten Elshof, J. E., Bouwmeester, H. J. M., Verweij, H., "Oxygen transport through $La_{1-x}Sr_xFeO_{3-\delta}$ membranes II. Permeation in air/CO, CO_2 gradients", Solid State Ionics, 89(1-2), 81–92 (1996)

Tsai, C. Y., Dixon, A. G., Moser, W. R., Ma, Y. H., "Dense perovskite membrane reactors for partial oxidation of methane to syngas", AIChE Journal, 43(11), 2741–2750 (1997)

Van Hassel, B. A., Ten Elshof, J. E., Bouwmeester, H. J. M., "Oxygen permeation flux through $La_{1-y}Sr_yFeO_3$ limited by carbon monoxide oxidation rate", Applied Catalysis : General, 119, 279–291 (1994)

Xu, S. J., Thomson, W. J., "Stability of $La_{0.6}Sr_{0.4}Co_{0.2}Fe_{0.8}O_{3-\delta}$ perovskite membranes in reducing and non-reducing environments", Industrial & Engineering Chemistry Research, 37, 1290–1299 (1998)

Yagi, S., Wakao, N., "Heat and mass transfer from wall to fluid in packed beds", AIChE Journal, 5, 7985 (1959)

List of Publications

Graduation work

1. D.J. Patil, J. Smit, M. van Sint Annaland and J.A.M. Kuipers, Wall-to-bed heat transfer in gas-solid fluidized beds: a computational and experimental study, AIChE Journal, 52(1), pp. 58-74 (2006)

This thesis

1. J. Smit, M. van Sint Annaland and J.A.M. Kuipers, Modelling of a reverse flow catalytic membrane reactor for the partial oxidation of methane, International Journal of Chemical Reactor Engineering, 1, Article A54 (2003)
   Presented at Chemical Reaction Engineering IX: Meeting The Challenges for New Technology, June 29 - July 4, 2003, Québec City, Canada

2. J. Smit, M. van Sint Annaland and J.A.M. Kuipers, Development of a novel reactor concept for the partial oxidation of methane to syngas, Chemical Engineering Research and Design, 82(2), pp. 245-251 (2004)
   Presented at the 3$^{\text{rd}}$ International Symposium on Multifunctional Reactors and the 18$^{\text{th}}$ Colloquium on Chemical Reaction Engineering, August 27-29, 2003, Bath, United Kingdom

3. J. Smit, M. van Sint Annaland and J.A.M. Kuipers, Grid adaptation with WENO schemes for non-uniform grids to solve convection-dominated partial differential equations, Chemical Engineering Science, 60(10), pp. 2609-2619 (2005)

4. J. Smit, G.J. Bekink, M. van Sint Annaland and J.A.M. Kuipers, A reverse flow catalytic membrane reactor for the production of syngas: an experimental

study, International Journal of Chemical Reactor Engineering, 3, Article A12 (2005)
Presented at Chemical Reaction Engineering X: Innovations in Chemical Reactor Engineering, August 28 - September 2, 2005, Zacatecas City, Mexico

5. J. Smit, M. van Sint Annaland and J.A.M. Kuipers, Feasibility study of a reverse flow catalytic membrane reactor with porous membranes for the production of syngas, Chemical Engineering Science, 60(24), pp. 6971-6982 (2005)

6. J. Smit, M. van Sint Annaland and J.A.M. Kuipers, Syngas production from natural gas with improved energy efficiency using reverse flow catalytic membrane reactors, NPT Procestechnologie, 12(6), pp. 8-10 (2005)

7. W. Zhang, J. Smit, M. van Sint Annaland and J.A.M. Kuipers, Feasibility Study of the RFCMR Concept with Perovskite Membranes. Part 1: O_2 permeation through a perovskite membrane under reducing and non-reducing atmospheres, in preparation

8. J. Smit, W. Zhang, M. van Sint Annaland and J.A.M. Kuipers, Feasibility Study of the RFCMR Concept with Perovskite Membranes. Part 2: Adiabatic reactor simulations, in preparation

9. J. Smit, M. van Sint Annaland and J.A.M. Kuipers, Experimental demonstration of the RFCMR concept for energy efficient syngas production. Part 1: Influence of operating conditions, in preparation

10. J. Smit, G.J. Bekink, M. van Sint Annaland and J.A.M. Kuipers, Experimental demonstration of the RFCMR concept for energy efficient syngas production. Part 2: Validation of reactor model, in preparation

Levensloop

Joris Smit werd op 17 december 1976 geboren in Sint-Oedenrode. Al na een jaar verhuisde hij naar "het dorp" Deurne, alwaar hij de R.K. Basisschool de Piramide en het St.-Willibord gymnasium bezocht. In juni 1995 nam hij het VWO diploma in ontvangst.

In augustus 1995 begon hij aan de opleiding Chemische Technologie aan de Universiteit Twente. In het kader van deze opleiding liep hij in het voorjaar van 2000 stage bij Christian Michelsen Research AS/Prototech AS te Bergen, Noorwegen. In augustus 2001 studeerde hij af bij de vakgroep Fundamentele Aspecten van de Proceskunde op een afstudeerscriptie getiteld: "Heat transfer in fluidised beds: Improvement of a CFD model and experimental validation". In september van hetzelfde jaar werd het *met lof* behaalde ingenieursdiploma in ontvangst genomen. Voor zijn afstudeerscriptie kreeg hij in november 2001 de Unilever Research Prijs 2001 uit handen van Unilever bestuursvoorzitter Antony Burgmans.

Direct na afloop van zijn studie begon hij in september 2001 in dienst van de vakgroep Fundamentele Aspecten van de Proceskunde om als assistent in opleiding een promotieonderzoek te verrichten naar energiezuinige productie van synthese gas uit aardgas. De resultaten van dit onderzoek staan beschreven in dit proefschrift.

Dankwoord

Met dit dankwoord komt er een eind aan dit proefschrift en dus ook aan mijn promotietijd. Derhalve zou ik graag de mensen willen bedanken die een (hoofd)rol gespeeld hebben bij het tot stand komen van dit proefschrift, maar ook de mensen die de promotietijd tot een hele plezierige tijd hebben gemaakt.

Hans Kuipers ben ik erg dankbaar voor het mij aanbieden van deze promotieplaats. Vooraf zei je dat het een uitdagend project was en dat bleek het ook op veel gebieden te zijn. Je gaf me de vrijheid in het begin mijn eigen weg te gaan en hebt me altijd gesteund in de gemaakte keuzes, dit heb ik bijzonder gewaardeerd. De 3-wekelijkse bespreken waren altijd nuttig en vruchtbaar en zorgden voor nieuwe zienswijzen, maar ook je interesse en enthousiasme buiten deze besprekingen alsmede de zeer korte termijn waarbinnen je artikelen en hoofdstukken corrigeerde waren erg stimulerend.

Martin van Sint Annaland ben ik zeer erkentelijk mij over te halen om een promotie te doen, ik heb hier geen seconde spijt van gehad. Je kritische houding om een zo hoog mogelijk wetenschappelijk niveau na te streven heb ik zeer gewaardeerd. Zonder jouw creatieve ingevingen, suggesties en jouw onschatbare theoretische en experimentele kennis hadden de verkregen resultaten niet gerealiseerd kunnen worden. Ik zal de vele vruchtbare discussies die we gehad hebben dan ook gaan missen, maar ook de hele prettige manier van samenwerken. Door het al vroeg stimuleren van het schrijven van artikelen zijn er reeds een aantal artikelen gepubliceerd en daar heb ik bij het schrijven van het proefschrift veel voordeel van gehad.

Wenxing Zhang is greatfully acknowledged for participating in this project as a post-doc and for his tremendous efforts on the sealing of the perovskite membranes and the extensive measurements of the O_2 permeation rates under extremely difficult

operating conditions. It was a lot of fun to work with you.

Mijn afstudeerders hebben ook belangrijke bijdrages geleverd aan het tot stand komen van dit proefschrift. Martijn van der Perk werkte aan de ontwikkeling van de sealing voor de poreuze membranen en heeft conversies en selectiviteiten met verschillende katalysatoren gemeten. Jeroen Hassink keek naar de invloed van inerte secties en gasfase reacties op het gedrag van reverse flow reactoren. Ger Bekink verrichte veel tijdrovend werk met de demonstratieopstelling en haalde zonder te klagen talloze keren de reactor uit elkaar om hem daarna weer terug in elkaar te zetten. Ik vond het heel plezierig om met jullie samen te werken en wil jullie hartelijk bedanken voor jullie inzet!

Jan van Ommen en Henny Bouwmeester wil ik bedanken voor menige vruchtbare discussies op het gebied van katalysatoren en perovskiet membranen. De leden van de gebruikerscommissie alsmede de andere academici die betrokken waren in het onderzoeksproject wil ik hierbij bedanken voor hun input tijdens de diverse project meetings. Ook Charudatta Patil en Toine Cents ben ik zeer erkentelijk voor hun input en de vele discussies.

Cikse Dillerop and Umesh Ramdhani studied the economical aspects of the novel reactor concepts within the course Fabrieksontwerp under the supervision of Louis van der Ham en Henk van den Berg. Thanks a lot for your efforts, hopefully your results will initiate a realisation of one of the novel reactor concepts in industry.

Aan de experimentele resultaten hebben een groot aantal mensen een belangrijke bijdrage gehad. Ten eerste wil ik Gerrit Schorfhaar hartelijk bedanken voor het zeer secuur bouwen van de opstellingen, maar ook voor de vele gezellige gesprekken over van alles en nog wat. Ik vond het zeer plezierig de afgelopen 5 jaar met je samen te werken. Benno Knaken ben ik zeer dankbaar voor het oplossen van zowel mechanische als elektronische problemen en met het meedenken over alternatieven. Tevens wil ik je bedanken voor het lassen van de eerste "kerstboom" die het lang heeft vol gehouden. Robert Brouwer wil ik bedanken voor het bouwen van de elektronicakasten en Robert Meijer voor het ontwerp daarvan. Robert Meijer wil ik tevens bedanken voor zijn computer gerelateerde hulp. Ook Henk Jan Moed en Wim Leppink worden bedankt voor hun diverse bijdragen. Ria Hofs-Winkelman en Nicole Haitjema wil ik heel hartelijk bedanken voor al hun administratieve werk.

Mieke Luijten wil ik bedanken voor haar adviezen bij de keuze van de poreuze membranen en Kimball Roelofs van Membraflow ben ik veel dank verschuldigd voor het kosteloos ter beschikking stellen van de poreuze alumina buizen. Gerrit Mollenhorst wil ik bedanken voor zijn adviezen en hulp in de ontwikkeling van de verschillende sealings. Joop Snoeyenbos ben ik zeer erkentelijk voor het slijpen van de vele keramiek buizen en membranen en ook Jan van Veen, Ruud van den Brink en Dick Witteveen worden bedankt voor hun diverse bijdragen. Theo Pünt wil ik bedanken voor het maken van de stalen filters en Bert Geerdink voor zijn hulp met het aansturen van de massflow controllers. Jianjun Zhu is greatfully acknowledged for the preparation of the Rh/YsZ catalyst. Patrick Graf wordt bedankt voor zijn adviezen voor het prepareren van de $Rh/Pt/Al_2O_3$ katalysator. Martin Pijl van Varian ben ik zeer erkentelijk voor het op zeer korte termijn oplossen van problemen met de Micro-GC.

Wim Platvoet en Nelly Voss wil ik bedanken voor de bestelling van alle benodigde onderdelen en Henk Bruinsma, Roy Schnör en Ineke Klinkenberg voor het afhandelen van de binnengekomen bestellingen. Tevens ben ik Karin Schildkamp en Benny Hövels dankbaar voor het bestellen van de chemicaliën en gassen. Ook de andere diensten binnen de faculteit CT/TNW wil ik bij deze bedanken.

Het lijkt nog maar kortgeleden dat ik aan mijn promotie begon, maar intussen zijn er alweer ruim vier jaar verstreken. Time flies when you're having fun! Ik wil dan ook al mijn collega-promovendi, studenten en anderen werkzaam bij FAP en OOIP bedanken voor de zeer gezellige tijd. Ik heb dan ook zeer dierbare herinneringen aan alle borrels, uitjes en zeilweekenden. Ik denk nog met veel plezier terug aan de zaalvoetbalwedstrijden vrijdag tussen de middag en de eeuwige discussies of we verloren hadden door gebrek aan kwaliteit, slechte tactieken of door gebrek aan fitheid. Verder wil ik Liesbeth Kuipers bedanken voor de organisatie van de gezellige skivakanties en de Waarbeekfeesten.

Na ruim 16 jaar met Wilbert van de Ven en Peter Derks samen op "school" gezeten te hebben, komt daar nu helaas een eind aan. Ook mede dankzij jullie waren de afgelopen vier jaar zeer plezierig. Op Calslaan 30 A stond er in de eerste jaren van mijn promotie na het werk altijd een warm bord eten te wachten en ook aan de gezellige kaart- en spelletjesavonden en aan de jaarlijkse kerstdiners heb ik warme herinneringen. Mijn biljartteamgenoten van BSV de Stoottroepen en mijn zaalvoet-

balteamgenoten van Z17 wil ik bedanken voor de vele plezierige avonden. Verder ben ik mijn uit Deurne afkomstige vrienden dankbaar voor de altijd gezellige weekenden.

Tenslotte wil mijn ouders bedanken voor al hun steun de afgelopen jaren. Misschien begrepen jullie niet altijd waar ik mee bezig was, maar zonder jullie had ik dit nooit kunnen bereiken. Ook mijn zusjes Marloes en Dorien, hun partners Hein en Jeroen alsmede mijn overige familie wil ik bedanken voor al hun steun.

Nogmaals heel erg bedankt iedereen!

Joris